

University of Southampton Research Repository ePrints Soton

Copyright © and Moral Rights for this thesis are retained by the author and/or other copyright owners. A copy can be downloaded for personal non-commercial research or study, without prior permission or charge. This thesis cannot be reproduced or quoted extensively from without first obtaining permission in writing from the copyright holder/s. The content must not be changed in any way or sold commercially in any format or medium without the formal permission of the copyright holders.

When referring to this work, full bibliographic details including the author, title, awarding institution and date of the thesis must be given e.g.

AUTHOR (year of submission) "Full thesis title", University of Southampton, name of the University School or Department, PhD Thesis, pagination

UNIVERSITY OF SOUTHAMPTON FACULTY OF NATURAL AND ENVIRONMENTAL SCIENCES SCHOOL OF CHEMISTRY

Electrodeposition of metallic and semiconducting nanocentres

Nawal Al Abass

Thesis for the degree of Doctor of Philosophy

October 2014

UNIVERSITY OF SOUTHAMPTON <u>ABSTRACT</u> FACULTY OF NATURAL AND ENVIRONMENTAL SCIENCES SCHOOL OF CHEMISTRY

Doctor of Philosophy

Electrodeposition of metallic and semiconducting nanocentres

by Nawal Al Abass

Nanoparticles, particularly those of noble metals, are of considerable importance for their applications in catalysis and fuel cells. Fundamentally they are interesting for their unusual physical and chemical properties due to their size and shape. Generally, they owe their large catalytic activity per gram to their high surface area to volume ratio but often nanoparticles are facetted and the large proportion of surface atoms located on edges and corners further enhances their reactivity. In the main part of this project the electrodeposition of palladium (from ammonium tetrachloropalladate (II)) on gold and carbon substrates was studied using cyclic voltammetry and chronoamperometry. Pd deposits on vitreous carbon substrates were prepared by electrodeposition from liquid crystal phases (both micellar and hexagonal phases) consisting of self-assembled non-ionic surfactant molecules. The morphology of the deposits varies with the concentration of surfactant but all are made up of aggregated nanoparticles circa 9 nm in diameter. The deposits from the micellar phase of the surfactant offer the largest electroactive area and specific activity for the hydrogen evolution, oxygen evolution and reduction reactions, formic acid and ethanol oxidations. Unexpectedly the deposits yield an increase in catalytic activity far in excess of that expected from an enhancement in electroactive area. The chronoamperometric transients recorded during the deposition were analysed using the nucleation and growth model from Heerman and Tarallo to investigate if and how the surfactant template affected the nucleation and growth parameters, number of nucleation sites and nucleation rate. Nanostructured palladium and platinum films were also produced on gold substrates with the micellar phase mixtures. Interestingly their specific catalyst area was found to be larger than those obtained when the films were prepared without template or with the hexagonal phase.

The second part of the work investigated the electrodeposition and doping of ZnSe particles for the purpose of developing a nano-scale light emitting diode. The ZnSe was electrochemically deposited and several trials were conducted to fabricate a p-n junction between two electrically conductive carbon nonporous materials. ZnSe was successfully deposited on different carbon substrates; the characterization by EDX indicated a good ratio between Zn and Se. XRD confirmed the presence of cubic ZnSe and current voltage curves recorded by contacting two doped ZnSe surfaces showed rectification indicative of a p-n junction.

Contents

1.	Introduction	1
	1.1 Nanoparticles	1
	1.2 Electrodeposition	1
	1.3 Nucleation and growth of metal centres	3
	1.3.1 The role of overpotential in the nucleation and growth process	4
	1.3.2 Theories for the chronoamperometric transients of nucleation and growth	7
	1.4 Preparation of palladium nanocentres	10
	1.5 Application of palladium nanocentres	14
	1.6 Surfactants	15
	1.6.1 Lyotropic liquid crystal phases LLC	15
	1.6.2 Lyotropic liquid crystal templating	17
	1.7 Platinum nanostructured films	19
	1.8 Semiconductors	20
	1.9 Electronic energy bands: basic theory	21
	1.10 Doping	22
	1.10.1 n-type semiconductor	24
	1.10.2 p-type semiconductor	25
	1.11 p-n junction diode	26
	1.12 Built – in potential barrier	27
	1.13 Applying bias to the p-n junction	27
	1.13.1 Forward Characteristic	28
	1.13.2 Reverse characteristic	28
	1.14 Semiconductor Photo-Electrochemistry	29
	1.14.1 Potential distribution across the electrode interface	31
	1.14.2 Photo-effects of semiconductor electrodes	33
	1.15 Zinc selenide semiconductor	35
	1.16 Thesis structure	36
2.	Experimental	37
	2.1 Reagents	37
	2.2 Instrumentation	37
	2.3 Electrochemical equipment	38
	2.4 Fabrication of electrodes	38
	2.5 Reference electrodes	40

	2.5.1 SCE reference electrode	40
	2.5.2 SMSE reference electrode	40
	2.5.3 Mercury-mercuric oxide reference electrodes (MMO)	41
	2.6 Electrode pre-treatment	42
	2.6.1 Gold	42
	2.6.2 Glassy carbon (GC)	42
	2.7 Electrode characterisation	43
	2.7.1 Gold electrode characterisation	43
	2.7.2 Glassy carbon electrode characterisation	43
	2.8 Electrodeposition of Palladium	44
	2.9 Preparing various concentrations of surfactant in lyotropic liquid crystal mixtures for Pt electrodeposition	47
	2.10 Electrodeposition of ZnSe semiconductors	48
	2.11 Electrochemical Analysis	48
	2.11.1 Cyclic Voltammetry (CV)	48
	2.11.2 Chronoamperometry	49
	2.11.3 Impedance spectroscopy (EIS)	49
	2.12 Characterization techniques	49
	2.12.1 Scanning Electron Microscopy (SEM)	49
	2.12.2 Atomic Force Microscopy (AFM)	50
	2.12.3 Helium ion microscopy (HIM)	50
	2.12.4 X-ray Diffraction (XRD)	50
	2.13 Software	51
3	. Early stages of electrodeposition of Pd nanoparticles on different carbon substrates	52
	3.1 Carbon fibres	52
	3.1.1 Single potential steps	54
	3.2 Highly Ordered Pyrolytic Graphite	60
	3.3 Glassy carbon (GC)	68
	3.4 Conclusion	74
4	. Pd electrodeposition from lyotropic liquid crystals mixtures	76
	4.1 Cyclic voltammetry of Pd in different plating mixtures with glassy carbon electrodes	76
	4.2 Nucleation and growth of Pd centres	79
	4.3 Kinetic analysis of the nucleation and growth	82
	4.3.1 The Scharifker-Hills model	82

	4.3.2 The Heerman-Tarallo model	85
	4.4 Conclusion	99
5.	The unexpected activity of Pd nanoparticles prepared within a non-ionic surfactant template	. 101
	5.1 Pd electrodeposition from lyotropic liquid crystals mixtures	. 101
	5.2 Characterization by voltammetry in acid	. 106
	5.3 Electrocatalytic activity:	. 109
	5.3.1 Oxidation of formic acid and ethanol	. 109
	5.3.2 Electrocatalytic activity: oxygen and hydrogen evolution	. 111
	5.3.3 Electrocatalytic activity: oxygen reduction	. 113
	5.4 Analysis	. 115
	5.5 Electrodeposition of Pd from lyotropic liquid crystal mixtures on highly ordered pyrolytic graphite (HOPG)	. 116
	5.6 Conclusion	. 119
	Nanostructured films of palladium from lyotropic liquid crystal mixtures on gold microelectrod	
	6.1 Electrodeposition of Pd from lyotropic liquid crystal mixtures on gold microelectrode	. 120
	6.1.1 Electrodeposition via cyclic voltammetry	. 120
	6.1.2 Electrodeposition via chronoamperometry	. 125
	$6.1.3$ Summary of films parameters evaluated from the CVs in 1 M H_2SO_4 and the current transient in different ratios of surfactant	. 133
	6.2 Conclusion	. 134
7.	Electrodeposition of ZnSe semiconductor	. 135
	7.1 Voltammetry of Zn, Se and ZnSe films on GC electrode	. 136
	7.1.1 Voltammetry when doping with N and Ga	. 139
	$7.1.2$ Influence of the SeO $_2$ concentration	. 145
	7.1.3 Influence of the deposition potential	. 147
	7.2 Electrodeposition of ZnSe on carbon paper	. 149
	7.2.1 Effect of ZnSO ₄ and SeO ₂ concentrations	. 152
	7.2.2 Simple p-n junction diodes	. 163
	7.3 Conclusion	. 163
8.	Conclusions and future work	. 165
9.	Electrodeposition of platinum from lyotropic liquid crystals mixture	. 168
	9.1 Electrodeposition via cyclic voltammetry	. 168
	9.2 Electrodeposition of platinum at various charge densities	. 172
10) References	175

List of Figures

Figure 1-1 Steps involved in the nucleation and growth of hemispherical nuclei on an electrode surface
Figure 1-2 Overview of Pd nanoparticle synthesis and stabilisation inside a dendrimer molecule.
Taken from [51]
Figure 1-4 TEM images of Pd nanoparticles prepared in air at (A) $t = 5$ min; (B) $t = 3$ h; (C) $t = 5$ h; and (D) $t = 7$ h 40 min. Twinned particles are indicated by tw. The inset of (A) shows the magnified image of a 5-fold twinned nanoparticle. Taken from [73].
Figure 1-5 Phase diagram of the non-ionic surfactant octaethylene glycol monohexadecyl ether $C_{16}EO_8$. The diagram displays temperature vs. surfactant wt.% in water. Reproduced from[82]
Figure 1-6 Shows the progression of hexagonal phase LLC templating, a) shows the hexagonal LLC columns adsorbed to the substrate surface, a potential is applied and reduction of the metal ions begins. b) Deposition of the metal has occurred around the hexagonal phase columns. c) The surfactant is removed by washing and pores remain in the film
Figure 1-7 on the left: resistivity vs. temperature for a metal, on the right: resistivity vs.
temperature for a semiconductor. Redrawn from reference [104]21
Figure 1-8 Comparison of the band gaps for a metal, a semiconductor and an insulator. Redrawn from reference [107]22
Figure 1-9 Diagram showing the electronic bonds in an intrinsic semiconductor (Si). Taken from [112]
Figure 1-10 <i>n</i> -doping with a group 5 element, the left side, band model of n-doped semiconductors, right side. Reproduced from [113]25
Figure 1-11 p-doping with group 5 elements, left side and band model of p-doped semiconductors, right side. Reproduced from [113]25
Figure 1-12 p-n junction, left, and its electrical schematic symbol, right. Redrawn from[114] 26 Figure 1-13 p-n junction I-V characteristic. Reproduced from [115]
Figure 1-14 Biasing the p-n junction (forward characteristic). Taken from [116]28
Figure 1-15 Biasing the p-n junction (reverse characteristic). Reproduced from [116]
Figure 1-17 Band bending for an n-type semiconductor (a) and a p-type semiconductor (b) in equilibrium with an electrolyte. Reproduced from [121]31
Figure 1-18 Effect of varying the applied potential (E) on the band edges in the interior of an p-
type semiconductor, left column, and of an n-type semiconductor, right column. a) $E > E_{fb}$, b) $E = E_{fb}$, c) $E < E_{fb}$. Reproduced from [121]
Figure 1-19 Ideal behaviour for an n-type semiconductor in the dark (a) and under irradiation. Reproduced from [121]
Figure 2-1 Schematic diagram of a three neck pear-shaped cell
Figure 2-2 Schematic diagram for the gold/ platinum electrode
Figure 2-3 Schematic diagram indicating the set up of the three electrode system for
electrodeposition on HOPG

Figure 2-4 The schematic diagram of a 7 μm diameter carbon fibre wire electrode40
Figure 2-5 A diagram of a) saturated calomel electrode (SCE) and b) saturated mercury sulphate
electrode (SMSE)41
Figure 2-6 A diagram of mercury mercurous oxide (MMO) reference electrode42
Figure 2-7 Cyclic voltammogram of a polished 50 μm diameter gold disc electrode in Ar purged
1 M sulphuric acid at scan rate of 100 mV s ⁻¹ 43
Figure 2-8 Cyclic voltammogram of a polished 3000 µm diameter glassy carbon disc electrode in
1 M sulphuric acid at scan rate 100 mV s ⁻¹ 44
Figure 2-9 Image of the hexagonal liquid crystalline phase observed with a polarising optical
microscope. The scale bar is 200 µm long46
Figure 2-10 Schematic diagram indicating the three electrode system for electrodeposition in
the 48 wt.% surfactant mixture46
Figure 2-11 Schematic diagram indicating the setup when using the falling sphere viscometer.47
Figure 3-1 Electron microscopy picture of a carbon fibre, taken from [148]52
Figure 3-2 Cyclic voltammogram (5th scan) recorded at a 5 mm long, 7 μm diameter carbon
electrode in 1 M sulphuric acid at 100 mV s ⁻¹ 53
Figure 3-3 Cyclic voltammograms recorded with a carbon fibre (\emptyset = 7 μ m, 5 mm long) electrode
in 1 mM (NH ₄) ₂ PdCl ₄ + 0.5 M KCl at υ =10 mV s ⁻¹ 54
Figure 3-4 Current transients recorded with carbon fibres (\emptyset = 7 μ m, 5 mm long) during
electrodeposition in 1 mM (NH_4) ₂ $PdCl_4$ + 0.5 M KCl. The potential was stepped from 0.7 V vs.
SCE to the deposition potentials indicated on the Figure55
Figure 3-5 SEM images of the carbon fibre (\emptyset = 7 μ m, 5 mm long) surface showing the Pd
particles after 1 min of electrodeposition in 1 mM $(NH_4)_2$ PdCl ₄ + 0.5 M KCl. The potential was
stepped from 0.7 V vs. SCE to the deposition potentials shown on the Figure56
Figure 3-6 SEM images of the carbon fibres (\emptyset = 7 μ m, 5 mm long) showing the initial stages of
the Pd electrodeposition in 1 mM (NH $_4$) $_2$ PdCl $_4$ + 0.5 M KCl after stepping the potential from 0.7
V to -0.15 V vs. SCE for 20, 15, 10, 5, 1, 0.5 and 0.1 s
Figure 3-7 Histograms of the particle count analysis performed on the SEM images shown in
Figure 3-6. The top, middle and bottom histograms respectively correspond to 1, 0.5 and 0.1 s
deposition times59
Figure 3-8 Cyclic voltammogram recorded at 10 mV s $^{-1}$ with a 5 mm Ø basal plane HOPG
electrode in argon purged 1 mM (NH $_4$) $_2$ PdCl $_4$ + 0.5 M KCl60
Figure 3-9 Current transients for the electrodeposition of Pd on 5 mm \emptyset HOPG in argon purged 1 mM
$(NH_4)_2PdCl_4 + 0.5 M KCl$ stepped from 0.7 V to different deposition potentials (as shown in the
Figure)61
Figure 3-10 SEM images of the HOPG (\emptyset = 5 mm) surface after electrodeposition of Pd in 1 mM
$(NH_4)_2$ PdCl ₄ + 0.5 M KCl at -0.2, -0.1, 0.0, 0.1 and 0.2 V vs. SCE for 20 s63
Figure 3-11 Particle size distribution histograms for the Pd deposits presented in Figure 3-10
for the deposition potential, from the top, -0.2 V, -0.1 V and 0.0 V vs. SCE64
Figure 3-12 AFM images, left, of the HOPG surface showing the initial stages of the Pd
electrodeposition at +0.2 V. Deposition time: (top) 10 s; (middle) 1 s; (bottom) 0.5 s.
Crosssection profiles, right, through the lines A-A', B-B' and C-C' shown on the corresponding
AFM images
Figure 3-13 Particle size distribution histograms for the Pd deposits presented in Figure 3-8 for
the deposition times shown in the legends67

Figure 3-14 Cyclic voltammogram recorded at 10 mV s ⁻¹ on a 3 mm diameter glassy carbon electrode in argon purged 1 mM (NH ₄) ₂ PdCl ₄ + 0.5 M KCl69
Figure 3-15 Current transients recorded on glassy carbon electrodes (3 mm diameter) in argon purged 1 mM (NH ₄) ₂ PdCl ₄ + 0.5 M KCl after stepping from +0.7 V to different deposition potentials, shown in legend
Figure 3-16 SEM images of Pd deposits formed on glassy carbon (3 mm diameter) after stepping from +0.7 V to -0.25, -0.20, -0.15 and -0.13 V vs. SCE for 20 s in argon purged 1 mM (NH_4) ₂ PdCl ₄ + 0.5 M KCl
Figure 3-17 SEM images of Pd deposits formed on glassy carbon (3 mm diameter) after stepping from $+0.7$ V to -120 mV, left, and -100 mV, right, for 20 s in argon purged 1 mM (NH ₄) ₂ PdCl ₄ + 0.5 M KCl71
Figure 3-18 Voltammograms, 5^{th} cycle, recorded in Ar purged 1 M sulphuric acid at 20 mV s ⁻¹ with 3 mm diameter glassy carbon electrodes after undergoing potential steps from +0.7 V to different deposition potentials, shown in the legend, in argon purged 1 mM (NH ₄) ₂ PdCl ₄ + 0.5 M KCl for 20 s
Figure 3-19 SEM images of Pd deposits formed on glassy carbon (3 mm diameter) after stepping from $+0.7$ V to $+350$ mV, top row with different magnifications, and $+300$ mV, bottom row with different magnifications, for 10 s in argon purged 1 mM (NH ₄) ₂ PdCl ₄ + 0.5 M KCl
Figure 4-1 Cyclic voltammograms recorded at 10 mV s^{-1} on $3 \text{ mm } \emptyset$ glassy carbon discs in aerated $10 \text{ mM } (NH_4)_2PdCl_4 + 0.5 \text{ M KCl with } 0, 2, 10 \text{ and } 48 \text{ wt. } \% \text{ of } C_{16}EO_8 as indicated by the legend. The labels respectively indicate: I) the onset of Pd deposition, II) H adsorption, III) H absorption, IV) the onset of H evolution, V) H desorption and VI) the onset of Pd dissolution. The inset shows the same data around the Pd deposition wave$
Figure 4-2 Cyclic voltammograms recorded at 10 mV s ⁻¹ on 3 mm \emptyset glassy carbon discs in aerated 10 mM (NH ₄) ₂ PdCl ₄ + 0.5 M KCl with 0, 2, 10 and 48 wt. % of C ₁₆ EO ₈ as indicated by the legend. Here the sweeps were reversed at -0.3 V compared to -1.3 V in Figure 4-1
Figure 4-3 Current transient recorded at -0.3 V vs. SCE with a 3 mm \emptyset glassy carbon disc in aerated 10 mM (NH ₄) ₂ PdCl ₄ + 0.5 M KCl without surfactant
Figure 4-4 Current transients for the electrodeposition of Pd at different potentials on 3 mm \emptyset glassy carbon discs in 10 mM (NH ₄) ₂ PdCl ₄ + 0.5 M KCl and different weight % of C ₁₆ EO ₈ (as shown in the Figures). The deposition potentials are respectively -500 mV (black), -400 mV (red), -300 mV (blue), -200 mV (green) and -100 mV (grey)80
Figure 4-5 Dependence of the peak current on deposition potentials for the current transients shown in Figure 4-481
Figure 4-6 Dependence of the peak time on the deposition potentials for the current transients shown in Figure 4-481
Figure 4-7 Normalised transients for the chronoamperograms shown in Figure 4-4 recorded in absence of surfactant are compared with theoretical transients for instantaneous (eq. 4-1) and progressive (eq. 4-2) nucleation for the different deposition potentials applied. On the left the whole current transients and on the right the current transients until 4 units of t / t _{max} 83
Figure 4-8 Normalised transients for the chronoamperograms shown in Figure 4-4 recorded in the 2 wt. % mixture are compared with theoretical transients for instantaneous (eq. 4-1) and progressive (eq. 4-2) nucleation for the different deposition potentials applied. On the left the whole current transients and on the right the current transients from 0 to 4 units of $t/t_{\rm max}$ 84 Figure 4-9 Normalised transients for the chronoamperograms shown in Figure 4-4 recorded in
the 10 wt. % mixture are compared with theoretical transients for instantaneous (eq. 4-1) and

progressive (eq. 4-2) nucleation for the different deposition potentials applied. On the left the whole current transients and on the right the current transient from 0 to 4 units of t / $t_{\rm max}$ 8. Figure 4-10 Normalised transients for the chronoamperograms shown in Figure 4-4 recorded in the 48 wt. % mixture are compared with theoretical transients for instantaneous (eq. 4-1) and progressive (eq. 4-2) nucleation for the different deposition potentials applied. On the left the whole current transients and on the right the current transient from 0 to 4 units of t / $t_{\rm max}$ 8! Figure 4-11 Typical chronoamperograms plotted as j vs $t^{-1/2}$ to determine the diffusion coefficient for the Pd salt during the electrodeposition of Pd on a 3 mm Ø glassy carbon disc in 10 mM (NH ₄) ₂ PdCl ₄ + 0.5 M aerated KCl and 0 wt. % of C ₁₆ EO ₈ after stepping from 0.7 V to -0.5 V vs SCE	5
Figure 4-12 Dependence of the diffusion coefficient on the surfactant wt.% and deposition	_
potentials. <i>D</i> was evaluated by fitting the transients for $t>20\times t_{\text{max}}$ to the Cottrell equation 85	
Figure 4-13 Theoretical (non-linear fit to eq. 4-3 without weighting), (\bigcirc) and experimental ($-$)	
current transients for the nucleation and growth of Pd particles at different deposition	
potentials for all mixtures	L
Figure 4-14 Theoretical (non-linear fit to eq. 4-3 with instrumental weighting (O) and	
experimental (—) current transients for the nucleation and growth of Pd particles at different deposition potentials for all mixtures93	2
Figure 4-15 Theoretical (non linear fit to eq. 4-3) with direct weighting (\bigcirc) and experimental	
(—) current transients for the nucleation and growth of Pd particles at different potential	
applied for all mixtures (as shown in Figures).	3
Figure 4-16 Plots of <i>D</i> values from tables 4-6 to 4-7 vs. deposition potentials for different	
concentrations of surfactant; on the left the <i>D</i> values were obtained with instrumental weighting	3
and on the right with direct weighting9	_
Figure 4-17 Plots of the kinetics parameters shown in Table 4-4 vs. wt. % of surfactant for the	
different deposition potentials99)
Figure 4-18 Plots of the kinetics parameters shown in Table 4-4 vs. the deposition potentials for	,
the different concentrations of surfactant99)
Figure 5-1 Cyclic voltammograms recorded at 10 mV s ⁻¹ on 3 mm Ø glassy carbon discs in aerated 10 mM (NH ₄) ₂ PdCl ₄ + 0.5 M KCl with 0, 2, 10 and 48 wt. % of $C_{16}EO_8$ as indicated by the legend. The insert shows the voltammogram recorded in the 48% mixture when reversing the	
sweep at -1.3 V102	2
Figure 5-2 Current transient recorded at -0.3 V vs. SCE with a 3 mm \emptyset glassy carbon disc in	
aerated 10 mM (NH ₄) ₂ PdCl ₄ + 0.5 M KCl without surfactant103	3
Figure 5-3 FEG-SEM images of Pd structures electrodeposited on GC after stepping from $+0.7$ V to -0.3 V vs. SCE for a 63.7 mC cm ⁻² deposition charge. a) 0, b) 2, c) 10, and d) 48 wt. %	
surfactant. In all cases the scale bar is 100 nm long104	1
Figure 5-4 He ion microscopy images of Pd structures electrodeposited on GC after stepping from +0.7 V to -0.3 V vs. SCE for a 63.7 mC cm ⁻² deposition charge. a) 0, b) 2, c) 10, and d) 48 wt.	
% surfactant. In all cases the scale bar is 50 nm long10	5
Figure 5-5 XRD patterns of palladium nanoparticles electrodeposited on GC after stepping from +0.7 V to -0.3 V vs. SCE for a 63.7 mC cm ⁻² deposition charge	5
Figure 5-6 Voltammograms (5th cycle) recorded in 1 M H_2SO_4 at 20 mV s ⁻¹ with 3 mm Ø glassy	•
carbon discs decorated with Pd structures electrodeposited by stepping the potential from +0.7	
V to -0.3 V vs. SCE up to a 63.7 mC cm-2 deposition charge. The legend indicates the corresponding plating mixtures. a) double layer region, b) oxide formation, c) oxide stripping, d)
corresponding planing minicures, ar abubic layer region, by balue formation, croaluc stripping, u	1

H adsorption, e) H absorption to form α-Pd _H , f) H absorption to form β-PdH, g) H extraction from β-PdH, h) H extraction from α-PdH, i) H desorption107
•
Figure 5-7 Voltammograms (first 5 cycles) recorded in 1 M H_2SO_4 at 20 mV s ⁻¹ with 3 mm \emptyset
glassy carbon disc decorated with Pd structures electrodeposited by stepping the potential from $+0.7 \text{ V}$ to -0.3 V vs. SCE up to a 63.7 mC cm- 2 deposition charge. The deposition conditions were
as shown in figure 5-6
Figure 5-8 Voltammograms for the oxidation of formic acid recorded in Ar purged 0.5 M HCOOH
+ 0.5 M H ₂ SO ₄ at 100 mV s ⁻¹ with GC electrodes decorated with the Pd deposits. The legend
indicates the corresponding plating mixtures. For clarity the reverse sweep is only shown for
the 10% mixture
Figure 5-9 Voltammograms for the oxidation of ethanol recorded in Ar purged 0.5 M ethanol +
0.1 M KOH at 100 mV s ⁻¹ with GC electrodes decorated with the Pd deposits. The legend
indicates the corresponding plating mixtures. For clarity the reverse sweep is only shown for
the 10% mixture
Figure 5-10 Linear sweep voltammograms for the evolution of H recorded in Ar purged 0.5 M
HClO ₄ at 100 mV s ⁻¹ with GC electrodes decorated with the Pd deposits. The legend indicates the corresponding plating mixtures112
Figure 5-11 Linear sweep voltammograms for the evolution of O ₂ recorded in Ar purged 0.5 M
ethanol + 0.5 M KOH at 100 mV s ⁻¹ with GC electrodes decorated with the Pd deposits. The
legend indicates the corresponding plating mixtures.
Figure 5-12 Linear sweep voltammograms for the reduction of oxygen recorded in O ₂ saturated
0.5 M KOH at 100 mV s ⁻¹ with GC electrodes decorated with the Pd deposits. The legend
indicates the corresponding plating mixtures
Figure 5-13 Linear sweep voltammograms for the reduction of oxygen recorded in O_2 saturated
0.5 M HClO $_4$ at 100 mV s $^{-1}$ with GC electrodes decorated with the Pd deposits. The legend indicates the corresponding plating mixtures114
Figure 5-14 SEM (low magnification) images of Pd structures electrodeposited on HOPG after stepping from +0.7 V to -0.3 V vs. SCE for a 63.7 mC cm ⁻² deposition charge, in aerated 10 mM
(NH ₄) ₂ PdCl ₄ + 0.5 M KCl with 0, 2, 10 and 48 wt. % of $C_{16}EO_8$ as indicated by the legend117
Figure 5-15 FEG-SEM (high magnification) images of Pd structures electrodeposited on HOPG
after stepping from +0.7 V to -0.3 V vs. SCE for a 63.7 mC cm ⁻² deposition charge
Figure 5-16 Voltammograms for the oxidation of ethanol recorded in Ar purged 0.5 M ethanol + 0.1 M KOH at 100 mV s ⁻¹ with with 5 mm \emptyset HOPG electrodes decorated with the Pd deposits.
The legend indicates the corresponding plating mixtures119
Figure 6-1 Cyclic voltammograms for the deposition of palladium in varying surfactant mixtures
0 wt.% (black), 2 wt% (red), 10 wt.% (blue) and 48 wt.% (pink), recorded on gold
microelectrodes (\emptyset = 50 μ m diameter) with a scan rate of 10 mV s ⁻¹
Figure 6-2 Cyclic voltammograms recorded with Pd modified gold microdisc electrodes ($\emptyset = 50$
μ m diameter) that shown in Figure 6-1 in 1 M H_2SO_4 at 20 mV s ⁻¹ . The plating mixtures used to
prepare the Pd deposits are shown in the legend
Figure 6-3 SEM images of the palladium coated gold microelectrodes (\emptyset = 50 μ m diameter) after
undergoing two consecutive cyclic voltammograms in ammonium tetrachloropalladate (II) (a)
aqueous solution (b) and (c) micellar phase of LLC mixture (d) hexagonal phase. The scale bare
is 20 μm12 ²

Figure 6-4 Current density vs. time transients recorded in 10 mM (NH ₄) ₂ PdCl ₄ + 0.5 M KCl after
stepping from 0.4 V to different deposition potentials with a fixed deposition charge density (2.5
C cm ⁻²), working electrode Au (\emptyset = 50 μ m)125
Figure 6-5 Cyclic voltammograms recorded at 20 mV / s in 1 M sulphuric acid with the
palladium coated gold microelectrodes (50 μm diameter) prepared in figure 6-4. The legend
indicates the deposition potentials used to prepare the Pd deposits126
Figure 6-6 SEM images of the palladium coated gold microelectrodes (\emptyset = 50 μ m diameter)
prepared by stepping the potential from +0.4 V to different deposition potentials (from top to
bottom: $+0.0$, $+0.1$, $+0.2$ and $+0.3$ V vs. SCE) until a fixed deposition charge density passed (2.5 C
cm ⁻²), in aerated 10 mM (NH ₄) ₂ PdCl ₄ + 0.5 M KCl. The left images were taken at 0° . The images
on the right were taken with a 70° tilt for the same films shown on the left. The scale bar is 20
μm for rows 1,2 and 4 and 50 μm for row 3
Figure 6-7 Current density vs. time transients recorded in aerated 10 mM (NH ₄) ₂ PdCl ₄ + 0.5 M
KCl with 2 wt. % of C ₁₆ EO ₈ after stepping from 0.4 V to different deposition potentials with fixed
deposition charge density (2.5 C cm ⁻²), working electrode Au (\emptyset = 50 μ m). The inset shows the
transient at 0.3 V
Figure 6-8 Cyclic voltammograms recorded at 20 mV / s in 1 M sulphuric acid of the electrodes
prepared in figure 6-7, by stepping from 0.4 V to different deposition potentials with fixed
deposition charge density (2.5 C cm ⁻²), working electrode Au (\emptyset = 50 μ m) in aerated 10 mM (NH ₄) ₂ PdCl ₄ + 0.5 M KCl with 2 wt. % of C ₁₆ EO ₈
Figure 6-9 Current density vs. time transients recorded in aerated 10 mM (NH ₄) ₂ PdCl ₄ + 0.5 M
KCl with 10 wt. % of C ₁₆ EO ₈ after stepping from 0.4 V to different deposition potentials with a
fixed deposition charge density (2.5 C cm ⁻²), working electrode Au (\emptyset = 50 µm). Inset shows
transient at 0.2 and 0.3 V
Figure 6-10 Cyclic voltammograms recorded at 20 mV s ⁻¹ in 1 M sulphuric acid for the electrodes
prepared in figure 6-9 by stepping from 0.4 V to different deposition potentials with a fixed
deposition charge density of 2.5 C cm ⁻² , working electrode Au (\emptyset = 50 μ m) in aerated 10 mM
(NH ₄) ₂ PdCl ₄ + 0.5 M KCl with 10 wt. % of C ₁₆ EO ₈
Figure 6-11 SEM images of the palladium coated microelectrodes prepared in figure 6-9 by
stepping from 0.4 V to different deposition potentials versus SCE at fixed deposition charge
density (2.5 C cm ⁻²), in mixture 10 wt.%. (\emptyset = 50 μ m diameter). Scale bare is 20 μ m for all
electrodes131
Figure 6-12 Cyclic voltammograms in 1 M sulphuric acid for the electrodes prepared by stepping
from $0.4~\rm V$ to different deposition potentials with a fixed deposition charge density (2.5 C cm $^{-2}$),
working electrode Au (\emptyset = 50 µm) in aerated 10 mM (NH ₄) ₂ PdCl ₄ + 0.5 M KCl with 48 wt. % of
$C_{16}EO_{8}$
Figure 6-13 SEM images of the palladium coated microelectrodes prepared by stepping from 0.4
V to different deposition potentials for a fixed deposition charge density (2.5 C cm ⁻²), in the
mixture 48 wt.%. (\emptyset = 50 μ m diameter). Scale bare is 20 μ m
Figure 6-14 EDX analysis of the Pd coated gold microdisk electrode Au(\emptyset = 50 μ m) prepared by
potential step from $+0.4 \text{ V}$ to 0.3 V vs. SCE with fixed deposition charge density (2.5 C cm^{-2}), in
10 mM (NH ₄) ₂ PdCl ₄ + 0.5 M KCl with 48 wt. % of $C_{16}EO_8$
Figure 7-1 Cyclic voltammograms recorded at 10 mV s ⁻¹ with a glassy carbon electrode (3 mm
\varnothing) in (top) 0.01 M ZnSO ₄ , (middle) 0.01 M SeO ₂ , and (bottom) 0.03 M ZnSO ₄ + 0.01 M SeO ₂
pH=2.5 (pH was adjusted by adding a small drop of H_2SO_4), Ar purged for 20 min, at 25 $^\circ$ C 137

Figure 7-2 Cyclic voltammograms recorded at 10 mV s ⁻¹ with on the left (25 μ m \varnothing) microdisc
electrode, on the right Pt (3 μ m \varnothing) electrode in (a) 0.01 M ZnSO ₄ , (b) 0.01 M SeO ₂ and (c) 0.03 M
ZnSO ₄ + 0.01 M SeO ₂ , pH=2.5 (pH was adjusted by adding a small drop of H ₂ SO ₄), Ar purged for
20 min, at 25° C
Figure 7-3 Cyclic voltammograms recorded at 10 mV s ⁻¹ with a Pt microdisc (25 μ m \varnothing) in 0.03 M
$ZnSO_4 + 0.01$ M SeO_2 , pH=2.5 (pH was adjusted by adding a small drop of H_2SO_4), Ar purged for
20 min, at 25° C. Voltammogram recorded in the dark (Black) and under artificial illumination
with a 450 nm light emitting diode (Red)139
Figure 7-4 Cyclic voltammograms recorded at 50 mV s ⁻¹ with a 3 mm Ø GC electrode: undoped
(black) ZnSe using 1 mM SeO ₂ and 0.1 M ZnSO ₄ ; N doped (red) ZnSe using 1 mM SeO ₂ , 0.1 M
ZnSO ₄ and 0.5 M (NH ₄) ₂ SO ₄ ; Ga doped (blue) ZnSe using 1 mM SeO ₂ , 0.1 M ZnSO ₄ and 0.5 M
$Ga_2(SO_4)_3$. All were measured at 60 °C, a pH of 2.4 (pH was adjusted by adding a small drop of
H_2SO_4) and purged with argon for 20 minutes. The inset shows the forward scan140
Figure 7-5 Current transients for ZnSe films on a 3 mm Ø GC electrode at -1.3 V vs. SCE for 180 s.
Undoped (black) ZnSe using 1 mM SeO ₂ and 0.1 M ZnSO ₄ ; N doped (red) ZnSe using 1 mM SeO ₂ ,
0.1 M ZnSO_4 and $0.5 \text{ M (NH}_4)_2\text{SO}_4$; Ga doped (blue) ZnSe using 1 mM SeO ₂ , 0.1 M ZnSO_4 and $0.5 \text{ M (NH}_4)_2$
$M Ga_2(SO_4)_3$
Figure 7-6 Linear sweep voltammograms recorded in 0.5 M Na ₂ SO ₄ at 50 mV s ⁻¹ for ZnSe film
electrodeposited on 3 mm Ø GC electrode by stepping the potential from 0.5 V to -1.2 V for 180 s
to grow the film. Undoped (top) ZnSe using 1 mM SeO ₂ and 0.1 M ZnSO ₄ ; N doped (middle) ZnSe
using 1 mM SeO ₂ , 0.1 M ZnSO ₄ and 0.5 M (NH ₄) ₂ SO ₄ ; Ga doped (bottom) ZnSe using 1 mM SeO ₂ ,
0.1 M ZnSO_4 and $0.5 \text{ M Ga}_2(\text{SO}_4)_3$. All purged with argon for 20 minutes. Illumination with a 450
nm LED. The photocurrent is the illuminated current minus the dark current142
Figure 7-7 Mott-Schottky plots recorded in 0.5 M Na ₂ SO ₄ for ZnSe prepared on 3 mm Ø GC
electrode by stepping the potential from 0.5 V to -1.3 V vs. SCE for 180 s in: a) Ga doped ZnSe
using 1 mM SeO ₂ , 0.1 M ZnSO ₄ and 0.5 M $Ga_2(SO_4)_3$, b) N doped ZnSe using 1 mM SeO ₂ , 0.1 M
ZnSO ₄ and 0.5 M (NH ₄) ₂ SO ₄ and c) undoped ZnSe using 1 mM SeO ₂ and 0.1 M ZnSO ₄ ; All purged
with argon for 20 minutes. pH=2.5 (pH was adjusted by adding a small drop of H_2SO_4)144
Figure 7-8 SEM images for ZnSe prepared on 3 mm Ø GC electrode by stepping the potential
from 0.5 V to -1.3 V vs. SCE and in (top left) 0.1 M ZnSO_4 + 1 m M SeO_2 + 0.5 M (NH ₄) ₂ SO ₄ , (top
right) $0.1 \text{ M ZnSO}_4 + 1 \text{ m M SeO}_2$, and (bottom) $0.1 \text{ M ZnSO}_4 + 1 \text{ m M SeO}_2 + 0.5 \text{ M Ga}_2(\text{SO}_4)_3$. All
purged with argon for 20 minutes.
Figure 7-9 Cyclic voltammograms recorded at 50 mVs ⁻¹ with a 3 mm Ø glassy carbon electrode
in (top- black) a solution of 1 M $2nSO_4 + 0.001$ M $SeO_2 + 0.5$ M (NH ₄) ₂ SO ₄ ; (top- red) a solution of
$0.1 \text{ M ZnSO}_4 + 0.01 \text{ M SeO}_2 + 0.5 \text{ M (NH}_4)_2\text{SO}_4$; (bottom black) in a solution of $0.1 \text{ M ZnSO}_4 +$
$0.001 \text{ M SeO}_2 + 0.5 \text{ M Ga}_2(\text{SO}_4)_3$; (bottom- red) a solution of 0.1 M ZnSO ₄ + 0.01 M SeO ₂ + 0.5 M
Ga ₂ (SO ₄) ₃ . Magnifications of the reduction peak of the 1 st forward scan are shown in the bottom
right corner of each graph. All solutions were kept at a constant temperature of 60 °C and within
a pH range of 2- 2.4 during the measurements. Between measurements, the solutions were
purged with argon for 20 minutes. The inset shows the forward scan (The y-axis is " i / mA" and
the x-axis is "E / V" vs. SCE)
Figure 7-10 EDX spectra for ZnSe films deposited on a 3 mm Ø glassy carbon electrode in 0.1 M
$ZnSO_4 + 0.01$ M SeO_2 and: (top) 0.5 M $Ga_2(SO_4)_3$ deposited by stepping from 0.5 V to -1.15 V vs.
SCE. (bottom) 0.5 M (NH ₄) ₂ SO ₄ deposited by stepping from 0.5 V to -1.2 V. The deposition time
was kept constant at 180 s. The accelerating voltage was 10 KeV147

Figure 7-11 SEM images for ZnSe films deposited on 3 mm \emptyset glassy carbon electrodes in 0.1 M
$ZnSO_4 + 0.01$ M SeO_2 and: (left column) 0.5 M $Ga_2(SO_4)_3$ (right column) 0.5 M $(NH_4)_2SO_4$. The
films were deposited by stepping the potential from 0.5 V vs. SCE to (a)-1.3 V, (b)-1.2 V, (c)-
1.175 V, (d)-1.15 V, (e)-1.3 V, (f)-1.275 V, (g) -1.25 V and (h)-1.2 V. The deposition time was kep
180 s
Figure 7-12 Current transients for the deposition of ZnSe on a carbon paper electrode. The
potential was stepped from +0.4 V to -1.3 V vs. SCE for (black) 1 hr, (dark grey) 2 hr, and (light
grey) 5 hr in 0.03 M ZnSO ₄ + 0.01 M SeO ₂ , pH=2.5, Ar purged for 20 min, at 25° C
Figure 7-13 SEM images of the ZnSe coated carbon paper electrode after undergoing a potential
step from +0.4 V to -1.3 V vs. SCE for (a) 1 hr, (b) 2 hr, and (c) 5 hr in 0.03 M ZnSO ₄ + 0.01 M
SeO ₂ , pH=2.5, Ar purged for 20 min at 25° C
Figure 7-14 EDX analysis of the ZnSe coated carbon paper electrodes prepared by potential step
from $+0.4 \text{ V}$ to -1.3 V vs. SCE for (top) 1 hr, (middle) 2 hr and (bottom) 5 hr in 0.03 M ZnSO ₄ +
0.01 M SeO ₂ , pH=2.5, Ar purged for 20 min at 25° C. The accelerating voltage wad 10 KeV15
Figure 7-15 CVs of N-doped ZnSe solutions (pH= 2-2.5) containing 0.5 M (NH ₄) ₂ SO ₄ , 0.3 M ZnSO
and SeO ₂ concentrations of: (black) 0.001 M, solution C; (red) 0.01 M, solution F; (blue) 0.1 M,
solution I. All CVs were recorded at room temperature, without temperature control, on a 5 mm
X 5 mm carbon paper electrode. All solutions were purged with argon for 20 minutes before
experiments. The inset plot shows a zoom on the reduction waves of ZnSe, the y-axis is " i / mA "
and the x-axis is "E / V" vs SCE15
Figure 7-16 SEM of ZnSe films deposited in solutions (pH= 2-2.5) containing 0.5 M (NH ₄) ₂ SO ₄ ,
$0.3~M~ZnSO_4~and~SeO_2~concentrations~of:$ (top) $0.001~M,$ solution C; (middle) $0.01~M,$ solution F;
(bottom) $0.1\mathrm{M}$, solution I. The deposits were prepared by stepping the potential from $0.5\mathrm{V}$ to -
1.195 V, -1.24 V and -1.315 V respectively for 2 h at room temperature, without temperature
control, on a 5 mm X 5 mm carbon paper electrode. Images in the right column were taken with
higher magnification than the images in left column
Figure 7-17 CVs for the deposition of ZnSe in solutions (pH= 2-2.5) containing 0.5 M (NH ₄) ₂ SO ₄ ,
0.2 M ZnSO ₄ and SeO ₂ concentrations of: (black) 0.001 M, solution B; (red) 0.01 M, solution E;
(blue) 0.1 M, solution H. All CVs were recorded at room temperature, without temperature
control, on 5 mm X 5 mm carbon paper electrodes. All solutions were purged with argon for 20
minutes before experiments. The foot of the reduction peak is magnified in the inset, the y-axis
is "i / mA" and the x-axis is "E / V" vs SCE
Figure 7-18 SEM images of ZnSe deposits prepared in solutions (pH= 2-2.5) containing 0.5 M
$(NH_4)_2SO_4$, 0.2 M ZnSO ₄ and SeO ₂ concentrations of: (a) 0.001 M, solution B; (b) 0.01 M, solution
E; (c) 0.1 M, solution H. All the films were prepared by stepping the potential from 0.5 to -1.215
V, -1.24 V and -1.33 V vs. SCE respectively, at room temperature, on a 5 mm X 5 mm carbon
paper electrode. The thermal treatment of ZnSe crystal was done in a nitrogen atmosphere at a
temperature of 300 °C
Figure 7-19 CVs for the deposition of ZnSe in solutions (pH= 2-2.5) containing 0.5 M (NH ₄) ₂ SO ₄ ,
0.1 M ZnSO_4 and SeO_2 concentrations of: (black) 0.001 M , solution A; (red) 0.01 M , solution D.
All CVs were recorded at room temperature, without temperature control, on a 5 mm X 5 mm
carbon paper electrode. All solutions were purged with argon for 20 minutes before
experiments. The inset shows the Se reduction wave on the forward scan, the y-axis is " i / mA"
and the x-axis is "E / V" vs SCE
Figure 7-20 SEM images of ZnSe deposits prepared in solutions (pH= 2-2.5) containing 0.5 M
$(NH_4)_2SO_4$, 0.1 M ZnSO ₄ and SeO ₂ concentrations of: (a) 0.001 M, solution A and (b) 0.01 M,

solution D. The potential was stepped from 0.5 V to -1.23 V and -1.27 V vs. SCE for solution A and D respectively for two hours at room temperature, on a 5 mm X 5 mm carbon paper electrode. The thermal treatment of ZnSe crystal was done in the nitrogen atmosphere at 300 °C
Figure 7-21 EDX patterns of the ZnSe deposits prepared in solutions (pH= 2-2.5) containing 0.5 M (NH ₄) ₂ SO ₄ and :(top) solution F 0.3 M ZnSO ₄ , 0.01 M SeO ₂ , (middle) solution H 0.2 M ZnSO ₄ , 0.1 M SeO ₂ and (bottom) I 0.3 M ZnSO ₄ , 0.1 M SeO ₂ . The potential was stepped from 0.5 V to - 1.24 V, -1.33 V and -1.315 vs. SCE for solution F, H and I respectively for two hours at room temperature, on a 5 mm X 5 mm carbon paper electrode. The accelerating voltage was 10 KeV.
Figure 7-22 XRD pattern of a ZnSe thin film deposited on carbon paper electrode prepared from a solution containing 0.3 M ZnSO_4 , 0.1 M SeO_2 and $0.5 \text{ M (NH}_4)_2\text{SO}_4$. The film was prepared by potential step from $+0.5 \text{ V}$ to -1.315 V vs. SCE for two hours
carbon paper by potential step from $+0.5$ V to -1.315 V vs. SCE for two hours at room temperature in 0.3 M ZnSO ₄ , 0.1 M SeO ₂ and 0.5 M (NH ₄) ₂ SO ₄ for n-type or 0.5 M Ga ₂ (SO ₄) ₃ for p-type Both films were annealed at 300 °C in an Ar atmosphere
$\label{eq:H2PtCl6} \begin{array}{l} H_2PtCl_6 \ (b) \ 2 \ wt.\% \ C_{16}EO_8 : 84 \ wt.\% \ H_2O : 14 \ wt.\% \ H_2PtCl_6 \ (c) \ 10 \ wt.\% \ C_{16}EO_8 : 77 \ wt.\% \ H_2O : 13 \ wt.\% \ H_2PtCl_6 \ (d) \ 60 \ wt.\% \ C_{16}EO_8 : 34 \ wt.\% \ H_2O : 6 \ wt.\% \ H_2PtCl_6. \ Voltammograms \ (a) \ , \ (b) \ and \ (c) \ recorded \ at \ 25 \ \mu m \ and \ (d) \ at \ 50 \ \mu m \ diameter. \ \ \ \ \ \ \ \ \ \ \ \ \ \ \ \ \ \ \$
different ratio of lyotropic liquid crystals mixture; (mixture 1) 0 wt.% $C_{16}EO_8$: 86 wt.% H_2O : 14 wt.% H_2PtCl_6 (mixture 2) 2 wt.% $C_{16}EO_8$: 84 wt.% H_2O : 14 wt.% H_2PtCl_6 (mixture 3) 10 wt.% $C_{16}EO_8$: 77 wt.% H_2O : 13 wt.% H_2PtCl_6 (mixture 4) 60 wt.% $C_{16}EO_8$: 34 wt.% H_2O : 6 wt.% H_2PtCl_6 . Voltammograms (mixture 1) , (mixture 2) and (mixture 3) recorded at 25 μ m and (mixture 4) at 50 μ m diameter
Figure 9-3 SEM images of the platinum coated microelectrodes after undergoing two consecutive cyclic voltammograms in (a) 0 wt.% $C_{16}EO_8$: 86 wt.% H_2O : 14 wt.% H_2PtCl_6 (b) 2 wt.% $C_{16}EO_8$: 84 wt.% H_2O : 14 wt.% H_2PtCl_6 (c) 10 wt.% $C_{16}EO_8$: 77 wt.% H_2O : 13 wt.% H_2PtCl_6 (d) 60 wt.% $C_{16}EO_8$: 34 wt.% H_2O : 6 wt.% H_2PtCl_6 . (a) , (b) and (c) recorded at 25 μ m and (d) at 50 μ m diameter electrodes. Scale bar is 10 μ m
Figure 9-4 Current transients recorded in 42 wt.% $C_{16}EO_8$: 49.7 wt.% H_2O : 8.3 wt.% H_2PtCl_6 at fixed electrodeposition potential 0.0 V vs SCE, at 50 μ m Au diameter microdisc
cm ⁻²

DECLARATION OF AUTHORSHIP

- I, Nawal Al Abass declare that the thesis entitled and the work presented in the thesis are both my own, and have been generated by me as the result of my own original research. I confirm that:
 - ➤ this work was done wholly or mainly while in candidature for a research degree at this University;
 - where any part of this thesis has previously been submitted for a degree or any other qualification at this University or any other institution, this has been clearly stated;
 - where I have consulted the published work of others, this is always clearly attributed;
 - ➤ where I have quoted from the work of others, the source is always given. With the exception of such quotations, this thesis is entirely my own work;
 - ➤ I have acknowledged all main sources of help;
 - > where the thesis is based on work done by myself jointly with others, I have made clear exactly what was done by others a nd what I have contributed myself;
 - ▶ parts of this work have been published as: Al Abass, N., Denuault, G. and Pletcher, D. (2014) The unexpected activity of Pd nanoparticles prepared using a non-ionic surfactant template. Physical Chemistry Chemical Physics, 16, (10), 4892.

| Signed: |
 | |
|---------|------|------|------|------|------|------|------|------|------|------|------|--|
| Date: |
 | |

ACKNOWLEDGEMENTS

First and foremost, I would like to thank my supervisor Dr. Guy Denuault to whom I am extremely grateful for his encouragement and support. I would like to thank him for his motivation, enthusiasm, patience and immense knowledge he has provided me during the period of my PhD.

I would like to thank my advisor Prof. Derek Pletcher for his assistance in this research. I would also like to acknowledge the assistance of Denuault group members who have contributed their time and knowledge. My thanks go to Laila, Aziz, Kelly, Ihsin, Mara, Sam, Ana and Saiful. It has been great to share my time with them in the lab, which has made it more productive and enjoyable.

I also like to acknowledge the financial support received from the ministry of higher education in Saudi Arabia. Without their support, I would not have had this opportunity to complete my PhD.

Finally, I should like to express my heartfelt gratitude to my supportive husband who has been putting all the effort to make it possible for me during the hard times of my PhD. My thanks go as well to my lovely kids. Their presence with me in the UK has made me stronger to accomplish my dream. I would also like this opportunity to express my sincere thanks to my parents in Saudi Arabia who have been supportive.

List of symbols

Symbols	Description	Unit
A	Nucleation rate	s ⁻¹
A_{geo}	Geometric area of electrode	cm ²
A_{elec}	Electroactive area	cm ²
C_{sc}	Capacity of space charge	mF
C_d	Capacity of diffuse layer	mF
C_H	Capacity of compact layer	mF
D	Diffusion coefficient	$cm^2 s^{-1}$
e	Charge of an electron	$1.602 \times 10^{-19} \text{ C}$
E_e	Equilibrium potential vs. reference electrode	V
E^o	Standard potential	V
E_{fb}	Flat band potential	V
ΔE_{sc}	Potential of space charge	V
ΔE_d	Potential of diffuse layer	V
ΔE_H	Potential of the compact layer	V
F	Faraday constant	96485 C mol ⁻¹
\dot{J}	Current density	mA cm ⁻²
M	Molecular weight	g mol ⁻¹
n	Number of electrons	
N_o	Number of nucleation sites	cm ⁻²
Q	Charge passed during the reduction process	mC cm ⁻²
Q_{Pd}	Pd oxide stripping charge	mC cm ⁻²
Q_{Pt}	Pt oxide stripping charge	mC cm ⁻²
r	Radius of electrode	cm, mm or µm
R_f	Roughness factor	
S	Specific catalyst area	$m^2 g^{-1}$
t	Time	S
T	Temperature	K
μ	Viscosity	cP
η	Overpotential	V
V_{M}	Molar volume	dm ³ mol ⁻¹
ho	Electric resistivity or the density	Ω cm or g cm ⁻³
ν	Scan rate, the velocity of electrons and holes	mV s ⁻¹

Abbreviations

Symbol	Meaning			
CE	Counter electrode			
I_1	Cubic phase			
H_1	Hexagonal phase			
H_2	Inverse hexagonal phase			
L_I	Micellar solution			
L_{lpha}	Lamellar phase			
V	Cubic phase			
SCE	Saturated calomel electrode			
SMSE	Saturated mercury sulphate electrode			
EDX	Energy dispersive X-ray			
HOPG	Highly ordered pyrolytic graphite			
SEM	Scanning electron microscopy			
HIM	Helium ion microscopy			
LLC	Lyotropic liquid crystal			
MMO	Mercury mercuric oxide electrode			
EIS	Electrochemical impedance spectroscopy			
AFM	Atomic force microscopy			
HT	Heerman and Tarallo model			
SH	Scharifker and Hills			
MFM	Magnetic force microscopy			
STM	Scanning tunnelling microscope			
SNOM/	Near field scanning optical microscopy			
NSOM	Near-field scanning optical microscopy			

1. Introduction

1.1 Nanoparticles

Nanoparticles have become a very productive area of studies because of their size-dependent properties that differ significantly from the properties of the bulk materials. Interest in metallic nanoparticles particularly with noble metals is considerable due to their high catalytic activities for many chemical reactions and fuel cell applications. Furthermore their applications expand into a large number of fields such as environmental, chemical and biomedical engineering. They have been used in the controlled release of drugs, low dielectric constant fillers, sensors, pigments, microelectronics, and electro-optics..[1-5] The intrinsic properties of a nanoparticle are mainly determined by its size, shape, composition, crystallinity, and structure (solid versus hollow). In principle, one could control any one of these parameters to fine-tune the properties of a nanoparticle.[6]

Nanoparticles can have either amorphous or crystalline form. They have unusual physical and chemical properties, relating to their size, shape, stabilizing agent and electronic structure. The electronic structure of a nanoparticle determines the electronic, optical, and magnetic features. These properties refer strongly to the large ratio of surface atoms to core atoms and the finite number of core atoms. [7,8] Thus numerous efforts have been made to control the electronic structure of nanoparticles by changing their size, shape, and composition; [9-11] it is still a challenge to find ways of controlling the properties of nanoparticles. [12]

Nanoscale metal centres have been researched to a high degree due to a host of benefits compared to the use of bulk metal films. The main purpose of small metal centres is to provide a greater catalytic activity than the bulk metal but with a vastly reduced quantity of deposited material. This is a benefit because many catalytic metals are highly expensive and the ability to deposit these centres on cheap substrates would prove advantageous in many industries.[13] Nanoparticles have a much higher catalytic activity per gram due to their high surface area to volume ratio, [14] the smaller size of the particles means a higher proportion of atoms are surface atoms on edges and corners which raises their reactive capacity.[15]

1.2 Electrodeposition

Electrodeposition is the process by which depositions are carried out using changes in potential across an electrochemical cell to drive electron transfer reactions. The deposition occurs when ions in solution or in complexes are reduced to a lower oxidation state and subsequently adsorb to a substrate surface.[16] Electrodeposition can be used to deposit metals onto electrode surfaces leading to the production of modified electrodes with a new set of properties compared to the bare electrode. Electrochemical deposition deals with the synthesis of solid films or particles from dissolved species by alteration of their oxidation states using electricity. Not only pure metals can be prepared by

electrochemical deposition but also compounds such as oxides, phosphides and semiconductors can be easily fabricated. Furthermore, electrodeposition has many advantages over other processing techniques including:[17-21]

- It provides a cost-effective and non-equipment-intensive method for the formation of materials (metals, alloys, compositionally modulated alloys and composites) either as coatings or as freestanding objects even in complex shapes (foils, wires, electroforms).
- The low processing temperature (around room temperature).
- > The particle size can be accurately controlled by monitoring the charges passed during the electrodeposition process.
- ➤ Electrodeposition can be used with conventional or modified electroplating baths and conditions to produce small nanoparticles (where subsequent crystallisation annealing can lead to the required nanostructure) to micrometric structure.
- > Deposition rates of the order of several tens of microns per hour can be easily achieved.
- > The capability of single-step production and the ability to produce fully dense materials, free of extraneous porosity.

Electrodeposition is favourable for control of catalytic activity as the properties of deposits such as morphology and film thickness can be easily modified by changing the deposition parameters. Electrodeposition has been found to provide more specific control of these properties than chemical deposition. A major advantage of electrodeposition compared to other deposition techniques is its mild reaction conditions. Also it can be carried out at near room temperature and often using water as the electrolyte. This has large benefits with regards to green chemistry.

Electrochemical deposition of metals is typically carried out by reduction of species in a solution. When a metal is inserted into a solution containing ions of that metal, equilibrium is set up between the metal desire to convert as ions in the solution and the opposing desire of the ions to lose their charge and deposit on or in the metal. At equilibrium, both of the driving forces for ionized metal atoms and metal ions being discharged are equal. The difference in potential between the metal and the solution phases under these conditions is the equilibrium potential difference. The equilibrium electrode potential is the electrical potential of an electrode measured versus a reference electrode in absence of current flowing through the electrode. The equilibrium potential *E* between a metal and a solution of its ions is given by the Nernst equation as follows:

$$E = E^{\circ} + \frac{RT}{nF} \ln \frac{[ox]}{[red]}$$
 (1-1)

where E° is the standard potential (the equilibrium potential when all the reactants and products are in their standard states), R is the standard gas constant (8.314510 J K⁻¹ mol⁻¹), T the absolute temperature in Kelvin, n is the number of electrons transferred and F the Faraday constant (96485.309)

C mol⁻¹). The potential also depends on the natural logarithm of the ratio of activities of the oxidized and reduced species.[21,22]

1.3 Nucleation and growth of metal centres

The formation of a metal phase on an electrode surface involves the nucleation and growth of metal centres Figure 1-1.

Nucleation considers the difficult step in the formation of a phase on a foreign substrate. Moreover, the formation of stable centres requires applying an overpotential to drive the electron transfer reaction. As the metal ions begin to be reduced they cluster together on the substrate surface and continue to grow as more metal is reduced and aggregates onto the metal centres. The initially formed nuclei are thermodynamically unstable due to their small size which leads to a high surface energy. Once nuclei of sufficient size have developed the clusters begin to grow rapidly as their stability continues to increase with the addition of more material, small nuclei are unstable and tend to dissolve. The metal centres tend to aggregate, if they are large enough, with other expanding centres across the substrate surface. Once the centres begin to overlap a film is produced as the rest of the substrate surface continues to be covered. This is the case of progressive nucleation.[23] In contrast, if the nucleation rate is fast, the maximum number of nuclei is formed just after the induction time; this is the case of instantaneous nucleation. The nuclei are three-dimensional (3D) and often assume a hemispherical or conical form.[24-26]

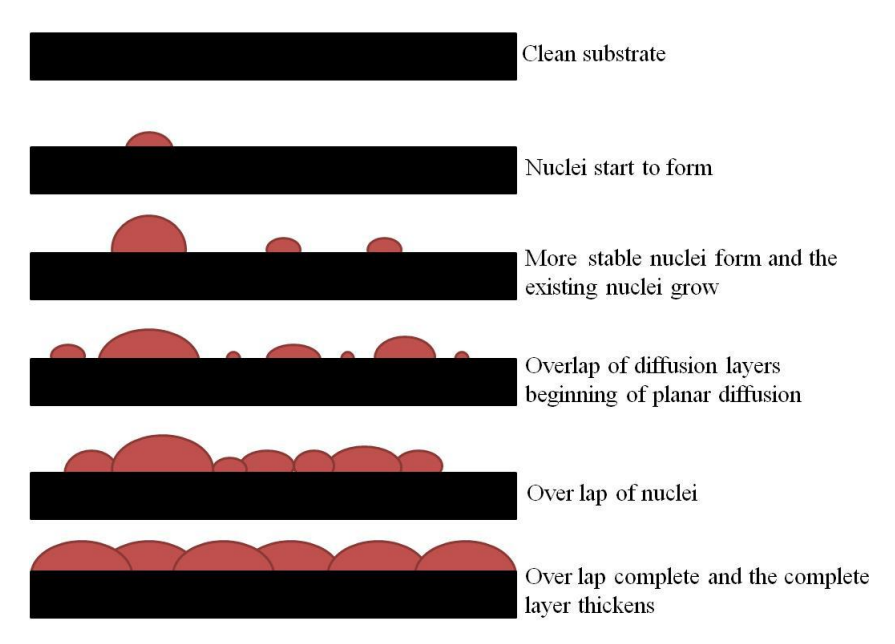


Figure 1-1 Steps involved in the nucleation and growth of hemispherical nuclei on an electrode surface.

The best experimental technique to study the early stages of metal deposition is chronoamperometry. The electrodeposition of the metal occurs by applying an overpotential that is more negative with respect to the equilibrium potential. The observed chronoamperometric response is called the current

transient; it is influenced by a number of processes, the rate of formation of growth sites, the geometry of the growing centres, the number of growth sites, the rate of propagation of growth sites in various dimensions and the overlapping of centres.[23] A spike and drop can be seen at very short time and this corresponds to a non-Faradaic process such as charge/discharge of the double layer and/or adsorption. Then, it is followed by a rise of the current with time as the nucleation and growth of the nuclei occurs. The rate determining step in the nuclei growth is mass transfer, electron transfer or a combination of both.[23] Metal nanocentres can be produced in a variety of ways. They can be produced by stopping the deposition before the metal nuclei begin to overlap with each other and form a continuous layer. A surfactant template can be used to reduce the chances of overlap between centres as the blocked sites cause the metal centres to be distributed further away from each other than would be the case on a bare substrate. The nuclei can grow parallel or / and perpendicular to the electrode surface.[36] Hemispherical nuclei can be formed if growth is uniform in all three directions of space. In fact, at short times, most theories consider the nuclei as hemispherical entities randomly distributed on the electrode surface where each isolated nucleus is surrounded by a hemispherical diffusion zone. Also nuclei that have different geometrical structures can follow the same concept. When the nuclei grow further, their diffusion zones will overlap. From this point, the established nuclei cannot be considered to grow independently of each other. If the diffusion zones are large enough, then some region in the vicinity of the electrode will be hindered for further nucleation. Now the deposition can occur only in a direction almost perpendicular to the electrode. Thus, at long times the growth of the deposit is controlled by linear diffusion to the electrode surface.[34]

1.3.1 The role of overpotential in the nucleation and growth process

In early stages of nucleation and growth, the relation between the applied overpotential and the kinetics of nucleation was studied by either direct observation by microscopy of the substrate or indirectly, by fitting the current transients with theoretical models, then estimating the total number of nuclei.[27]. In recent studies, measurements with the electrochemical quartz crystal microbalance EQCM and in situ with the scanning tunnelling microscope STM were performed for determining the electrochemical phase formation on the electrodes.[28] At the same time, many theoretical models[29] were built to explain the kinetics of a phase change.[30,31] First, galvanostatic deposition can also be performed to force the nucleation process to take place at a determined rate. In this case, the potential changes are monitored during the nucleation process; a maximum potential is indicative of a new phase.[32] Second, potentiostatic depositions are intensively used, with either a single or double potential step.

The nucleation and growth processes can be classified into two cases: interfacial (or charge transfer) controlled and diffusion controlled.

A-The charge controlled system is when the nucleus growth rate is limited by the rapidity with which ions can be incorporated into the new phase. It is favoured by high concentrations of the electrolyte and low deposition overpotentials. Fleischmann et al. have considered the case when the growth of the nucleus is controlled solely by the rate of charge transfer (i.e. the mass transfer is relatively fast).[33] The current vs. time depends on a geometric factor and the rate of appearance of nuclei. When a suitable potential is applied to an inert electrode, the growth centres (nuclei) will appear at the surface and then grow. Assuming that the rates are time invariant and the resultant current is due to the quantity of the material transformed, the current at any time *t* is expressed by

$$I = nFkS ag{1-2}$$

where I is the current, n is the number of electrons involved in the reaction, F is Faraday's constant, k is the electrochemical rate constant at a particular overpotential, S is the surface area of deposit which is expanding. The surface area of one centre will increase with time. In the interval, dt, the centre expands dr in one dimension then

$$dr = \frac{Mckdt}{\rho} \tag{1-3}$$

where M is the molecular weight of the depositing material, c is the surface concentration and ρ is the density. Integrating the above equation within limits r = 0 at t = 0 yields

$$r = \frac{Mckt}{\rho} \tag{1-4}$$

Also the current into a hemispherical nucleus is

$$I = nFk2\pi r^2 \tag{1-5}$$

Then substituting the value of r in equation 1-4 gives

$$I = \frac{nF\pi M^2 c^2 K^3 t^2}{\rho^2} \tag{1-6}$$

Similarly, the current obtained for two dimensional cylindrical growth is

$$I = \frac{2nF\pi MLk^2t}{\rho} \tag{1-7}$$

Derivation for other geometries has also been reported in the literature. In all the above mentioned equations the currents are for the growth of single nuclei before the overlapping of individual zones.[34-37]

B-The diffusion controlled process characterizes the deposition from a low concentration electrolyte and high overpotentials in which the nucleus growth is limited by the rate at which material is

transported through the solution to the electrode surface. [33] Astley et al. [38] considered that linear diffusion is the dominant form of mass transport at all t, and then the current at a single hemispherical nucleus is given by the equation below

$$I = 2\pi r t^2 n F c \left(\frac{D}{r_t}\right)^{1/2} \tag{1-8}$$

where r_t is the radius of effective surface area, c is the concentration and D is the diffusion coefficient

$$r_t = \frac{2McD^{1/2}t^{1/2}}{\rho^2} \tag{1-9}$$

Substituting the value of r_t in equation (8) yields

$$I = \frac{8nFM^2c^3D^{3/2}t^{1/2}}{\rho^2} \tag{1-10}$$

and hence a linear dependence between I and $t^{1/2}$ is predicted. On the other hand Hills et al.[39] have given more importance to hemispherical diffusion in the growth of nuclei. Neglecting linear diffusion, the flux for hemispherical diffusion at small value of r_t is given by:

$$I = 2\pi r^2 ZFc \frac{1}{r_t} \tag{1-11}$$

where

$$r_t = \frac{2DMct}{\rho} \tag{1-12}$$

Then the final expression for the current is

$$I = \frac{ZF\pi(2Dc)^{3/2}M^{1/2}t^{1/2}}{\rho^{1/2}}$$
 (1-13)

Again a linear dependence of I vs $t^{1/2}$ is obtained but with a different slope. The equations so far obtained are for a mass transfer controlled process (the overpotential is high so that the concentration at the surface is zero).[39,40] The rate with which a new phase incorporates in an old one is considered the limiting step for nuclei growth in case of the interfacial controlled growth. For the diffusion controlled growth the rate at which the ions are transported in the solution toward the electrode is the limiting step.[33] Another classical model was proposed by Gruz and Volmer in 1931 [41] where the shape of the current transient during an electrodeposition depends mostly on the active surface of the cathode, and it can change strongly during the deposition. At lower overpotentials (small current densities) the ion concentration in the double layer is just slightly higher than the equilibrium one, established in the super-saturated state. Therefore, the deposition will occur just in the active sites but not all over the electrode surface. The further formation of new nuclei is

suppressed and the crystal growth occurs. In contrast, at higher overpotentials, the formation of new nuclei is accelerated. Thus, large grains are expected at low overpotentials and fine ones at higher overpotentials. Plieth[42] showed that from the electrochemical expression of the Kelvin equation (12), the critical radius of a spherical nucleus, r_{crit} , can be described to be inversely proportional to the overpotential, η , and thus to the current. As predicted also by the model of Gruz and Volmer, smaller and numerous particles are expected to appear at higher current densities.[33,42]

$$r_{crit} = -\frac{2\gamma V_M}{nF\eta} \tag{1-14}$$

where γ is the surface energy, n the number of transferred electrons, F the Faraday constant, η the overpotential and V_M the molar volume. When the diffusion fields around the growing nuclei overlap, the nucleation process will stop in these regions of the electrode. On longer time scales, nucleation will occur also in these regions because of the onset of natural convection, which will disturb the diffusion zones.

1.3.2 Theories for the chronoamperometric transients of nucleation and growth

The current transients can reveal information about the nucleation rate or about the number of nucleation sites. [43] Electrodeposition by a single potential step was chosen in the present study in order to see how the nucleation and growth parameters N_o and A were affected by the concentration of a surfactant added to the plating mixture. Different theories elaborated to describe the current transients in terms of the number of nucleation sites (N_o) and nucleation rate (A) were chosen for fitting our experimental data: the Scharifker-Hills model (SH), Scharifker-Mostany (SM), and Heerman-Tarallo model (HT).

a) The Scharifker-Hills model (SH)

Scharifker and Hills considered the nuclei to be hemispherical and randomly distributed on the surface, that the nuclei are growing under diffusion control and associated with two- or three-dimensional nucleation processes. The hemispherical diffusion zone radiates from each nucleus centre and grows at a radial velocity such that its radius, δ , is described as a function of time by the following equation[31]

$$\delta(t) = (kDt)^{1/2} \tag{1-15}$$

The overlap of diffusion fields is thus reduced to a two-dimensional problem, which is solvable using Avrami's theorem which states that

$$\theta = 1 - e^{-\theta_{ex}} \tag{1-16}$$

in which θ is the area on which new nuclei can appear and θ_{ex} is the extended area, the theoretical fraction of the area θ which has been nucleated if overlap is ignored. Avrami's theorem allowed Scharifker and Hills to relate the radial flux density through the real diffusion zones to an equivalent diffusive flux to an electrode of area θ . Analysing current time transients is an important technique for studying the kinetics of electrocrystallization. The form of the current transient is a typical characteristic of an electrochemical nucleation and growth process. According to Sharifker and Hills, the rate law for growth of 3D islands during electrochemical deposition is dependent on the mechanism of nucleation and growth. The final equations of SH (see chapter 4) are usually used in the form of dimensionless curves where $(I/I_{max})^2$ is plotted against t/t_{max} , with I_{max} and t_{max} being the current maximum of the measured current transient, and the corresponding time, respectively. These dimensionless curves have distinct characteristic shapes for instantaneous and progressive nucleation[31,33]. For short deposition times, the diffusion zones will be hemispherical, but for long times the diffusive flux and growth current can be written in terms of semi-infinite linear diffusion. Normally, the nucleation is a complicated problem between 2D and 3D, as the nuclei grow first at the plane of the electrode surface, but later, they will grow also in the bulk electrolyte. The rate law for growth of 3D islands during electrochemical deposition is dependent on the mechanism of nucleation and growth. Two limiting cases can be ascribed to the early stages of nucleation. The two limiting models are instantaneous or progressive three-dimensional nucleation with hemispherical diffusioncontrolled growth of nuclei. Progressive nucleation corresponds to a fast growth of nuclei on many active sites, all activated during the electroreduction. In this mechanism nuclei are continuously born during the whole time period at which overpotential is applied. So progressive nucleation will occur when the nucleation rate is low. Instantaneous nucleation corresponds to a slow growth of nuclei on a small number of active sites, all activated at the same time. In this case all active sites available on the electrode surface are occupied in a very short time period after applying overpotentials and then, the nuclei only grow. Therefore instantaneous nucleation occurs when the nucleation rate is very high. In practice, however, it is difficult to extract useful parameters from the SH model, and it suffers from the requirement that progressive and instantaneous cases be treated separately. [31,33,44] This model will be further discussed in chapter four.

b) The Scharifker-Mostany model (SM)

Scharifker and Mostany[31] developed a model of the current transient for 3D nucleation on a finite number of active sites, under diffusion controlled growth conditions. The number of active sites N_o and the nucleation rate per site A can be obtained from the current maximum I_{max} of the experimental current transient. The improvement introduced by the SM model compared to the SH theory is that the nucleation mechanisms (instantaneous and progressive) are treated together. The k (numerical constant) values are considered to be the same for both nucleation types and equal to $k = (8\pi cM/\rho)^{1/2}$, the k used in the Scharifker and Hills model for the instantaneous limit. As in the SH model, an

expression was derived to describe the total current that was obtained from the material flux to the growing centres considering diffusion zones around the growing centres. These diffusion zones are 2D projections of 3D hemispherical diffusional fields that develop around hemispherical nuclei during their growth. Thus the approach to the problem of nucleation becomes 2D. The diffusion zones are circular, whose radius will depend on the ages of the nucleation centres (*t-u*) where the age of a nucleus is given by the difference between the time that passed from the moment when the potential was applied (*t*) and the moment when the nucleus was born (*u*). In the SM formulation, the diffusion zones born at different times grow at exactly the same rate. Another particularity of this model is that the heights of the diffusion cylinders grow immediately after their appearance. The current transients obtained by the SM model can be compared to those given by Sluyters-Reybach (SRWBS).[45] The only difference is the way the authors considered the evolution of the radius of diffusion zones in time.[46]

$$I_{SM} = \left(\frac{zFD^{\frac{1}{2}}c}{\pi^{1/2}t^{1/2}}\right) \left(1 - exp\left\{-N_{\circ}\pi kD\left[t - \frac{(1 - e^{-At})}{A}\right]\right\}\right), \text{ where } k = \left(\frac{8\pi cM}{\rho}\right)^{1/2}$$
(1-17)

The Scharifker and Mostany model is similar to the Sluyters-Rehbach model, which described accurately the instantaneous nucleation cases, while, the SM model can describe the progressive and instantaneous nucleation.[46] However, both models fail to describe accurately the intermediate case. By an intermediate case one can define a nucleation which is not pure instantaneous (very large A and small N_o) or pure progressive (very large N_o and very low A). Another disadvantage is that the fitting of the experimental transients will look the same for different values of N_o and A.[33] Heerman and Tarallo[47] considered the problems of the SM model and said that SM is not correct and cannot be used to describe correctly the experimental current transient obtained at high values of N_o and low values of A. Also, the SM equation does not reduce to the correct expression for the limit of very short times when there is no overlap of diffusion fields. Moreover, the thickness of the diffusion layer in the case of overlap is a function only of time variable t. They argued that this is physically incorrect because such procedure allows the diffusion layer to expand always at the same rate whether all the nuclei are born or not. Thus the thickness of the diffusion layer must be a function not only of t but also of the nucleation rate constant A, except of course in the case of instantaneous nucleation (all nuclei are born immediately after the application of nucleation pulse).[48] This model will not be applied for our experimental data.

c) The Heerman-Tarallo model (HT)

Heerman and Tarallo derived a theoretical expression for electrochemical nucleation on microelectrodes, describing the case of diffusion-controlled growth. They reconciled the two approaches of Sluyters-Rechbach [45] (not discussed) and the approximate solution of Shoup and

Szabo[18]. The former depends on the idea that the height of all the diffusion cylinders is taken equal to the thickness of the Nernst diffusion layer for a simple redox reaction, and the later describes the chronoamperometric transient on microdisc electrodes. The HT model consists in expressing the current not via Cottrell's equation with only time variable, but also as a function of the thickness of the uniform diffusion layer in the case of overlap. The final equation has some mathematical complexity due to the presence of Dawson's integral in the general equation for nucleation kinetics. This difficulty is easily overcome by an approximation of Dawson's integral by a rational function and by the use of a fitting procedure based on the Levenberg–Marquardt algorithm for the analysis of experimental results. This procedure can be used to obtain the values of both the nucleation site density and the nucleation rate constant from potentiostatic transients.[29,47,48] The final equation and more details can be found in chapter four.

1.4 Preparation of palladium nanocentres

The most common palladium oxidation states are Pd(0), Pd(IV) and Pd(II) are known but the first two oxidation states are not normally stable and generally only exist as reaction intermediates.[49] Pd(II) is the only common stable oxidation state. The preparation of nanoparticles has been the subject of much research over the years. One of the major issues with the production of nanoparticles is their inherent low stability. Nanoparticles have high surface areas to volume ratios that lead to more edge and corner sites on the particle surface. This in turn leads to high surface energies which decreases their stability and often leads to increased aggregation.[50] In order to prevent this aggregation from progressing there have been several methods developed to help stabilise the nanoparticles. One method for improving stability is the encapsulation of the nanoparticle inside a dendrimer. Dendrimers are multi branched compounds that have a variety of active sites for the nanoparticle to bind to help reduce its surface energy and therefore increase its stability. The nanoparticles can be synthesised by the chemical reduction of metal salts inside the dendrimer molecules leading to mono dispersed nanoparticles. The process has been found to work well with palladium as once bound to the dendrimer it was found that a significant portion of the nanoparticle surface was unaffected by the binding and was sterically free to participate in catalytic reactions.[51] Figure 1-3 below shows a basic overview of the metal ion association and chemical reduction to yield the stabilised nanoparticle.

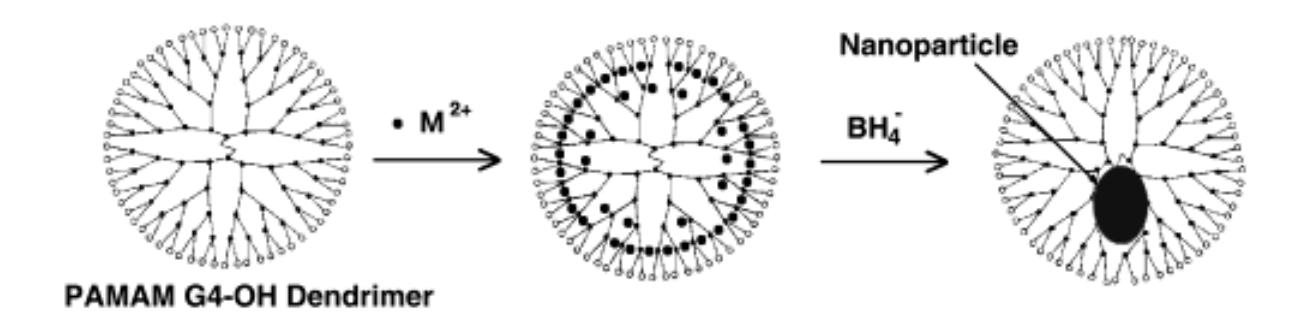


Figure 1-2 Overview of Pd nanoparticle synthesis and stabilisation inside a dendrimer molecule. Taken from [51]

Palladium nanoparticles are commonly stabilised in poly-vinyl-pyrrolidone (PVP) which again helps to reduce the surface energies of the particles increasing stability. The synthesis of these PVP stabilised nanoparticles is most commonly a chemical reduction of palladium metal salts in the presence of PVP. For chemical reduction ethanol is commonly used to reduce the Pd ions to Pd nanoparticles which then bind to the PVP molecules due to the increased stability this affords.[50]

Another method by which mono dispersed palladium nanoparticles have been synthesised is by thermal decomposition; the process involved the production of a palladium surfactant complex which was aged at high temperatures leading to decomposition of the complex into highly mono dispersed nanoparticles. The palladium particles were found to lack uniformity when first produced but the aging process led to the final mono dispersed product which was isolated from solution. It is noted that while there has been intensive development of palladium nanoparticles it has proven difficult to produce these in a uniform manner.[52]

Moreover, nanoparticles can be stabilised by immobilisation on a supporting substrate that reduces the surface energy in a similar fashion to the dendrimer molecules by adsorption to the substrate surface. Common substrates used with palladium nanoparticles have been glassy carbon and other forms of graphite.[53] Palladium nanoparticles are commonly produced via the electroreduction of metal ions in solution onto substrates and the electroreduction of metal complexes inside stabilising compounds. Palladium nanoparticles have been deposited by electrodeposition via several different approaches. Direct deposition of palladium nanoparticles from metal salts has been achieved. The deposition was found to be non-uniform with particle sizes ranging from 10-200 nm in diameter. The deposition was performed via chronoamperometry having determined an appropriate potential from cyclic voltammetry analysis. The particles were produced without a supporting surfactant.[54]

Highly dispersed palladium nanocentres have also been produced through the formation of highly distributed metal complexes adsorbed to the substrate surface. Following production of the metal

complexes, electroreduction was performed to convert the metal ions into palladium metal which retained the distribution pattern of the surface complexes.[13]

A green method was used by Mallikarjuna N. Nadagouda et al.[55] to form Ag and Pd nanoparticles using coffee and tea extracts. They described an environmentally friendly one-step method to synthesize noble nanoparticles, such as Ag and Pd, by reduction of corresponding metal solutions using tea and coffee extract without usage of any special capping agents at room temperature. The obtained nanoparticles are in the size range of 20–60 nm and crystallized in face centred cubic symmetry.[55]

The two-step metal organic chemical vapour deposition (MOCVD) of allylcyclopentadienyl palladium (Pd(allyl)Cp) is used to produced highly dispersed palladium nanoparticles supported on carbon nanofibres, which show high catalytic activity and stability in the hydrogenation of cyclooctene.[56]

Sang-Wook Kim et al.[52] developed the synthesis of monodispersed Pd nanoparticles from the thermal decomposition of Pd-surfactant complexes. The particle size of Pd nanoparticles was controlled by varying the concentration of the stabilizing surfactant. Pd nanoparticles had sizes of 3.5, 5 and 7 nm.[52]

S. Mubeen et al.[57] developed a simple and cost-effective fabrication technique to construct a hydrogen nanosensor by decorating single-walled carbon nanotubes with Pd nanoparticles. The sensing performance was optimized by varying the sensor's synthesis conditions (e.g. Pd electrodeposition charge, deposition potential and initial baseline resistance of the single-walled carbon nanotube SWNT network). The sensor after optimizing showed excellent sensing properties toward hydrogen (0.42% ppm) with a lower detection limit of 100 ppm and a linear response up to 1000 ppm.[57]

To investigate the physical and chemical properties of metal nanoparticles, especially the size-dependent properties, precise control of the particle size is basically required. Moreover, the precise control of particle size is also required for the organization of metal nanoparticles.[58,59] It has been found from mass spectral studies that the binding energies of metal nanoparticles consisting in fewer than ca. 1000 atoms vary periodically due to the quantum size effect.[60] This effect was found first by Knight et al. through experiments involving Na nanoparticles.[61] For noble metals, nanoparticles with the atomic shell structures as shown in Figure 1-3 are considered to be stable. So, a synthetic method is required to form any size of nanoparticles within a few angstroms. The synthetic methods to make such nanoparticles are either chemical or electrochemical reduction of metal ions in presence of stabiliser as linear polymers[62], ligands[63], surfactants [64,65], tetraalkylammonium salts[66], or heterogeneous [67] supports which could prevent the particles from aggregating and allow them to grow individually.[68] Studies have been done to control the size by using stabilising ligands such as

phenanthroline, triphenylphosphine derivatives, etc... The stabilised ligands are used to give stable metal-P bonds; and they stabilize the metal particles by the ionic moieties. An example where ligands were used to fabricate gold particles is the reduction of diluted aqueous HAuCl₄ with citric acid or trisodium citrate. When using trisodium citrate a very narrow size distribution can be obtained. Varying the experimental conditions allows the formation of particles with diameters between 14 and 900 nm. For more distinct sizes the use of so-called germ-growth is preferred. It is a two-step procedure which starts with a smaller colloid, e.g. 18 nm that can be formed by addition of citrate. The second step is the addition of HAuCl₄ that can be reduced by hydroxylammonium chloride. The 18 nm particles are now used as nuclei to germinate and grow the particles to the desired size.

Adding water soluble phosphines such Ph₂P(m-CH₄SO₃Na) or P(m-C₆H₄SO₃Na)₃ can stabilize the nanoparticles to such an extent that they can be isolated as solid materials. They can then be dissolved in water in any concentration forming blood-red colour.[69] Different shell structures were synthesized in respect to stabilized ligands, such as 2-shell Au[70], 4-shell Pt, and 5, 7, and 8-shell Pd,[71] Figure 1-3.

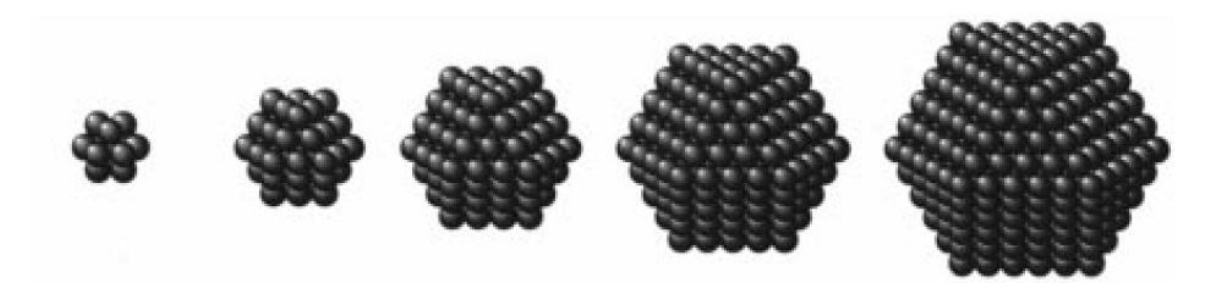


Figure 1-3 Shell structures of noble metal nanoparticles. From the left 1 shell, 2 shell, 3 shell, 4 shell and 6 shell. Taken from [72]

Oxidative etching in air has been used to form Pd nanoparticles; the study was done by Yujie Xiong et al.[73] who found that the oxidative etching might lead to the removal of twinned particles in the early stage and the dissolution of single-crystal cubooctahedra in the late stage. Figure 1-4 shows TEM images of Pd nanoparticles sampled at different stages from a reaction performed in air. At t = 5 min Figure 1-4 A, the sample mainly contained cubooctahedra 4-8 nm in size and 10% multiply twinned particles (MTPs). A magnified image of the 5-fold MTP is shown in the inset. As the reaction reached t = 1 h, all the twinned particles disappeared while the average size of the cubooctahedra grew to 8 nm. After 2 h, there was no significant change for both size and shape. Figure 1-4B shows a typical image of the sample obtained at t = 3 h. After the first 2 h, the cubooctahedra were seen slowly to dissolve until they reached an average diameter of 3 nm (Figure 1-4C). Through this time, the Pd particles started to grow again until they had an average size of 10 nm at t = 7 h 40 min (Figure 1-4D).[73]

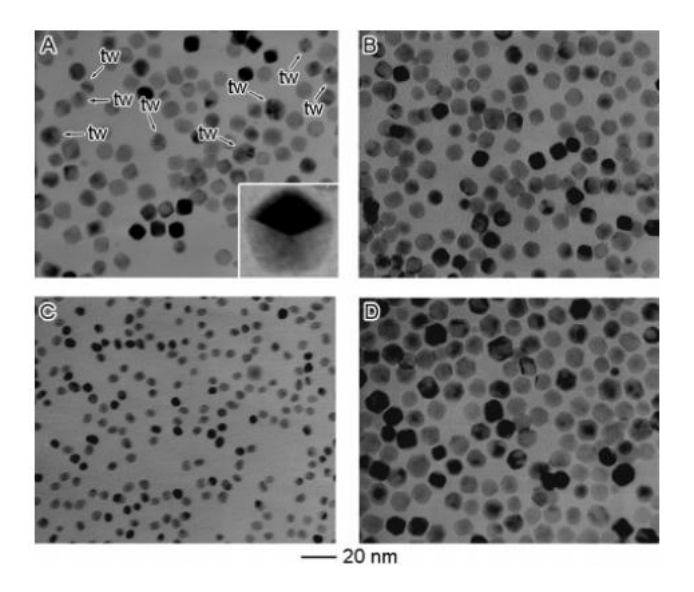


Figure 1-4 TEM images of Pd nanoparticles prepared in air at (A) t = 5 min; (B) t = 3 h; (C) t = 5 h; and (D) t = 7 h 40 min. Twinned particles are indicated by tw. The inset of (A) shows the magnified image of a 5-fold twinned nanoparticle. Taken from [73].

1.5 Application of palladium nanocentres

Palladium nanoparticles have found many uses as catalysts and electrochemical sensors. An example of this was as an electrochemical sensor for the detection of hydrazine.[54] Cyclic voltammetry with a palladium nanoparticle modified boron doped diamond disc electrode showed that the use of nanoparticles allowed for much better detection limits at lower concentration of hydrazine than is commonly possible with bulk catalytic electrodes.[54] Another benefit that has been discovered in the use of nanoparticles is in the area of flexible sensors; traditional palladium sensors that are fabricated on stiff substrates such as glassy carbon are limited in their usefulness in environments where a significant amount of mechanical strain is common. The palladium often suffers from fracturing under strain which greatly decreases its sensing capabilities. It was found that deposition of palladium nanoparticles onto a flexible plastic substrate already containing a network of carbon nanotubes allowed for hydrogen sensing to take place even while under mechanical strain.[74]

Platinum was employed as the catalyst for formic acid oxidation. It was noticed that the rate of formic acid oxidation on platinum is insufficient for different applications and that, because the formic acid oxidation in this case was mainly through the CO pathway, the Pt was easily poisoned by the amount of CO intermediate.[75] Recent researches have been explored Pd to catalyse the reaction of formic acid oxidation.[76] Pd also suffers from CO poisoning when used without any additional metal support. In this case the idea of alloying has proved to be an effective method to improve the activity of the Pd catalyst. Moreover palladium catalysts with different morphologies and structures have been synthesized, most of them in the range of nanostructures. Their ultra-small size offers a large specific surface area and they have a great potential to be employed in various electrochemical reactions

including oxidation of formic acid.[77] A study of size effects in electronic and catalytic properties of unsupported palladium nanoparticles in electrooxidation of formic acid was reported by Wei Ping Zhou et al.[78]; they found that the smallest particles with a size of 9 nm were the most active Pd nanoparticle catalyst in the formic acid electrooxidation, compared with particles of 11 and 40 nm. The particles were analysed by XPS and the smallest particles display the highest binding energy shift and the highest valence band centre downshift with respect to the Fermi level.[78]

Furthermore, the activity of ultrafine nonporous palladium is excellent and corresponds to high electrocatalytic activity and stability toward electrooxidation of ethanol and methanol.[79]

1.6 Surfactants

1.6.1 Lyotropic liquid crystal phases LLC

Non-ionic surfactants are molecules that consist of a hydrophobic hydrocarbon chain and a hydrophilic polar head group. They are often referred to as soaps. Surfactants are of particular interest with regards to creating nanostructures during deposition due to their ability to self-organize into lyotropic liquid crystals (LLC) when mixing the correct concentration of polar solvents with the most commonly used being water. Lyotropic crystals differ from regular thermotropic crystals in that the change in phase structure is more closely affected by the concentration of surfactant rather than due to thermal conditions.[80,81] An example of a LLC phase diagram is shown below in Figure 1-5.

Different phase structures can be produced by varying the weight percentage of surfactant in a reaction mixture. Non-ionic surfactant solubility in water depends on the temperature T, when the temperature increases the solubility decreases. Once a phase system has been identified for a particular surfactant it is relatively easy to produce the desired phase mixture simply by combining the appropriate concentrations of surfactant in water.[82,83]

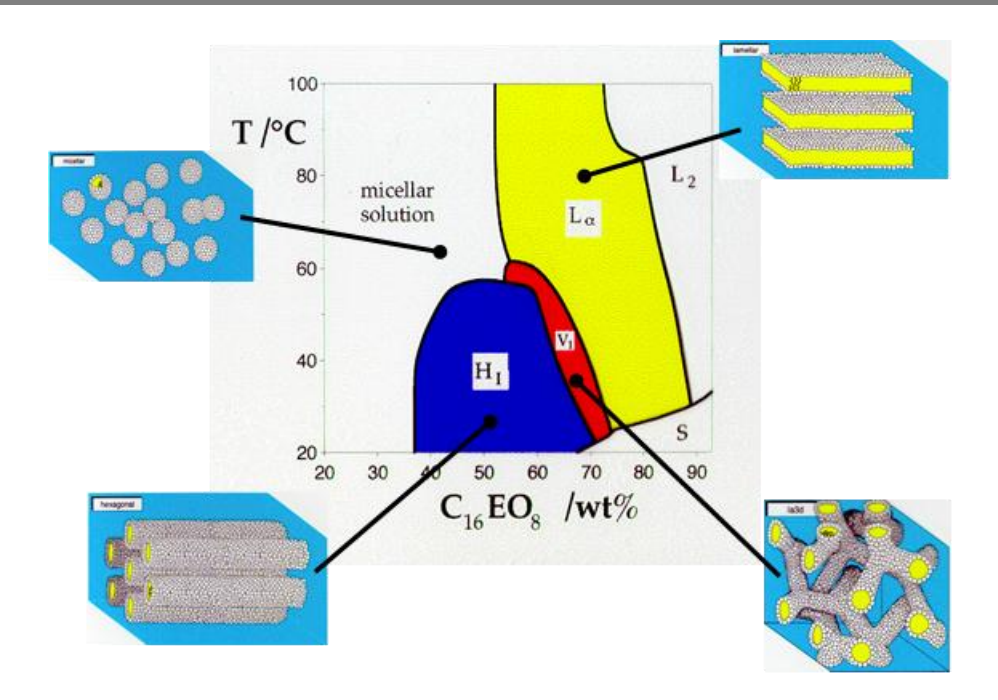


Figure 1-5 Phase diagram of the non-ionic surfactant octaethylene glycol monohexadecyl ether $C_{16}EO_8$. The diagram displays temperature vs. surfactant wt.% in water. Reproduced from[82]

The phases occur in water due to the hydrophobic nature of the chain groups and the hydrophilic nature of the head groups. The phase which forms is dependent on the concentration of surfactant in the water.[3] At very low concentrations the molecules dissolve in solvent, however as the concentration increases, the molecules aggregate into different structures. Micelles are formed first even if the surfactant concentration is lower than the critical micelle concentration; this is due to surface forces which generate a surface excess of surfactant molecules. The shape of micelles depends strongly on the surfactant concentration, electrolyte level and temperature. The micelle shapes are spherical in diluted mixture; where the hydrocarbon tails are shielded from the polar solvent by the closely packed polar heads of the molecules (forming the shell of the sphere). This is the lowest free energy state and is formed due to the hydrophobic effect; the interaction between non-polar solutes and water.[84] As the molecules begin to aggregate into micelles, a micellar solution is formed, usually denoted by L_I phase.[85] The micellar phase is more viscous than a standard water solution and this viscosity increases as the concentration of surfactant increases.[82]

Micelles usually require a minimum concentration before they will begin to form, below this critical concentration the surfactant molecules move randomly throughout the solution. However it has been observed that at the solution/electrode interface there are sufficient surface forces that micellar particles will form and adsorb to the surface. This means that surfactant templating can in fact occur at concentrations below the critical micellar concentration. [86]

At high concentration of surfactant there is a phase change in water at room temperature and a hexagonal phase can be formed. In the hexagonal phase the micelles pack together into cylindrical structures of infinite length arranged in a hexagonal formation. There are two distinct hexagonal phase structures; the hexagonal phase (H₁) and the reverse hexagonal phase (H₂). Both phases are viscous and have anisotropic structures; they interact with light depending upon the phase structure orientation with respect to the incident light. Therefore they exhibit birefringence when observed under a polarizing optical microscope; the hexagonal phases have a characteristic 'fan' texture.[80,86] The hexagonal phase is very viscous as there are strong interactions between the columns in solution. The hexagonal phase is stable over a wide range of temperatures and concentrations. The hexagonal phase has been researched to a high degree due to its diverse applications in deposition of mesoporous materials.

The hexagonal phase can exist in a normal hexagonal phase as described above but also as a reverse hexagonal phase where the concentration of surfactant has increased to the point where there is a higher concentration of surfactant in the mixture than the concentration of water. At this point the hydrophobic effect causes a reverse in structure so that the hydrophilic head groups surround hexagonal columns of water with the hydrophobic chains facing outwards. This phase has a much smaller range of concentrations and temperatures at which it is stable compared to the normal hexagonal phase.[87]

As the concentration increases there is another phase change at approximately 75 wt.% to the lamellar phase. The surfactant molecules line up into bilayers with hydrophobic chains in the middle of each bilayer with the hydrophilic heads on the top and bottom of each bilayer. The bilayers are separated from each other by layers of water. While there is a lower amount of water in the lamellar phase than in the hexagonal there is in fact a decrease in viscosity due to the greater variation in the thickness of the water layers compared to the rigid alignment of the hexagonal phase columns.[88]

The surfactant can form two cubic phases which occur at the upper and lower boundaries of the hexagonal phase in terms of concentration. The lower concentration cubic phase is a face centred cubic arrangement of the spherical micellar particles. The more concentrated cubic phase occurs between the hexagonal and lamellar phases over a very narrow concentration range. The surfactant in this phase forms large networks of connected micelles.[86]

1.6.2 Lyotropic liquid crystal templating

The concept of LLC templating is based on a specific surfactant phase or solution interacting with the substrate surface prior to deposition. The surfactant molecules adsorb on the substrate and prevent the metal deposition on the area of the electrode that they occupy; once the metal deposition is complete, the surfactant is removed by soaking the film in water to leave a porous metal film with a hexagonal

array of cylindrical pores as a direct cast of the lyotropic liquid crystalline phase. The key benefit of these pores is a significant increase in the effective surface area of the film. This increased surface area often leads to greater catalytic activity as there is a greater electroactive area available for reactions to occur on.[82] For the deposition of mesoporous materials, there has been a large amount of research into the use of LLC templating with specific focus on the hexagonal phase.

The object of the templating is to block some areas of the working electrode with LLC, and the deposited material will have widely increased surface area after surfactant removal as the hexagonal pores extend from the film surface to the substrate underneath. Deposition has been observed by both chemical and electrochemical reduction of metal salts in solution. Figure 1-6 shows the progression of LLC templating using the hexagonal phase. During the aqueous electrodeposition the metal reduction will only take place in the aqueous regions between the surfactant rods. Once deposition has occurred the surfactant can be removed by washing with water to leave behind a mesoporous material on the surface. The pores in the nanostructured material can be controlled by varying the chain length of the carbonyl group of the surfactant. Also the insertion of swelling agents (such as heptane) to the mixture helps to increase the diameter of the pores.[3]

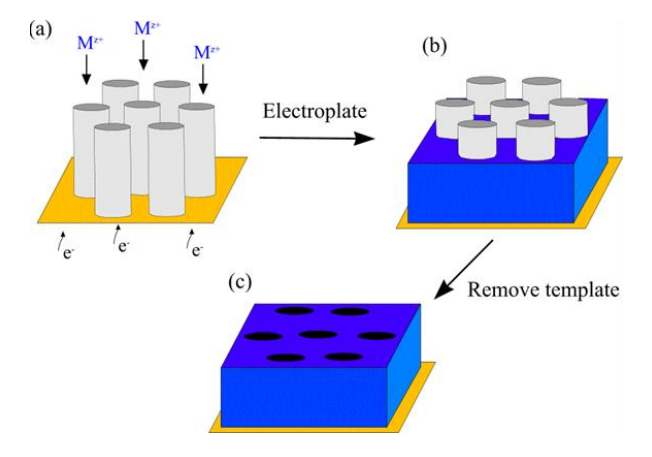


Figure 1-6 Shows the progression of hexagonal phase LLC templating, a) shows the hexagonal LLC columns adsorbed to the substrate surface, a potential is applied and reduction of the metal ions begins. b) Deposition of the metal has occurred around the hexagonal phase columns. c) The surfactant is removed by washing and pores remain in the film.

In addition to the normal hexagonal phase templating there has also been research done on the use of the reverse hexagonal phase to control the metal nanoparticles as the deposition is limited to the water rods surrounded by the surfactant. It has been found that the surfactant can facilitate the reduction of metal salts without need of an external reducing agent; this is accomplished by incorporating reducing groups into the hydrophilic head groups of the surfactant molecules.[81] The reverse hexagonal phases can be used to produce metal nanowires as the continued metal reduction in the water rods leads to the construction of long wires which remain after the surfactant is removed.[89]

Electrodeposition has also been performed using lamellar phase LLC. Rather than forming pores as would be the case with the hexagonal phase, it was observed that the deposited metal was formed in vertical layers with specific spacing between the layers. It was found that the spacing matched the shape of the lamellar bilayer that deposition had occurred in the aqueous layers between each lamellar bilayer. Surfactants have been used with various electrodeposition techniques including cyclic voltammetry and chronoamperometry. The surfactant templating functions in the same way regardless of the deposition technique which allows surfactants to be used in a wide range of experiments.[90]

1.7 Platinum nanostructured films

Platinum is widely known as a good catalyst for many chemical and electrochemical reactions including oxygen reduction, hydrogen oxidation, methanol oxidation and hydrogenations.[91,92] Platinum has several oxidation states, ranging from 0 to +6. However, the common and stable oxidation states are Pt(0), Pt(II) and Pt(IV).[93] Pt(IV) has a d⁶ electron configuration. The complexes of Pt(IV) can be either neutral or anionic and are generally octahedral.[94] Pt nanostructures were electrodeposited onto microelectrodes to raise the surface area and increase mass transport characteristics thus leading to efficient amperometric sensors that can be used for H₂O₂ within a wide range of concentrations.[4] Also it can serve as an excellent catalyst for CO/NOx oxidation in catalytic converters, refining of petroleum and lots of organic reactions such as hydrogenation.[95] Moreover, platinum particles play an important role in a component of fuel cell technology, where Pt acts as an excellent electrocatalyst for the oxygen reduction reaction and fuel, including hydrogen, methanol, ethanol, and formic acid, oxidation reaction.[4,95-98]

Well-defined Pt nanostructured films can be prepared by either chemical or electrochemical reduction of platinum compounds (Hexachloroplatinic acid H₂PtCl₆).[99] Platinum was deposited chemically by wet impregnation of the substrate, using water soluble metal salts, followed by calcination and reduction. This resulted in well-dispersed catalysts with high activity and good thermal stability, but this method has some weakness with controlling the particle size and getting high degree of control over the particle size. Then many techniques have been developed in order to improve control over the particle size, such as electron beam lithography, colloidal lithography, and spin-coating techniques.[100] Also small particles can be produced by laser ablation of a platinum metal plate in liquid medium of sodium dodecyl sulphate (SDS). The Pt crystals are stable but tend to grow progressively in a time scale of a month.[101] Electrochemical deposition has been developed to overcome the disadvantages of chemical deposition, and the main aim is to reduce the Pt amount used while keeping a good catalytic performance. This effort can be done by preparing porous Pt with high surface area and interconnected structure. The interconnected structure can have another feature: it can increase the catalytic activity for reactions including two or more reactants, because they can provide different adsorption sites.[102]

Nanostructured platinum can be produced by the electrochemical reduction of metal salts in a lyotropic liquid crystal (LLC). The preparation of hexagonal phase mesoporous Pt material (denoted H_1 -Pt) was prepared by implementing a true liquid crystal template technique by the reduction of hexachloroplatinic acid (HCPA). First reported in 1997,[103] it appears as a perfect method for the synthesis of nanoparticles with pore sizes in the mesoporous range (2-50 nm) under potentiostatic control. The pores are cylindrical in shape with diameters in the range 18-25 Å depending on the concentration of surfactant and the alkyl chain length.[3]

1.8 Semiconductors

While most work in this research involved the electrodeposition of noble metal nanocentres, the reminder of the work investigated the electrodeposition and doping of ZnSe semiconducting nanocentres for the purpose of developing a nano-scale light emitting diode.

Semiconductors are materials having conductivity between those of metals (10^4 to 10^6) Ω^{-1} cm⁻¹ and insulators (10^{-22} to 10^{-10}) Ω^{-1} cm⁻¹. The fundamental difference between those three materials will be discussed in terms of energy band theory but another distinct feature between them is the effect of temperature on the conductivity; for semiconductors the conductivity increases with the temperature whereas for metals the temperature dependence is typically weak but here the resistivity increases with increasing temperature, Figure 1-7. The resistivity of these three materials at room temperature is shown in table 1-1.

Table 1-1 Room temperature resistivities for the categories of materials

Category	ρ (Ω cm)
Insulator	10 ¹²
Semiconductors	$10^6 - 10^{-3}$
Metals	10 ⁻⁶

Other aspects of the electrical properties of semiconductors should be considered:

- > non-Ohmic behaviour and rectifying effects;
- > large impurity effects;
- both positive and negative charge carriers;
- ➤ high thermoelectric power;
- > sensitivity to light-production of photovoltage and change in resistance.[104]

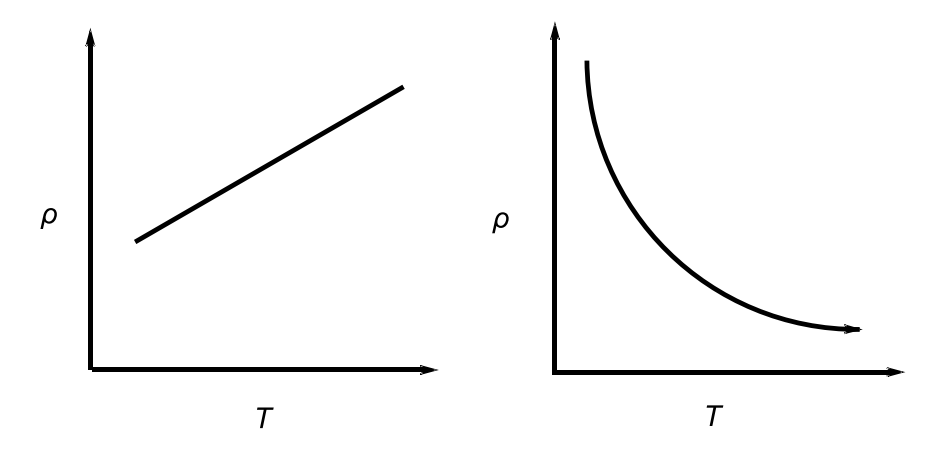


Figure 1-7 on the left: resistivity *vs.* temperature for a metal, on the right: resistivity vs. temperature for a semiconductor. Redrawn from reference [104]

1.9 Electronic energy bands: basic theory

In order to explain the electrical conductivity in solids as a function of energy level, it is essential to give some information about band theory of solids. We need to know about three energy bands namely: valence band, conduction band and forbidden band or energy gap, Figure 1-8.[105] Also, an important parameter in the band theory is the Fermi level, is the highest filled ground state level at K. The position of the Fermi level with respect to the conduction band is a crucial factor in determining electrical properties.

Conductors have a large number of free electrons. When a potential difference is applied across a conductor the free electrons move from the negative terminal to the positive terminal of the supply, thereby constituting an electric current. Conductors allow the flow of electric current through them. For example copper, aluminium, brass and all metals are conductors. Furthermore, in conductors, the valence and conduction bands overlap in such a way that there is no band gap. There is a slight potential difference across the conductor resulting from the movement of electrons.[106]

An insulator is a substance that does not allow the flow of electronic current through it. In terms of energy bands, the valence band is full while the conduction band is empty and the distance between the conduction and valence bands is very large. As a result of this a high electric field is needed to push the valence electron into the conduction band and electrical conductivity of such a material is extremely small and can be regarded as negligible in normal conditions; diamond, wood and glass are examples of insulators.[106]

The semiconductor is a substance whose electrical conductivity lies between that of conductors and insulators. According to the energy band levels, the valence band is almost full and the conduction band is almost empty, but the energy gap between them is also very small, therefore a small potential difference is enough to push valence electrons into the conduction band.[106]

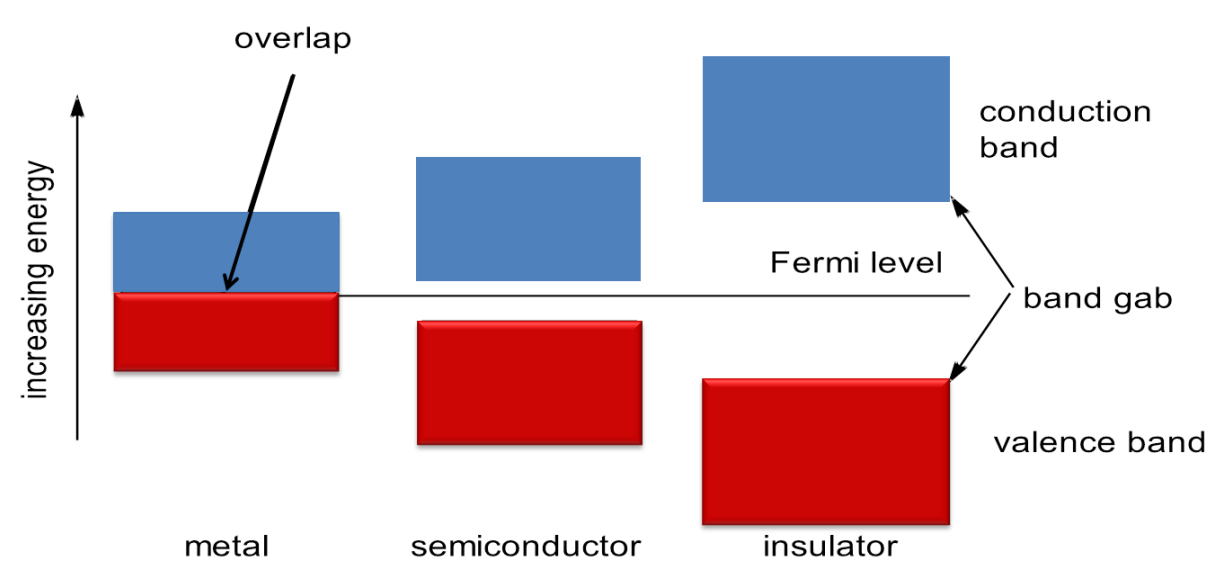


Figure 1-8 Comparison of the band gaps for a metal, a semiconductor and an insulator. Redrawn from reference [107]

1.10 Doping

Intrinsic semiconductors are semiconductors without any impurities added and the conductivity is related to the electrons in the conduction band and the holes in the valence band, Figure 1-9. For intrinsic materials the number of electrons is equal to the number of holes, since one conduction electron gives rise to one valence band hole, and we have bipolar conduction with the net current carried by equal amounts of electrons and holes (intrinsic conduction). So, for intrinsic semiconductors:

$$N = p = n_i \tag{1-18}$$

where, N is the concentration of electrons per unit volume, p is the concentration of holes per unit volume, n_i is the intrinsic carrier concentration of the semiconductor under consideration which depends on the semiconductor material and the temperature.[108] To ensure predominance of on carrier type in the semiconductor, it is necessary to introduce some impurities into the semiconductor lattice. These impurities can act as acceptor (A) or donor (D). This addition of impurities is called doping. Doping materials can migrate through the semiconductor either interstitially (i) or substitutionally (s). Addition of dopant material affects the electrical properties, e.g. carrier generation and mobility, resistivity and conduction type. The addition of impurities can be achieved by many methods,

- Addition of an element in the melt during crystal growth.
- Addition of an element during epitaxial deposition of a semiconductor film.
- > Solid-state diffusion of elements from the surface or a suitable interface.
- > Ion implantation of elements into the semiconductor at relatively low temperature.
- Addition of element during electrodeposition of a semiconductor film.

The first two methods produce uniform doping of the semiconductor, while the last three methods result in an impurity concentration gradient. Before describing the n-type and p-type semiconductors, it is worth giving an example of an intrinsic semiconductor and some details about energy levels. The two very important semiconductors that are used in the fabrication of electronic devices are silicon Si and germanium Ge. Figure 1-9 illustrates the electronic structure for Si. It is tetravalent which means they have 4 electrons in their outermost or valence shell. Each valence electron is shared with 4 surrounding atoms through covalent bonds. At 0 K° all the valence electrons are firmly bound to the nucleus and they cannot move at all, the covalent bonds are strong.[109] At room temperature some electrons acquire sufficient energy to be able to break the covalent bonds and form an electron – hole pair in its place. The electron – hole pair is called the charge carrier and these pairs conduct electricity by moving within the material when the semiconductor is connected to an external electrical source. The mechanism of charge transfer by holes is simple: when an electron on atom Si₁ moves out it leaves a hole behind and the atom acquires a positive charge which attracts a neighbouring electron from atom Si₂. The electron from Si₂ moves to the vacancy on Si₁ creating a hole on position 2 and a positive charge on Si₂. This process continues with the motion of holes in opposite direction to that of the electrons. Generally, all electron – hole pairs contribute to the flow current I. So the total current can be written as

$$I = neAv_h + neAv_e (1-19)$$

where A is the area that the charges are moving through, v_h and v_e are the velocities of holes and electrons respectively. The velocity of electrons is much larger than that of holes but n the number particles is the same for holes and electrons, as mentioned in eq. 1-18, for intrinsic semiconductors.[110] At absolute zero the valence band is completely filled, the conduction band is empty and the bands are separated by an energy gap, E_g , which is less than 3 eV. At very low temperatures there are no free electrons so these materials behave like insulators as for conduction to take place electrons must be able to move when an external field is applied across the material. When the temperature increases the electrons in the valence band acquire sufficient energy to be able to jump the gap and move into the conduction band; the electrons in the conduction band and the holes left in the valance band contribute to the flow of current when an external field is applied to the semiconductor. In reality, the numbers of electrons and holes are very small so to make the semiconductor as good as a conductor, it is necessary to dope the material to increase their numbers.[111]

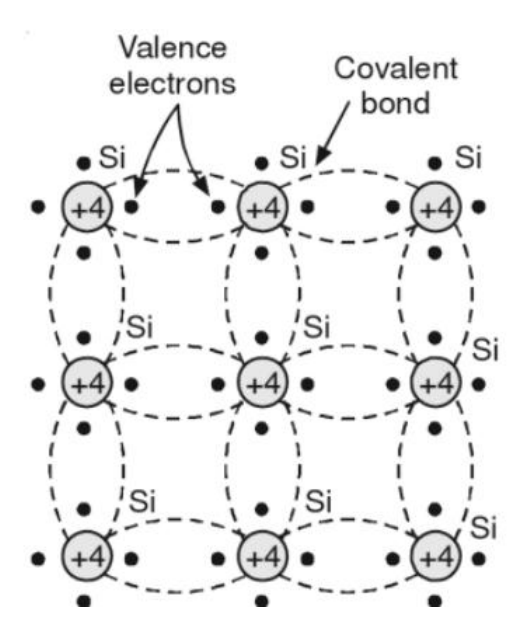


Figure 1-9 Diagram showing the electronic bonds in an intrinsic semiconductor (Si). Taken from [112]

1.10.1 n-type semiconductor

The *n*-type dopant materials are group V elements in the periodic table like N, P, As, etc... and thus their atoms have 5 valence electrons that can form covalent bonds with the 4 valence electrons that silicon atoms have. Figure 1-10 shows that if a dopant element from group 5 is added, it will take the place of a Si atom. In this case four electrons from the dopant are shared with neighbouring silicon atoms but the fifth electron remains free to move around in the material. Adding a dopant increases the concentration of electrons available and affects the conductivity of the semiconductor. The majority carriers are the electrons and the minority carriers are the holes. Also, there are always a few thermally generated electrons and holes.[108,111] The number of electrons is already so large that those few thermally generated electrons do not make much difference, but it should be considered that there are a few holes that are present and these are now called the minority carriers as there are fewer of them.

Looking at Figure 1-10 we see that the energy levels of the donor atoms are just below the conduction band, about 0.01 eV below. So these levels are called donor levels. At room temperature the thermal energy of the electrons is about 0.025 eV which is bigger than the energy gap, hence the electrons present in the donor levels can move into the conduction band as they have sufficient energy to jump this small gap. In the conduction band there is a very large number of majority carriers as well as a few thermally generated electron hole pairs, because the electrons will jump the energy gap and leave behind holes. Holes in the valence band are the minority carriers.[108,110]

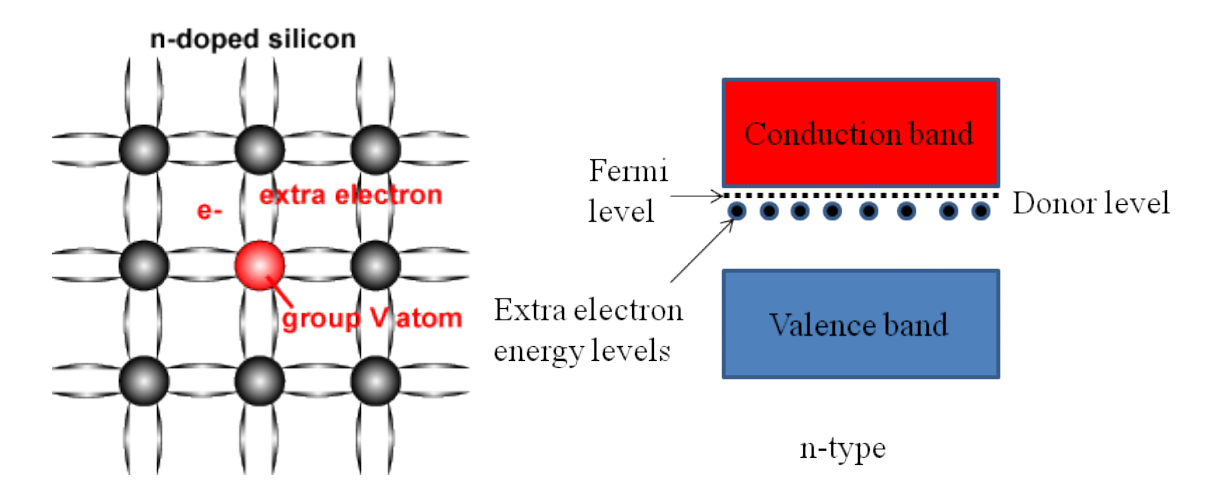


Figure 1-10 *n*-doping with a group 5 element, the left side, band model of n-doped semiconductors, right side. Reproduced from [113].

1.10.2 p-type semiconductor

The *p*-type dopant materials are group III elements in the periodic table like B, Al, Ga, etc... and thus their atoms have 3 valence electrons. They can replace the silicon atoms, so they are substitution impurities, Figure 1-11. In this case 3 dopant electrons are shared with neighbouring silicon atoms but the forth is a hole, an electronic vacancy, which borrows a neighbouring electron. Since the material ends up with an excess of positive charges or holes, it is called p-type and where p stands for positive. These holes can move through the material and help improve the conductivity of semiconductors.[108,110,111]

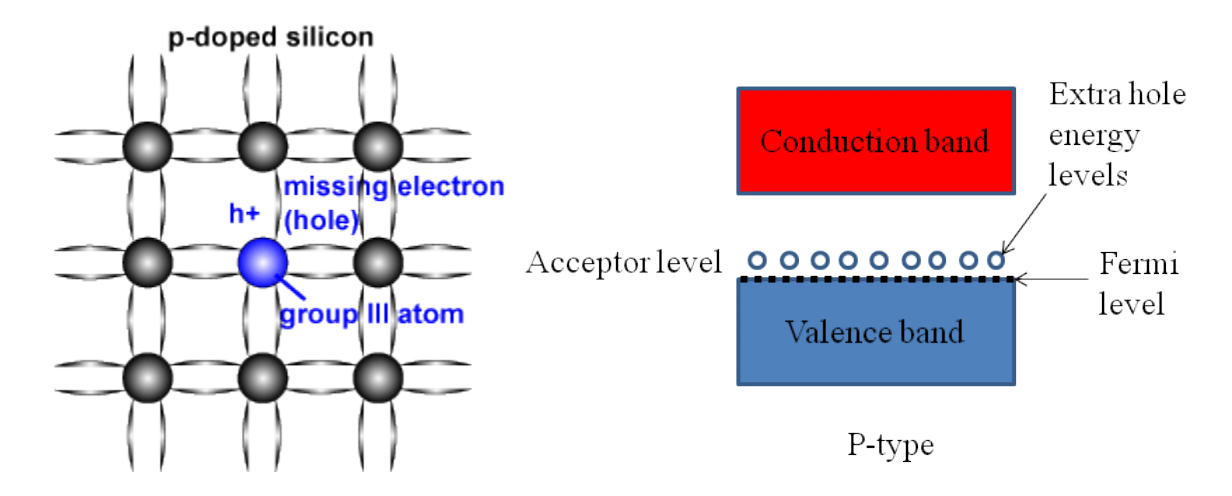


Figure 1-11 p-doping with group 5 elements, left side and band model of p-doped semiconductors, right side. Reproduced from [113].

Figure 1-11, show the Si atoms after adding acceptor dopant. Acceptor levels are slightly above the valence band, about 0.01 eV, and electrons can transfer from the valence band to an acceptor level,

leaving a hole in the valence band. These holes are free to move and these are the ones that provide the conductivity. In a p-type semiconductors holes are majority carriers and the very few thermally generated electron are the minority carriers.[108]

1.11 p-n junction diode

In order to examine the ZnSe electrodes doped with n- and p-type, tests were done by creating an electrical contact between separate electrodes, respectively bringing a p- and n-type ZnSe centre, by micromanipulation under an optical microscope. When an n-type semiconductor is brought into contact with a p-type one, a p-n junction is formed. Since the n-type region has a high free electron concentration and the p-type a high free hole concentration, electrons diffuse from the n-type side to the p-type side leaving behind a positive charge on the n- side region. Similarly, holes flow by diffusion from the p-type side to the n-type side creating a negative charge on the p- side. The junction behaves very differently than either type of material alone. As a result of the movement of holes and electrons, the region close to the junction will not have any free mobile carriers but there will be some charges as a part of the lattice itself and this creates a region depleted of any moving charges. On the other hand the donor and acceptor impurities do not move (unless exposed to high temperature) but the electrons and holes coming from them are free to move. However, this movement cannot go on forever. The increasing number of fixed charges left behind attracts the carriers that are trying to diffuse away (the acceptor centres want to retain the holes and the donor centres want to keep the electrons), hence an electrical field made up by the fixed charges builds up to such an extent that it slows down the diffusion process. This diffusion process does not stop entirely but reaches an equilibrium. So, around the p-n junction is the region that has lost its free charge carriers (holes and electrons) and it has only ions. This region is known as the depletion region, since it is depleted of free carriers. At the equilibrium state there is no net current flow.[108-111]

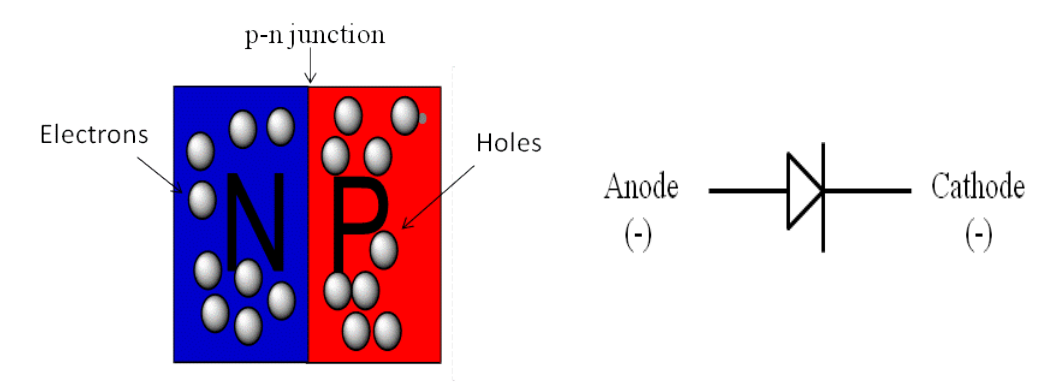


Figure 1-12 p-n junction, left, and its electrical schematic symbol, right. Redrawn from [114].

Figure 1-12 (left) is a simplified physical representation of a p-n junction diode, while Figure 1-12 (right) depicts its electrical schematic symbol. There are many types of p-n junction diode used for different applications, such as the following: photodiode – light sensitive diode, LED - light emitting diode, varactor diode – variable capacitance diode.[110]

1.12 Built - in potential barrier

The junction is considered in thermal equilibrium when no voltage is applied across the p-n interface. The Fermi level energy level is constant. When more electrons from the n-side want to diffuse across the junction, they will be prevented by the negative charges within the depletion zone, so they will be repulsed and opposed for the diffusion from other charges on the other side of depletion region. Thus, there is now some kind of barrier and the difference in potential between the two sides is called the potential barrier; it is the potential difference across the depletion region that stops further diffusion of electrons or holes.[109]

When increasing the temperature above 0 K, there is a minority of electrons on the p-side and a minority of holes on the n-side; these are thermally generated charge carriers. As mentioned above the potential barrier stops any electrons or holes from crossing over to the other side. In contrast, the minority carriers are accelerated and tend to cross to the other side. The electrons and holes that are present will sweep across the junction and they will constitute the drift current. Thus, a drift current is created by the minority carriers (the electrons on the p-side or holes on the n-side) that are swept across the junction by barrier potential difference.[108-110]

1.13 Applying bias to the p-n junction

A p-n junction diode is a one-way device offering low resistance when forward-biased and behaving almost as an insulator when reverse-biased. The basic difference between a forward bias and reverse bias is the way of applying a voltage (bias) to the p-n junction. It is possible to connect either the positive terminal of the voltage source to the n-side or the p-side of the junction. Figure 1-13 shows a current – voltage or *I-V* characteristic for a p-n junction. From the Figure it is obvious that current flows easily in one direction (forward bias) and that there is only a small current flow with the bias reversed. The forward bias current increases rapidly with increasing applied voltage, and the rise is in fact exponential. A very low constant current is observed under reverse bias until a breakdown of the junction occurs. The junction is always able to pass a current when a bias is applied but its magnitude depends on the direction of the bias.[108-111]

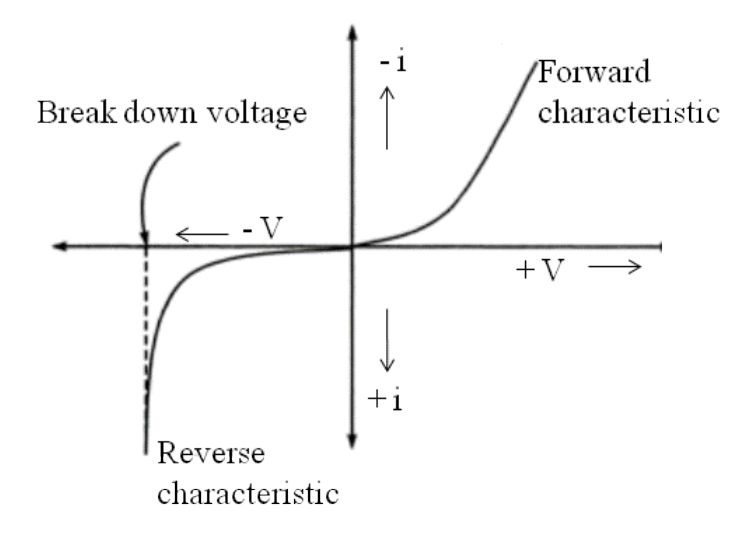


Figure 1-13 p-n junction I-V characteristic. Reproduced from [115].

1.13.1 Forward Characteristic

When the diode is forward-biased and the applied voltage is increased from zero, the energy barrier height of the junction reduces, electrons and holes are no longer prevented from diffusing across the structure and an electrical current appears in the junction due to the diffusion mechanism, Figure 1-14. The electrical resistance of the junction is now low and the diode behaves like a conductor. It is clear from the diagram that the reduction of the depletion region width leads to a reduction in the energy barrier height for electrons and holes in the potential difference across the junction. [108-111]

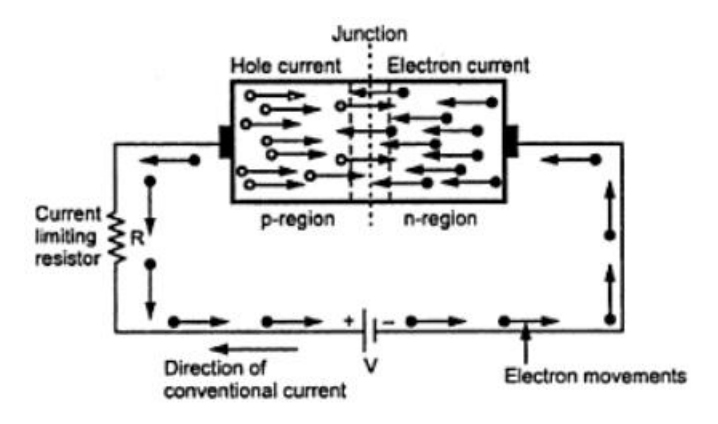


Figure 1-14 Biasing the p-n junction (forward characteristic). Taken from [116].

1.13.2 Reverse characteristic

When the diode is reverse-biased, as the voltage is reversed and becomes greater in the p-n region, the barrier height increases preventing the diffusion of electrons and holes, the electrical current then is negligible and reflects the minority carriers which are easily swept across the region by the electric field. Now, the resistance becomes greater and the diode acts like an insulator. The value of the generated current is independent of the applied reverse voltage but depends on (a) temperature, (b) degree of doping and (c) physical size of the junction.

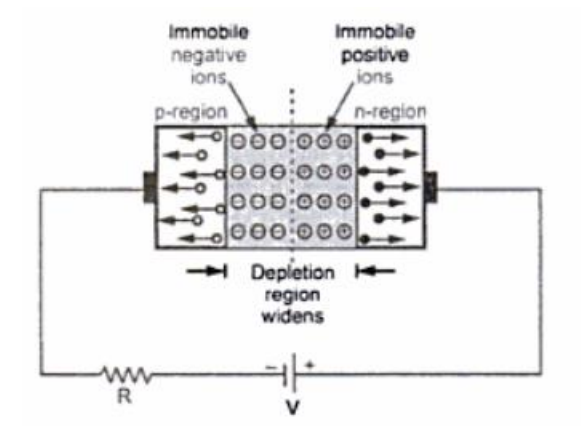


Figure 1-15 Biasing the p-n junction (reverse characteristic). Reproduced from [116].

1.14 Semiconductor Photo-Electrochemistry

The first report published on semiconductor electrochemistry was in 1955 by Brattain and Garrett.[117] Since then much research has focused on this topic. Electrode processes on semiconductor materials have different characteristics which completely differ from electrode reactions on metals. When the semiconductor is in contact with the electrolyte, the interface of the semiconductor electrode, as shown in Figure 1-16A, consists of three layers: a significant part of the applied potential operates across the space charge region within the semiconductor, a compact ionic layer at the interface, which is also called the outer Helmholtz plan (OHP) layer, and a diffuse layer on the side of aqueous solution. The interfacial charge consists of: the charge Q_{sc} in the space charge layer, the charge Q_{ss} in the surface states, the charge Q_{ad} of adsorbed ions in the compact layer, and the ionic excess charge Q_s carried by hydrated ions in the diffuse layer in the aqueous solution. Electroneutrality at the interface can be written as:

$$Q = Q_{sc} + Q_{ss} + Q_{ad} + Q_s (1-20)$$

Moreover, the total potential ΔE across the electrode interface is given by the sum of the three potentials across the space charge layer, the compact layer, and the diffuse layer as shown below:

$$\Delta E = \Delta E_{sc} + \Delta E_{OHP} + \Delta E_d \tag{1-21}$$

where ΔE_d is the potential of the diffuse layer referred to the solution interior, ΔE_{OHP} is the potential of the compact layer referred to the outer Helmholtz plane, and ΔE_{sc} is the potential of the space charge layer referred to the semiconductor surface (ΔE_{sc} is often referred to the semiconductor interior in texts of semiconductor physics).[106,118-120] The thickness of these layers is in the order of 0.4 to 0.6 nm for the compact layer and can be determined by the radius of the ions, 10 to 1000 nm for the space charge layer, and 1 to 10 nm for the diffuse layer. The thickness of the space charge layer and of the diffuse layer depend on the concentrations of mobile charge carries in the semiconductor and in the aqueous solution, respectively.

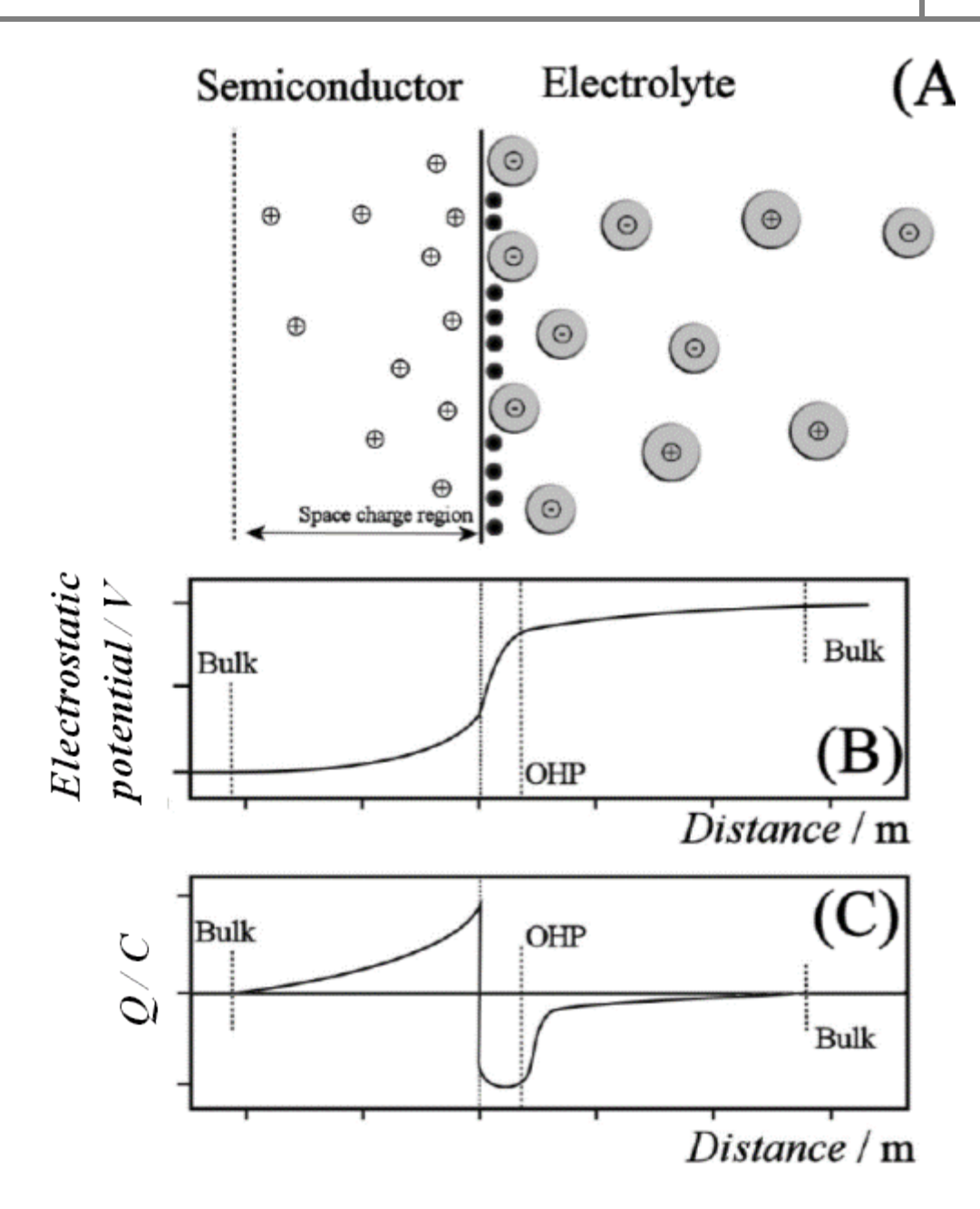


Figure 1-16 (A) Structure of the double layer and (B) the potential distribution from the bulk semiconductor to the bulk solution and (C) charge at the semiconductor / electrolyte. Reproduced from [119,120].

In the practical study of the double layer at semiconductor / electrolyte interfaces, the capacity of the interfaces C considers the important parameter can be measured. The capacity C can be measured as a function of the electrode potential E. The total measured capacity of a semiconductor in contact with an electrolyte can be represented by a series connection of three capacities as shown below

$$\frac{1}{c} = \frac{1}{c_{sc}} + \frac{1}{c_{OHP}} + \frac{1}{c_d} \tag{1-22}$$

where C_{sc} , C_{OHP} , and C_d are the capacities of the space charge layer, the compact layer, and the diffuse layer. With germanium electrodes (an intrinsic semiconductor), $C_{sc} \sim 0.01 \, mF$, $C_{OHP} \sim 10 \, mF$, and $C_d \sim 0.1 \, mF$. Since the total capacity is determined by the smallest capacity, the interfacial capacity of ordinary semiconductor electrodes may be approximated by the capacity of the space charge layer, C_{sc} . [105,106,119,120]

1.14.1 Potential distribution across the electrode interface

For a p-type semiconductor, generally the Fermi level is lower than the redox potential of the electrolyte solution, and thus electrons should move from the solution to the electrode to gain equilibrium. This movement forms a negative charge in the space charge region and leads to a downward bending in the band edges, Figure 1-17b and Figure 1-18c (left). The holes in the space charge region are removed by this process and this region is now called a depletion layer. In contrast, in the case of n-type semiconductor the Fermi level is higher than the redox potential of the electrolyte, so in this case the electrons will immigrate from the semiconductor surface to the solution, Figure 1-17a and 1-18a, thus a positive charge will be formed in the depletion region as a result of movement; this is reflected in an upward bending of the band edges.

The second process that can occur is the accumulation of majority carriers at the interface, when the initial electrochemical potential of the solution becomes more negative than the Fermi level of the semiconductor; when reaching the equilibrium state, charges tend to transfer from the solution phase to the semiconductor phase. The electrons that have moved into the semiconductor are not restricted to the impurity atom sites. Instead, the majority carriers exist as delocalized charges in the conduction band. The localized region in the semiconductor where the negative charges accumulate is called the accumulation region.

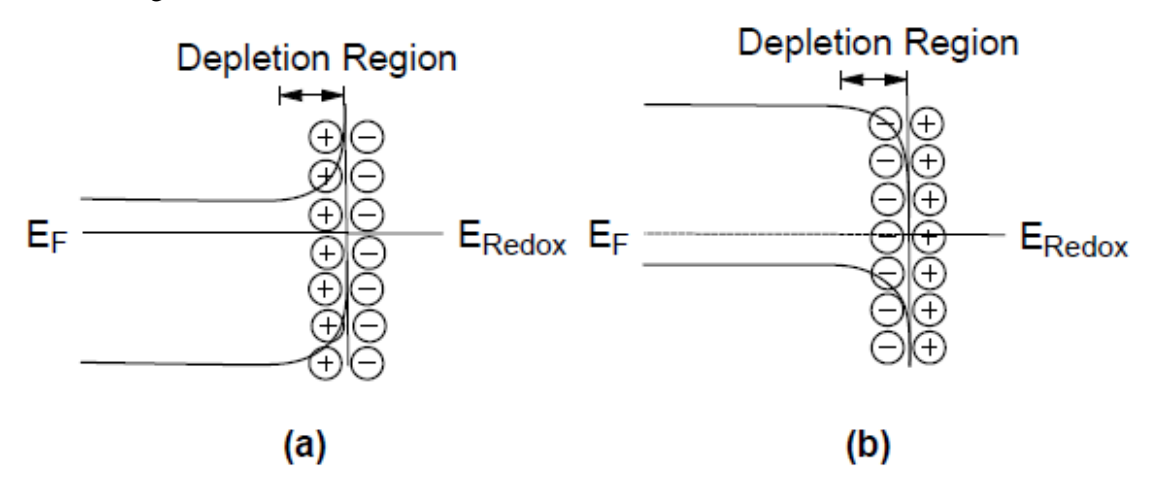


Figure 1-17 Band bending for an n-type semiconductor (a) and a p-type semiconductor (b) in equilibrium with an electrolyte. Reproduced from [121].

Furthermore, the most important variation between the depletion and accumulation is that, the carriers are removed from immobile dopant atom sites under depletion conditions. While in accumulation the charges get in orbitals that are a part of the conduction band, these excess of majority carriers can stay either on dopant atoms or the lattice atoms of the semiconductor. The thickness of an accumulation region is smaller than the depletion region at least for the same dopant materials and semiconductor. The width is less than 100 Å, while the width of the depletion region is on the order of micrometres. However, electrode reactions at semiconductor | electrolyte interfaces are strongly dependent on the existence of charge carriers and the change in the energies of the band edges on going from the interior of the semiconductor to the interface, thus the magnitude and direction of band bending depend on the applied potential. Three different cases should be considered:

- a. At a certain potential, both the Fermi energy and the solution redox potential have the same energy level, Figure 1-18b (right) and (left). In this case there is no charge transferred and hence there is no band bending. This potential is therefore referred to as the flat band potential, E_{fb} which is equivalent to the potential of zero charge.
- b. Depletion regions can be considered when potentials positive of the flat band potential are applied for an n-type semiconductor and potentials negative of the flat band potential for a p-type semiconductor, Figure 1-18a (right) and Figure 1-18c (left).
- c. An accumulation region arises at potentials negative of the flat band potential for an n-type semiconductor, there is now an excess of the majority charge carrier (electrons) in this space charge region, Figure 1-18c. An accumulation region arises in a p-type semiconductor at potentials more positive than the flat band potential, Figure 1-17a.

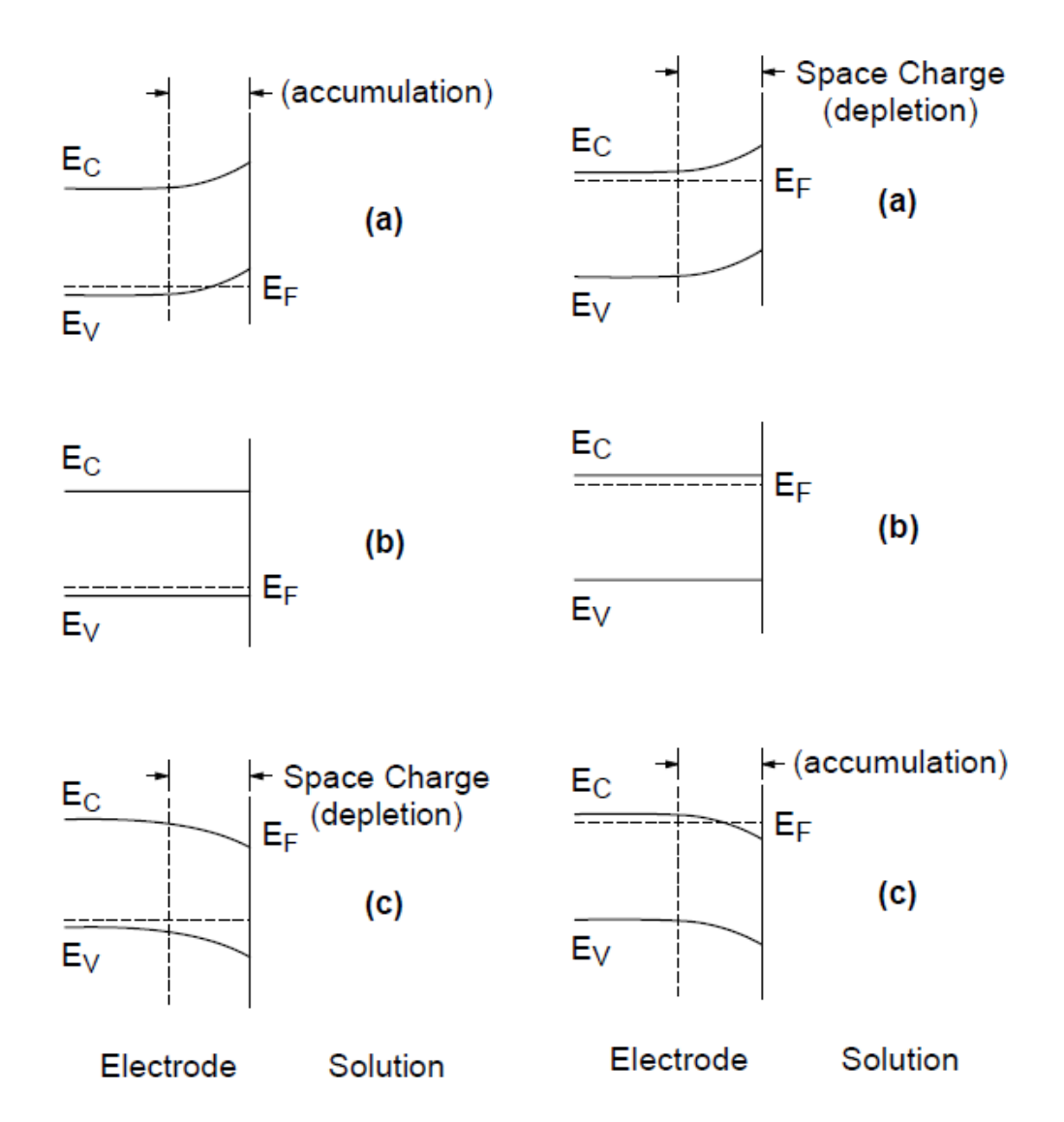


Figure 1-18 Effect of varying the applied potential (E) on the band edges in the interior of an p-type semiconductor, left column, and of an n-type semiconductor, right column. a) $E > E_{fb}$, b) $E = E_{fb}$, c) $E < E_{fb}$. Reproduced from [121].

The semiconductor electrode behaviour will vary depending on whether there is an accumulation layer or a depletion layer, if a depletion region is available then there are few charge carriers available for charge transfer and electron transfer reactions take place slowly. In contrast, the semiconductor behaves as a metallic electrode if there is an accumulation layer, since there is an excess of the majority of charge carriers available for charge transfer.[119,121,122]

1.14.2 Photo-effects of semiconductor electrodes

As discussed in the previous section, an increase in the number of charge carriers at the semiconductor | electrolyte interface will increase the conductivity and allow electron transfer to occur between the electrode and the electrolyte. When shining a light (with a photon energy hv greater than the band gap energy of the semiconductor) minority carriers will be created holes h^+_{cb} and e^-_{cb} , as equation 1-24.

$$hv + e_{vb}^- \rightleftharpoons h_{cb}^+ + e_{cb}^-$$
 (1-24)

This excitation leads to the promotion of an electron from an orbital in the valence band e_{vb} into the conduction band, and creates a hole in the valance band. For example, with an n-type semiconductor, when positive potentials are applied, the band edges curve upward and the holes transfer towards the interface. Also the electrons move to the interior of the semiconductor. Because the hole has a high level of energy that can help extracting an electron from the solution species, in this case we can consider the semiconductor acts as a photoanode.

Figure (1-19) shows an ideal behaviour for an n-type semiconductor electrode in the dark and under illumination. There are three different zones: at zone II there is no current in dark or upon illumination and the potential is called the flat band potential. At potential negative to the flat potential region I, an accumulation layer exist, and in this case the electrode will behave as a cathode whether the electrode in dark or under the irradiation. At potentials negative to the redox potential of the analyte (E°) , zone III, there is a significant anodic current under illumination, while no current can be observed in the dark. This region is attributed to depletion region. In contrast, the p-type electrode can act as anode in dark and as a cathode under illumination. The other process is the recombination, in which the electron can be promoted to the conduction band after exposing a light to the electrode. The recombination process occurs in the interior of the semiconductor. The recombination of the promoted electron with the resulting hole occurs together with the release of heat.[121,123]

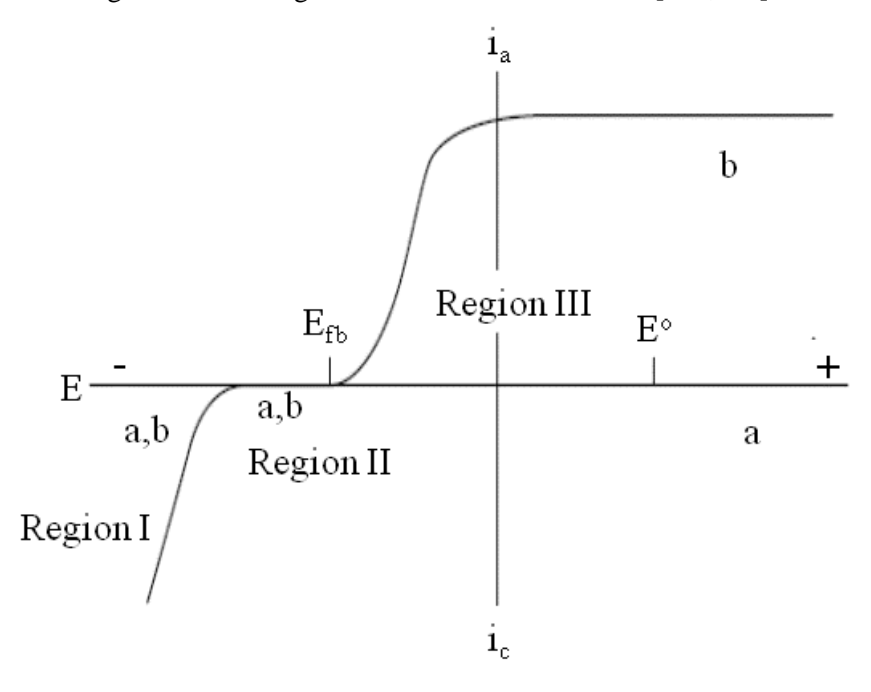


Figure 1-19 Ideal behaviour for an n-type semiconductor in the dark (a) and under irradiation. Reproduced from [121].

1.15 Zinc selenide semiconductor

Zinc selenide (ZnSe) is a wide bandgap II-VI semiconductor. It has been used intensively in a number of semiconductor devices and solar cells, because its bandgap of 2.7 eV corresponds to the visible region of the electromagnetic spectrum. Moreover, ZnSe and its alloys with sulphur, cadmium and magnesium are promising materials for fabrication of light-emitting devices, such as blue-green laser diodes. Short wavelengths lead to smaller diffraction limited spot sizes and are thus great for high density optical storage technologies such as CD-ROM and photo-refractive devices.[124] ZnSe crystallizes in the zincblende lattice structure with the Zn and Se atoms located on separate face-centred cubic sublattices. Due to the large difference in the electronegativity of the Zn and Se atoms, the Zn-Se bond is more ionic than covalent in character. It is calculated that the bonding of Zn and Se atoms in the tetrahedral environment of the zincblende lattice has a 63% ionic component. The polar nature of ZnSe implies that electrons are localized about the Se anion. In terms of band structure, the tighter binding results in relatively large electron and hole effective masses. The interest in ZnSe is due to its large direct bandgap (2.67 eV at room temperature) and large non-linear optical coefficient, due in part, to its non-centrosymmetric crystal structure.[125]

ZnSe has been investigated as a potential light emitter in the blue of the visible spectrum for over 30 years. The bandgap 2.7 eV corresponds to a photon with a wavelength of 400 nm. Many efforts have been put to improve light emitting devices fabrication and the first successful attempt was in 1988 when the first p-n junction was produced used Li as the p-type dopant atoms.[126] Furthermore, the first ZnSe laser diode was fabricated in 1991 doped with nitrogen atoms to form a p-type semiconductor; After that lots of attempts were made to produce the blue-green light.[125] Many methods have been used in order to fabricate the LED e.g. via a solution growth method or a vapour phase deposition method. J. N. Nishizawa et al.[127] succeeded in fabricating a p-type blue ZnSe single crystal. The method used was a temperature difference method under controlled vapour pressure (TDM-CVP). Their idea was to lay ZnSe solid material on a Se melt under a saturated vapour pressure of Zn, and Li atoms were used as dopant material in order to have a p-type Se melt. The p-type ZnSe was grown at 1050 °C under 7.2 atm. No one except them managed to get a LED using their method. It has not yet been confirmed by other groups. It is also reported that Li-doped ZnSe was widely used to form the p-type layer of a p-n junction, but it was found that Li atoms in ZnSe are very diffusive, so it is hard to fabricate high quality p-n junctions by means of Li doping.[128,129] K. Akimito et al. deposited n-type ZnSe using Ga dopant atoms and p-type ZnSe doped with O by molecular beam epitaxy (MBE) on GaAs substrate at 240 °C.[130] Migita et al. reported that undoped ZnSe films and N-doped ZnSe could be grown on n-type GaAs as substrate by MOCVD method.[131] The film was grown at temperatures between 250 °C and 450 °C. The undoped ZnSe was n-type and they claimed that this was due to the presence of chloride that had been included in the material gas. These vapour phase growing methods were good to grow ZnSe crystal

films with low degree of defect and impurities at low temperature (300-400 °C). However these methods have not managed to give sufficiently good quality p-type ZnSe and could not produce materials able to generate light.[131]

In 1987 Singh et al. reported the growth of p-type films of ZnSe by electrochemical technique.[132] Their method involved several steps of coating one surface and four sides of a titanium (Ti) plate (1.3×1.3) cm. The other surface of (Ti) plate should be left uncoated. This step followed by immersing the half coated titanium plate in a solution of ZnSO₄ + SeO₂, then applying a current through the solution for four hours. A thick film (5 µm) of ZnSe polycrystalline was formed on the uncoated surface of (Ti) plate. This procedure produced ZnSe/Ti which is not a real diode of pure ZnSe, but a junction of a metal and semiconductor. Also, they immersed the Ti/ZnSe plate into a solution of $ZnSO_4 + KI + I_2$ and measured the photovoltaic effect, the capacitance of the Ti/ZnSeplate. The Ti/ZnSe showed a response to X-ray irradiation, and they claimed that a p-type polycrystal was obtained without clarifying the reason which led to the making of a p-type material. Their material also failed to emit light.[132] Moreover, most of the conventional methods for making p-type ZnSe films require in general such conditions as high vacuum, high temperature or high pressure. So these conditions need large scale equipment.[129] In 1991 Matsuura et al.[133] described a novel and simple method for producing a blue light emitting diode with a p-n junction of ZnSe with good films having minor defects and impurities at low temperature. In this method SeSO₃ and ZnCl₂ are used to prepare a plating solution; the working electrode was an n-type ZnSe single crystal substrate; it was immersed into the solution controlling the temperature to 70 °C. By applying appropriate potentials, the p-type ZnSe was deposited on the top of the n-type ZnSe. So then a p-n junction was produced. The diode worked well after sending direct current of 60 mA to the diode under the voltage of 4.8 V at 300 K. The diode with this procedure was able to emit blue light.[129]

1.16 Thesis structure

This thesis is organized into 8 chapters and 1 appendix. Chapter 2 illustrates all the chemicals, fabrication of electrodes, instrumentation, characterisation and software used in this research. In chapter 3 the early stages of electrodeposition of Pd nanoparticles on different carbon substrates will be discussed. Chapter 4 indicates a study of how to prepare surfaces with controlled size and dispersion of nanoparticles by electrodepositing palladium in presence of a surfactant. The work will focus on the nucleation and growth of the electrodeposition of Pd from different aqueous mixtures of octaethyleneglycol monohexadecyl ether (C₁₆EO₈). The electrocatalytic activity of the particles that prepared by the same method in chapter 4 will be discussed in chapter 5. Chapter 6 indicates how to prepare metal nanostructure film using different concentration of surfactants. In chapter 7 we will discuss our investigation of electrodeposition and doping of ZnSe particles for the purpose of developing a nano-scale light emitting diode. Chapter 8 is the conclusions and future work.

2. Experimental

In this chapter, the chemicals, fabrication of electrodes, instrumentation, characterisation and software used in this research will be explained in detail. This will be followed by a presentation of the procedures for the electrodeposition of palladium and platinum from aqueous solutions and from lyotropic liquid crystal mixtures; also the electrodeposition of ZnSe will be discussed in detail.

2.1 Reagents

Table 2-1 contains details of the reagents used during the experimental work. The table includes chemical name, formula, manufacturer and grade/purity where specified. All reagents were used at room temperature. No further purification was performed on the provided reagents. All glassware was soaked for 24 hours in a solution consisting of 5% Decon 90 (BDH) and deionised water from a Whatman RO50 system combined with a Whatman STILLplus carbon filter.

Table 2-1 Reagents used within the experimental work.

Reagent	Formula	Manufacturer	Purity
Alumina powder	Al_3O_2	Buehler	
Epofix resin and hardener		Struers	
Silver paint		RS Component	
Silver loaded epoxy resin		RS Component	
Ammonium tetrachloropalladate (II)	NH ₄ PdCl ₄	Aldrich	97.00
Hydrogen hexachloroplatinate hydrate (IV)	H ₂ PtCl ₆ .3H ₂ O	Aldrich	99.9
Octaethylene glycol monohexadecyl ether	$C_{16}EO_8$	Aldrich	98.00
Sulphuric acid	H_2SO_4	BDH	Gr. 1.84
Potassium chloride	KCl	Fischer Scientific	99.81
Argon	Ar	BOC Gases	99.99
Potassium hydroxide	KOH	BDH	85.00
Ethanol	C_2H_5OH	Fisher	99.9
Formic acid	HCO_2H	BHD	98.00
Perchloric acid	$HClO_4$	Aldrich	70.00
Argon	Ar	Bos gases	99.90
Oxygen	O_2	Boc gases	99.90
Zinc sulphate	$ZnSO_4$	BDH	99.50
Selenium (IV) oxide	SeO_2	Acros organics	99.999
Ammonium sulphate	$(NH_4)_2SO_4$	Hogg chemical	98.50
Gallium (II) sulphate hydrate	$Ga_2(SO_4)_3$	Aldrich	99.99
Sodium sulphate	Na_2SO_4	BDH	99.00
Gold (wire, \emptyset =50, 25 μ m)	Au	Goodfellow	99.99
Platinum (wire, \emptyset =50, 25 μ m)	Pt	Goodfellow	99.99
Mercury	Hg	Alfa Aesar	99.999

2.2 Instrumentation

Chronoamperometry, cyclic and linear sweep voltammetry were carried out with a Micro Autolab type III (Ecochemie) controlled with the GPES v.4.9 software (Ecochemie). All experiments were performed in an earthed aluminium Faraday cage in order to minimise electrical noise with a three electrode configuration.

2.3 Electrochemical equipment

All electrodes and cells were home made by the glass workshop of the School of Chemistry, University of Southampton. Glass electrochemical cells were used with a three electrode configuration, Figure 2-1. The reference electrode used during deposition was a homemade saturated calomel electrode (SCE); the reference electrode used during characterisation in 1 M sulphuric acid was a homemade saturated mercury sulphate electrode (SMSE) and mercury mercurous oxide (MMO) was used for the experiment designed to record voltammograms for the oxidation of ethanol. The counter electrode was a large area platinum mesh electrode.

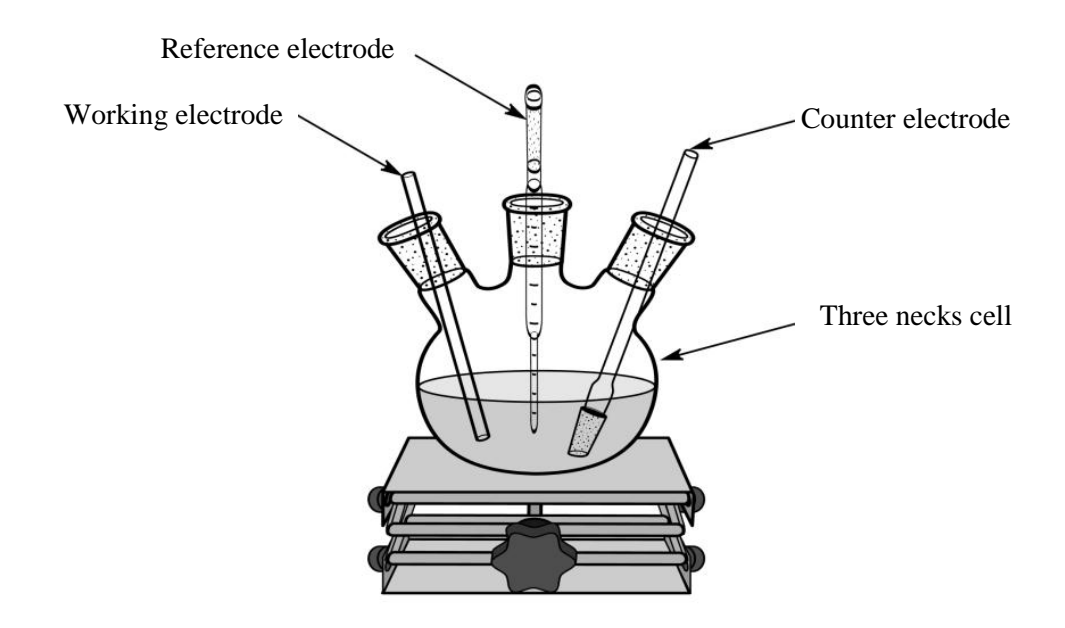


Figure 2-1 Schematic diagram of a three neck pear-shaped cell.

2.4 Fabrication of electrodes

Homemade platinum 25 µm Ø, gold 25 and 50 µm Ø and 3 mm Ø glassy carbon rods (Tokai Carbon Co. Ltd.) were used as working electrodes. They were fabricated in soda glass tube as disc electrodes. A copper wire was mounted in the tube until reaching one end of the working electrode wire. To make the connection between the working electrode and copper wire, an equal mixture of silver loaded epoxy adhesive and hardener was made then one end of the connecting wire was dipped into that mixture. It was immediately inserted into the glass body to make contact with the exposed working electrode wire then kept overnight to dry. Then the connecting wire was held in place by putting a mixture of quick set epoxy resin and hardener around the wire onto the glass; this step is required to strengthen the connection between the copper and working electrode and avoid losing the connection when pulling the copper wire. The epoxy mixture was left to dry and harden. Figure 2-2 illustrates a sketch of the working electrodes used for most experiments.

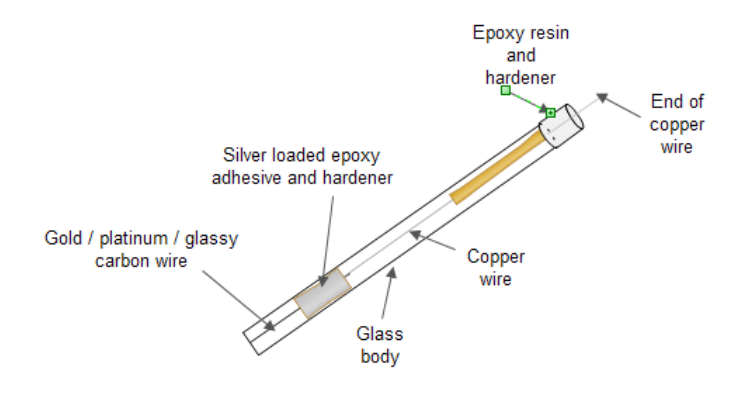


Figure 2-2 Schematic diagram for the gold/ platinum electrode.

Highly ordered pyrolytic graphite HOPG grade ZYH, 12 mm x 12 mm x 2 mm (Advanced Ceramics) was used in this research as a working electrode. Immediately prior to each experiment, the HOPG was cleaved using double sided adhesive carbon tape, which exposed an atomically smooth basal surface, then it was stuck on a metal support material. A special cell was designed in order to facilitate dealing with the HOPG layer. The cell was fabricated in the Southampton mechanical workshop and made of Teflon. The working electrode was placed in the middle of a sandwich cell with exposed area left for making the contact with crocodile clips then the two parts of the cell were screwed. The upper part (overturned T shaped) had a long cylindrical part that could be filled with 10 ml of solution and the reference and counter electrodes could be immersed inside it. The counter electrode was a large platinum mesh that was wrapped on the lower part of the reference electrode. Figure 2-3 shows the schematic diagram of the setup of HOPG in the sandwich cell.

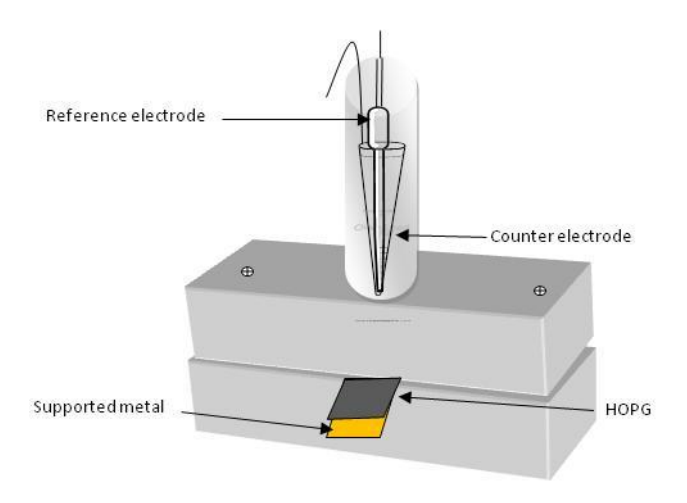


Figure 2-3 Schematic diagram indicating the set up of the three electrode system for electrodeposition on HOPG.

Figure 2-4 shows the schematic diagram of the fabrication of carbon fibre wire electrodes. A carbon fibre microcylinder electrode (CF) of 7 μ m diameter with a length of 5 mm was used as the working electrode in a three electrode system neck cell (a large cell with wider necks to avoid breaking the

fibre). The glass capillary tube was snapped into an approximately 10 mm length, then rinsed with distilled water and transferred to the oven for about 30 minutes. Later, a single carbon fibre was mounted into the capillary tube using a cross-locking tweezers. To make the connection a copper wire was initially dipped in silver loaded epoxy and hardener then sealed into the capillary tube to make the contact with the carbon fibre. The electrode was then left for about an hour to dry. Once the connection had been made, the capillary tube was filled with epoxy resin and hardener and it was left overnight to dry. The approximate length of the exposed carbon fibre wire was measured using a ruler of high precision. The carbon fibre was also measured using the scanning electron microscope to accurately determine the length of the exposed carbon fibre. This working electrode could be used immediately without any pre-treatment before carrying out any voltammetric experiment. All experiments were conducted in a Faraday cage to minimize surrounding electrical noise. It was important for the electrode surface to be free from palladium before commencing any experiments. Therefore, each fabricated cylindrical fibre electrode was used for one experiment. Hence, this successful fabrication of disposable cheap electrode helped to save time from polishing the electrode surface.

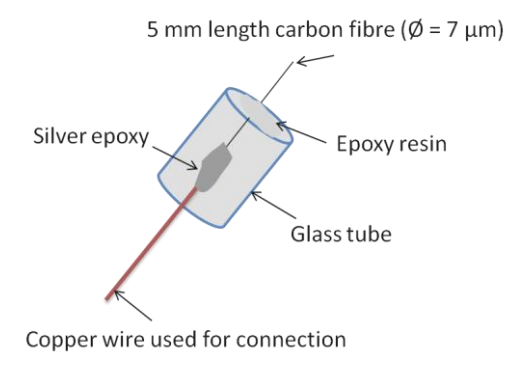


Figure 2-4 The schematic diagram of a 7 μm diameter carbon fibre wire electrode.

2.5 Reference electrodes

2.5.1 SCE reference electrode

The electrode, Figure 2-5a, consists of an outer and inner glass tube. The inner tube contains a paste composed of a mix of mercury, Hg_2Cl_2 and KCl with a platinum wire running into it. The outer tube is filled with a saturated aqueous KCl solution. The end of the outer tube has a porous sinter. The tubes are screwed together ensuring that no air bubbles are present.

2.5.2 SMSE reference electrode

The electrode, Figure 2-5b, consists of an outer and inner glass tube. The inner tube contains a paste composed of a mix of mercury, Hg_2SO_4 and K_2SO_4 with a platinum wire running into it. The outer tube is filled with a saturated aqueous K_2SO_4 solution. The end of the outer tube has a porous sinter.

The tubes are screwed together ensuring that no air bubbles are present. The reference electrodes were stored in saturated potassium sulphate and potassium chloride solutions respectively between each set of experiments.

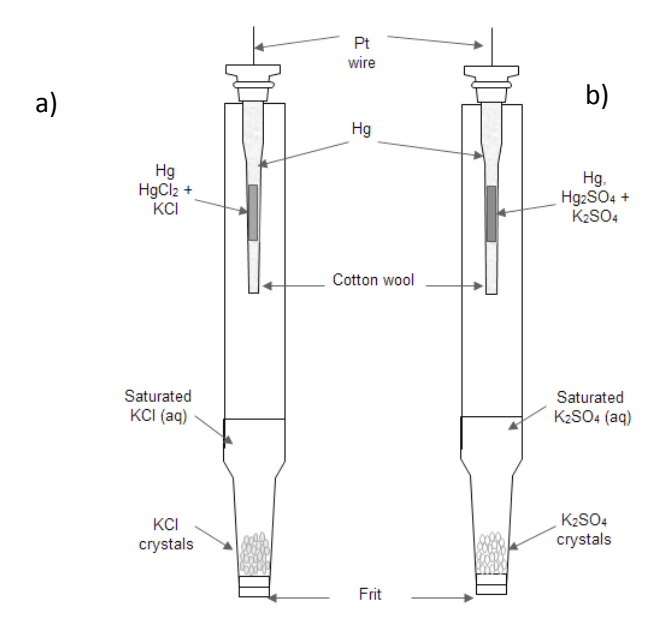


Figure 2-5 A diagram of a) saturated calomel electrode (SCE) and b) saturated mercury sulphate electrode (SMSE).

2.5.3 Mercury-mercuric oxide reference electrodes (MMO)

A mercury-mercuric oxide reference electrode was used for the experiment designed to record voltammograms for the oxidation of ethanol in Ar purged 0.5 M ethanol + 0.1 M KOH at 100 mV s^{-1} with GC electrodes decorated with the Pd deposits in chapter five. Figure 2-6 shows the diagram of a MMO.

The Hg/HgO electrode was prepared using the same method as described for the SCE but instead, the calomel paste was replaced by a paste consisting of a 1:1 mixture of NaOH:HgO and the saturated KCL solution was replaced by a saturated NaOH solution. The electrode was then tested against a commercial Hg/HgO reference and was only deemed suitable for use if the potential difference between the two electrodes was less than 4 mV. The reference electrodes were stored in saturated NaOH solution between each set of experiments. Before use the electrode was rinsed with ultra-pure water to remove the NaOH solution from the outside of the glassware.

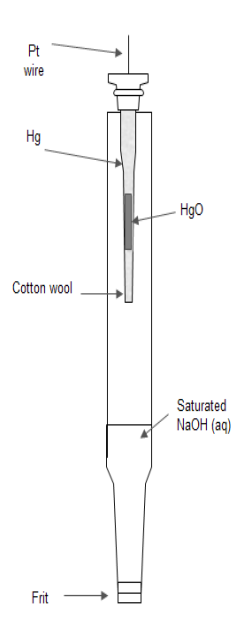


Figure 2-6 A diagram of mercury mercurous oxide (MMO) reference electrode.

2.6 Electrode pre-treatment

2.6.1 **Gold**

The electrodes were initially polished on a polishing wheel with silicon carbide paper grade CC-240 for 2 minutes, CC-600 for 4 minutes and finally CC-1200 for 8 minutes. The electrodes were then polished by hand using alumina powder suspended in water on nylon polishing cloth, 5 μ m for 15 minutes, then 1 μ m for 20 minutes and finally 0.3 μ m for 25 minutes. Before each set of experiments, the electrodes were polished for 1 min with silicon carbide CC-1200 grit, and then polished using a 5 μ m for (2 minutes) and 1 μ m (4 minutes) alumina slurry and finally a 0.3 μ m (10 minutes) alumina suspension.

2.6.2 Glassy carbon (GC)

The glassy carbon electrode was polished on silicon carbide (CC-1200 grit) for 1 min, then on polishing cloth (Buehler) with alumina powder (successively 5, 1, 0.3 and 0.05 μ m) for 2, 4, 8 and 16 min respectively. After each polishing step the electrode was rinsed with deionised water and cleaned in an ultrasonic bath of acetone for 15 min then in an ultrasonic bath of water for further 30 min. This procedure was chosen to ensure that the electrode surface was free from old Pd particles and that its surface roughness remained constant. Unless otherwise stated all voltammograms were recorded on the first cycle.

2.7 Electrode characterisation

2.7.1 Gold electrode characterisation

After being washed with distilled water the gold electrodes were characterised by cyclic voltammetry in 1 M sulphuric acid to determine that the electrodes displayed the gold oxidation/reduction features that are expected and that no palladium features were present. Figure 2-7 displays a typical voltammogram.

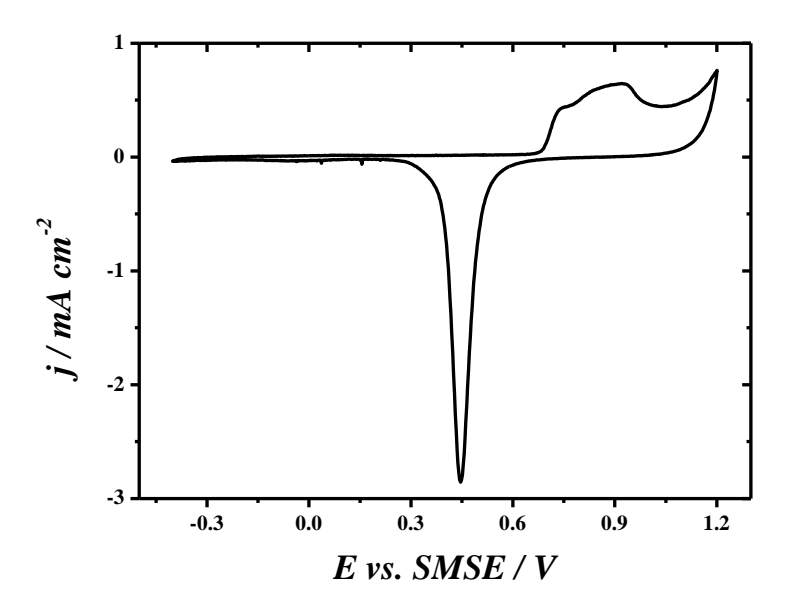


Figure 2-7 Cyclic voltammogram of a polished 50 μ m diameter gold disc electrode in Ar purged 1 M sulphuric acid at scan rate of 100 mV s⁻¹.

The CV scan was performed between -0.4 V and +1.2 V vs. SMSE with a scan rate of 200 mV s⁻¹. The gold electrode displays a gold oxide reduction peak between +0.35 V and +0.55 V vs. SMSE in addition to a gold oxidation peak from +0.7 V to +1.2 V vs. SMSE. The double layer was observed below +0.3 V.

The area of the gold oxide reduction peak can be used to calculate the electroactive area which can in turn be used to calculate the roughness factor of the gold electrode. Before each experiment the roughness factors were calculated from the plain gold CV scans and a roughness factor of between 1 and 5 was considered acceptable for use. If the roughness factor was found to be outside this range then the polishing process and characterisation was repeated.

2.7.2 Glassy carbon electrode characterisation

After being washed with distilled water the glassy carbon electrodes were characterised by cyclic voltammetry in 1 M sulphuric acid to determine that no palladium features were present and that the electrodes were clean. Figure 2-8 displays a typical voltammogram.

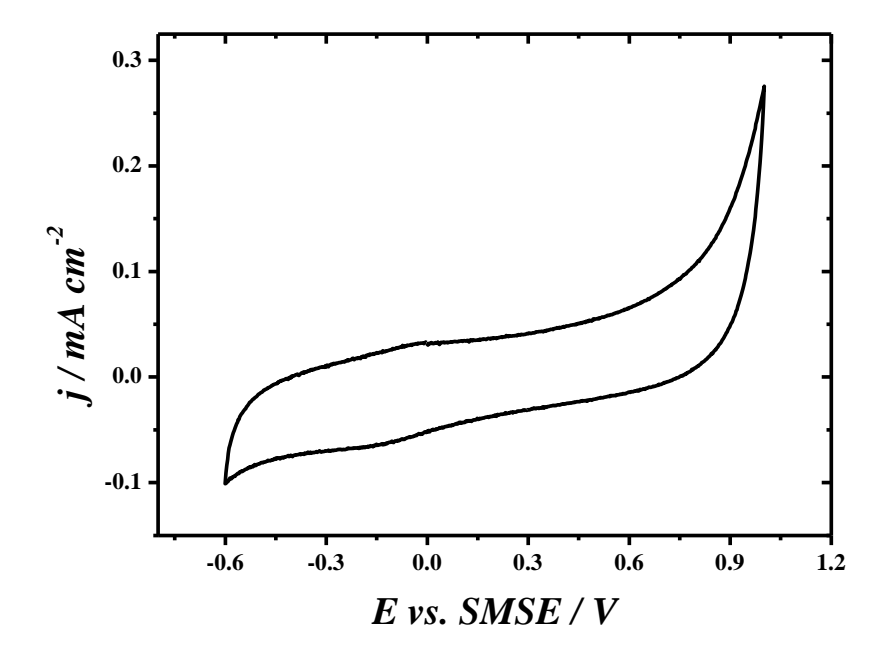


Figure 2-8 Cyclic voltammogram of a polished 3000 μ m diameter glassy carbon disc electrode in 1 M sulphuric acid at scan rate 100 mV s⁻¹.

The CV scan was performed between +1.0 V and -0.6 V vs. SMSE with a scan rate of 200 mV s⁻¹. There is no indication of palladium features so the electrode was therefore clean. In the potential window used for electrode characterisation the glassy carbon does not produce large reduction peaks for use in the calculation of roughness factor. For these electrodes only the roughness factor of the palladium films after deposition was calculated using the geometric area of the 3 mm diameter GC electrode. Before each experiment the glassy carbon electrodes were polished until the voltammogram for each electrode were similar, to ensure that each experiment was conducted with a similar surface.

2.8 Electrodeposition of Palladium

The Pd plating solutions were made with varying surfactant weight ratios purposely selected to be well within the composition ranges known to form at room temperature the micellar (2 and 10 wt. %) and hexagonal (48 wt. %) liquid crystal phases in the presence of a palladium salt. Each mixture was prepared with a set percentage weight of (NH₄)₂PdCl₄, C₁₆EO₈, KCl and water such that the Pd salt concentration in the aqueous phase remained constant throughout, table 2-2. From now on all mixtures are referred to their surfactant percentage weight. The constituents were separately weighed, mixed in a glass vial and stirred using a plastic rod until the mixture appeared homogeneous.

Table 2-2 Composition of the plating mixtures used to prepare the Pd deposits, corresponding liquid crystal phase (m-micellar, h-hexagonal), consistency and pH. In all cases, the concentrations of Pd salt and KCI were respectively 0.01 and 0.5 M.

	Name of mixture			
	0 %	2 %	10 %	48 %
(NH ₄) ₂ PdCl ₄ / mg	2.8	2.7	2.4	1.4
KCl / mg	35.5	35.1	32.4	18.6
H ₂ O / mg	961.7	942.2	865.2	500.0
C ₁₆ EO ₈ / mg	0	20	100	480
Phase	-	m	m	h
Consistency	liq.	liq.	liq.	paste
pН	3.27	3.23	2.95	2.17

The viscosity of the mixture varies widely, typically from liquid to paste depending on the amount of surfactant. To ensure that the correct liquid crystal phase was obtained, the mixtures were then annealed at 40 °C for 30 min, manually stirred for 2 min and finally placed in an ice bath for 30 min. This process was repeated three times before allowing the mixture to cool down to room temperature. No attempt was made to remove oxygen from the mixtures. Depositions were performed at room temperature with a small volume from the stock mixtures. The latter were used for circa three weeks then discarded, but each time the annealing-cooling process was carried out before use. Where required the phase was confirmed by polarisation microscopy as reported previously.[81] Typically the plating mixture was observed using a polarising optical microscope (Olympus BH2) equipped with a heating/cooling stage (Linkam TMS 90). For this a small amount of the mixture was sandwiched between a glass slide and a cover slip and placed in the microscope between two polarisers with their axes rotated at 90°. The hexagonal phase is anisotropic and changes the polarisation of the light thereby producing a characteristic black and white 'fan' like optical texture with non-spherical air bubbles, Figure 2-9. In contrast the isotropic cubic and micellar phases do not alter the polarisation of the light and cannot be viewed through the crossed polarisers. Phase transitions were noted by observing changes in optical texture while slowly heating/cooling the mixture. To electrodeposit the particles all the electrodes were immersed in the plating mixtures except for the hexagonal phase which, due to its paste-like consistency, was placed onto a platinum mesh that acted as the counter electrode while the working and reference electrodes were pushed closely together into the paste, Figure 2-10.

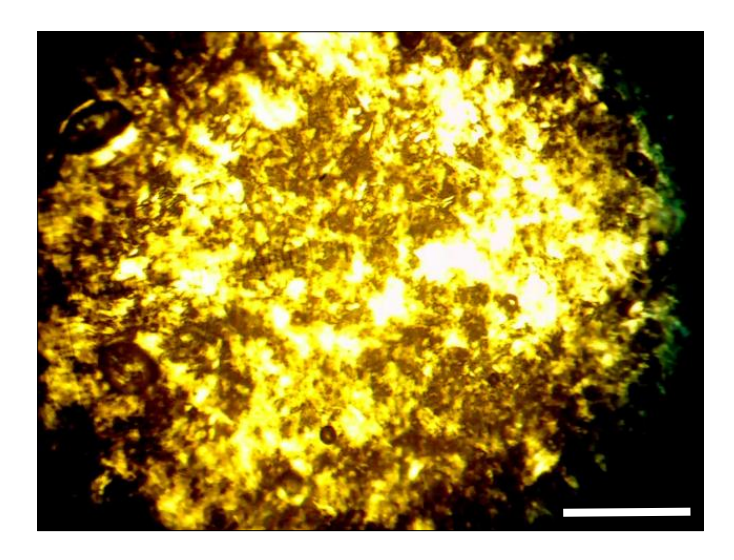


Figure 2-9 Image of the hexagonal liquid crystalline phase observed with a polarising optical microscope. The scale bar is $200~\mu m$ long.

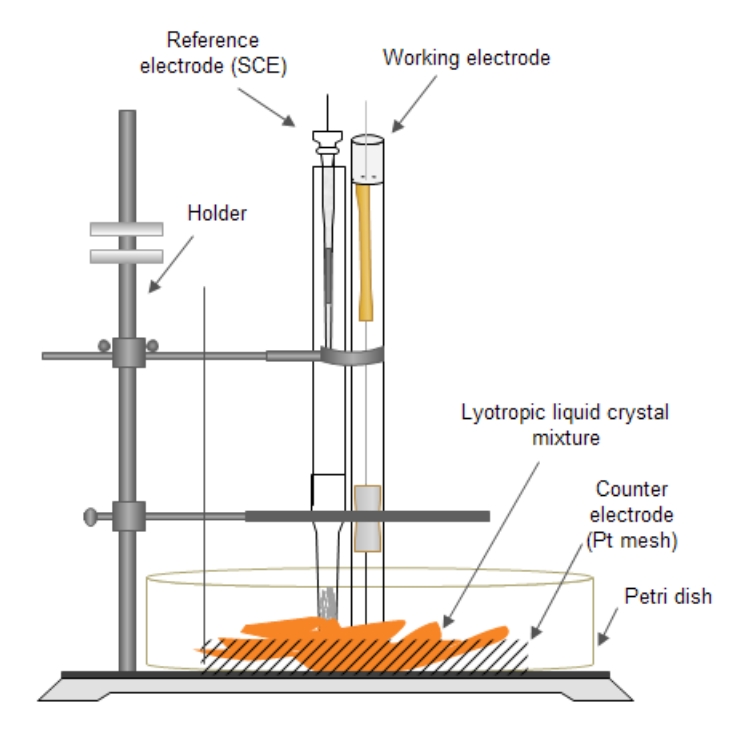


Figure 2-10 Schematic diagram indicating the three electrode system for electrodeposition in the 48 wt.% surfactant mixture.

The viscosity for palladium mixtures was measured using a falling sphere viscometer (GV-2300-Gilmont). The ball is made of tantalum and was used as the suitable ball. It was chosen because its density (16.60 gm ml⁻¹) is greater than the density of the palladium plating mixture (10.38 g ml⁻¹). The viscometer tube and ball were cleaned and dried before the measurements. The required solution to fill the tube is proximately 8 ml and for accurate measurement the tube was placed in a beaker filled with water then placed on hot plate to control the temperature to 25 °C, Figure 2-11. After releasing

the ball, the time of descent between the two sets of lines was measured with a stop watch. The measurement of the time was repeated ten times and then the average time was used to calculate the viscosity as the formula below:

$$\mu = K(p_f - p)t \tag{2-1}$$

where, μ = viscosity in centipoises (cp), p_f =density of ball $(g \ ml^{-1})$, p=density of liquid $(g \ ml^{-1})$, t=time of descent (min) and K= viscometer constant (0.3).

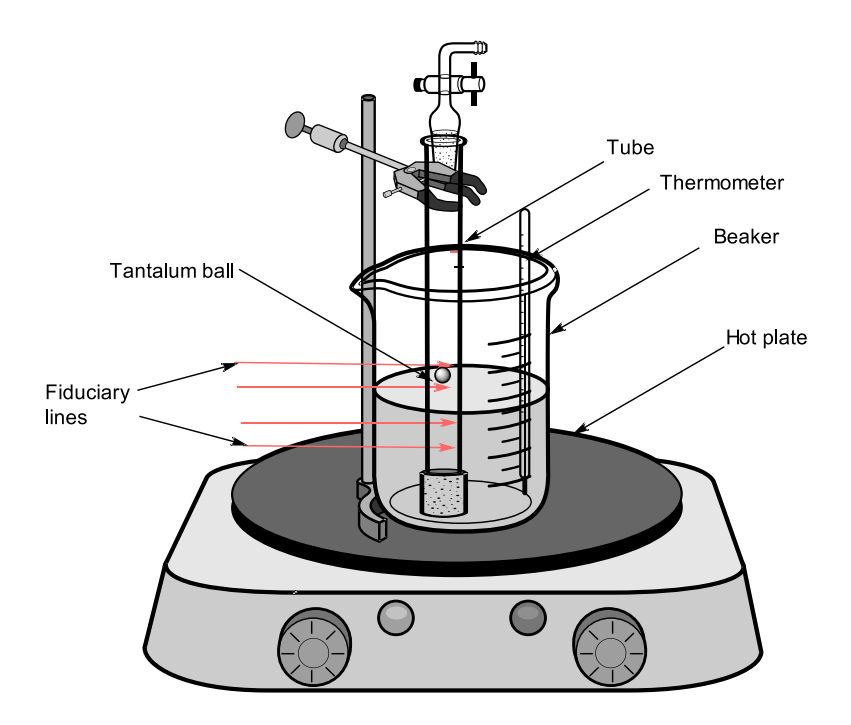


Figure 2-11 Schematic diagram indicating the setup when using the falling sphere viscometer.

2.9 Preparing various concentrations of surfactant in lyotropic liquid crystal mixtures for Pt electrodeposition

The plating mixtures were prepared by weighing hexachloroplatinic (IV) acid, water and octaethyleneglycol monohexadecyl ether in a small vial. The mixture was heated to around 40 °C for 30 min and stirred with a plastic rod. Heating and stirring were repeated three times in order to ensure homogeneity and then the mixture was left to cool at room temperature before use. Table 2-3 indicates the compositions of all mixtures, texture and phases.

Table 2-3 The compositions (in terms of weight percentage), the resultant texture, optical observation of the ternary plating mixture and the corresponding phase of the lyotropic liquid crystalline mixture.

Weight percentage of compositions in plating mixture (LLC phase)	Observation under polarizing optical microscope	Texture	Phase
0 wt.% C ₁₆ EO ₈ : 86 wt.% H ₂ O: 14 wt.% H ₂ PtCl ₆	Black	Fluid	Aqueous solutions
2 wt.% C ₁₆ EO ₈ : 84 wt.% H ₂ O: 14 wt.% H ₂ PtCl ₆	Isotropic	Less viscous than 10 wt.%	Micellar
10 wt.% C ₁₆ EO ₈ : 77 wt.% H ₂ O: 13 wt.% H ₂ PtCl ₆	Isotropic	Less viscous than 42 wt.%	Micellar
42 wt.% C ₁₆ EO ₈ : 49.7 wt.% H ₂ O: 8.3 wt.% H ₂ PtCl ₆	Anisotropic (fan- like optical texture)	Very viscous	Hexagonal

2.10 Electrodeposition of ZnSe semiconductors

The electrodeposition of zinc selenide was achieved using different concentration of soluble salts of ZnSO₄ and SeO₂ dissolved in distilled water with the solution stirred for 14 min using a magnetic stirrer. The formation of p- and n- type deposits of ZnSe were done by performing co-deposition with 0.5 M (NH₄)₂SO₄ or 0.5 M Ga₂(SO₄)₃ as dopant. To determine the type of doping an aqueous solution of 0.5 M Na₂SO₄ was used to record linear sweep voltammograms using a cell with quartz window to allow the light to pass through it. The light was from a blue (450 nm) LED.

2.11 Electrochemical Analysis

The electrodeposition of metal on different substrates was analysed by various methods including cyclic voltammetry (CV) and chronoamperometry (CA). The electrochemical characterization was performed using CV, linear sweep voltammetry (LSV) in the dark and under illumination, chronopotentiometry (CP) and electrochemical impedance spectroscopy (EIS).

2.11.1 Cyclic Voltammetry (CV)

Cyclic voltammetry is an efficient method which allows probing the mechanics of redox and transport properties of a system in solution. It follows that the potential limits and the potential scan rate are the basic adjustable parameters.[134-136] In this work CV will be used to create new phase forms and study the appropriate potential for electrodeposition that can be chosen to use the chronoamperometry method. The simplest technique is linear sweep voltammetry (LSV). The potential is swept starting at the initial potential and ending at the final potential. CV is an extension of LSV in that the direction of the potential scan is reversed at the end of the first scan (the first Switching Potential), and the potential range is scanned again in the reverse direction.[137,138] LSV was used to study hydrogen evolution, oxygen evolution and oxygen reduction reactions to test the electrocatalytic activity of Pd nanoparticles. Also, the LSV was used to measure the photocurrent of ZnSe.

2.11.2 **Chronoamperometry**

Chronoamperometry (CA) is an electrochemical method in which a step potential is applied and the current, i(A), is measured as a function of time, t(s). It is a good way to obtain quantitative data and qualitative information after analysing the shape of the current vs. time transient. This technique was used to control deposition potential, deposition time and / or the charge passed during the reduction. So these parameters were varied to help control the amount of deposits formed.

2.11.3 Impedance spectroscopy (EIS)

Electrochemical impedance spectroscopy (EIS) or ac impedance methods have seen a significant increase in popularity in recent years. Mainly applied to the determination of the double-layer capacitance and in ac polarography, they are now applied to the characterization of electrode processes and complex interfaces. The measurement was done with a Metrohm Autolab PGSTAT 302N with ECD and FRA module. In this work measurements were carried out with electrochemical impedance spectroscopy to record the capacitance of the semiconductors as a function of applied potential under depletion condition; this approach is based on the Mott-Schottky plot and can be used to determine the conductivity type(n or p) and estimate the flat band potential, E_{fb} , and the number of acceptors and / or donors per cm³ in the semiconductor.

2.12 Characterization techniques

Several techniques were used to characterize the electrodeposits. X-ray diffraction was performed with scanning angles ranging from 30 to 150° at a scanning rate of 2° s⁻¹ with the CuKα radiation (λ=1.5406 Å) using a Philips X' PERT System X-Ray Diffractometer. A JEOL scanning electron microscope (SEM) at low acceleration voltages, and an atomic force microscope (AFM) were employed to examine the morphology, particle size and microstructure of the electrodeposits of the deposited film. The chemical composition/purity of the electrodeposits was determined by energy dispersive spectroscopy (EDX) analysis.

2.12.1 Scanning Electron Microscopy (SEM)

A scanning electron microscope (SEM) is a type of electron microscope that produces images of a sample by scanning it with a focused beam of electrons. The electrons interact with atoms in the sample, producing various signals that can be detected and that contain information about the sample's surface topography and composition. The electron beam is generally scanned in a raster scan pattern, and the beam's position is combined with the detected signal to produce an image.[139,140] The morphology of the electrode surface was monitored by two models of scanning electron microscopy. The first model is a Philips XL30 SEM which is capable of imaging magnifications of up to 50,000, with an accelerating voltage of up to 30 kV. It has two modes, environmental and high vacuum modes. The environmental mode is suitable to prevent charging up of the glass surrounding the electrode. The high vacuum mode is suitable for electrically conductive samples that can be imaged using the secondary electron detector, while non-conducting materials may be studied, without the need for coating, with the gaseous secondary electron detector. Also this instrument is linked with a waveform dispersive X-ray spectroscopy (WDS) system that provides greatly enhanced X-ray resolution and light element analysis capability. The images of carbon electrodes were taken under high vacuum mode using a secondary electron detector at a beam of 20 kV. For the microelectrodes, the images were recorded under environmental mode using a gaseous secondary electron (GSE) detector at an accelerating voltage of 12 - 15 kV. The samples with nanocentres smaller than 50 nm were imaged by a JEOL JSM-6500F Field Emission Gun Scanning Electron Microscope (FEG-SEM). The JSM 6500 SEM has an accelerating voltage of 0.5 to 30 kV, magnifications up to 500,000 and a resolution of 1.5 nm. No treatment was done to the samples before using the SEM.

2.12.2 Atomic Force Microscopy (AFM)

The atomic force microscope (AFM) is a very high resolution type of scanning probe microscopy with demonstrated resolution of fractions of a nanometre. The AFM is one of the foremost tools for imaging, measuring and manipulating matter at the nanoscale. The information is gathered by feeling the surface with a mechanical probe. Piezoelectric elements that facilitate tiny but accurate and precise movements on command enable the very precise scanning. To achieve atomic resolution with AFM, a first necessary condition is that the mechanical vibrations between tip and sample are smaller than the atomic corrugations. In addition, frictional forces and elastic and plastic deformations can be detected under appropriate conditions.[141,142] AFM images were taken in tapping mode using a Scanning Probe Microscopy Nanoscope III 5.1.2.3a (Digital Instruments) in air. AFM was used to image Pd nanocentres deposited on HOPG; the sample had to be less than 3 mm in height to avoid crashing with the tip and less than 7 mm for either the width or the length to fit on the AFM holder.

2.12.3 Helium ion microscopy (HIM)

HIM was performed with an Orion Plus helium ion microscope (Carl Zeiss, Peabody, MA). The accelerating voltage was 35 kV and the beam current was between 0.2 and 3 pA with a 10 mm aperture and a working distance of between 7.5 and 9.3 mm. The samples were cleaned by soaking in isopropanol at room temperature to remove organic materials and left in vacuum oven at 40 °C to dry before loading into the HIM. Cleaning the sample should be done to avoid any hydrocarbon contamination that can be efficiently cross-linked by the helium beam, leading to a build-up of material in the area where the beam is scanned and thus affecting the image resolution.[143]

2.12.4 X-ray Diffraction (XRD)

X-ray scattering techniques are a family of non-destructive analytical techniques which reveal information about the crystallographic structure, chemical composition, and physical properties of materials and thin films. The X-ray diffraction was collected using a SmartLab X-ray diffractometer Rikagu, with the source producing $Cu \ K\alpha$ radiation. The X-ray diffraction was used in this project to

identify the Pd nano particles phase, to analyse the ZnSe structure and to confirm the presence of this compound.

2.13 Software

Origin is a technical graphing package. It was used to produce all graphs in this thesis. Also, it includes linear and non-linear curve fitting, worksheets that accommodate large datasets and summary statistics. The software was also used to analyse experimental data. Both linear fitting and non-linear fitting were used to fit the current transient with theoretical models to obtained kinetic parameters.

Gwyddion is a modular program for SPM (scanning probe microscopy) data visualization and analysis. Primarily it is intended for analysis of height fields obtained by scanning probe microscopy techniques (AFM, MFM, STM, SNOM/NSOM) and it supports many SPM data formats. It was used in this project to obtain some statistical information from AFM images of the Pd nanocentres.

ImageJ With this software 8-bit, 16-bit and 32-bit images can be displayed, edited, analyzed, processed, saved and printed. It can also read many image formats including TIFF, GIF, JPEG, BMP, DICOM, FITS and "raw". Moreover, it calculates area and pixel value statistics of user-defined selections. Also, it can measure distances and angles and create density histograms and line profile plots.

In the next chapter the early stages of formation of palladium nanoparticles from ammonium tetrachloropalladate (II) on different carbon substrates will be discussed.

3. Early stages of electrodeposition of Pd nanoparticles on different carbon substrates

Palladium nanocentres have wide spread applications in catalysis and electrochemical sensor applications [144]. Palladium nanocentres have been highly researched due to the unique properties that are produced when a high surface area to volume ratio is achieved. In this chapter the electrodeposition of palladium (from ammonium tetrachloropalladate (II)) on different carbon substrates was studied using cyclic voltammetry and chronoamperometry. Palladium nanocentres were produced on carbon substrates with the use of low deposition overpotentials and short deposition times. The results of each experiment were characterised by either scanning electron microscopy or atomic force microscopy and in some cases by cyclic voltammetry in acid.

3.1 Carbon fibres

Carbon fibres (CF) could possibly offer attractive, large surface-area materials, suitable for a number of electrochemical applications. This is because the properties of the CF electrochemically active surface area could be extensively modified, e.g. by surface pre-treatment or by catalyst electrodeposition. Carbon fibres (CF) have been widely used as reinforcements in composite materials such as CFs reinforced metals, ceramics, plastics, and carbon-carbon composites due to the high specific strength, specific modulus, high thermal and electric conductivity, low expansion coefficient, and good self-lubrication properties.[145,146] Other desirable physical properties of carbon fibres and other composites include their resistance to corrosion, fire and high stress tolerance levels as well as their chemical inertness. It is difficult to get an idea of the exact structure of individual carbon fibres, but X-Ray crystallography has provided an idea of what a very small piece of carbon fibre looks like and strangely enough it is virtually identical to graphite.[147] Each of the fibres produced is about the fifth of the diameter of a human hair. Figure 3-1 shows the structure of CF; it contains straight lines in the plane of the fracture which have been linked to that particular part of the fibre having a structural arrangement very similar to that of graphite.[148]

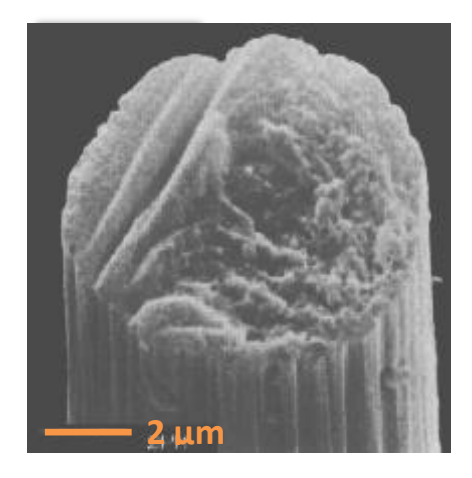


Figure 3-1 Electron microscopy picture of a carbon fibre, taken from [148].

CF working electrodes can be used immediately without any polishing before carrying out any experiment but they are fragile. It is important for the electrode surface to be free from deposits before commencing any experiments. It was therefore intended to be used only for one electrodeposition experiment and to be characterised later. Hence, this successful fabrication of disposable cheap electrodes helped to save time from polishing the electrode surface. Cyclic voltammetry was recorded before the experiment to activate the surface and electrochemically clean the electrode. Figure 3-2 shows the cyclic voltammogram obtained at a clean carbon electrode surface at a scan rate of 100 mV s⁻¹. The cyclic voltammograms were scanned in a potential range between +1.0 V and -0.6 V vs SMSE. At +1.0 V versus SMSE there is an increase in current due to oxygen evolution, a double layer region can be seen negative to +0.7 V versus the SMSE. There are small anodic oxidation and cathodic reduction peaks at +0.2 V and -0.2 V respectively. These peaks correspond to the oxidation and reduction of the surface functional groups such as quinone-hydroquinone redox couple eq. (3-1).[149] Hydrogen evolution can be observed at potentials negative to -0.4 V.

$$(quinone) = C = O + H^+ + e^- \rightleftharpoons (hydroquinone) = C - OH$$
 (3-1)

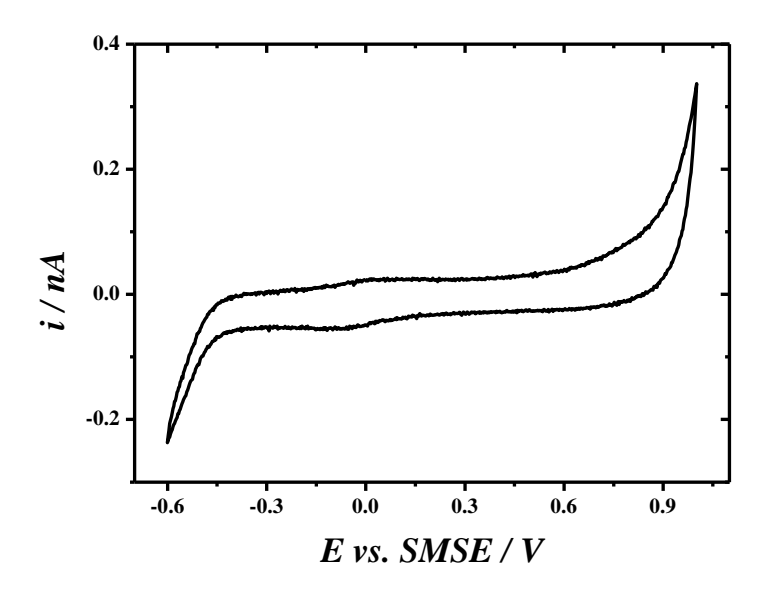


Figure 3-2 Cyclic voltammogram (5th scan) recorded at a 5 mm long, 7 μ m diameter carbon electrode in 1 M sulphuric acid at 100 mV s⁻¹.

The voltammograms for the reduction of ammonium tetrachloropalladate (II) in a potassium chloride solution were recorded at a 7 μm diameter carbon fibre wire electrode. The carbon fibre wire electrode was assembled and measured, so that the length of the exposed carbon fibre was 5.0 ± 0.1 mm. The carbon fibre electrodes were too fragile to be polished with alumina and were intentionally only used once. The potential scan rate was 10 mV s⁻¹. Two consecutive cyclic voltammograms recorded at a carbon fibre wire electrode in the palladium plating bath solution are shown in Figure 3-3. The cyclic voltammograms were scanned in a potential range between +0.75 V and -1.3 V versus SCE in order to observe the reduction wave of palladium.

The cyclic voltammogram shown in Figure 3-3 presents the typical characteristics of an electrodeposition process on a foreign substrate with subsequent removal of the deposited layer. A clear steady state reduction wave is observed with a significant hysteresis. A well-defined oxidation peak is observed on the reverse sweep. On the forward scan, the onset of the reduction wave started at -0.12 V versus SCE. This is followed by an increase in current that is ascribed to hydrogen adsorption, absorption and hydrogen evolution.[150-152] On the reverse scan the reduction wave is shifted by approximately +500 mV. This is consistent with a nucleation loop. The electrodeposition of palladium onto a palladium coated carbon electrode surface is much easier than on a clean carbon electrode surface. Thus less overpotential is required; hence the $E_{\frac{1}{2}}$ for the backward scan is shifted to a more positive potential, +0.25 V.

Moreover, there is a small stripping peak around -0.25 V that refers to the extraction of hydrogen from the Pd lattice. Interestingly the charge under the hydrogen stripping peak and that under the Pd stripping peak are not changing between the first and second cycles, therefore suggesting that the amount of Pd deposited is the same in each cycle. However, a higher overpotential is required for the nucleation to take place on the carbon fibre wire electrode.

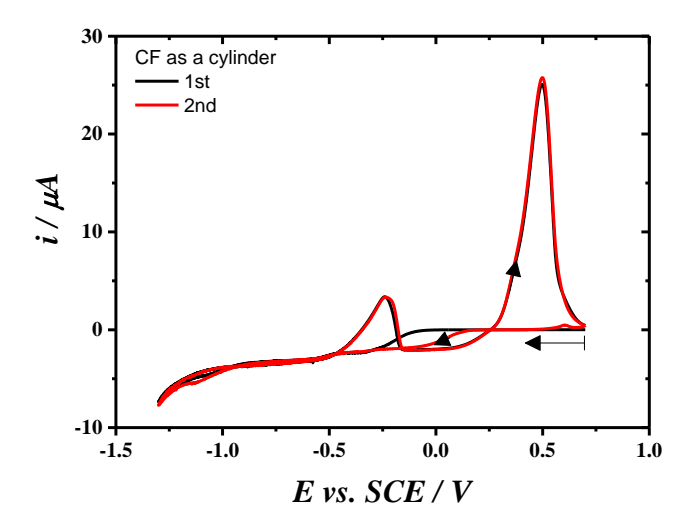


Figure 3-3 Cyclic voltammograms recorded with a carbon fibre ($\emptyset = 7 \mu m$, 5 mm long) electrode in 1 mM (NH₄)₂PdCl₄ + 0.5 M KCl at υ =10 mV s⁻¹.

3.1.1 Single potential steps

The nucleation and growth of palladium particles on fresh CFs was studied by using chronoamperometry for a set of deposition potentials chosen in different regions of the palladium cyclic voltammogram shown in Figure 3-3, namely -0.45, -0.35. -0.25 and -0.15 V vs. SCE. The deposition potential was varied in order to explore whether it could affect the size, distribution and density of particles on the electrode. The deposition time was fixed in order to facilitate comparison of the current-time transients and distribution (the number density and size) of nuclei onto the electrode surface. The chronoamperometry for the electrodeposition at various potentials is shown in Figure 3-

4. All the current transients follow the expected trend where increasing overpotentials generate increasing current magnitudes. The charges passed were calculated by integrating the area under the transients, and their values are respectively 0.76, 0.63, 0.45 and 0.37 μ C for the transients recorded at -0.45, -0.35, -0.25 and -0.15 V vs. SCE respectively.

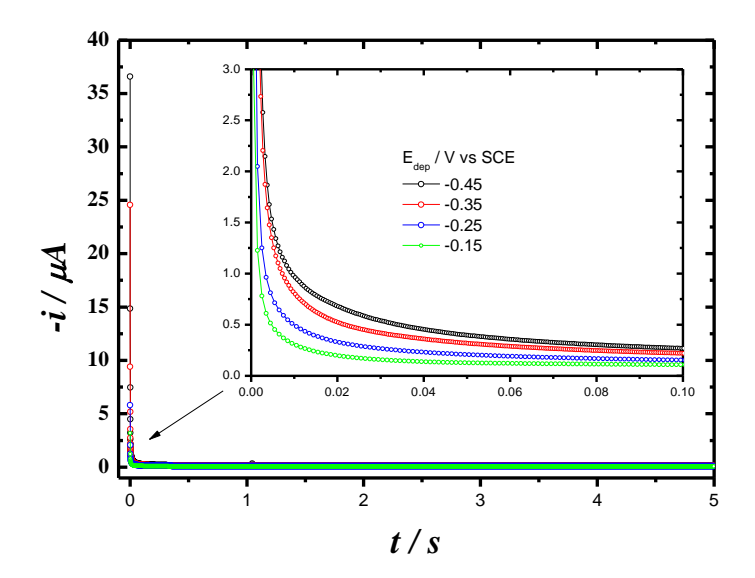


Figure 3-4 Current transients recorded with carbon fibres ($\emptyset = 7 \mu m$, 5 mm long) during electrodeposition in 1 mM (NH₄)₂PdCl₄ + 0.5 M KCl. The potential was stepped from 0.7 V vs. SCE to the deposition potentials indicated on the Figure.

The SEM images, Figure 3-5, of carbon fibres coated with Pd show a good quantity of deposits at the different applied potentials after 1 min of deposition. At -0.45 V we notice that the Pd particles aggregate and form a film in some regions on the side and top of the CF; with low magnification some areas seem free of Pd deposits, which might indicate that these regions had fewer active sites or maybe that the particles came off the surface after the deposition. Also it can be observed that the particles are agglomerated and distributed randomly on the top of the CF; some edge effect can be observed on the top of the surface. Decreasing the applied potential to -0.35 V while keeping the deposition time at 1 min shows a distribution of palladium particle sizes. The deposits possess clear 3D characteristics with hemispherical morphology, appearing either randomly distributed or decorating the lines[147] from the underlying structure of the fibres or other surface defects; this indicates that these defects behave as active sites for the deposition. Lower densities of particles were observed when using the deposition potentials of -0.25 V and -0.15 V.

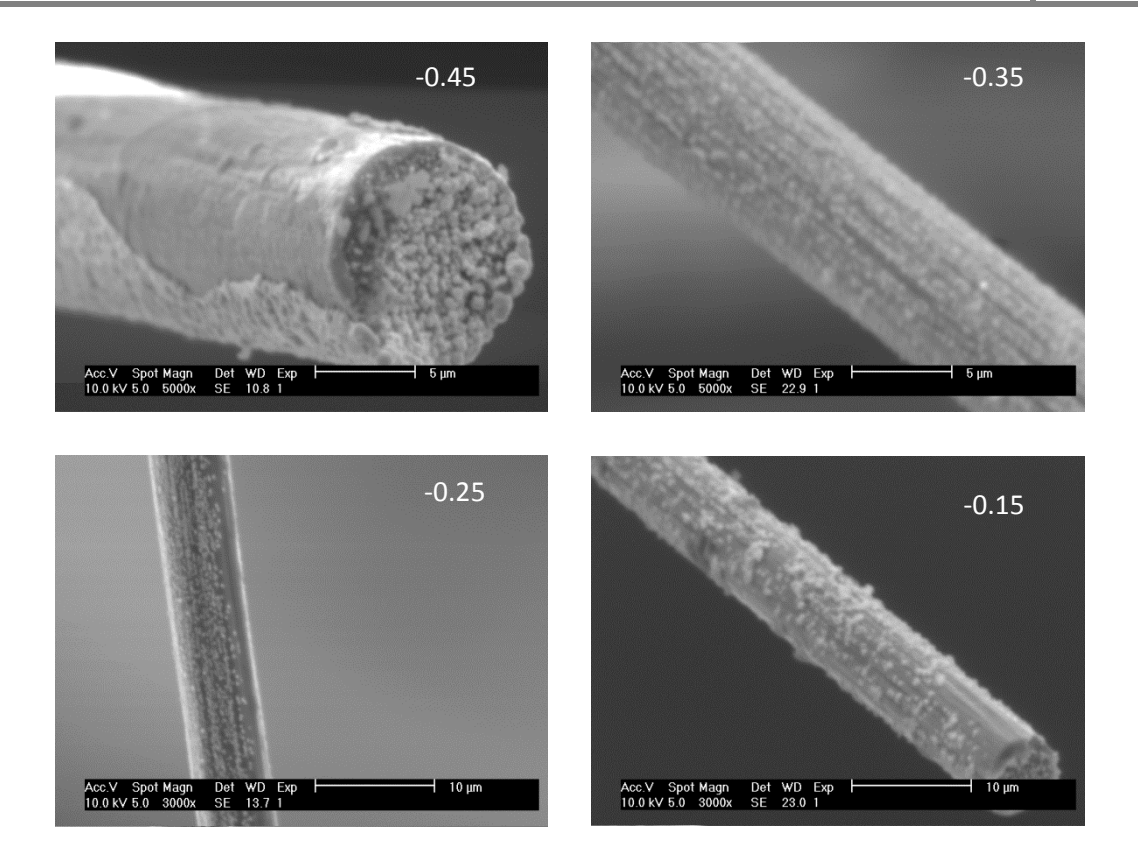


Figure 3-5 SEM images of the carbon fibre ($\emptyset = 7 \mu m$, 5 mm long) surface showing the Pd particles after 1 min of electrodeposition in 1 mM (NH₄)₂PdCl₄ + 0.5 M KCl. The potential was stepped from 0.7 V vs. SCE to the deposition potentials shown on the Figure.

The deposition time was varied in order to reduce the number of particles and obtain an overview of the initial stages of nucleation and growth; for this the potential was kept constant at -0.15 V corresponding to the foot of the reduction wave of Pd and the deposition time was varied from 20 to 15, 10, 5, 1, 0.5 and 0.1 s. Figure 3-6 shows that in all cases the palladium deposits appeared to form hemispherical centres randomly distributed along the ridges of the CF structure. For deposition times of 20 s there are many large particles ranging between 2.0 and 0.7 μ m, but particles smaller than 0.2 μ m can also be clearly seen. Some particles grew to form dimers, trimers and chains of islands; the particles were found to have different sizes therefore indicating a mechanism of progressive nucleation. At 15 s the number of large particles with sizes circa 0.8-0.7 μ m is much smaller but there is clearly a huge density of tiny particles smaller than 0.2 μ m. Decreasing the deposition time to 10 s affected the growth of particle size and produced smaller particles; the large particles have almost disappeared while the tiny particles are still there but their density appears smaller than at 15 s. At 5 s there are virtually no large particles and the density appears smaller than that seen for 10 s.

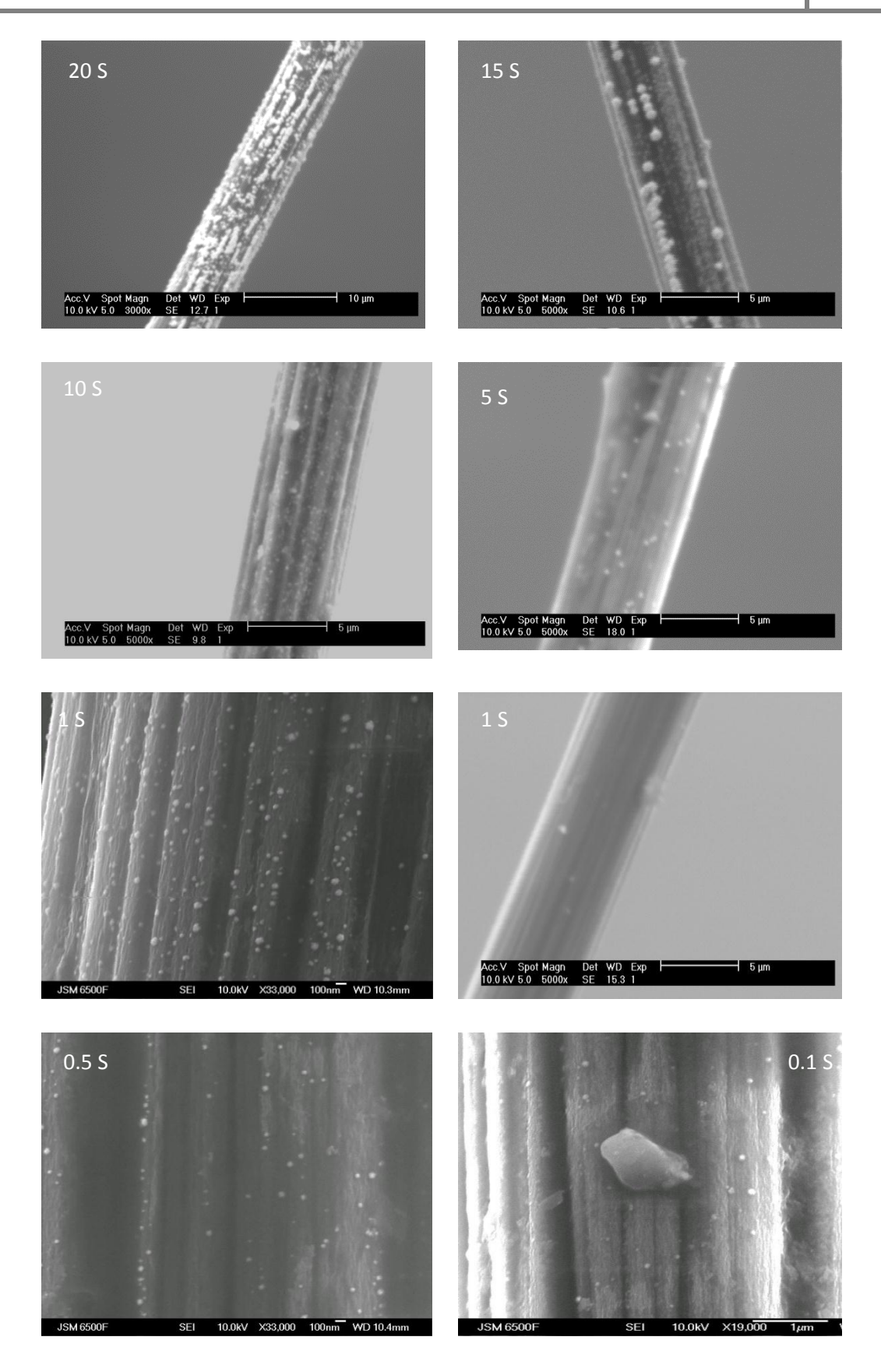


Figure 3-6 SEM images of the carbon fibres (\emptyset = 7 μ m, 5 mm long) showing the initial stages of the Pd electrodeposition in 1 mM (NH₄)₂PdCl₄ + 0.5 M KCl after stepping the potential from 0.7 V to -0.15 V vs. SCE for 20, 15, 10, 5, 1, 0.5 and 0.1 s.

However, the resolution is very poor and it could well be that we cannot see smaller particles; also we faced an added difficulty when imaging this kind of substrate: the fibres vibrated during scanning which caused fuzzy images. With 1 s deposition time the low resolution image barely shows any particles but the high resolution one shows a good density of particle sizes ranging between 119 and 27 nm. So, it can be concluded that the number of Pd nanoparticles decreased when decreasing the deposition time. At 0.5 and 0.1 s the density of particles decreases further and their size are of the order of 31-59 nm and 20-178 nm respectively. The deposits formed for deposition times of 1, 0.5 and 0.1 s were analysed with ImageJ.[153] This software can display, edit, analyse, process, save and print a variety of image formats. Importantly, it can calculate area and pixel value statistics for user-defined selections, measure distances and angles and create density histograms and line profile plots. Here we used ImageJ to analyse nanoparticle sizes and distribution. The SEM images were imported to the software then calibrated using the dimension of the scale bar. An area of interest was selected using a threshold to contain a reasonable number of particles. A threshold image is the simplest method of image segmentation. From a grey scale image, thresholding can be used to create binary images; also in this step it is recommended to remove most of the noise that might make the result less accurate. However, the thresholding did not affect the distributions, as every single image was duplicated to keep one as a reference and compare it with the image that had been processed with a threshold. The last step is analysing the particles which can provide data that can be converted in Origin to plot a histogram. The particle size can be obtained by assuming a spherical particle shape having previously obtained the diameter from the software. ImageJ only measures the projected area of the particles, so to convert to particle size (i.e. diameter of particle), the particles were assumed to be spherical and the formula below was used where A is the projected area calculated by ImageJ

Diameter =
$$2\sqrt{A/\pi}$$
 (3-2)

Figure 3-7 shows the histograms for the three SEM images that were analysed by ImageJ and Origin. The statistical information is summarized in table 3-1. From the analysis it seems that the sample with 0.1 s deposition time has no reliable statistical information which might reflect that this sample surface is rough and the software might be accounted the defects as well as the particles. The second reason is that, the number of particles is much less than the required number of particles that is recommended by the software, 500 particles (at least), to be analysed to ensure adequate statistical confidence. The comparison is reasonable between the samples prepared with 1 and 0.5 s deposition times, as we can see, as the deposition time increases the number and size of particles also increase.

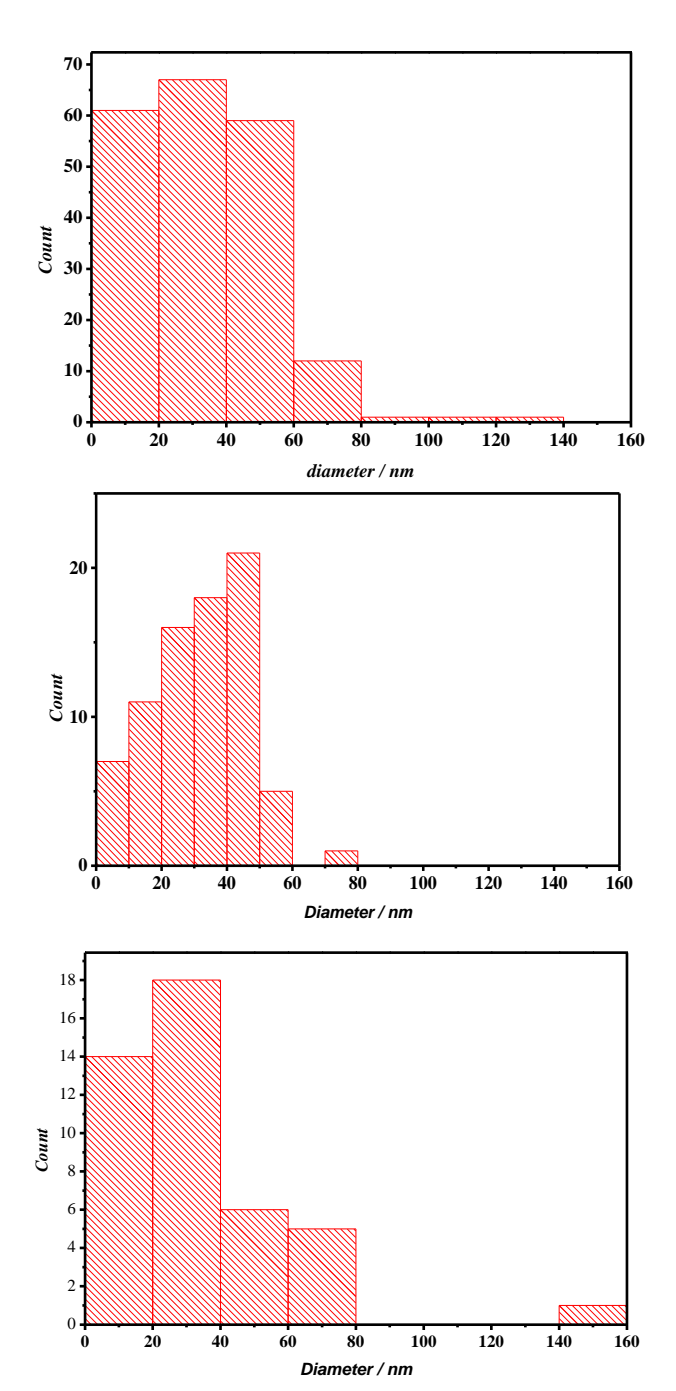


Figure 3-7 Histograms of the particle count analysis performed on the SEM images shown in Figure 3-6. The top, middle and bottom histograms respectively correspond to 1, 0.5 and 0.1 s deposition times.

Table 3-1 Statistical information from the particle count analysis performed on the SEM images shown in Figure 3-6. The analysis corresponds to 1, 0.5 and 0.1 s deposition times.

4 / 2	N (Total)	Mean	SD	
$t_{\rm dep}$ / s		/ nm	/ nm	
1	202	33.02	20.61	
0.5	79	31.91	14.48	
0.1	44	33.6	25.28	

3.2 Highly Ordered Pyrolytic Graphite

The graphite basal plane is a hexagonal network of sp^2 covalently bonded carbon atoms. Graphite is very chemically stable in non-oxidizing environments, and is mechanically very stiff; these properties lead to its use in a variety of applications including in high-temperature, high strength composites. It is well established that the graphite basal plane is inert to chemical reaction with molecular oxygen, while it has limited resistance to atomic oxygen;[154] at only 323 K, attack by atomic oxygen of graphite takes place readily. Highly oriented pyrolytic graphite, HOPG, is a man-made material which is polycrystalline with highly oriented graphene sheets.[155-157]

Figure 3-8 shows a voltammogram associated with the electrodeposition and stripping of a metal from a graphite electrode surface by cyclic voltammetry. The cyclic voltammetric response was recorded in a solution of 1 mM (NH₄)₂PdCl₄ + 0.5 M KCl. The potential was swept from +0.85 V to -1.3 V vs. SCE. On the forward scan, the start potential is 0.85 V vs SCE at which no reaction is taking place, there is no cathodic current positive to +0.25 V while negative to this value a reduction wave is observed which corresponds to the electrochemical reduction of Pd^{2+} to Pd^{0} on the HOPG surface. Small peaks negative to -0.3 V refer to hydrogen adsorption and absorption. On the reverse scan there are two peaks, a small stripping peak around -0.25 V which refers to the extraction of hydrogen from the Pd lattice. A crossover between the forward and reverse voltammetric responses appears at a potential of about 0.15 V. This nucleation loop indicates that nucleation overpotential is needed to deposit Pd on HOPG, forward scan, compared to Pd on Pd, reverse scan. The deposited Pd^{0} is then voltammetrically stripped at 0.02 V reforming Pd^{2+} .

HOPG electrodes have similar voltammetric features to those recorded on CF electrodes however, a higher overpotential is required for the nucleation to take place on the carbon fibre wire electrode.

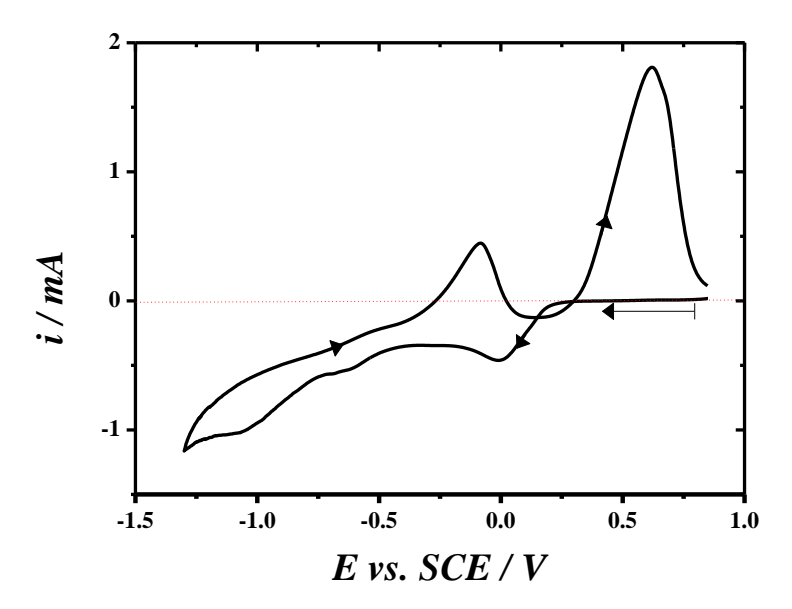


Figure 3-8 Cyclic voltammogram recorded at 10 mV s⁻¹ with a 5 mm \emptyset basal plane HOPG electrode in argon purged 1 mM (NH₄)₂PdCl₄ + 0.5 M KCl.

Current transients, Figure 3-9, were recorded with freshly cleaved surfaces of HOPG electrodes (5 mm diameter) in argon purged solution of 1 mM (NH₄)₂PdCl₄ + 0.5 M KCl, for a series of potentials steps from 0.7 V to potentials between -0.2 and 0.2 V. In each experiment, the deposition time was kept constant at 20 s. At lower overpotentials, close to the onset of the palladium deposition, the current increases approximately exponentially with potential, a characteristic of kinetically limited growth and the current in this region is considered to be kinetically controlled. At more negative potentials -0.2, -0.1 and 0.0 V, growth becomes diffusion limited and is controlled by the supply of ions to the growing nuclei. The resulting chronoamperograms have the characteristic shape for an electrochemically driven, diffusion controlled process with the initial current spike due to a non-Faradaic process (charging the double layer), followed by a rise of current as nuclei begin to form on the electrode. The growth of the nuclei and birth of new nuclei leads to a sharp increase in current. As the number of nuclei increases their diffusion layers begin to overlap and the current goes through a maximum which reflects the switch from hemispherical to planar diffusion. At longer times nuclei coalesce to form a film which grows under planar diffusion thereby yielding a current which drops as $t^{-1/2}$. The peak is significantly affected by the deposition potential: as the overpotential increases the peak current increases, the peak time decreases and the peak width appears to decrease.

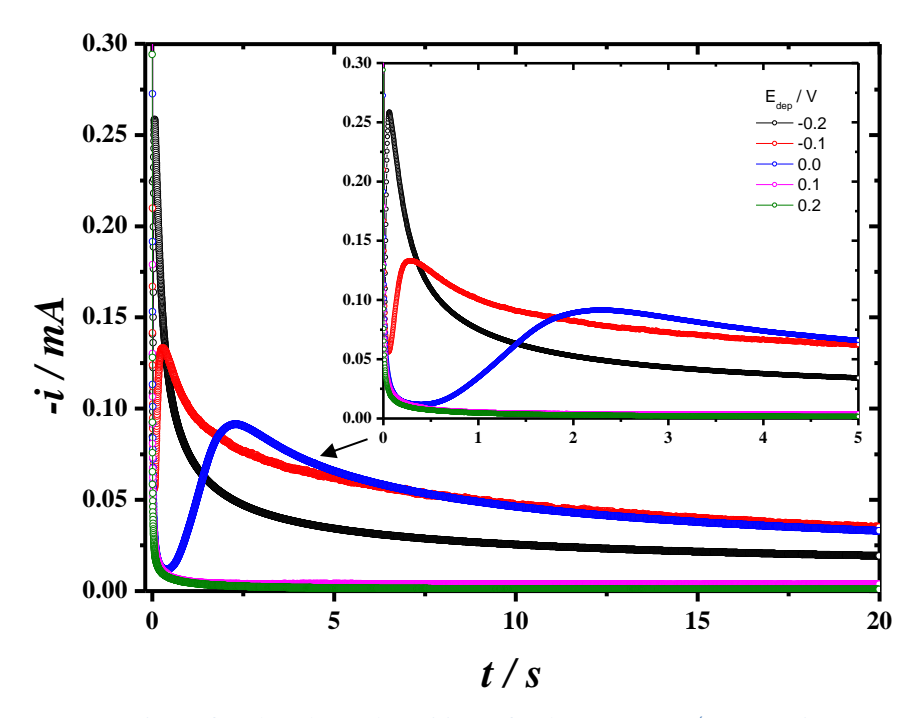


Figure 3-9 Current transients for the electrodeposition of Pd on 5 mm Ø HOPG in argon purged 1 mM $(NH_4)_2PdCl_4 + 0.5$ M KCl stepped from 0.7 V to different deposition potentials (as shown in the Figure).

Low magnification SEM images for Pd particles produced at different deposition potentials are shown in Figure 3-10. General inspection of these Figures demonstrates that the density of Pd particles (number of particles per unit area) dramatically depends on the deposition potential. At -0.2 V, high overpotential, all Pd clusters possess clear 3D characteristics with hemispherical morphology, diameters ranging between 170 and 114 nm, and appear either randomly distributed or decorating

linear surface defects. These defects clearly act as active sites for the Pd deposition. The presence of Pd particles with different sizes suggests a progressive nucleation mechanism. In addition, deposited Pd clusters appear to form dimers, trimers, and chains of islands. Zooming in, Figure 3-10 (1st row right), shows massive dense nanoparticles smaller than 20 nm. Decreasing the deposition potential to -0.1 V forms Pd particles that appear to have the same morphology as at -0.2 V, but we notice that the particles size decreases to the range 120-40 nm. It is also clear that some particles preferentially grow along lines. Although HOPG is known to have large terraces separated by step edges, the latter should only be visible at much higher resolution, e.g. with an atomic force microscope, hence the lines are more likely to be grain boundaries between different HOPG crystals. At 0.0 V the number of particles significantly drops and the particles look larger than the cases mentioned above; this might be attributed to the change of deposition regime from diffusion control for deposition at -0.2 and -0.1 V to electron transfer kinetics control at +0.1 V, see Figure 3-8. The second possibility to interpret the large size of the particles might be that the low magnification of the SEM images may not reveal the presence of nanometre size particles and a large particle at low magnification could be an aggregation of smaller centres; indeed at 0 V very small particles can be seen on the Figure. At 0.1 V and 0.2 V the density of large particles is dramatically reduced but there seem to be no smaller particles. Overall, it is clear from the SEM images that choosing increasingly positive deposition potential significantly decreases the density of particles.

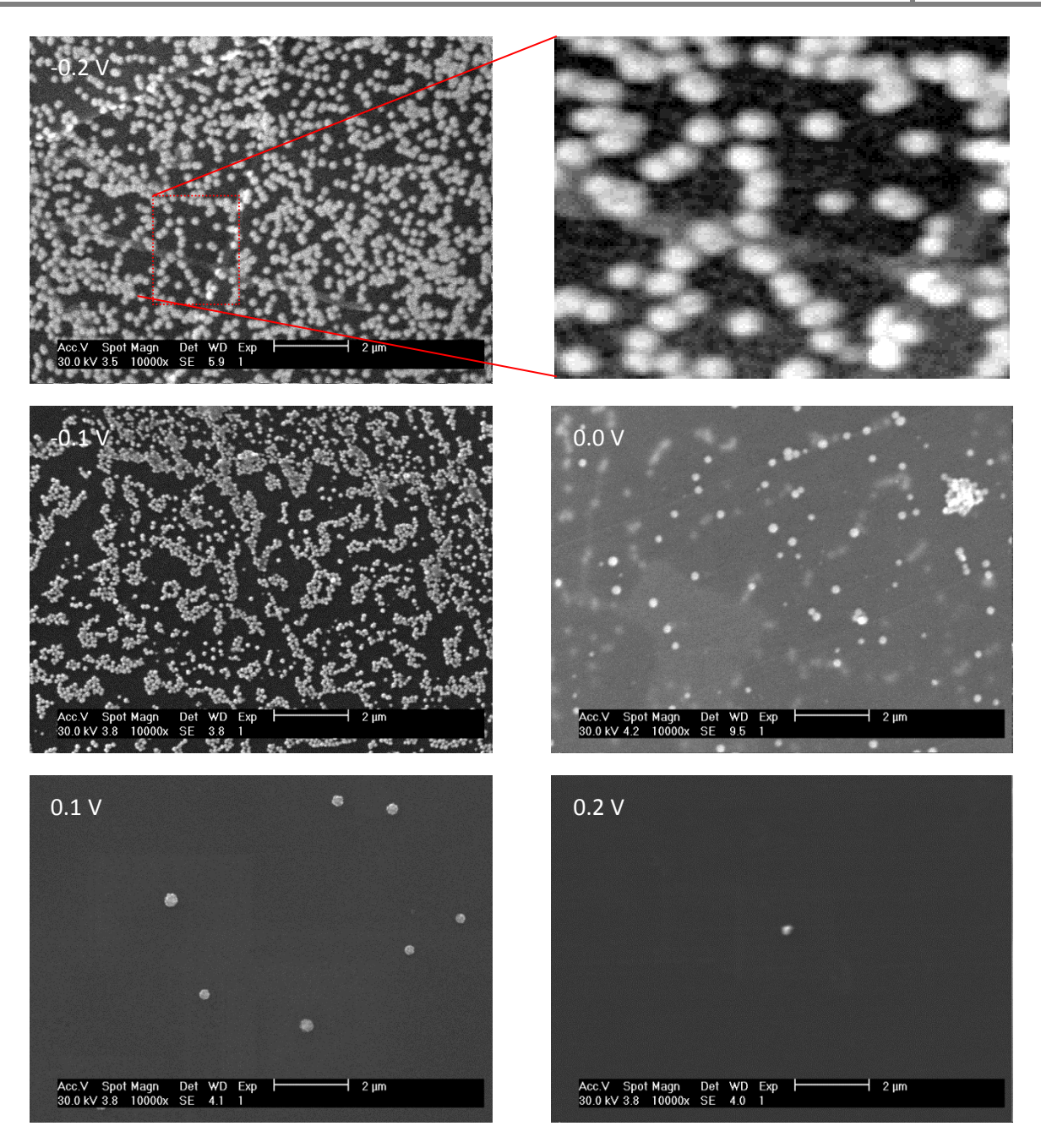


Figure 3-10 SEM images of the HOPG (\emptyset = 5 mm) surface after electrodeposition of Pd in 1 mM (NH₄)₂PdCl₄ + 0.5 M KCl at -0.2, -0.1, 0.0, 0.1 and 0.2 V vs. SCE for 20 s.

Figure 3-11 shows the particles distribution for the images shown in Figure 3-10; all of the statistical information from the histograms is summarized in table 3-2. For all the images analysed by the software the area was $12.4\times8.1~\mu\text{m}^2$. The samples deposited at 0.1 and 0.2 V were not involved in the analysis by ImageJ, because the software required at least 500 particles to ensure adequate statistical confidence. So images with low particle numbers were not analysed. The important step in the analysis is selecting the threshold level. To analyse the images above the threshold, the latter was carefully selected to ensure that the threshold detected a reasonable number of particles. Since the

threshold might strongly affect the particles distribution, a test was done for an image with several threshold levels. The number and size of particles were compared. It was found that small variations in the threshold produced similar results, while a large difference in threshold affected both the size and number of detected particles. The statistical information of the particle count analysis performed on the SEM images shown in Figure 3-10 is summarized in table 3-2.

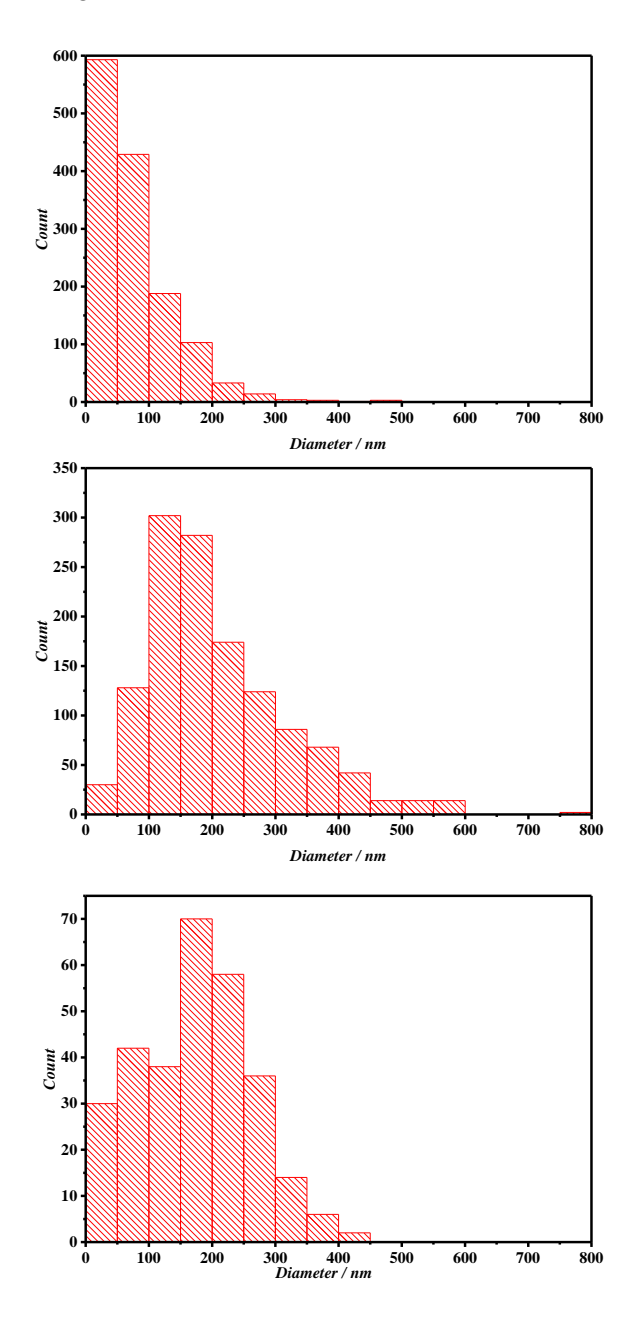


Figure 3-11 Particle size distribution histograms for the Pd deposits presented in Figure 3-10 for the deposition potential, from the top, -0.2 V, -0.1 V and 0.0 V vs. SCE.

From the table 3-2, the number of particles seems to depend on the applied potential, we found that with the same deposition time the number of particles increases when applied higher overpotential.

Also, the minimum particles size seems to be constant and probably reflects the limit of resolution of the SEM with particles smaller than 20 nm being undetected.

Table 3-2 Statistical information of the particle count analysis performed on the SEM images shown in Figure 3-10. The analysis corresponds to deposition potential, -0.2, -0.1 and 0.0 V vs. SCE.

E_{dep} / V	N (Total)	Mean	SD	
vs. SCE	IV (10tai)	/ nm	/ nm	
-0.2	1371	76.77	60.70	
-0.1	1280	207.90	111.71	
0.0	296	175.08	89.15	

To gain more insight from increased resolution the HOPG surfaces were imaged with an atomic force microscope. Figure 3-12 shows the AFM images of electrodeposited palladium particles on HOPG at different deposition times. The AFM imaging provides more detailed information about the surface morphology and homogeneity of the Pd nanocentres. The deposition potential was chosen to be at the foot of the reduction wave at a value of +0.2 V vs. SCE, Figure 3-8, to slow down the growth of large particles. Figure 3-12 shows that fine Pd particles nucleated and spread uniformly on the HOPG plane terraces. The AFM images were analysed with Gwyddion, a software dedicated to SPM images. Primarily it is supposed to be used for analysis of height fields obtained by means of scanning probe microscopy techniques (AFM, MFM, STM, NSOM), but generally it can be used for any other height field analysis or image analysis. The AFM data are usually collected as line scans along the x axis that are concatenated together to form the two dimensional image. Therefore, the scanning speed in the x direction is considerably higher than the scanning speed in the y direction. As a result, the statistical properties of AFM data are usually collected along the x profiles as these are less affected by low frequency noise and thermal drift of the sample.[158]

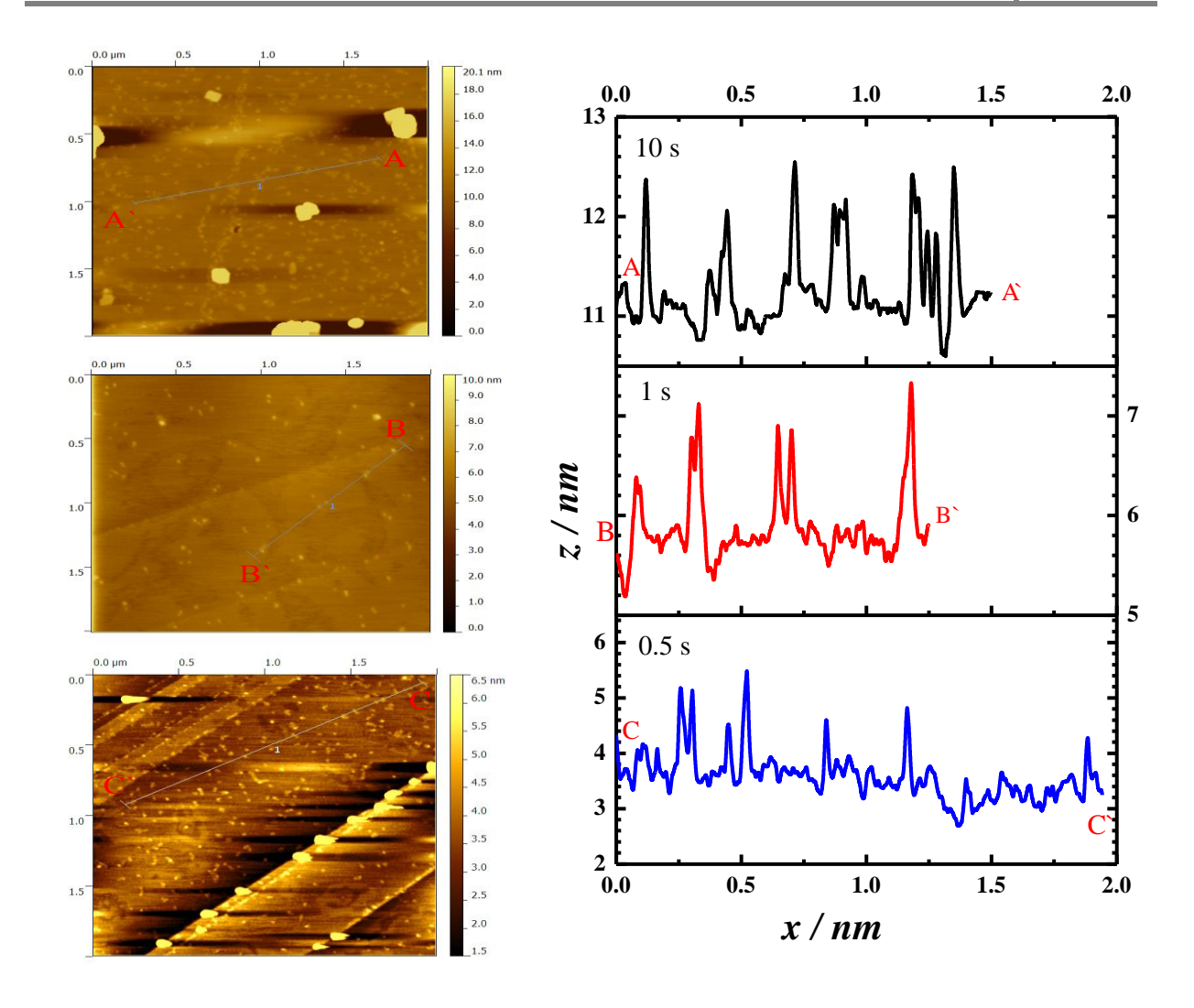


Figure 3-12 AFM images, left, of the HOPG surface showing the initial stages of the Pd electrodeposition at +0.2 V. Deposition time: (top) 10 s; (middle) 1 s; (bottom) 0.5 s. Crosssection profiles, right, through the lines A-A', B-B' and C-C' shown on the corresponding AFM images.

To obtain the cross section from Gwyddion a line was selected on the image, making sure to include particles and avoiding oversized features. The software then converted the image information to z-x data. Analysis of the line scans showed the height of particles was circa 1 nm. We could not find an obvious trend when investigating the effect of varying the deposition time in this set of experiments: for example looking at the shortest deposition time, the AFM image shows a high density of particles compared with that at the longer deposition time of 10 s; this may either reflect the fact that the HOPG surface used for the 0.5 s experiment had more defects than that used for the 10 s experiment or that the particles are sufficiently mobile to diffuse on the surface and form a small number of larger clusters. Moreover, the line scans only show particles between 0.5 and 1 nm. Furthermore, AFM is much more accurate along z than along x and y because of tip size effects. Also the line scans were arbitrarily chosen whereas the image analysis picks up everything on the surface. The corresponding particle size distribution histograms for the three deposition times are shown in Figure 3-13.

Gwyddion was used to obtain the data plotted in Figure 3-13. The AFM images were imported to Gwyddion then the dimensions and units of x, y and z were calibrated. An area of interest was selected using a threshold to contain a reasonable number of particles, the threshold level was neither too low to avoid detecting large grain boundaries with a large number of particles nor too large to avoid detecting very small grain boundaries. A simple threshold algorithm was used based on the height of the particles and the software analysed the geometry of the particles. After that the particle distribution option was chosen to have raw data for mean particle height. Table 3-3 summarizes the descriptive statistics for the histograms shown in Figure 3-13. The Pd nanoparticles had a relatively narrow particle size distribution and the number of particles for the sample with a long deposition time have a large number of particles; this number decreases with 1 s deposition times then increases with 0.5 s, thus the trend for the effect of deposition time on the number of particles is not clear. This may be related to the surface defects as each image was recorded on different HOPG surfaces. Moreover, the AFM images are 2×2 µm and may not be representative of the rest of the electrode; in addition the tip could cause damage or move some particles from their area. Also, the AFM images show very small particles on the terraces and few big ones. The particles with bigger size are resulting from the coalescence of the smaller ones. There is a discrepancy between the results coming from the line scan and the size distribution; the differences suggest that one of the techniques is not working well.

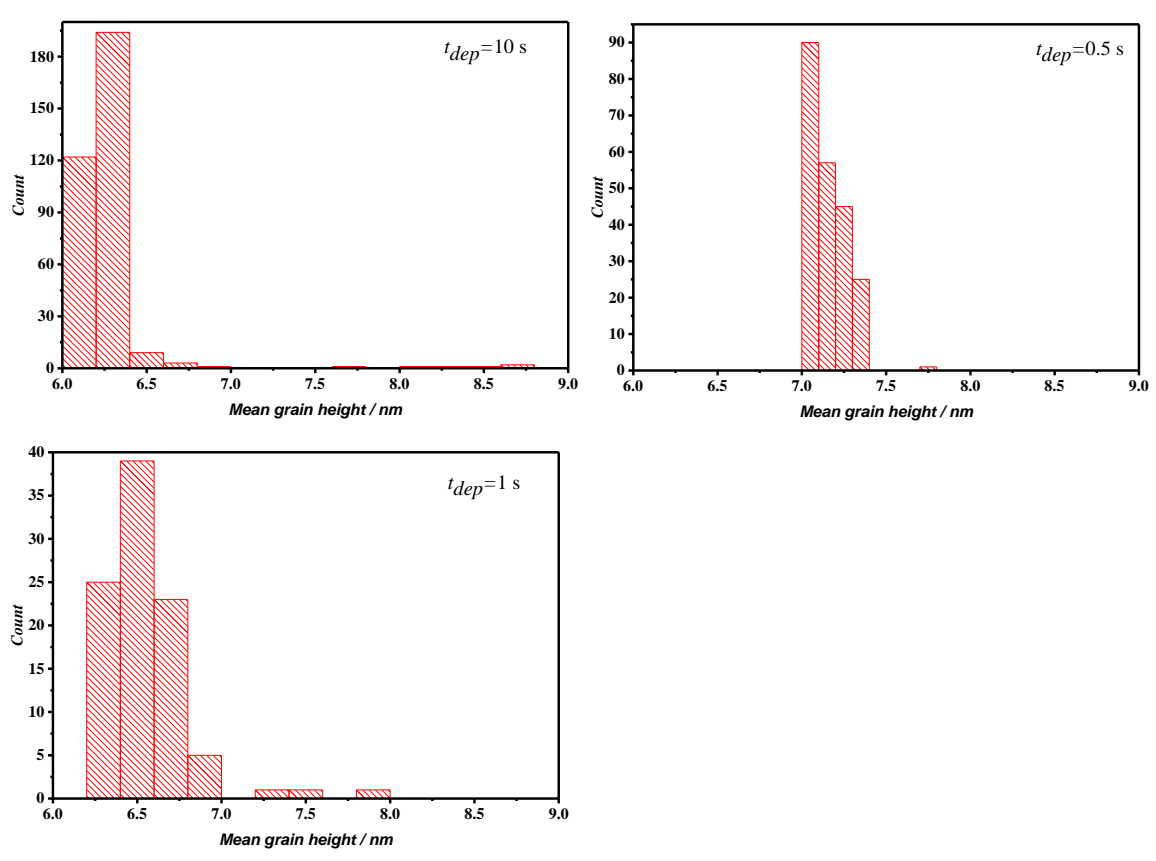


Figure 3-13 Particle size distribution histograms for the Pd deposits presented in Figure 3-8 for the deposition times shown in the legends.

Table 3-3 Statistical information of the particle count analysis performed on the AFM images shown in Figure 3-12. The analysis corresponds to deposition time, from the top, -0.2 V, -0.1 V and 0.0 V vs. SCE.

t _{dep} / s	N (Total)	Mean / nm	SD / nm
10	335	6.27	0.29
1	95	6.55	0.24
0.5	218	7.15	0.01

3.3 Glassy carbon (GC)

Glassy carbon is an example of a non-graphitizing carbon that is a carbon which cannot be transformed into crystalline graphite even at temperatures of 3000 °C and above. GC has a very high thermal stability, it is extremely resistant to chemical attack, including from acids and it has been demonstrated that the rates of oxidation of glassy carbon in oxygen, carbon dioxide or water vapour are lower than those of any other carbon. This property makes glassy carbon a useful material for crucibles. The surface chemistry of glassy carbon allows tailoring of its interfacial properties (surface energy, electron-transfer kinetics) by physisorption or chemisorption of molecules, polymers, or metals, or by procedures involving electrochemical pretreatments, polishing, or laser activation.[159-161] Sensors and biosensors have been prepared by immobilization of recognition elements and enzymes on the surface of glassy carbon electrodes. It is also used widely as an electrode material in electrochemistry and its biocompatibility makes it a potential component of prosthetic devices. Some of the earliest structural models assumed that both sp²- and sp³-bonded atoms were present. The structure also has a high proportion of edge atoms, which are known to have a relatively high reactivity compared with 'in-plane' carbon atoms.[162]

Deposition by cyclic voltammetry was performed in 1 mM $(NH_4)_2PdCl_4 + 0.5$ M KCl to determine the deposition potentials suitable for subsequent chronoamperometry experiments. The potential range for these CV experiments was from +0.7 V to -1.3 V at a scan rate of 10 mV s⁻¹. A large area platinum mesh counter electrode and an SCE reference electrode were used. From the cyclic voltammogram presented in Figure 3-14 it is observed that on the forward scan there is a very steep reduction wave starting at -0.1 V related to the electroreduction of Pd(II) to Pd(0) species, and then followed by a sharp reduction peak. At potential negative to -0.5 V the current increases due to the hydrogen adsorption, absorption and hydrogen evolution respectively. In all three cases, the current increases with the amount of palladium deposited. On the reverse scan, two anodic peaks can be observed positive to -0.5 V versus SCE. The more negative one is attributed to hydrogen desorption from the Pd lattice and the second one corresponds to the electrooxidation of Pd(0) to Pd(II) species and stripping of palladium from the GC surface.

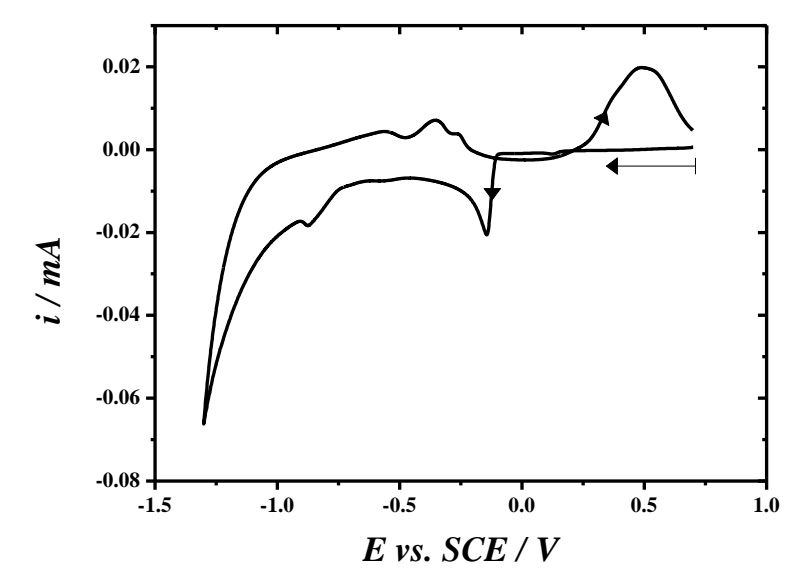


Figure 3-14 Cyclic voltammogram recorded at 10 mV s $^{-1}$ on a 3 mm diameter glassy carbon electrode in argon purged 1 mM (NH₄)₂PdCl₄ + 0.5 M KCl.

In a separate chronoamperometry experiment, the potential was stepped from 0.7 V vs. SCE to various deposition potentials as shown in Figure 3-15. The transients have the typical shape of nucleation and growth processes and these will be the subject of detailed analysis in the next chapter. The rate of both nucleation and growth increases with applied overpotential. At high overpotential, the timescale of the rise decreases. As the potential is made more positive a rising current-time transient is still observed. The thickening of the metal layer under diffusion control leads to the falling of the current-time transients. The transients in Figure 3-15 show that, at low overpotential the nucleation is clearly delayed and appears as low current. At high overpotentials (-250 and -200 mV), the current transient reaches the peak faster than at lower overpotential.

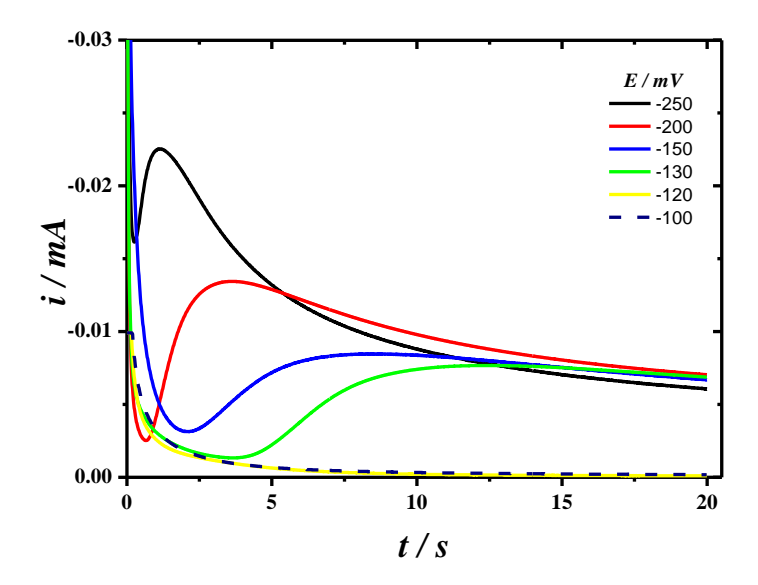


Figure 3-15 Current transients recorded on glassy carbon electrodes (3 mm diameter) in argon purged 1 mM $(NH_4)_2PdCl_4 + 0.5$ M KCl after stepping from +0.7 V to different deposition potentials, shown in legend.

The morphology of the Pd centres deposited onto glassy carbon after undergoing the potential steps are shown in Figure 3-16. Typical SEM images display the hemispherical shape of Pd centres deposited onto the glassy carbon electrode surface. The number of Pd centres increases with deposition potential, at more negative potentials. The size of the palladium centres produced at -0.25 V ranges between 95 nm and 250 nm. Within the limited deposition time, the amount of deposition charge passed decreases as the deposition potentials are made more positive. Thus, the diameter of the Pd nuclei deposited is smaller. At -0.2 V, the deposited Pd centres are sparsely distributed with smaller diameter nuclei (ranging from 400 nm to 150 nm). At more positive potentials, growth of existing nuclei takes place more readily than the formation of further nuclei. The nuclei at more positive potentials are larger. However, the electrode surface has not been fully covered by the deposited Pd nuclei. This may be attributed to the active nucleation sites on the electrode surface. In addition, nuclei of diameter smaller than 50 nm could not be observed with the scanning electron microscope, even at high magnification. At -0.15 and -0.13 V the images show a lower density of spherical particles. The influence of deposition potential is clear in the SEM images with more dense deposits of small spherical particles observed at high overpotentials. Figure 3-16 clearly shows that progressive nucleation has taken place over the duration of these experiments.

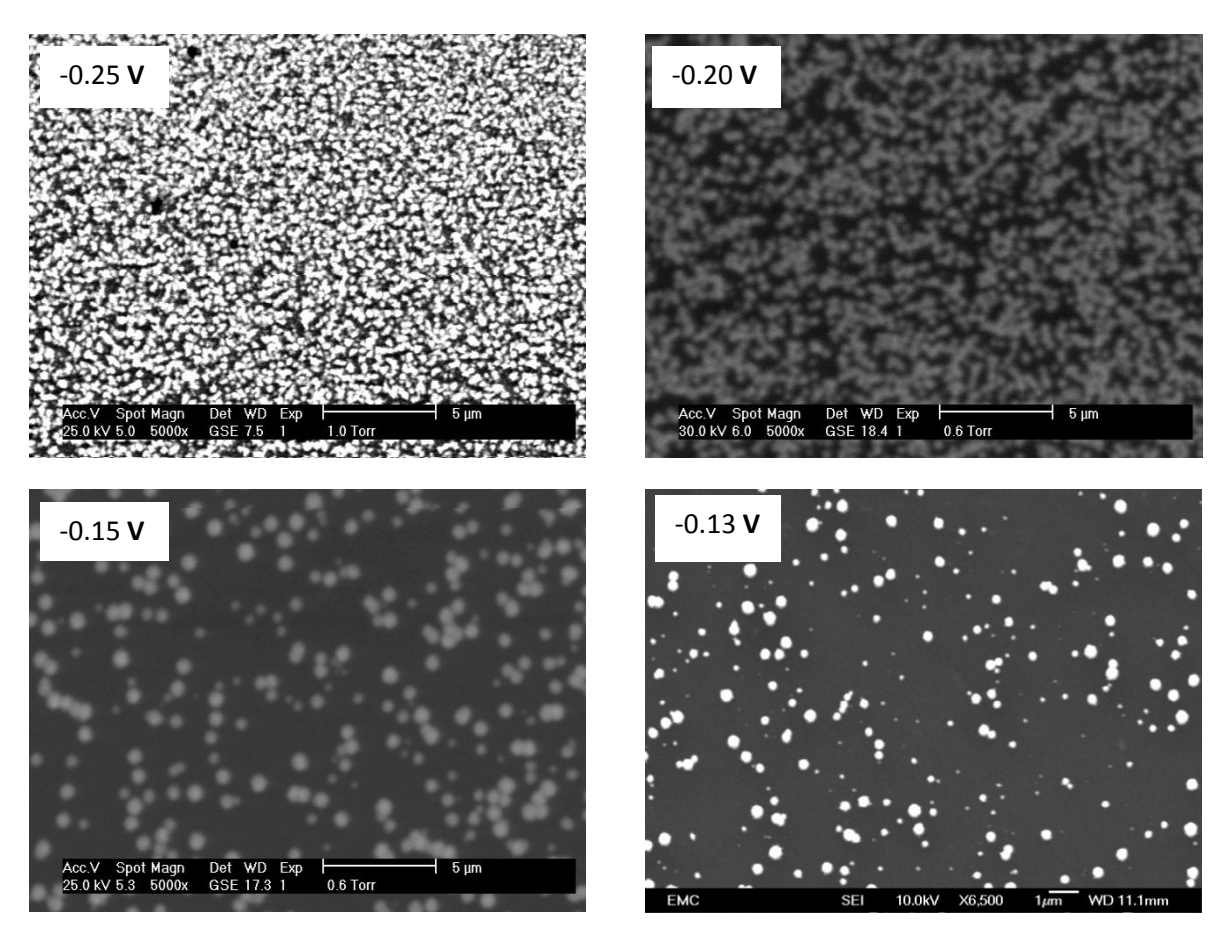


Figure 3-16 SEM images of Pd deposits formed on glassy carbon (3 mm diameter) after stepping from +0.7 V to -0.25, -0.20, -0.15 and -0.13 V vs. SCE for 20 s in argon purged 1 mM (NH₄)₂PdCl₄ + 0.5 M KCl.

Two potentials in the foot of the deposition wave, -120 and -100 mV, were chosen to reduce the number of particles and decrease the particles size. Interestingly, the palladium centres deposited at -120 mV formed a large number of sub 100 nm clusters made of much smaller nanoparticles. Surprisingly at -100 mV a random distribution of apparently conical centres was observed, see Figure 3-17.

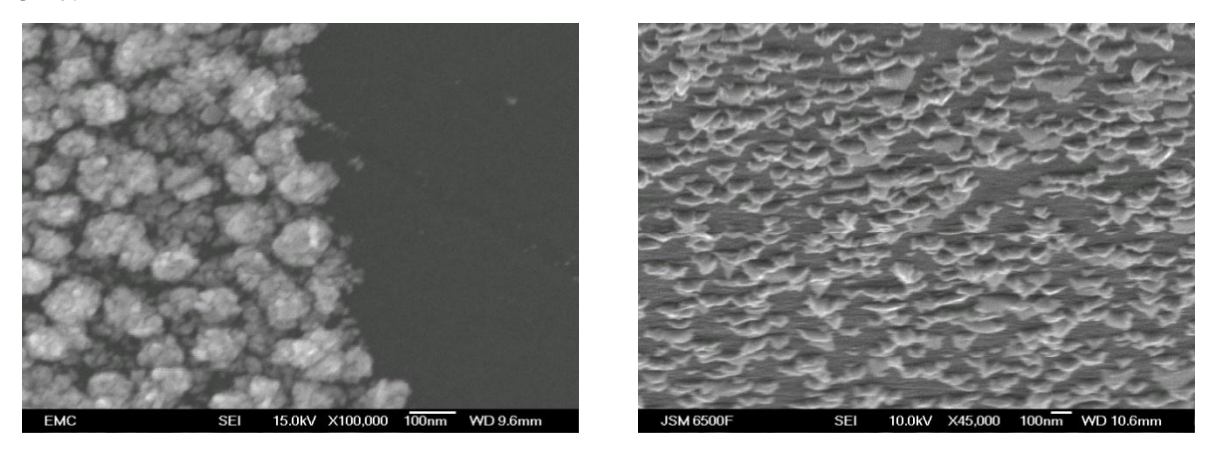


Figure 3-17 SEM images of Pd deposits formed on glassy carbon (3 mm diameter) after stepping from +0.7 V to -120 mV, left, and -100 mV, right, for 20 s in argon purged 1 mM (NH₄)₂PdCl₄ + 0.5 M KCl.

The increase in surface area of Pd can be characterised by recording the cyclic voltammogram in 1 M sulphuric acid and comparing the charges for the Pd reduction peak. Figure 3-18 shows cyclic voltammograms in 1 M sulphuric acid saturated with argon recorded at modified glassy carbon electrodes at 20 mV s⁻¹. It is clear that all electrodes present voltammetric features characteristic of palladium. The voltammograms include palladium oxide reduction features with clear hydrogen adsorption / desorption and hydrogen absorption / extraction peaks prior to the onset of hydrogen evolution. The extremely small size of the Pd oxide reduction peak compared to the hydrogen region suggests that only partial coverage of the GC electrode has taken place but that the Pd particles are able to promote a high rate of hydrogen evolution.

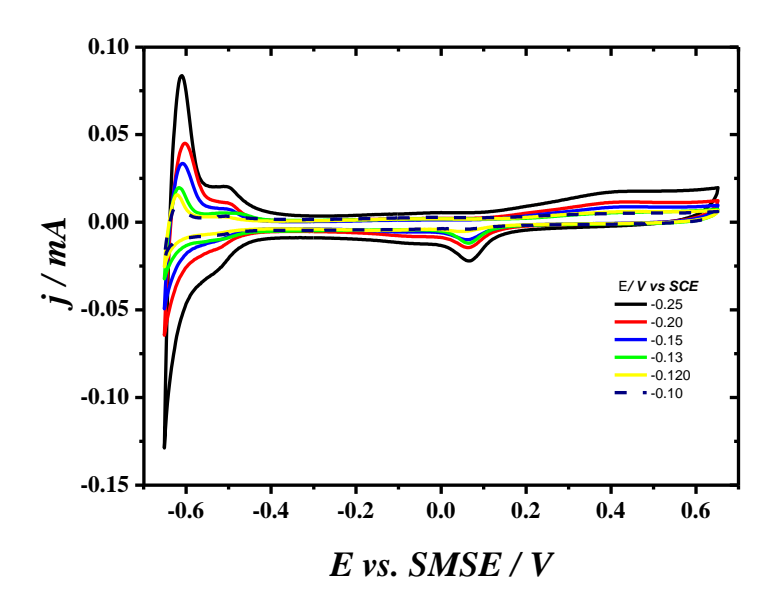


Figure 3-18 Voltammograms, 5^{th} cycle, recorded in Ar purged 1 M sulphuric acid at 20 mV s⁻¹ with 3 mm diameter glassy carbon electrodes after undergoing potential steps from +0.7 V to different deposition potentials, shown in the legend, in argon purged 1 mM (NH₄)₂PdCl₄ + 0.5 M KCl for 20 s.

Table 3-1 shows the Pd oxide reduction charges that represent the amount of Pd deposited. The table shows decreasing palladium oxide reduction charges as the deposition potential becomes more positive, this is the expected trend as the reduced overpotential resulted in a lower deposition current which should lead to a smaller amount of Pd on the surface.

Table 3-4 Dependence of the Pd oxide stripping charge, Q_{Pd} , on the deposition potential.

Deposition potential / V	Q_{Pd}/C
-0.25	7.6×10 ⁻⁴
-0.20	3.9×10 ⁻⁴
-0.15	3.8×10 ⁻⁴
-0.13	4.5×10 ⁻⁴
-0.12	1.4×10 ⁻⁴
-0.10	6.0×10^{-5}

Two potentials far from the start of the reduction of palladium, +0.3 and +0.35 V, were selected for further investigations. Two GC electrodes were prepared by chronoamperometry, one for each deposition potential, and the deposition time was kept constant at 10 s. Both produced a very small number of large spherical particles which mostly decorated the edges of the glassy carbon, with a handful of particles distributed randomly in the centre of the electrode. The difference between the particles is that, particles formed at +0.35 V had a diameter circa 91.7 μ m while those formed at +0.3 V had a diameter circa 68.3 μ m, Figure 3-19. The difference between the particles shown in the Figure 3-16, Figure 3-17 and 3-19 is the applied potential that was used to form the particles. The high over potential used for the particles in Figure 3-16 was located on the plateau of the reduction wave of palladium where the electrodeposition is under diffusion control, this cause very dense of small spherical particles. The applied potential that was chosen to deposit particles shown in Figure 3-17 was -120 and -100 mV and they are governed by a mixed charge and mass transfer control mechanisms. They produced a large number of sub 100 nm clusters with conical shape. While Figure 3-19 shows a smaller number of big spherical particles > 60 μ m, their applied potential was close to the start of the reduction potential of palladium so as to grow under kinetic control.

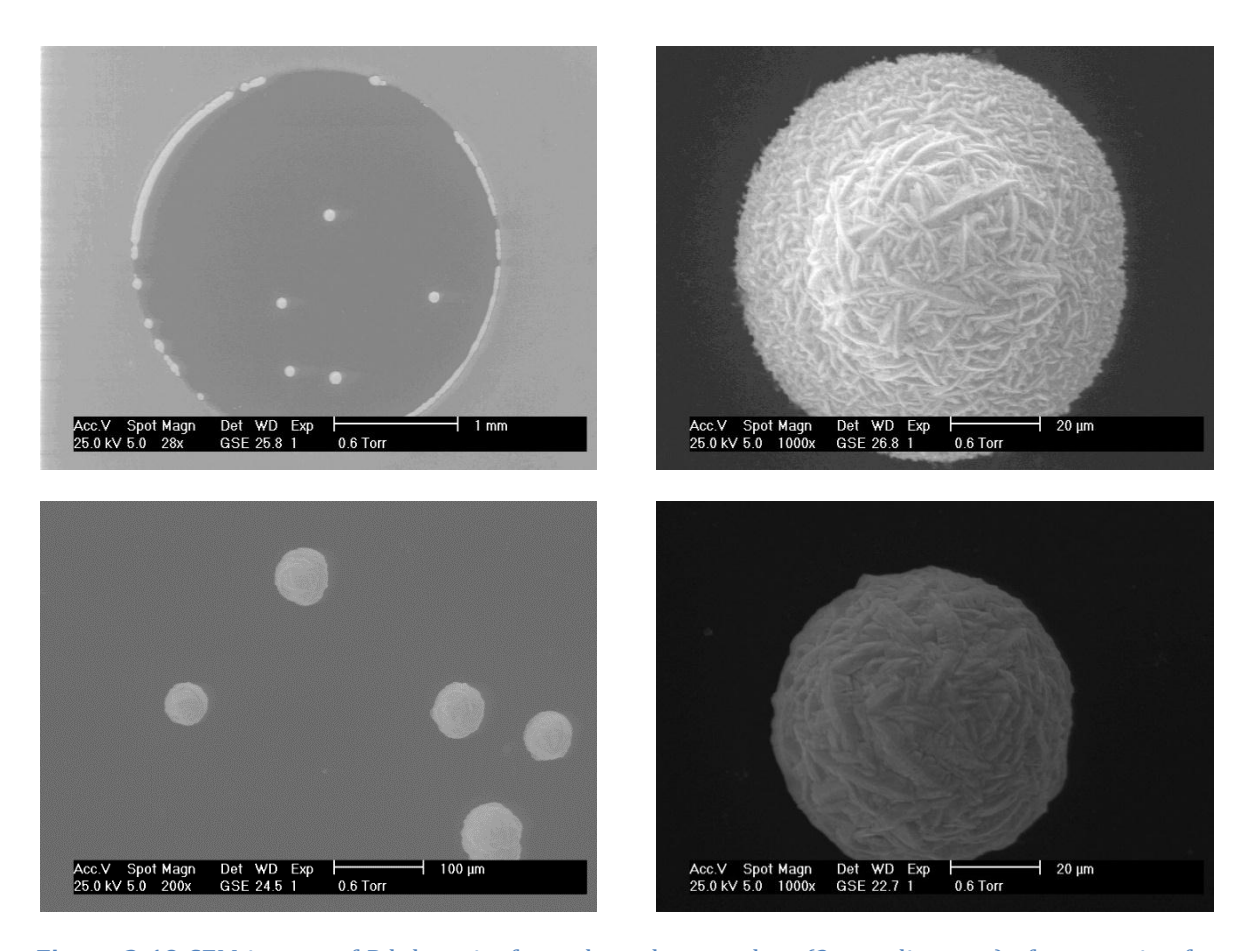


Figure 3-19 SEM images of Pd deposits formed on glassy carbon (3 mm diameter) after stepping from +0.7 V to +350 mV, top row with different magnifications, and +300 mV, bottom row with different magnifications, for 10 s in argon purged 1 mM (NH₄)₂PdCl₄ +0.5 M KCl.

3.4 Conclusion

The initial aim of this project was to deposit palladium nanocentres onto different carbon electrodes and study the initial stages of their nucleation and growth. Useful software was used to determine the particle distribution. ImageJ was used with SEM images and Gwyddion was employed to determine the overall grains size and numbers of AFM images.

- 1. The nucleation and growth of palladium particles was studied on the CF; experiments were carried out by varying the deposition potential and the deposition time. The potentials were chosen in different regions from the palladium cyclic voltammogram and it was decided to choose a low overpotential, -0.15 V, to drop the density of particles. Using high resolution electron microscopy enabled us to clearly observe particles ranging between 50 and 20 nm. The density of Pd nanoparticles decreased with decreasing deposition times.
- 2. Nanoparticles were successfully electrodeposited on HOPG, the deposition time was controlled to be ≤ 10 s and deposition potential was chosen to operate under kinetically controlled conditions, 0.2 V. AFM images show a higher density of particles at 0.5 s than for a longer deposition time of 10 s. It is a challenge to get good reproducibility on HOPG because the work on HOPG required a fresh layer for each experiment, the way of peeling off the HOPG layer could result in different surface roughness.
- 3. Once the substrate was switched to 3 mm glassy carbon electrodes progress towards small palladium metal centres was observed. Small metal centres were produced on glassy carbon with 1 mM (NH₄)₂PdCl₄ + 0.5 M KCl. However the observed metal centres were not uniformly distributed and not uniform in size. The SEM images showed Pd clusters of different sizes appearing either randomly distributed or decorating any surface defects which acted as active sites.
- 4. 0.30~V and 0.35~V were investigated and chosen for 10~s deposition on GC. Both potentials produced few spherical particles which decorated the edges of the glassy carbon with some particles distributed randomly on the centre of the electrode. Both potentials produced a very small number of large spherical particles with a diameter circa $91.7~\mu m$ for 0.35~mV and circa $68.3~\mu m$ for 0.30~mV.
- 5. The early stages of palladium particle growth on different carbon substrate showed that the substrate structure can influence the distribution of particles. We found on carbon fibre that the preferred area of deposition was the lines related to the structure of the CF, when we switched to HOPG, we found that the most of particles appeared either randomly distributed or decorating linear surface defects. These defects clearly act as active sites for the Pd deposition. The presence of Pd particles with different sizes suggests a progressive nucleation mechanism. It was noticed that Pd nanoparticles on glassy carbon decorated the edges of disc

electrode. The palladium deposition CV showed the same features for all the substrates and the shape of current transients have a similar shape to the classical transient when sufficient overpotential has been applied.

In the next chapter we will attempt to prepare surfaces with controlled size and dispersion of nanoparticles by electrodepositing palladium in the presence of a surfactant template. For this Pd deposits were produced on different substrates by electrodeposition within liquid crystal phases (both micellar and hexagonal phases) consisting of self-assembled non-ionic surfactant molecules.

4. Pd electrodeposition from lyotropic liquid crystals mixtures

In this chapter we will discuss how to prepare surfaces with controlled size and dispersion of nanoparticles by electrodepositing palladium in presence of a surfactant. The work presented in this chapter focuses on the early stages of the electrodeposition of Pd from different aqueous mixtures of octaethyleneglycol monohexadecyl ether (C₁₆EO₈). In water this non-ionic surfactant behaves as a liquid crystal[163] and the mixtures were chosen to explore its micellar and hexagonal phases. Pd nanoparticles were electrodeposited on various carbon substrates for different deposition potentials. Voltammetry and chronoamperometry were used to form the palladium centres and study their growth. Theoretical models were used to investigate the effect of the surfactant on the early stages of nucleation and growth of the Pd nanoparticles by analysing the current transients. Firstly, using the Cottrell equation at long deposition times to calculate the diffusion coefficient D, secondly with the Scharifker-Hills model (SH)[31] to assess whether the dimensionless curves have the characteristic shape for instantaneous or progressive nucleation and thirdly, with the Heerman-Tarallo model (HT)[164] to estimate the number of active sites A and nucleation rate N_o as a function of the experimental conditions. In all cases no attempt was made to remove dissolved oxygen as bubbling the surfactant mixtures with Ar was not possible either because of the formation of foam with the 2 and 10 wt.% mixtures or because of the very high viscosity of the 48 wt.% mixture.

4.1 Cyclic voltammetry of Pd in different plating mixtures with glassy carbon electrodes

The cyclic voltammograms recorded in each of the plating mixtures with a GC electrode are shown in Figure 4-1. Two different phases of the liquid crystal were investigated, the micellar phase (2 and 10 wt.%) and the hexagonal phase (48 wt.%), to form palladium nanoparticles at room temperature; deposition was also performed in absence of surfactant for comparison. The voltammograms were all recorded within the same potential window, +0.7 V to -1.3 V with respect to SCE, at a potential scan rate of 10 mV s⁻¹. A platinum mesh and saturated calomel electrode were used as the counter and reference electrodes respectively. On the forward scan the onset of waves related to the electroreduction of Pd (II) to Pd (0) species were observed at +0.06, +0.02, -0.02 and -0.04 V for 0, 2, 10 and 48 wt.% respectively. Increasing surfactant concentrations required greater overpotentials to deposit the Pd as illustrated by the pronounced shift of the deposition wave towards negative potentials for the 48 wt.% mixture. This is thought to reflect the adsorption of surfactant on the substrate. The rate of nucleation and growth was also found to drop when increasing the surfactant concentration: the current observed at the reduction peak is highest in the 0 wt.% solution, the micellar solutions, 2 and 10 wt.%, have smaller but otherwise similar peak heights but the 48 wt.% mixture produces significantly lower peak heights. Although the same concentration of palladium salt was used in each case, the presence of surfactant affects the solution viscosity and therefore the diffusion of the metal salt to the electrode surface.

At potentials below -0.2 V the current increases due to the hydrogen adsorption, absorption and hydrogen evolution respectively. The current for the hydrogen evolution increases with the amount of palladium deposited.

On the reverse scan, two anodic peaks can be observed positive to -0.5 V. The peak circa -0.25 V is attributed to hydrogen desorption and the peak circa +0.5 V is attributed to the electrooxidation of Pd (0) to Pd (II) species leading to the stripping of Pd from the GC surface. The stripping peak is much smaller in presence of surfactant thereby indicating that a smaller amount of Pd is deposited during the potential scan. All CVs show a clear nucleation loop (the potential needed to plate Pd on GC during the forward sweep is more negative than that needed to strip Pd from Pd on the reverse sweep) therefore indicating that even in the presence of surfactant a nucleation overpotential is necessary to initiate the nucleation of Pd centres on the carbon surface.

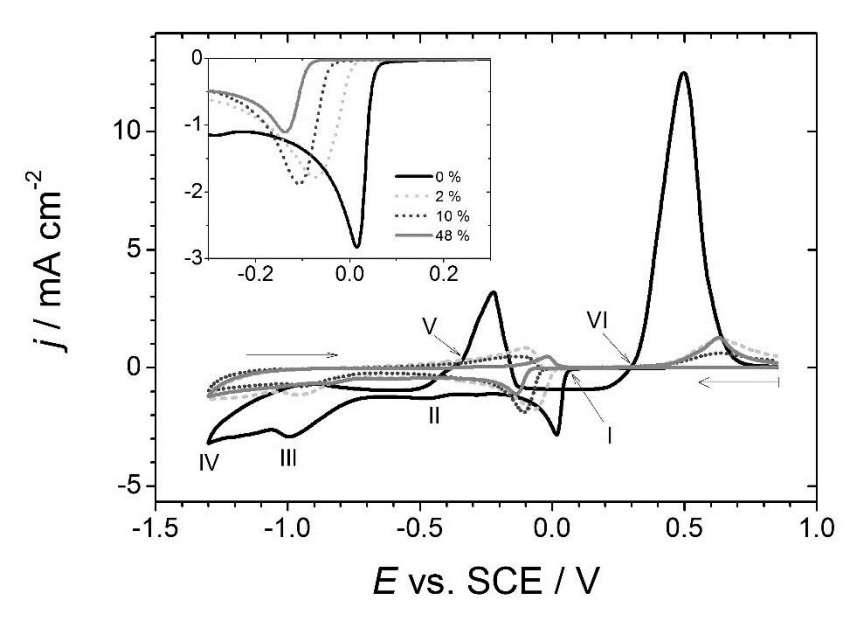


Figure 4-1 Cyclic voltammograms recorded at 10 mV s⁻¹ on 3 mm \emptyset glassy carbon discs in aerated 10 mM (NH₄)₂PdCl₄ + 0.5 M KCl with 0, 2, 10 and 48 wt. % of C₁₆EO₈ as indicated by the legend. The labels respectively indicate: I) the onset of Pd deposition, II) H adsorption, III) H absorption, IV) the onset of H evolution, V) H desorption and VI) the onset of Pd dissolution. The inset shows the same data around the Pd deposition wave.

Figure 4-2 shows the electrodeposition of Pd with a narrow potential window avoiding the hydrogen region. Overall the same observations can be made as in Figure 4-1, except for the absence of oxidation peak circa -0.25 V reflecting the fact that no hydrogen was loaded into the Pd lattice when the sweep was reversed at -0.3 V. The charges associated with deposition and stripping of Pd are summarized in table 4-1. It is clear that the deposition charge, $Q_{\rm dep}$, is greater in absence of surfactant and decreases as the surfactant wt.% increases. Similarly, the striping peak, charge $Q_{\rm strip}$, decreases systematically as the amount of surfactant increases. The charge coming from the reduction of oxygen will make $Q_{\rm dep}$ greater than expected since as

soon as the Pd forms on glassy carbon the ORR will be promoted, so some of the charge reflects the ORR since no attempt was made to remove oxygen from the mixtures. $Q_{\rm strip}$ is only one half or one third of $Q_{\rm dep}$ as shown in table 4-1 which suggests either that a lot of Pd is not removed or that $Q_{\rm dep}$ has a small contribution from other processes, e.g. H- adsorption, H-absorption.

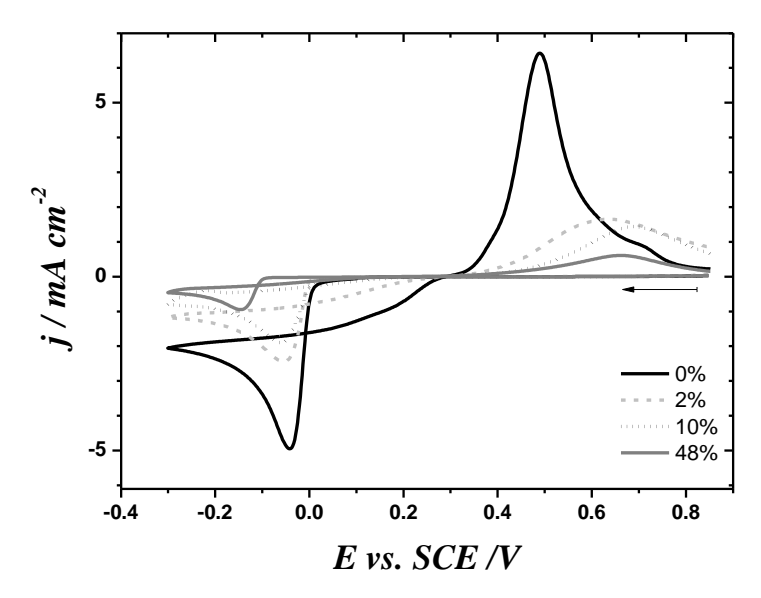


Figure 4-2 Cyclic voltammograms recorded at 10 mV s⁻¹ on 3 mm Ø glassy carbon discs in aerated 10 mM $(NH_4)_2PdCl_4 + 0.5$ M KCl with 0, 2, 10 and 48 wt. % of $C_{16}EO_8$ as indicated by the legend. Here the sweeps were reversed at -0.3 V compared to -1.3 V in Figure 4-1.

Table 4-1 Dependence of the Pd reduction charge, Q_{dep} , stripping charge, Q_{strip} and Q_{strip} / Q_{dep} on the amount of surfactant. The charges were calculated from Figure 4-2.

C ₁₆ EO ₈ wt.%	Q_{dep} / mC cm $^{-2}$	Q_{strip} / mC cm ⁻²	Q_{dep} / Q_{strip}
0	12.0	6.7	1.8
2	6.1	2.0	3
10	3.6	1.3	2.9
48	1.5	0.8	1.9

4.2 Nucleation and growth of Pd centres

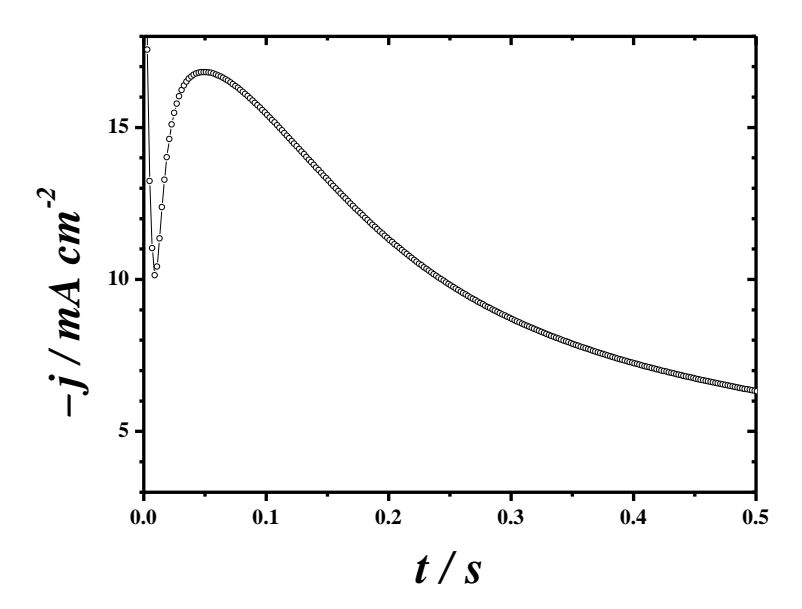


Figure 4-3 Current transient recorded at -0.3 V vs. SCE with a 3 mm \emptyset glassy carbon disc in aerated 10 mM (NH₄)₂PdCl₄ + 0.5 M KCl without surfactant.

A typical deposition transient presents several characteristic features, Figure 4-3. At the beginning, the current drops sharply. This corresponds to the charge / discharge of the double-layer. After reaching a minimum the current rises as nuclei begin to form on the electrode. The growth of the nuclei and birth of new nuclei lead to a sharp increase in current. As the number of nuclei increases their diffusion layers begin to overlap and the current goes through a maximum which reflects the switch from hemispherical to planar diffusion. At longer times nuclei coalesce to form a film which grows under planar diffusion thereby yielding a current which drops as $1/\sqrt{time}$.

Transients recorded for different deposition potentials and surfactant concentrations are presented in Figure 4-4 and summarised using two characteristic parameters, the peak time, t_{max} , and the peak current, j_{max} , in table 4-2.

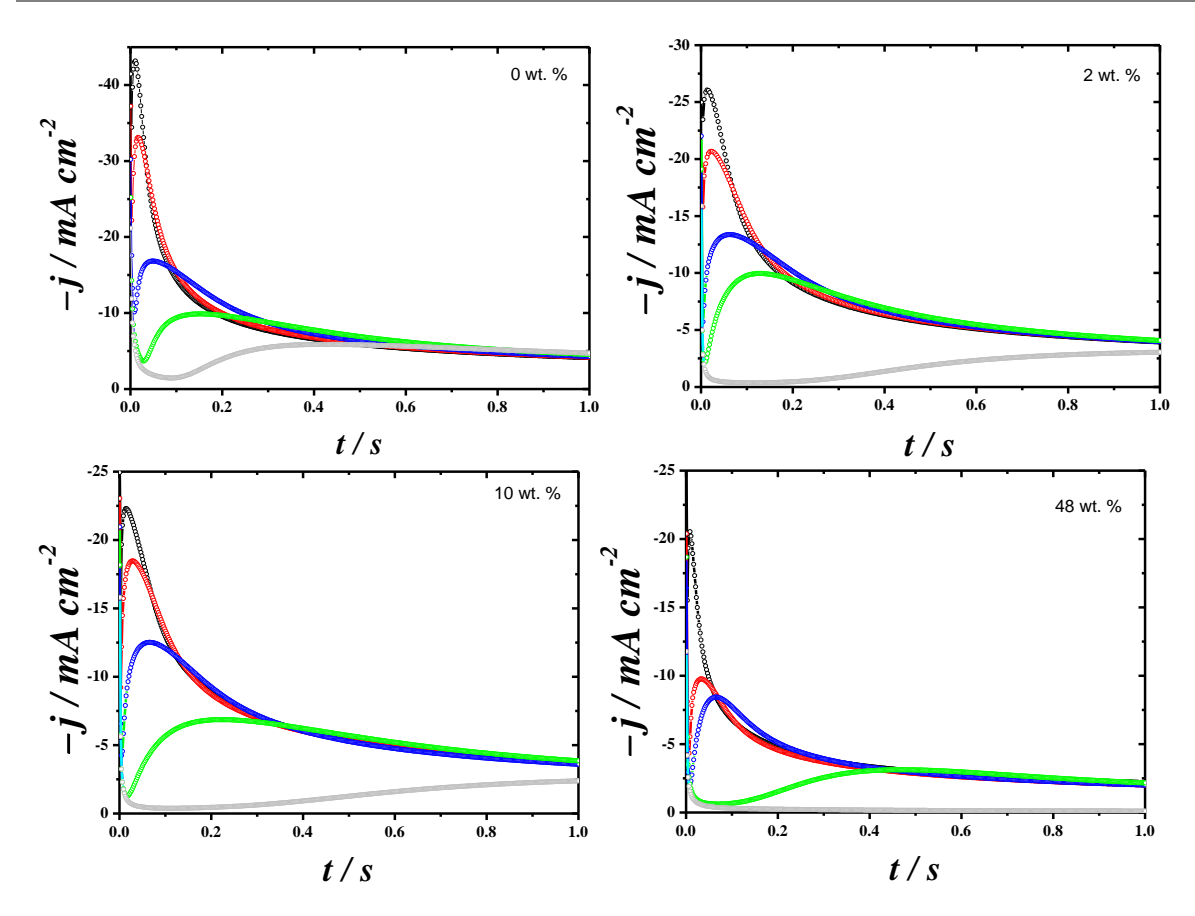


Figure 4-4 Current transients for the electrodeposition of Pd at different potentials on 3 mm Ø glassy carbon discs in 10 mM (NH₄)₂PdCl₄ + 0.5 M KCl and different weight % of $C_{16}EO_8$ (as shown in the Figures). The deposition potentials are respectively -500 mV (black), -400 mV (red), -300 mV (blue), -200 mV (green) and -100 mV (grey).

Table 4-2 Analysis of the current transients shown in Figure 4-4 using two characteristic parameters, the peak time, t_{max} , and the peak current, j_{max} .

	0 wt.%		2 w	2 wt.%		10 wt.%		48 wt.%	
E/mV	t _{max} / s	j_{max} / mA cm ⁻²	t_{max} / s	j_{max} / mA cm $^{-2}$	t _{max} / s	j_{max} / mA cm $^{-2}$	<i>t_{max}</i> / s	j_{max} / mA cm ⁻²	
-500	0.011	42.9	0.014	26.0	0.015	22.9	0.010	20.5	
-400	0.017	32.9	0.023	20.7	0.029	18.6	0.035	9.7	
-300	0.049	17.1	0.065	13.4	0.067	12.5	0.067	8.4	
-200	0.153	9.9	0.129	10.0	0.217	6.9	0.465	3.1	
-100	0.421	5.9	1.175	3.1	1.494	2.6	6.067	0.7	

Figure 4-5 illustrates the relationship between the current maxima extracted from all the current transients and the deposition potentials for different weight % of $C_{16}EO_8$. The peak current systematically decreases as the deposition potential increases; this reflects the fact that the deposition rate decreases when the overpotential decreases. In addition the peak current decreases as the surfactant concentration increases, whatever the deposition potential. This is thought to reflect the increasing viscosity of the medium. The second plot in Figure 4-5 attempts to find a Tafel like

dependence of current on potential but it is difficult to analyse these potential dependences further because the reduction waves shown in Figure 4-1 clearly show the shift in potential when the surfactant is added and the contribution form H adsorption and absorptions are different in each case. That is particularly observed in the 0 wt.% mixture.

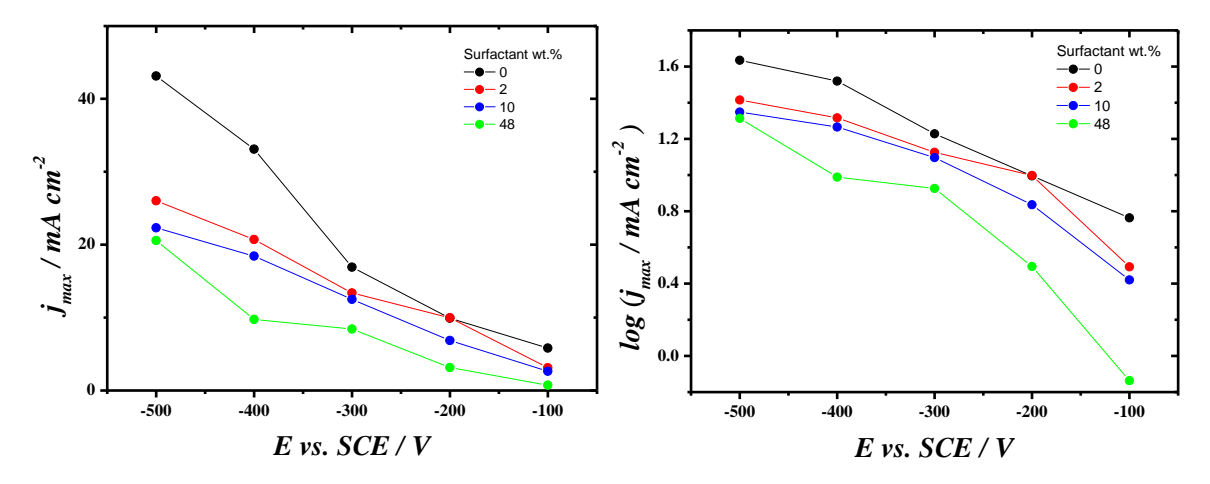


Figure 4-5 Dependence of the peak current on deposition potentials for the current transients shown in Figure 4-4.

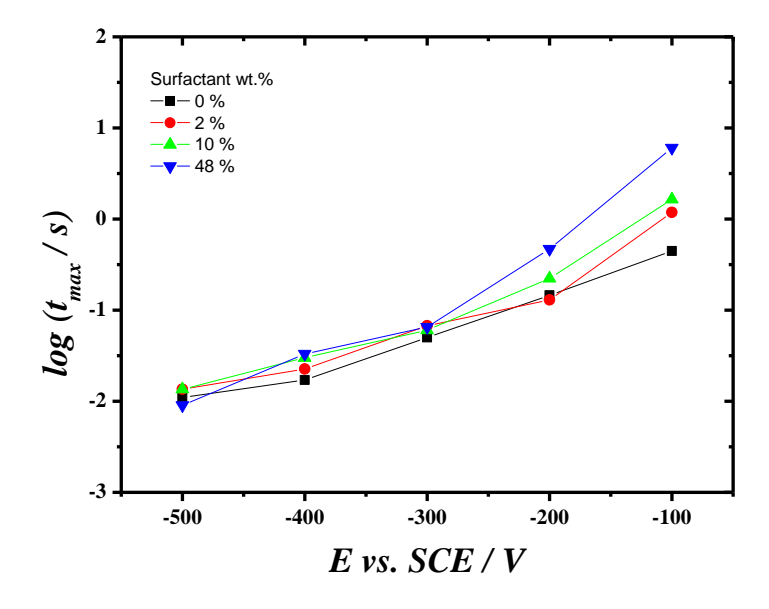


Figure 4-6 Dependence of the peak time on the deposition potentials for the current transients shown in Figure 4-4.

Figure 4-6 shows the relationship between t_{max} and the deposition potential for the different plating mixtures. As expected, the larger the overpotential, the faster the nucleation and growth processes are. For large overpotentials, -500, -400 and -300 mV, the amount of surfactant present in the mixture has little influence over the peak time which is primarily determined by the electrochemical driving force but for low overpotentials increasing amounts of surfactant significantly delay the growth process. Interestingly the amount of surfactant seems to have virtually no influence on the peak time for high overpotentials. However for low potentials increasing the amount of surfactant clearly delays the

nucleation and growth process; this is mostly likely due to the shifting of the reduction wave observed when increasing the surfactant weight percent.

4.3 Kinetic analysis of the nucleation and growth

Different theories have been elaborated to describe the current transients as a function of the number of nucleation sites, N_o , and nucleation rate, A. Two theoretical models were chosen for fitting our experimental data: the Scharifker-Hills model (SH)[31] and the Heerman-Tarallo model (HT).[164] SH is usually used in the form of dimensionless curves, in which $(i/i_{max})^2$ is plotted against t/t_{max} , with i_{max} and t_{max} being the current maximum of the measured current transient, and the corresponding time, respectively. These dimensionless curves have a characteristic shape for instantaneous and progressive nucleation and comparison with experimental data has been used widely to examine the progressive/instantaneous character of reactions. In practice, however, it is difficult to extract useful parameters from this model, and it suffers from the requirement that progressive and instantaneous cases be treated separately.[33,44] The interesting feature of the HT model is that it allows estimation of the number of active sites and nucleation rate as a function of experimental conditions without invoking the concept of instantaneous or progressive nucleation. This has been attempted by many authors.[165-169] In particular, it has been noted for a variety of systems that both N_o and A are extremely sensitive to the applied potential, with increases in overpotential increasing the number of active sites and nucleation rate.[170,171]

4.3.1 The Scharifker-Hills model

To assess the deposition mechanism the transients were normalised (current with respect to its peak i_{max} and time with respect to the peak time t_{max}) and compared to the Scharifker and Hills model eq. 1 for instantaneous nucleation where all nuclei are formed at the same time after applying the potentiostatic step, and eq. 2 for progressive nucleation where the number of nuclei increases gradually with the deposition time.[44,172-175]

$$\left(\frac{i}{i_{max}}\right)^{2} = 1.9542 \left(\frac{t}{t_{max}}\right)^{-1} \left[1 - \exp\left\{-1.2564 \left(\frac{t}{t_{max}}\right)\right\}\right]^{2}$$
 (4-1)

$$\left(\frac{i}{i_{max}}\right)^2 = 1.2254 \left(\frac{t}{t_{max}}\right)^{-1} \left[1 - \exp\left\{-2.3367 \left(\frac{t}{t_{max}}\right)^2\right\}\right]^2$$
 (4-2)

a) Deposition in absence of surfactant

Figure 4-7 shows a dimensionless plot of the experimental current transients at different potentials in aerated 10 mM (NH₄)₂PdCl₄ + 0.5 M KCl without surfactant on GC. At longer deposition time $t/t_{\rm max}$ > 7 the transients show good agreement with the theoretical curve for progressive nucleation; before $t/t_{\rm max}$ < 7, the curves no longer fit the theoretical model. It seems that at short times most of the current transients approach the instantaneous nucleation mechanism. With lower overpotential (-100 mV), the

nucleation mechanism of Pd deposition appears to follow the progressive nucleation model of Scharifker and Hills.

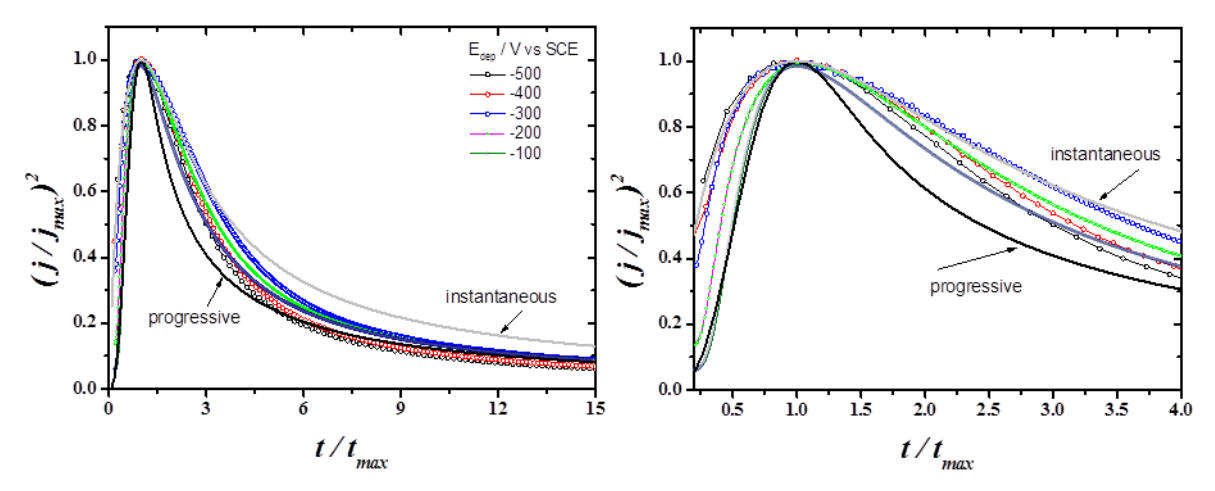


Figure 4-7 Normalised transients for the chronoamperograms shown in Figure 4-4 recorded in absence of surfactant are compared with theoretical transients for instantaneous (eq. 4-1) and progressive (eq. 4-2) nucleation for the different deposition potentials applied. On the left the whole current transients and on the right the current transients until 4 units of $t/t_{\rm max}$.

b) Deposition in the micellar phase

The corresponding fit of experimental data (2 wt. %) to the Scharifker and Hills model is presented in Figure 4-8. The current transient at high overpotentials (-500, -400 and -300) mV seem to follow instantaneous nucleation, while -200 mV cannot refer to any particular mechanism, it is located in between the two nucleation mechanisms. -100 mV is clearly following progressive before the peak rising.

After the peak -500 and -400 transform to follow instantaneous while the others follow progressive. Moreover, -500 and -400 mV appear to produce more current than expected thus suggesting the presence of another process is taking place, progressive nucleation mechanisms were obtained for long times (falling part).

The current transients in the presence of 10 wt.% surfactant are displayed in Figure 4-9. Before the peak, it appears that -500 mV, -400 mV and -300 mV follow instantaneous nucleation; while at -200 mV it is not possible to categorize the nucleation as instantaneous or progressive. The transient at -100 is progressive before the peak. After t_{max} this slightly changes with -500 mV remaining instantaneous while the others become progressive.

Cleary the -500 mV transients in 2 and 10 wt.% mixtures give more current than predicted by either forms of nucleation thus indicating that this extra current comes from extra processes.

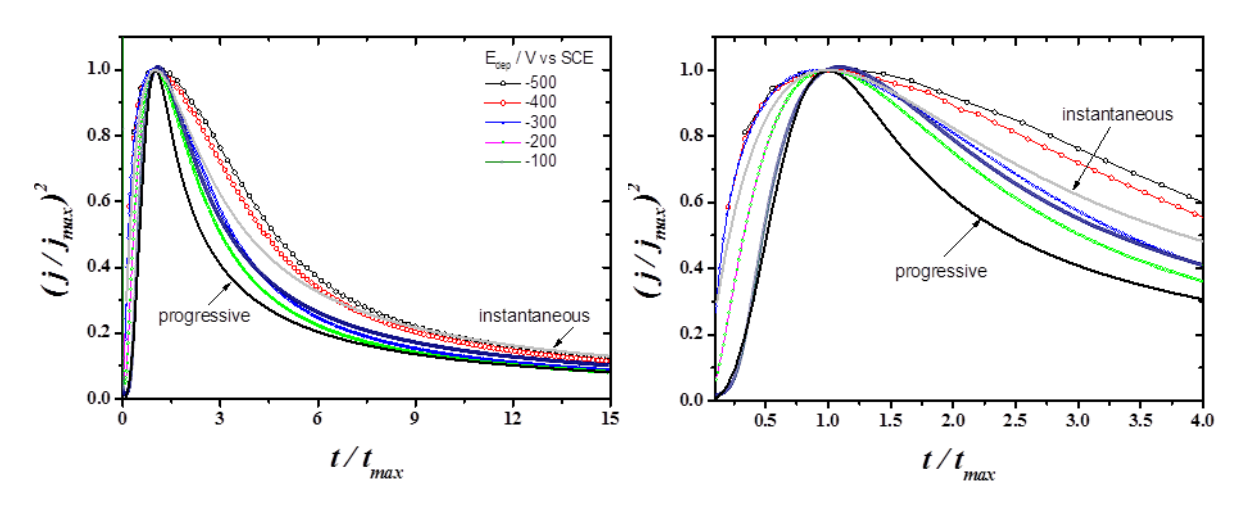


Figure 4-8 Normalised transients for the chronoamperograms shown in Figure 4-4 recorded in the 2 wt. % mixture are compared with theoretical transients for instantaneous (eq. 4-1) and progressive (eq. 4-2) nucleation for the different deposition potentials applied. On the left the whole current transients and on the right the current transients from 0 to 4 units of $t/t_{\rm max}$.

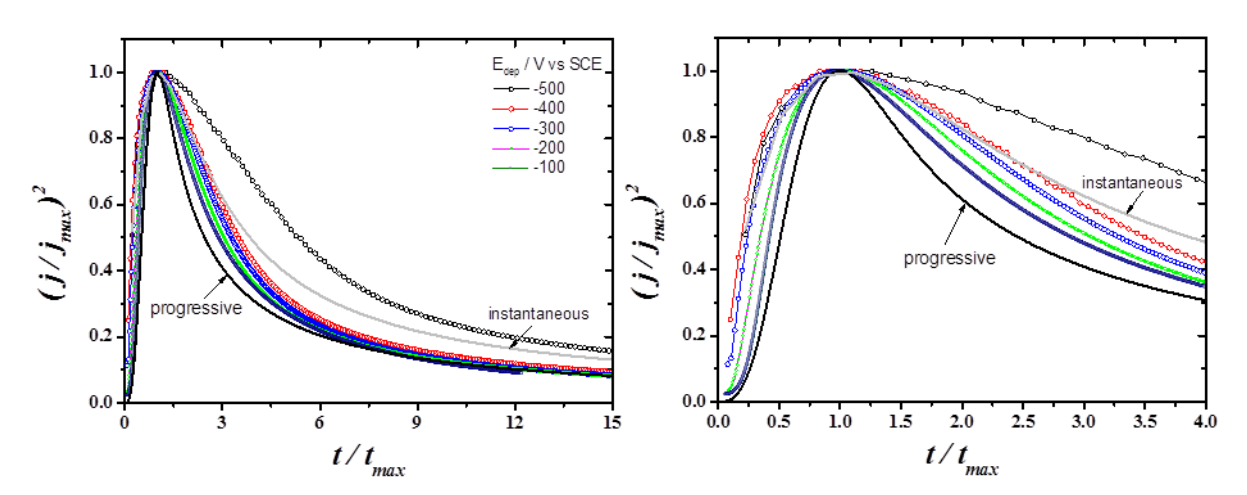


Figure 4-9 Normalised transients for the chronoamperograms shown in Figure 4-4 recorded in the 10 wt. % mixture are compared with theoretical transients for instantaneous (eq. 4-1) and progressive (eq. 4-2) nucleation for the different deposition potentials applied. On the left the whole current transients and on the right the current transient from 0 to 4 units of $t/t_{\rm max}$.

c) Deposition in the hexagonal phase

Figure 4-10 show the normalised transients for the 48 wt.% mixture. The transients at -500 mV and -400 mV are close to instantaneous before the t_{max} while -300 mV does not match any nucleation mechanism while -200 and -100 mV seem to follow progressive nucleation. After the peak it is clear that all potentials produce transients that follow progressive nucleation.

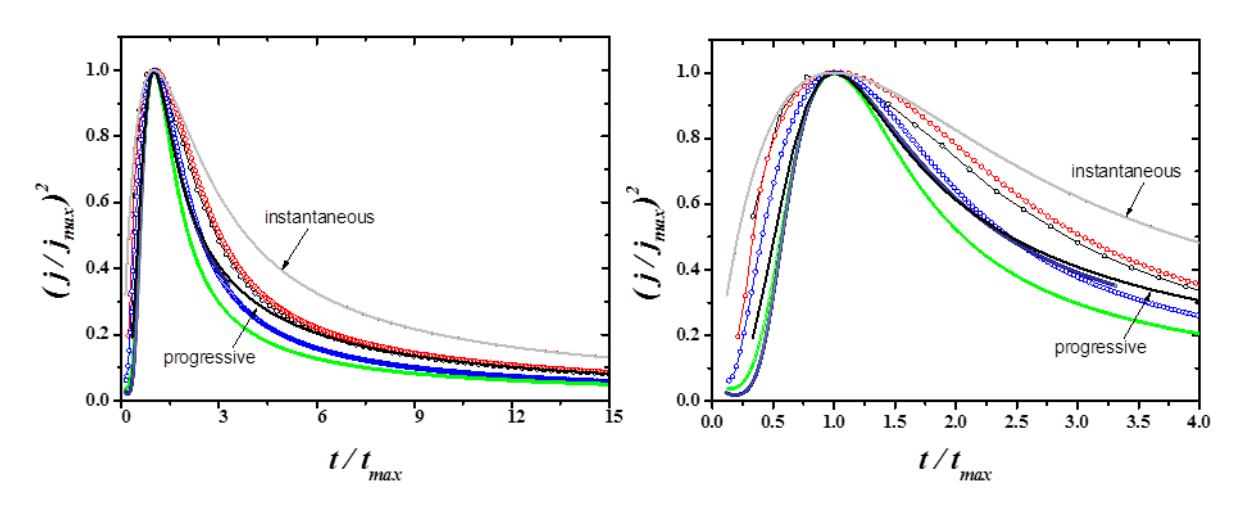


Figure 4-10 Normalised transients for the chronoamperograms shown in Figure 4-4 recorded in the 48 wt. % mixture are compared with theoretical transients for instantaneous (eq. 4-1) and progressive (eq. 4-2) nucleation for the different deposition potentials applied. On the left the whole current transients and on the right the current transient from 0 to 4 units of $t/t_{\rm max}$.

The analysis of the early stages of nucleation leads to two nucleation mechanisms. The two limited models are instantaneous and progressive three-dimensional nucleation with hemispherical diffusion-controlled growth of nuclei. In practice, as shown above, it is difficult to extract useful parameters from the SH model; it suffers from the requirement that progressive and instantaneous cases must be treated separately and cannot predict accurately the changes that occur at the transition from one nucleation type into the other. The SH model can just describe the limiting cases of instantaneous and progressive nucleations. Nevertheless, it is the method most largely used to compare experimental data obtained for different systems. Moreover, the two models are extreme cases which are unlikely to fully represent what happens in reality. For example it could be that progressive nucleation occurs on some parts of the electrode while instantaneous nucleation occurs elsewhere.

4.3.2 The Heerman-Tarallo model

All current transients were analysed using the model developed by Heerman and Tarallo, eq. 4-3 to 7.[164] According to these authors it is not necessary to classify the nucleation process as progressive or instantaneous to calculate the kinetic parameters.

$$i = nFA_{geo}DC(\pi Dt)^{-1/2} \frac{\phi}{\theta} \left[-\exp\left\{ -\alpha N_{\circ}(\pi Dt)^{\frac{1}{2}} t^{\frac{1}{2}} \theta \right\} \right]$$
 (4-3)

$$\phi = 1 - \frac{1 - \exp(-At)}{(At)^{1/2}} \int_0^{(At)^{1/2}} \exp(\lambda)^2 d\lambda$$
 (4-4)

$$\theta = 1 - \frac{1 - \exp(-At)}{At} \tag{4-5}$$

and

$$\alpha = 2\pi \left(\frac{2MDC}{\rho}\right)^{1/2} \tag{4-6}$$

where nF is the molar charge transferred during electrodeposition, C is the metal ion bulk concentration, M is the molar mass of the deposit, D is the diffusion coefficient, ρ is the density of the deposited material, A is the nucleation rate constant and N_o is the active site density. The function ϕ is directly related to the Dawson's integral [176] and reflects the retardation of the current by slow nucleation; θ on the other hand reflects the retardation of the growth of the coverage as a result of slow nucleation.[48,177,178] The function ϕ can be efficiently approximated with the polynomial shown in eq.4-7.[29,47,164,179]

$$F(x) = -x^2 \int_0^x \exp(\lambda)^2 d\lambda \cong \frac{0.051314213 + 0.47910725x}{1 - 1.2068142x \, b \, 1.185724x^2}$$
(4-7)

To extract the kinetics parameters, A and N° , the experimental transients were fitted to eq. 4-3 via non-linear regression having set n, F, A_{geo} , ρ , M and D as non-adjustable constants. Before fitting the current transients to the Heerman and Tarallo model, the diffusion coefficients were estimated by fitting the long-time end of the transients to the Cottrell equation. The transients are typical of three-dimensional growth controlled by the diffusion of electroactive species toward the electrode surface. At long times the current evolves according to the Cottrell eq. 4-8,[44]

$$j = \frac{nFD^{1/2}C}{\pi^{1/2}t^{1/2}} \tag{4-8}$$

To ensure the determination of D was not affected by the early stages of the deposition process the fit to the Cottrell equation was implemented on the falling part of the transients from $t=20 \times t_{max}$ till $t=\infty$, and D was estimated from the slope of j vs. $t^{-1/2}$ plots. Figure 4-11 shows an example of the linear relationship between the current density and $t^{-1/2}$ for the current transient recorded in the 0% mixture at -0.5 V vs. SCE. The diffusion coefficient of the Pd salt was estimated for all current transients in Figure 4-4.

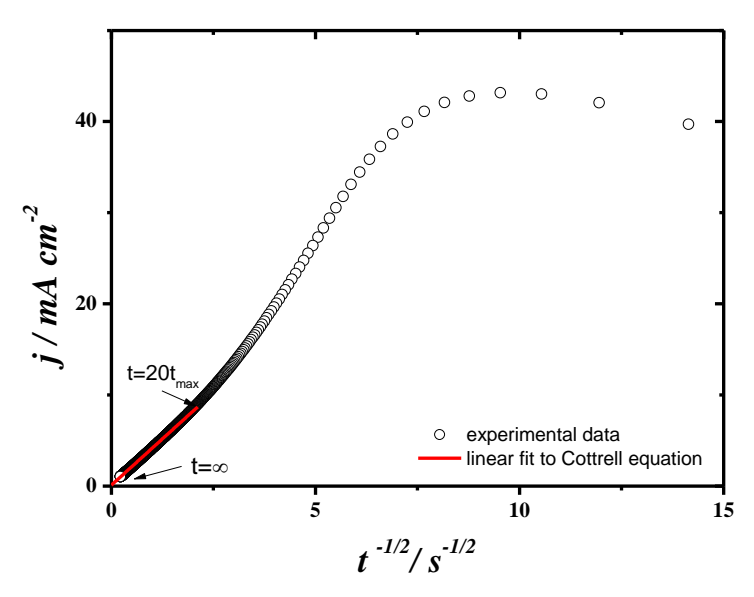


Figure 4-11 Typical chronoamperograms plotted as j vs $t^{1/2}$ to determine the diffusion coefficient for the Pd salt during the electrodeposition of Pd on a 3 mm \emptyset glassy carbon disc in 10 mM (NH₄)₂PdCl₄ + 0.5 M aerated KCl and 0 wt. % of C₁₆EO₈ after stepping from 0.7 V to -0.5 V vs SCE.

The D values change slightly when varying the deposition potential, table 4-3, but this is negligible compared to the decrease observed when the percentage weight of surfactant increases, Figure 4-12. This behaviour is thought to reflect the dependence of the diffusion coefficient on viscosity as shown by equation (4-9),

$$D = \frac{kT}{6\pi \eta \, r_{eff}} \tag{4-9}$$

where k is the Boltzmann constant, T temperature, η is the viscosity of the medium and r_{eff} is the radius of an effective sphere representing the ion; it is also known as the hydrodynamic radius, i.e. the radius of the solvated ion.[23] The D error bars obtained from the fit were far too small, of the order of 10^{-13} cm² s⁻¹, to be realistic. The viscosity of the fluid mixtures were measured by falling ball viscometer and their values are summarized in table 4-3, it is clear that the viscosity increases with increasing the concentration of surfactant. The falling sphere viscometer was not appropriate for such a viscous paste and the rotating disc viscometer was not available at the time the work was done.

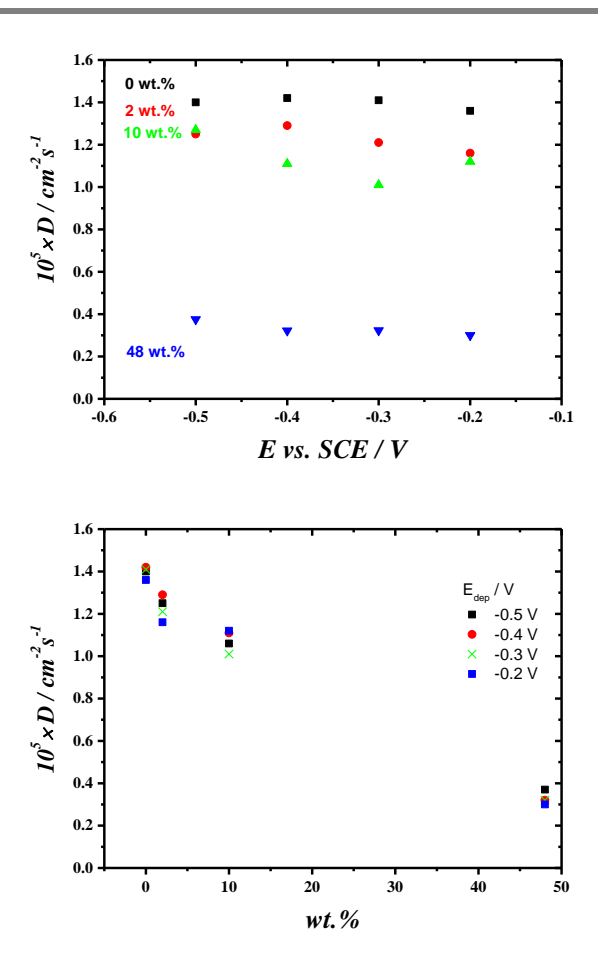


Figure 4-12 Dependence of the diffusion coefficient on the surfactant wt.% and deposition potentials. *D* was evaluated by fitting the transients for $t>20 \times t_{\text{max}}$ to the Cottrell equation.

Table 4-3 Summary of the *D* values evaluated by fitting the transients for $t>20\times t_{\text{max}}$ to the Cottrell equation. The fit was performed on chronoamperograms recorded with different deposition potentials.

wt.	u/an	$10^5 \times D / cm^2 s^{-1}$				
%	η/cp	-0.5 V	-0.4 V	-0.3 V	-0.2 V	
0	2.75	1.40	1.42	1.41	1.36	
2	3.85	1.25	1.29	1.21	1.16	
10	4.81	1.06	1.11	1.01	1.12	
48	ı	0.37	0.32	0.32	0.30	

Having determined *D* values for all cases, the transients were fitted to the H&T equation via non-linear regression in Origin. Each fit also yields the Reduced Chi-squared and Adjustable R-squared, two statistical parameters which come from the non-linear regression and give an indication of how good the fit is. The Reduced Chi-squared should be as small as possible while the Adjustable R-squared should be as close to 1 as possible. The Reduced Chi-squared is obtained by dividing the residual sum of squares (RSS) by the degrees of freedom (DOF). In statistics, the residual sum of squares (RSS)[180] is the sum of squares of residuals. It is also known as the sum of squared residuals

(SSR) or the sum of squared errors of prediction (SSE). It is a measure of the discrepancy between the data and an estimation model. A small RSS indicates a tight fit of the model to the data. Although this is the quantity that is minimized in the iteration process, this quantity is typically not a good measure to determine the goodness of fit. For example, if the y data is multiplied by a scaling factor, the Reduced Chi-squared will be scaled as well. A better measure would be the R-squared value, which is also known as coefficient of determination. The closer the fit is to the data points, the closer R-squared will be to the value of 1. A larger value of R-squared does not necessarily mean a better fit because the degrees of freedom can also affect the value, thus if more parameters are introduced, the R-squared value will rise, but this does not imply a better fit. The Adjusted R-squared value accounts for the degrees of freedom and this could be a better measure of the goodness of fit.

Looking at the current transients in Figure 4-4, it is clear that the peak current occurs at short times and the majority of the transient data points reflect the current after the peak yet the nucleation and growth kinetic information is reflected by the peak shape. So for this reason we tried different weightings to give more emphasis to the 200 or so data points which correspond to the peak out of the 20000 points in the whole transient. Some current transients at high overpotentials were very difficult to fit because of the very low number of data points before the peak.

Statistically it is more appropriate to analyse the experimental data with two or more weighting methods and decide which one is the most accurate. So the nonlinear fitting was done here with and without weighting to compare the fit results to a single dataset. The weighting is used when the measurement errors are unknown, w_i are set to 1 for all i (the index for a given data point), and the curve fitting is performed without weighting. However, when the experimental errors are known, we can treat these errors as weights and use weighted fitting.

The weights will be used in the procedure of reducing Chi-Square. There are a number of weighting methods available in Origin but here we will use no weighting which $w_i = 1$, instrumental, i.e. $w_i = 1/t_i$, and direct weighting which $w_i = t_i$ where t_i is the time for data point i.

1) No weighting, i.e. $w_i = 1$

This approach may not provide accurate values for A and N_o because it treats every data point in the same way and the majority of the data points recorded occur well after the peak. However the approach should yield D values in agreement with those obtained from the Cottrell equation. Figure 4-13 compares the experimental deposition transients with the theoretical ones derived from the Heerman and Tarallo theory. For each plating mixture and several deposition potentials the experimental transients were fitted to the theoretical models and the growth parameters, A and N_o were derived from the fit while keeping D fixed as their values had been previously extracted from the Cottrell analysis. The corresponding A and N_o values are included in Table 4-4.

In this approach no attempt was done to fit the current transients at -100 mV, because the method we follow to determine D values from Cottrell equation is to fit the current transient from $20 \times t_{max}$ to $t=\infty$, and with this transient $20 \times t_{max}$ is bigger than $t=\infty$.

2) Weighting

The current transients from Figure 4-4 were analysed with HT model using Origin software to fit the experimental data with the eq. 3. The weighting was used in order to obtain the fitting parameters with more accuracy. In this section we will discuss the effect of weighting on the fitting. In Origin software there is an option to specify the weighting methods. So, two methods of weighting were used as attempts to improve the fit and minimize the error estimate. The fitting results, Chi-squared and Adjustable R-squared which come from the non-linear regression were compared for both methods of weighting.

a) Instrumental weighting, i.e. $w_i = 1/t_i$

These weights emphasize the short-time part of the transients and so are expected to produce accurate values for the kinetic parameters since the peak carries the information about nucleation kinetics. In contrast this approach is not expected to yield accurate D values. After specifying the weighing (w_i) process. The initial data related to the charging current of the double layer was excluded. D here was set free to be determined from the fitting.

b) Direct weighting, i.e. $w_i = t_i$

Direct weighting was used to see if it could improve the fitting. As this weight emphasises the longtime data this approach is expected to give less accurate values for A and N_0 but accurate D values which should be in agreement with those determined with the Cottrell equation. All the transients in Figure 4-4 were fitted by direct weighting.

3) Analysis

Figure 4-13 compares the theoretical (non-linear fit to eq. 4-3) and experimental current transients for the nucleation and growth of Pd particles at different deposition potentials for all mixtures without weighting. All the current transients for 0 wt.% fit well at all deposition times, except the current transient at -200 mV which only fits well after 0.7 s.

The comparison of the experimental current transients for 2 wt.% with the theoretical curves generated by non-linear fitting of experimental data to eq. 4-3 is shown in Figure 4-13. It can be observed, that the model expressed by eq. 4-3 adequately accounts for the behaviour of all experimental transients. However, all the current transients did not fit well around the top of the peak; -500 and -300 mV fitted well at short time, -400 and -200 mV show poor fitting in the first data points. After the peak all transients fit well with the theoretical curves. For the 48 wt.% mixture all current transients fitted well at all parts of current transient except the current transient at -200 mV.

For each case considered, the kinetic parameters at different deposition potentials, obtained through the fitting process of the experimental transients are summarized in table 4-5.

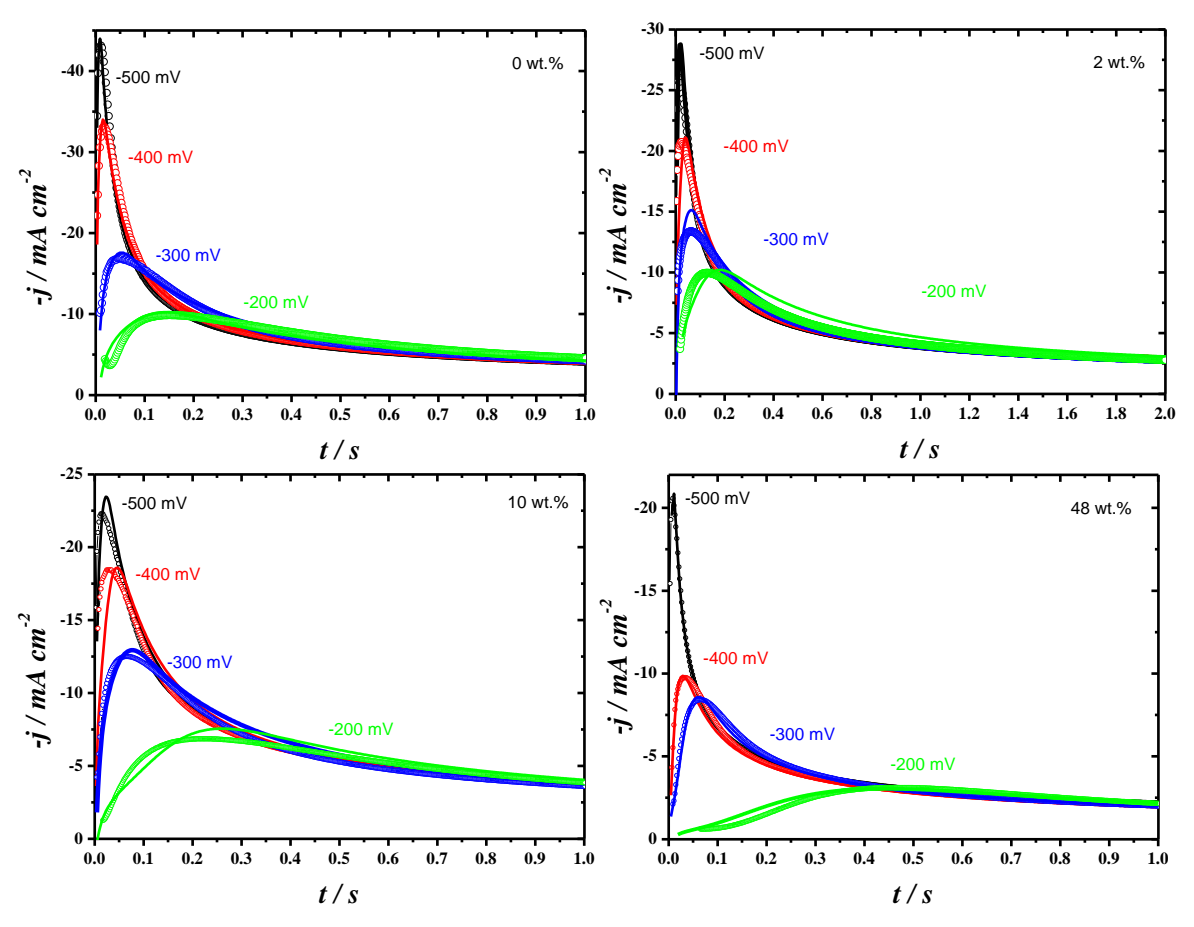


Figure 4-13 Theoretical (non-linear fit to eq. 4-3 without weighting), (\circ) and experimental (-) current transients for the nucleation and growth of Pd particles at different deposition potentials for all mixtures.

Figure 4-14 illustrates comparison between the experimental and theoretical current density transients for the deposition of Pd nanoparticles that were presented in Figure 4-4 using instrumental weighting. It is noticed that the peak shapes are fitted better than when fitting without weighting. This is because the instrumental weighting uses weights defined as $w_i=1/t_i$ so the data points at the beginning of the transients have more emphasis in the non-linear algorithm than those at longer times. In contrast, the falling part is not fitted well specially at high overpotentials, for example -500 and 400 mV; the fit is worse at long times because the $1/t_i$ weights give little emphasis to the long time data. The HT model has the correct Cottrell response at long times. The more negative E_{dep} is the more current can come from additional processes but the voltammograms in Figure 4-2 seem to indicate that this is more of a problem in the absence than in presence of surfactant. The extra current might include hydrogen insertion into Pd to form the alpha phase of Pd-H. All the fitting parameters with their standard error are summarized in tables 4-6.

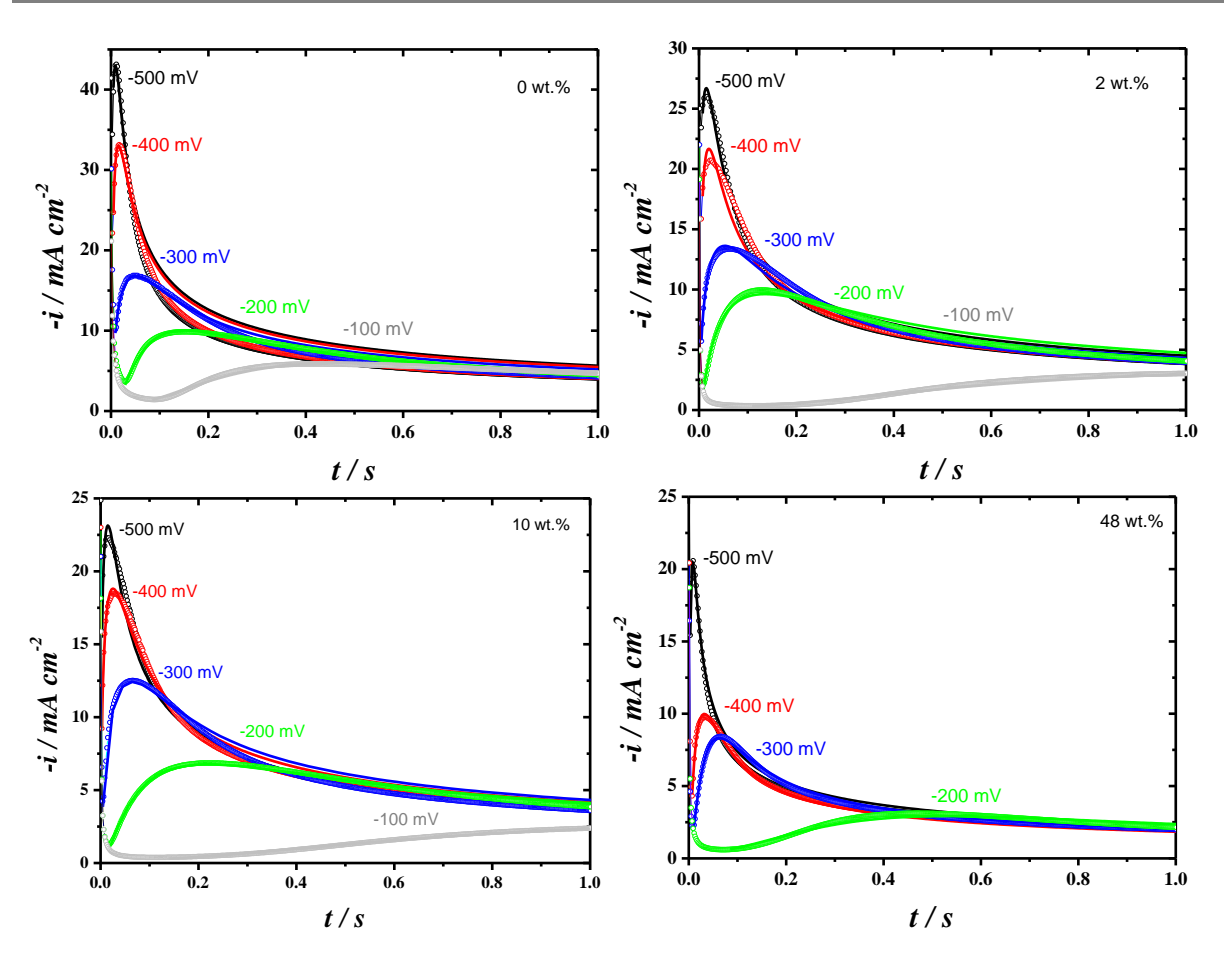


Figure 4-14 Theoretical (non-linear fit to eq. 4-3 with instrumental weighting (o) and experimental (—) current transients for the nucleation and growth of Pd particles at different deposition potentials for all mixtures.

The direct weighting method ($w_i = t_i$) was applied to fit all the transients in Figure 4-15. Most transients fitted well at all deposition times except -500, -400 and -300 mV in mixtures 2 wt.% and 10 wt.%.

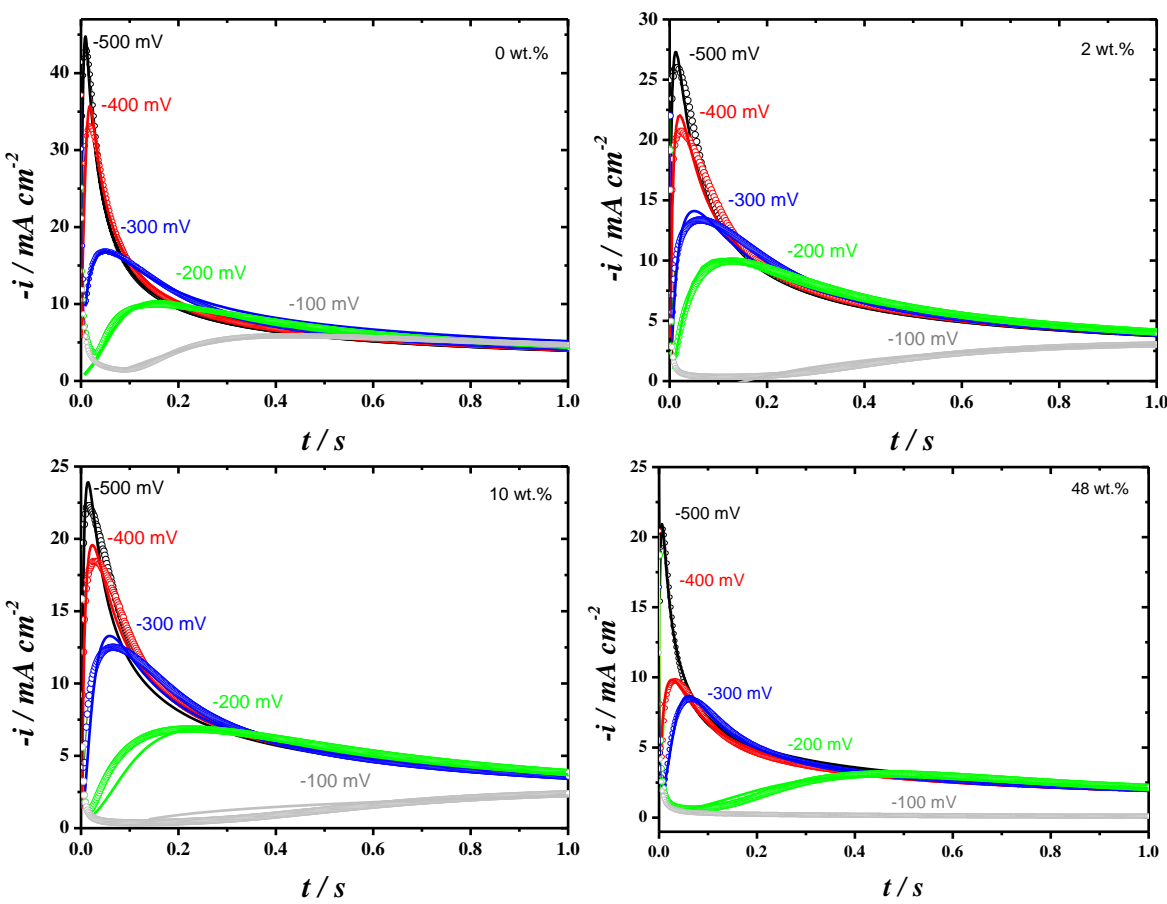


Figure 4-15 Theoretical (non linear fit to eq. 4-3) with direct weighting (\circ) and experimental (-) current transients for the nucleation and growth of Pd particles at different potential applied for all mixtures (as shown in Figures).

All the kinetic parameters A and N_o with their standard errors resulted from the fitting with HT without weighting present in table 4-4. Also the Reduced x^2 and adjustable R^2 that give an indication about the goodness of fitting are displayed in the tables.

Table 4-4 Kinetic parameters for the electrodeposition of Pd on glassy carbon obtained by fitting the experimental transients to the Heerman and Tarallo model, eq. 4-3 without weighting. Different deposition potentials were considered for each plating mixture.

		0 wt.%										
E/V	A/s^{-1}	Standard Error / s ⁻¹	N_o/cm^{-2}	Standard error / cm ⁻²	Reduced χ ²	Adj. R ²						
-0.5	42.0	0.3	5.9×10 ⁸	1.8×10 ⁶	9.6×10 ⁻¹¹	0.9955						
-0.4	26.6	0.2	3.3×10 ⁸	8.8×10 ⁵	6.4×10 ⁻¹¹	0.9970						
-0.3	6.0	0.1	9.2×10 ⁷	2.9×10 ⁵	8.3×10 ⁻¹¹	0.9943						
-0.2	3.2	0.0	4.4×10 ⁷	1.3×10 ⁵	7.2×10 ⁻¹¹	0.9913						

		2 wt.%										
E/V	A/s^{-1}			Standard error / cm ⁻²	Reduced χ ²	Adj. R ²						
-0.5	20.8	0.3	3.2×10 ⁸	1.5×10 ⁶	1.3×10 ⁻¹⁰	0.9917						
-0.4	14.0	0.2	1.3×10 ⁸	1.2×10 ⁶	1.5×10 ⁻¹⁰	0.9900						
-0.3	5.4	0.0	8.7×10 ⁷	3.0×10^{5}	1.2×10 ⁻¹⁰	0.9900						
-0.2	3.0	0.0	2.7×10 ⁷	7.9×10^4	4.3×10 ⁻¹¹	0.9953						

		10 wt.%										
E/V	A/s^{-1}	Standard Error / s ⁻¹	N_o / cm^{-2}	Standard error / cm ⁻²	Reduced χ ²	Adj. R ²						
-0.5	16.1	0.1	2.9×10 ⁸	9.9×10 ⁵	8.9×10 ⁻¹¹	0.9935						
-0.4	13.8	0.2	1.2×10 ⁸	1.1×10 ⁶	1.2×10 ⁻¹⁰	0.9903						
-0.3	5.3	0.1	8.5×10 ⁷	9.9×10 ⁵	7.2×10 ⁻¹¹	0.9921						
-0.2	2.9	0.0	2.1×10 ⁷	1.1×10 ⁵	1.4×10 ⁻¹¹	0.9900						

		48 wt.%										
E/V	A/s^{-1}	Standard Error / s ⁻¹	N_o / cm^{-2}	Standard error cm ⁻²	Reduced χ ²	Adj. R ²						
-0.5	195.8	1.8	5.6×10 ⁸	2.8×10 ⁶	1.8×10 ⁻¹¹	0.9963						
-0.4	121.0	1.4	1.4×10 ⁸	6.7×10 ⁵	2.5×10 ⁻¹¹	0.9922						
-0.3	21.0	0.1	1.6×10 ⁸	6.6×10 ⁵	6.7×10 ⁻¹²	0.9978						
-0.2	3.1	0.0	2.2×10 ⁷	1.4×10^{5}	1.4×10 ⁻¹¹	0.9900						

From table 4-4, the values for Adj R^2 and reduced χ^2 are considered good, since reduced χ^2 are very small and $Adj R^2$ are between $0.9900 \le Adj R^2 \le 0.9978$, so all values are close to one which reflects best fitting for most of the data point. Despite getting good values of Adj R^2 , they only reflected the good fitting for the data points of the falling part, and the most important part of the transient that has information for N_o and A refers to the peak.

It is clear from the tables that, at large overpotentials, both A and N_o decrease gradually from 0 to 2 to 10 wt.%. The values of A and N_o related to 48 wt. % are very large compared with other mixtures and deviate from the trend followed by the other mixtures. At 0.2 V A appears to be unaffected by the surfactant concentration, furthermore, the number of particles formed decreases with $E_{\rm dep}$ for all mixtures.

Table 4-5 summarizes all the parameters obtained when fitting with instrumental weighting. The Adj. R^2 values are between 0.9641 and 0.9955; they are not as good as the values found when fitting without weighting. However, those values give more emphasis to the short-time part of the transients and so are expected to produce more accurate values for the kinetic parameters since the peak carries the information about nucleation kinetics. The nucleation rate A at -500,-200 and -100 mV seems to decreases gradually from 0 to 2, 10 to 48 wt.%. In contrast the number of active sites N_o increases

from 0 to 2, 10 to 48 wt.%. All the values of standard error that come from the fitting in these tables are so small compared to their values, so the errors are meaningless in these tables.

Table 4-5 Kinetic parameters for the electrodeposition of Pd on glassy carbon obtained by fitting the experimental transients to the Heerman and Tarallo model with instrumental weighting. Different deposition potentials were considered for all mixtures.

		0 wt.%										
E/V	$D / cm^2 s^{-1} / cm^2 s^{-1}$	Standard Error	A/s^{-1}	Standard Error / s ⁻¹	N_o / cm^{-2}	Standard error / cm ⁻²	Reduced χ ²	Adj. R ²				
-0.5	2.7×10 ⁻⁵	5.2×10 ⁻⁸	4121.0	121.5	3.6×10 ⁷	1.4×10^{5}	8.4×10 ⁻⁸	0.9806				
-0.4	2.5×10 ⁻⁵	3.9×10 ⁻⁸	718.7	4.2	2.4×10 ⁷	7.6×10 ⁴	1.9×10 ⁻⁸	0.9878				
-0.3	2.3×10 ⁻⁵	4.9×10 ⁻⁸	391.1	2.7	7.8×10^6	3.2×10 ⁴	4.1×10 ⁻⁹	0.9822				
-0.2	1.8×10 ⁻⁵	3.2×10 ⁻⁸	25.4	0.0	4.6×10 ⁶	1.8×10^4	2.9×10 ⁻¹⁰	0.9939				
-0.1	1.5×10 ⁻⁵	7.0×10 ⁻⁸	4.1	0.0	2.6×10^6	3.4×10^4	1.3×10 ⁻¹⁰	0.9832				

		2 wt.%										
E / V	$D/cm^2 s^{-1}$	Standard Error / cm² s ⁻¹	A/s^{-1}	Standard Error / s ⁻¹	N_o / cm^{-2}	Standard error / cm ⁻²	Reduced χ ²	Adj. R ²				
-0.5	1.7×10 ⁻⁵	4.5×10 ⁻⁸	4098.0	614.5	3.4×10^7	1.9×10 ⁵	1.5×10 ⁻⁸	0.98145				
-0.4	1.4×10 ⁻⁵	1.9×10 ⁻⁸	753.0	52.9	3.2×10 ⁷	1.6×10 ⁵	6.3×10 ⁻¹¹	0.9955				
-0.3	1.6×10 ⁻⁵	2.9×10 ⁻⁸	647.3	2.6	1.0×10 ⁷	3.3×10 ⁴	2.3×10 ⁻⁹	0.9944				
-0.2	1.9×10 ⁻⁵	8.1×10 ⁻⁸	84.5	0.3	3.7×10^6	2.9×10^4	2.5×10 ⁻⁹	0.98625				
-0.1	1.4×10 ⁻⁵	7.4×10 ⁻⁸	1.8	0.0	7.8×10 ⁵	9.6×10 ³	2.7×10 ⁻¹¹	0.9856				

					10 wt.%			
E/V	$D/cm^2 s^{-1}$	Standard Error / cm² s⁻¹	A/s^{-1}	Standard Error / s ⁻¹	N_o / cm^{-2}	Standard error / cm ⁻²	Reduced χ ²	Adj. R ²
-0.5	1.3×10 ⁻⁵	3.4×10 ⁻⁸	3245.0	76.6	4.4×10^7	2.2×10 ⁵	3.7×10 ⁻⁸	0.9641
-0.4	1.4×10 ⁻⁵	1.9×10 ⁻⁸	1375.8	4.7	2.3×10 ⁷	5.3×10 ⁴	4.2×10 ⁻⁹	0.9935
-0.3	1.6×10 ⁻⁵	6.7×10 ⁻⁸	334.5	1.6	8.8×10^6	5.4×10 ⁵	8.9×10 ⁻⁹	0.9940
-0.2	1.4×10 ⁻⁵	4.1×10 ⁻⁸	29.8	0.0	3.4×10^6	1.9×10^4	3.1×10 ⁻¹⁰	0.9938
-0.1	1.3×10 ⁻⁵	4.0×10 ⁻⁸	1.6	0.0	6.9×10 ⁵	5.0×10^{3}	5.3×10 ⁻¹²	0.9943

		48 wt.%										
E/V	$D/cm^2 s^{-1}$	Standard Error	A/s^{-1}	Standard Error	N_o / cm^{-2}	Standard error	Reduced χ^2	Adj. R ²				
-0.5	4.6×10 ⁻⁶	3.8×10 ⁻⁹	764.9	1.5	2.9×10 ⁸	5.3×10 ⁵	4.2×10 ⁻⁹	0.9964				
-0.4	2.5×10 ⁻⁶	4.8×10 ⁻⁹	184.0	0.3	1.7×10 ⁸	6.3×10 ⁵	1.2×10 ⁻⁹	0.9935				
-0.3	2.7×10 ⁻⁶	7.9×10 ⁻⁹	67.2	0.2	9.4×10^7	5.4×10 ⁵	8.6×10 ⁻¹⁰	0.9940				
-0.2	3.6×10 ⁻⁶	1.9×10 ⁻⁹	3.1	0.0	1.2×10 ⁷	2.0×10 ⁵	6.3×10 ⁻¹¹	0.9700				

The data in tables 4-6 show that, the Adj R^2 values are close to one but reflected the good fitting of the falling part instead of the peak. Consequently, the kinetic parameters A and N_o values might not be realistic. Values were found quite large in the presence of surfactant especially at higher overpotential. Moreover, the number of active sites decreases when the surfactant is present in the

plating mixture and this fact can be found at all applied potentials. Interestingly, the micellar mixture has the lowest number of active sites. Both A and N_o increase dramatically with large overpotentials in all mixtures and this relation between the applied potential and A and N_o are in agreement with the published work.[177,179,181] The second observation is that the 2 wt.% mixture has the lowest number of nucleation sites and offers a high nucleation rate. In contrast, 0 wt.% has a higher number of active sites and lower nucleation rate.

Table 4-6 Kinetic parameters for the electrodeposition of Pd on glassy carbon obtained by fitting the experimental transients to the Heerman and Tarallo model with direct weighting. Different deposition potentials were considered for 0 wt.%.

				(0 wt.%			
E/V	$D/cm^2 s^{-1}$	Standard error / cm ² s ⁻¹	A/s^{-1}	Standard error / s ⁻¹	N_o / cm^{-2}	Standard error / cm ⁻²	Reduced χ^2	Adj. R ²
-0.5	1.4×10 ⁻⁵	1.1×10 ⁻⁷	45.9	2.6	5.6×10 ⁸	2.9×10^{7}	1.1×10 ⁻¹⁰	0.9925
-0.4	1.6×10 ⁻⁵	1.1×10 ⁻⁸	40.0	1.2	2.0×10^{8}	7.9×10^6	1.0×10 ⁻¹⁰	0.9884
-0.3	1.6×10 ⁻⁵	8.5×10 ⁻⁹	34.6	0.8	2.3×10 ⁷	3.6×10 ⁵	5.9×10 ⁻¹¹	0.9937
-0.2	1.6×10 ⁻⁵	7.8×10 ⁻⁹	14.0	0.2	7.2×10^6	5.7×10 ⁴	4.6×10 ⁻¹¹	0.9952
-0.1	1.6×10 ⁻⁵	4.9×10 ⁻⁹	5.3	0.0	2.1×10^6	5.7×10^3	1.4×10 ⁻¹¹	0.9986

				2	wt.%			
E/V	$D/cm^2 s^{-1}$	Standard error / cm ² s ⁻¹	A / s^{-1}	Standard error / s ⁻¹	N_o / cm^{-2}	Standard error / cm ⁻²	Reduced χ ²	Adj. R ²
-0.5	1.5×10 ⁻⁵	1.1×10 ⁻⁸	2021.7	1386.0	4.8×10 ⁷	1.6×10 ⁶	7.9×10 ⁻¹¹	0.9901
-0.4	1.4×10 ⁻⁵	7.0 ×10 ⁻⁹	434.3	61.0	3.4×10 ⁷	6.4×10^5	3.7×10 ⁻¹¹	0.9955
-0.3	1.4×10 ⁻⁵	7.7×10 ⁻⁹	157.9	13.0	1.4×10 ⁷	1.7×10^5	5.5×10 ⁻¹¹	0.9932
-0.2	1.4×10 ⁻⁵	8.6×10 ⁻⁹	49.2	2.0	7.4×10^6	7.2×10^4	6.6×10 ⁻¹¹	0.9917
-0.1	1.0×10 ⁻⁵	5.6×10 ⁻⁹	0.2	0.0	5.6×10^6	1.1×10^4	5.1×10 ⁻¹¹	0.9926

	10 wt.%								
E/V	$D/\text{cm}^2\text{s}^{-1}$	Standard error / cm ² s ⁻¹	A / s^{-1}	Standard error / s ⁻¹	N_o / cm ⁻²	Standard error / cm ⁻²	Reduced χ ²	Adj. R ²	
-0.5	1.1×10 ⁻⁵	1.0×10 ⁻⁸	437.0	88.0	7.6×10^7	3.3×10 ⁶	1.3×10 ⁻¹⁰	0.9848	
-0.4	1.2×10 ⁻⁵	6.3×10 ⁻⁹	295.2	29.0	3.6×10^7	6.3×10 ⁵	4.5×10 ⁻¹¹	0.9937	
-0.3	1.1×10 ⁻⁵	4.5×10 ⁻⁹	52.1	1.2	2.1×10^7	2.0×10 ⁵	2.3×10 ⁻¹¹	0.9966	
-0.2	1.1×10 ⁻⁵	3.4×10 ⁻⁹	9.3	0.0	6.9×10^6	2.8×10 ⁴	1.2×10 ⁻¹¹	0.9984	
-0.1	0.9×10 ⁻⁵	4.3×10 ⁻⁹	0.3	0.0	4.3×10 ⁶	1.1×10 ⁴	1.6×10 ⁻¹¹	0.9976	

	48 wt.%								
E/V	$D/cm^2 s^{-1}$	Standard error / cm ² s ⁻¹	A/s^{-1}	Standard error / s ⁻¹	N_o/cm^{-2}	Standard error / cm ⁻²	Reduced χ ²	Adj. R ²	
-0.5	0.4×10 ⁻⁵	2.0×10 ⁻⁹	600.0	68.5	3.1×10 ⁸	8.5×10 ⁶	1.3×10 ⁻¹¹	0.9948	
-0.4	0.4×10 ⁻⁵	1.9×10 ⁻⁹	400.0	57.7	9.4×10^7	1.5×10 ⁶	1.3×10 ⁻¹¹	0.9940	
-0.3	0.3×10 ⁻⁵	8.2×10 ⁻¹⁰	22.2	0.2	1.4×10^7	1.1×10^6	2.4×10 ⁻¹²	0.9989	
-0.2	0.3×10 ⁻⁵	2.0×10 ⁻⁹	3.2	0.0	2.2×10 ⁷	1.8×10 ⁵	1.1×10 ⁻¹¹	0.9940	
-0.1	0.2×10 ⁻⁵	9.8×10 ⁻⁹	0.2	0.0	1.7×10^6	3.0×10^4	1.8×10 ⁻¹¹	0.9669	

Figure 4-16 illustrates D values vs. applied potential for all mixtures by weighting methods. The D values come from instrumental weighting change slightly or remain constant when varying the deposition potential. The values from HT with instrumental weighting are significantly larger than those evaluated by Cottrell. Moreover, the D values from the fitting with direct weighting vary slightly or are unchanged when varying the deposition potential. Also we found the D values obtained by HT with direct weighting are in agreement with the values obtained from Cottrell. In contrast, in both weighting methods, the diffusion coefficient decreases as the percentage weight of surfactant increases. This behaviour is thought to reflect the dependence of the diffusion coefficient on viscosity as shown by equation 9.

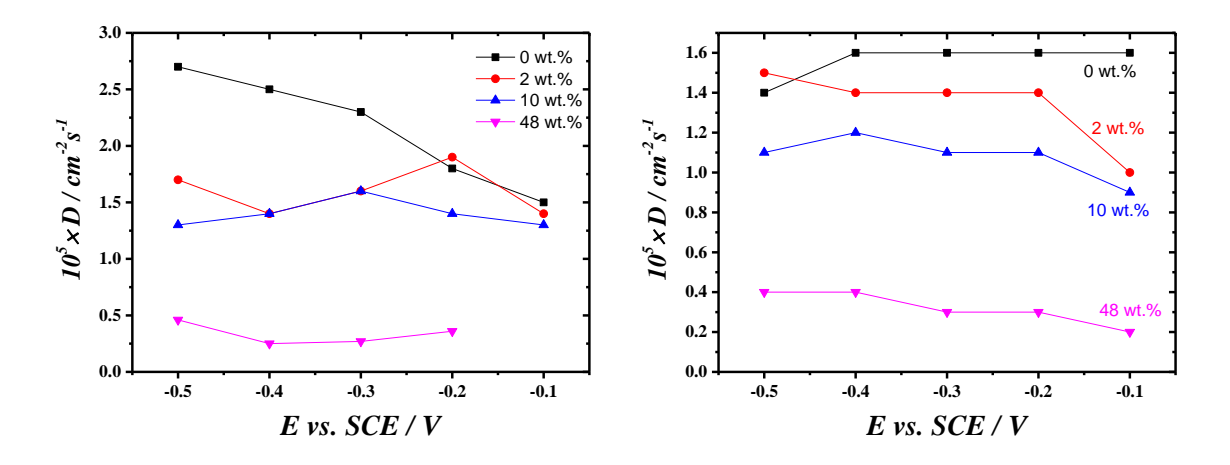


Figure 4-16 Plots of *D* values from tables 4-6 to 4-7 vs. deposition potentials for different concentrations of surfactant; on the left the *D* values were obtained with instrumental weighting and on the right with direct weighting.

After comparing the different weighting methods we could conclude that there are very large discrepancies between the results for the values of A and N_o obtained with different weights, with the instrumental weighting giving very large numbers for A and N_o compared with other weights. From the transient shape, the peak data points should give the more accurate fitting parameters for the nucleation and growth while the data points at long times should produce the best D values as the current at long time is under planar diffusion controlled. So fitting with no weights, w_i =1, treats all data points in the same way; since there are few data points $200\le$ over the peak and the rest of the data approximately 19800 data points on the falling part, it is a good method to determine D. Instrumental weighting, w_i =1/ t_i , offers a good determination for the nucleation and growth parameters but is worst for D. In contrast direct weighting, w_i = t_i , puts a strong emphasis on the long time which is good to obtain D values and worse to determine A and N_o . However, there was no consistency between the parameters obtained from the different weighting approaches; it seemed that the treatment with weighting made the analysis more difficult and made the values of the nucleation and growth parameters not reliable, so from this point we only analysed the dependence of A and N_o from the fits

carried out without weights. To facilitate the analysis of the kinetic parameters A and N_o from no weighting, the results were plotted first in terms of wt.% of surfactant and then in terms of E_{dep} as shown in Figures 4-17 and 4-18 respectively.

Figure 4-17, illustrates the relation between A and N_o and the wt.% of surfactant for the deposition potentials considered. The nucleation rate seems to decrease from 0 to 2 to 10 wt.% then surprisingly increases at 48wt.%, this is markedly noticed at -500 and -300 mV. Moreover, the number of nucleation sites decreases from 0 to 2 to 10 wt.% then significantly increases with 48wt. %. Except for the 48 wt.% mixture, the trends for A and N_o are reasonable. Figure 4-18 shows the nucleation rate at higher overpotential is larger for the 48wt.% mixture then the trend is considered acceptable, with A decreasing from 0 to 2 to 10 wt.%. Only one published work was found that studied the nucleation kinetics of mercury on platinum single crystal in presence and absence of a surfactant (sardonic dye), they found that both of the nucleation parameters A and N_o decreased in presence of surfactant.[182] At -0.5 V the nucleation rate A is lower than expected probably because this driving force is so large that the growth is now completely diffusion controlled and A becomes independent of E_{dep} . Although the HT model assumes that the growth is under diffusion control it seems applicable even if the growth is partly kinetically controlled. Although D is much lower in the 48% mixture the growth is much faster there than in the other mixtures. At lower overpotential, -200 mV, it seems that the nucleation rate is not affected by the amount of surfactant added into the deposition bath and at this potential the current is thought to be kinetically controlled. In terms of E_{dep} ; it can be seen that at high overpotential the number of active sites is higher in absence of surfactant, again here at lower overpotential it seems there is no effect of the amount of surfactant on the number of active sites. The strange behaviour for the 48 wt.% mixture might be attributed to the fact that the H_I phase is highly organised and the active sites are defined by the surfactant rods. In contrast the micellar phase will have a random distribution of micelles at the surface. Interestingly, the fact that all A values for the 48 wt.% mixture are greater than one suggests that nucleation is instantaneous since according to Heerman and Tarallo A << 0.1 is a limiting case analogous to progressive nucleation and A >> 1 to instantaneous nucleation.[47] It is probably true that the absolute values of N_o and A are in many cases not really as important as their relative variations when the experimental conditions are changed, for example by adding surfactant to the plating mixture. We could therefore conclude that with 48 wt.% the growth is definitely instantaneous since this mixture produces the largest A values.

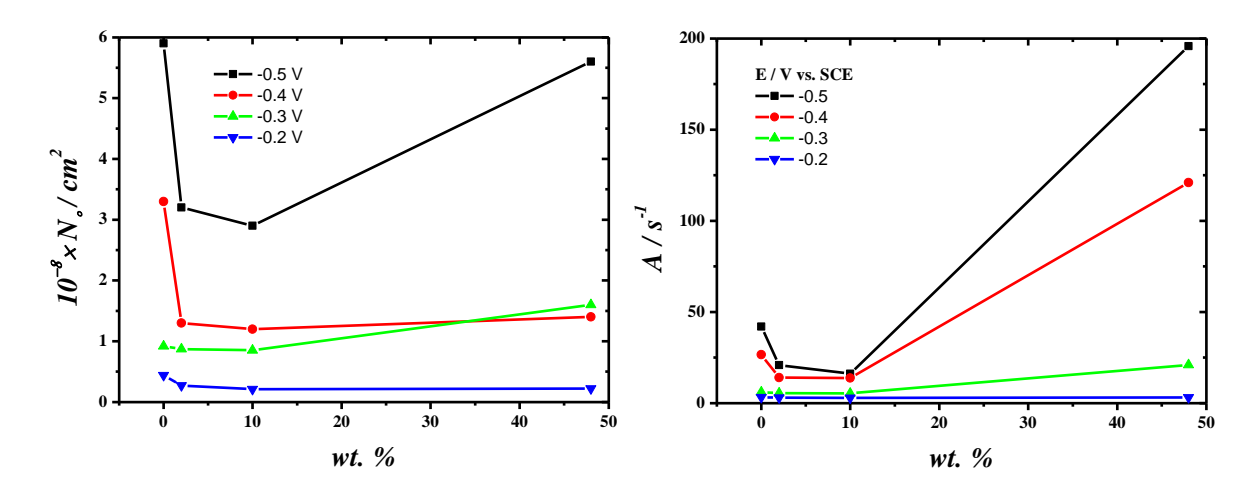


Figure 4-17 Plots of the kinetics parameters shown in Table 4-4 vs. wt. % of surfactant for the different deposition potentials.

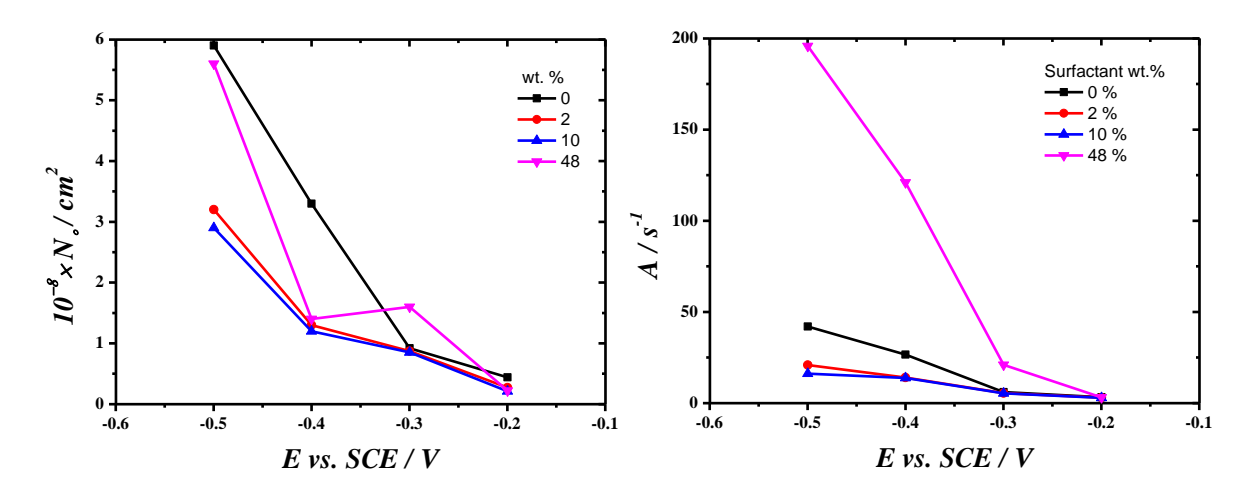


Figure 4-18 Plots of the kinetics parameters shown in Table 4-4 vs. the deposition potentials for the different concentrations of surfactant.

4.4 Conclusion

In summary, the very initial stages of the palladium electrodeposition process on GC from aerated 10 mM (NH_4)₂PdCl₄ + 0.5 M KCl with different concentrations of $C_{16}EO_8$ were analysed using CV and chronoamperometry. The high viscosity of the plating mixture leads to lower rates of diffusion and thus smaller plating currents. The analysis of the early stages of nucleation was done firstly with SH but it was difficult to extract useful parameters from the SH model as it treats progressive and instantaneous nucleation separately and cannot predict accurately the changes that occur at the transition from one nucleation type into the other. Secondly, the current transients from Figure 4-4 were analysed with the HT model using Origin software to fit the experimental data with to eq. 3. The set of transients for all mixtures were fitted with and without weighs. We found from the fitting that there were very large discrepancies between the results for the values of A and N_o obtained with different weights, with the instrumental weighting giving very large values for A and N_o compared

with other weights. The transients plotted in Figure 4-4 have 20000 data points, with fewer than 200 data points related to the peak that could give good indication about nucleation and growth information. The remaining data points (falling part) are accurate to determine values of diffusion coefficient. When comparing the result of fitting from different approaches, we found that the weighting methods give strange and unreliable values of A and N_o . So the analysis was made for the values that came from fits carried out without weighting. For all mixtures A and N_o were found to decrease when making the deposition potential more positive, in agreement with what we found in articles.

Moreover, A and N_o decrease from 0 to 2 to 10 wt.% and this trend is reasonable, interestingly that, once the concentration of surfactant is high to form the hexagonal phase, the A and N_o values become significantly higher, the reason is unknown, but might be attributed to the nucleation mechanism since all A values obtained for this mixture at different applied potentials are much greater than one, the second possibility, is the structure of hexagonal may play role to offer high nucleation rate and large numbers of active sites.

From the analysis we found that, except for the effect of viscosity on diffusion coefficient, there are no clear effects of the concentration of surfactant on the nucleation parameters. The current transients could be repeated with shorter deposition time to allow having more data points around the peak. Also, smaller working electrodes of glassy carbon could be used in order to reduce the contribution from charging current.

5. The unexpected activity of Pd nanoparticles prepared within a nonionic surfactant template

Metallic nanoparticles, particularly those of noble metals, are of considerable importance for their applications in catalysis and fuel cells. Fundamentally they are interesting for their unusual physical and chemical properties due to their size and shape.[4,5,14]

Generally, they owe their large catalytic activity per gram to their high surface area to volume ratio but often nanoparticles are facetted and the large proportion of surface atoms located on edges and corners further enhances their reactivity.[15] Here we report the electrochemical activity of surfaces with controlled size and dispersion of Pd nanoparticles obtained by electrodeposition from a palladium salt in presence of a molecular template consisting of self-assembled surfactant molecules. The nanoparticles were grown under potentiostatic conditions on glassy carbon (GC) substrates in different aqueous mixtures of octaethyleneglycol mono-hexadecyl ether (C₁₆EO₈), a non-ionic surfactant known to behave as a lyotropic liquid crystal and to form well characterised phases defined by the temperature and surfactant to water mass ratio.[3,99,183] The plating mixtures were chosen to investigate the influence of the surfactant micellar and hexagonal phases on the deposits. We used large overpotentials to operate under mass transfer control so as to produce particles. This approach differs from previous studies of Pd electrodeposition with a C₁₆EO₈ template which were conducted on metal substrates at low overpotentials so as to operate under kinetic control and grow uniform films, and specifically with the hexagonal phase to produce nanostructured films with well-defined tubular pores.[163,184-187] We controlled the nucleation and growth of the nanoparticles with the deposition potential and the amount of Pd formed with the charge passed during the deposition. A separate study was carried out to investigate the effect of the surfactant on the nucleation and growth of the Pd nanoparticles. In the next sections we report the preparation and characterisation of the modified GC and HOPG electrodes. Scanning electron microscopy, voltammetry and chronoamperometry were used to investigate the palladium centres. The particle size, electroactive area and roughness factor were estimated. The electrocatalytic activity of the particles was assessed by voltammetry using the oxidation of ethanol and formic acid, the evolution of hydrogen and oxygen and the reduction of oxygen as test reactions. Overall we find that the electrochemical activity of the nanoparticles depends on the presence of the surfactant template during preparation of the deposits and on the amount of surfactant used. We also show that deposits prepared with the surfactant template are significantly more active than expected from their electroactive area.

5.1 Pd electrodeposition from lyotropic liquid crystals mixtures

The electrodeposition of Pd is systematically affected by the amount of surfactant present in the plating mixture as shown on the cyclic voltammograms recorded at GC electrodes in each of the plating mixtures, Figure 5-1.

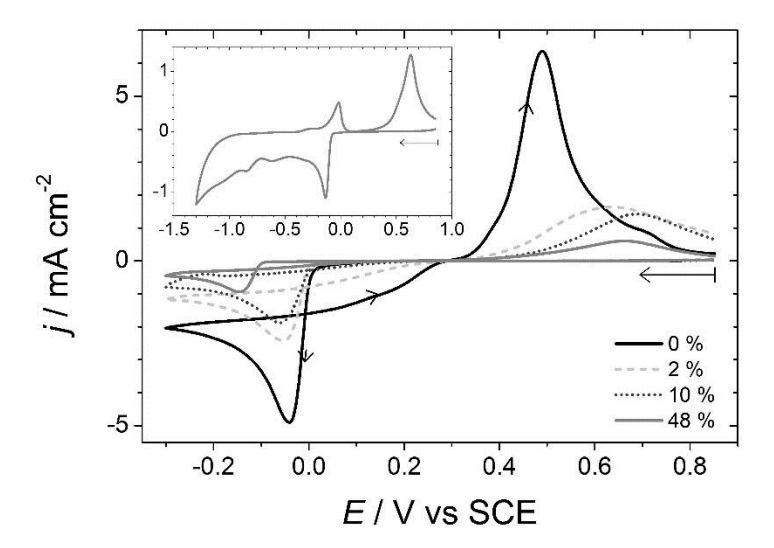


Figure 5-1 Cyclic voltammograms recorded at 10 mV s⁻¹ on 3 mm Ø glassy carbon discs in aerated 10 mM $(NH_4)_2PdCl_4 + 0.5$ M KCl with 0, 2, 10 and 48 wt. % of $C_{16}EO_8$ as indicated by the legend. The insert shows the voltammogram recorded in the 48% mixture when reversing the sweep at -1.3 V

These voltammograms were recorded not to produce deposits but solely for diagnostic purposes. For each mixture they have the characteristic features for the plating of a metal on a foreign substrate namely a deposition wave showing a clear nucleation loop and a stripping peak for the removal of the metal from the surface. Increasing surfactant concentrations require a greater overpotential to deposit the Pd as illustrated by the pronounced shift of the deposition wave towards negative potentials for the 48% mixture. This is thought to reflect the adsorption of surfactant on the substrate. The peak current for the deposition decreases when going from no surfactant to the micellar phase then to the hexagonal phase and this reflects the lower rate of mass transport arising from the increasing viscosity of the mixture. As shown in the insert of Figure 5-1 the characteristic voltammetric features of Pd, peaks for hydrogen adsorption, absorption and extraction (small stripping peak circa -0.1 V) are observed when taking the lower reversal potentials to -1.3 V but are suppressed with increasing surfactant content. Similarly the stripping peak is much smaller in presence of surfactant thereby indicating that a smaller amount of Pd is deposited during the potential scan.

To assess the electrochemical activity of the modified electrodes Pd was electrodeposited by stepping from +0.7 V vs. SCE, a potential sufficiently positive to ensure no Pd would remain on the surface, to -0.3 V vs. SCE, a potential sufficiently negative that plating would occur even with the most concentrated surfactant mixture and also sufficiently negative to ensure that growth would be mass transport controlled. For all mixtures the deposition was stopped when the charge reached 63.7 mC cm⁻², a value such that the largest deposits found on the edges of the electrodes were never bigger than a few micrometres (edge effects at the GC-

glass boundary lead to higher current densities and produce larger particles than in the centre of the electrode). The resulting chronoamperograms have the characteristic shape for an electrochemically driven, diffusion controlled (the current is proportional to $t^{-1/2}$ at long times), nucleation and growth process as illustrated in Figure 5-2 for the 0% mixture. The current transients were systematically analysed to assess the influence of the surfactant template on the nucleation and growth parameters (see chapter 4).

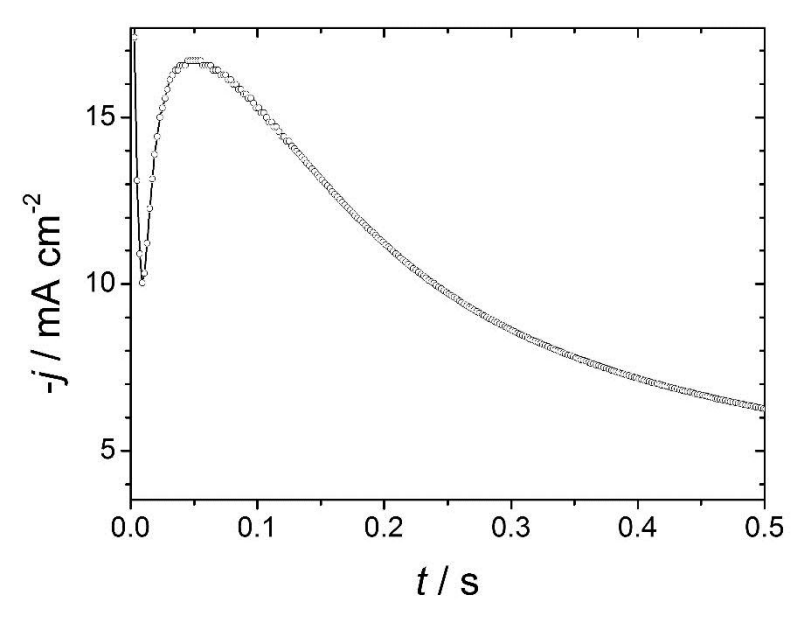


Figure 5-2 Current transient recorded at -0.3 V vs. SCE with a 3 mm \emptyset glassy carbon disc in aerated 10 mM (NH₄)₂PdCl₄ + 0.5 M KCl without surfactant.

After the potential steps the deposits formed were easily seen by eye as a dull grey coating. The deposits prepared with the surfactant template were found to be mechanically stable as they remained on the GC after rubbing against a clean polishing cloth; the 48% deposit was unaffected by rubbing while the 2 and 10% deposits lost circa a quarter of their activity. In contrast the deposit formed without surfactant was removed by rubbing. All deposits retained their electrochemical activity over several weeks. Figure 5-3 shows typical SEM images of the Pd deposits observed in regions unaffected by edge effects and free from obvious defects (visible defects in the GC generally produced micrometre size deposits) for each of the plating solutions considered. In absence of surfactant, Figure 5-3a, Pd is deposited as a very dense monolayer of agglomerates with a size averaging circa 100 nm. These appear to be formed of smaller clusters, typically 25 nm and below, some of which are found on the GC electrode in between the agglomerates. However zooming on the deposits reveals they consist of particles circa 11±3 nm in diameter. With 2 wt. % of surfactant, Figure 5-3b, a very dense monolayer of smaller Pd aggregates, with sizes ranging from sub 25 nm clusters to 100 nm aggregates, is found. Gaps between agglomerates are smaller than in absence of surfactant and it is difficult

to observe the surface of the GC substrate. While this low concentration of surfactant retains the granular texture of the deposit it clearly improves the Pd coverage. Zooming on the Figure reveals that the aggregates consist of particles circa 6±3 nm in diameter. The 10% mixture produces deposits with a very different, almost scaly, texture, Figure 5-3c. Pd is deposited as one or two layers of large flakes, several hundred nm across, randomly distributed over smaller aggregates. Voids reaching 100 nm in size can be seen between the deposits. The flakes and aggregates beneath consist of particles circa 7±3 nm in diameter. In contrast the 48% mixture produces a monolayer of circa 100 nm diameter joined up granular aggregates which appear to align along parallel rows, Figure 5-3d. 100 nm wide voids can be seen in several places indicating a lower coverage of the GC substrate compared to the previous mixtures. Zooming also reveals the aggregates consist of particles circa 9±3 nm in diameter. All mixtures therefore produce porous deposits with aggregated particles averaging 9 nm in diameter but these particles appear more distinct with the 10% mixture. In addition, it is unlikely that the 9 nm centres produced from the hexagonal phase can have a nanotubular structure with a repeat of circa 6 nm as identified with continuous layers deposited on Pt substrates.[163]

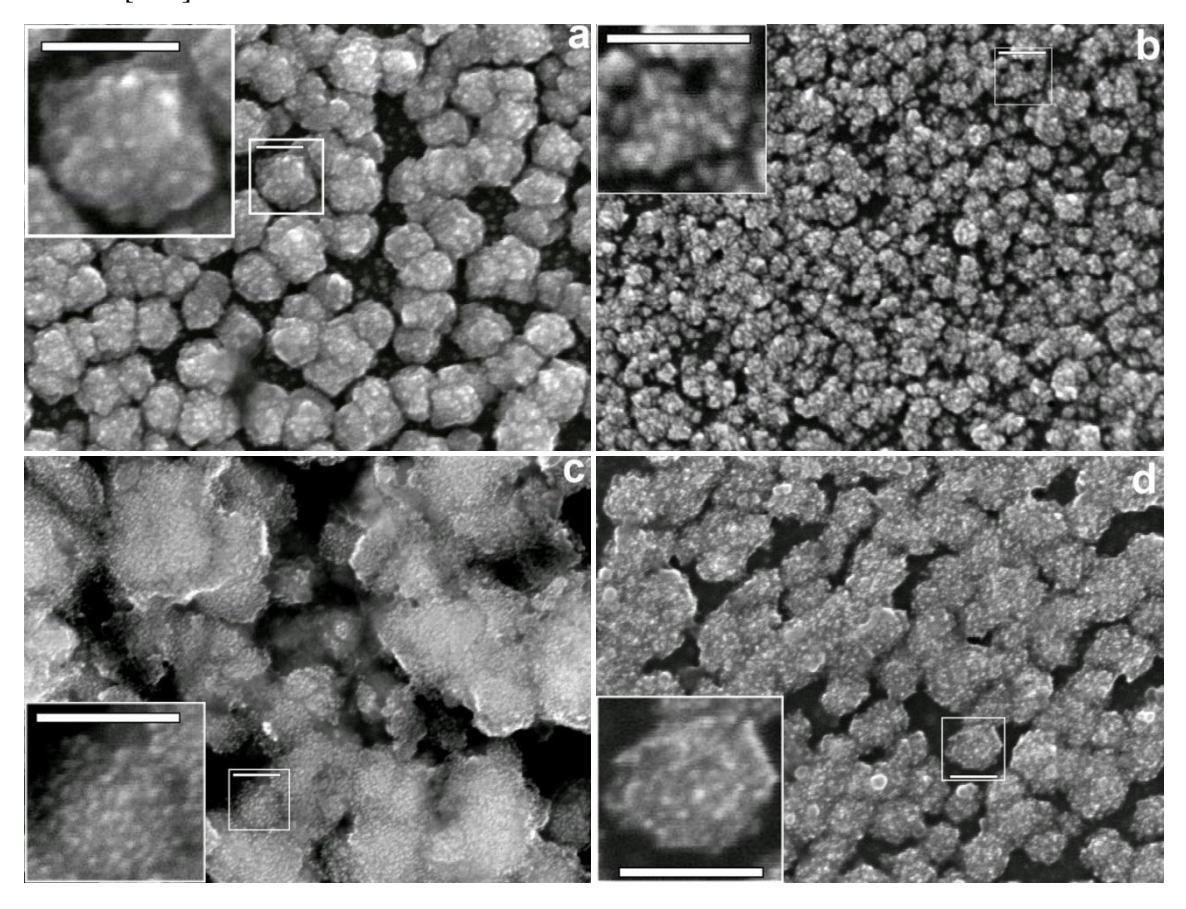


Figure 5-3 FEG-SEM images of Pd structures electrodeposited on GC after stepping from +0.7 V to -0.3 V vs. SCE for a 63.7 mC cm⁻² deposition charge. a) 0, b) 2, c) 10, and d) 48 wt. % surfactant. In all cases the scale bar is 100 nm long.

Helium ion microscopy (HIM), was then used to reveal more information than that obtained with FEG-SEM images. The same region scanned by FEG-SEM was also imaged by HIM (not shown) and the size of particles compared well with that from FEG-SEM images. The HIM images in Figure 5-4 show different regions on the electrodes, the deposits consist of a network of coalesced and the deposits have very clear porous structures for the films prepared with the 10 and 48 wt.% mixtures. The deposit from 10 wt.% certainly has pores smaller than 5 nm and the pores appear more uniform than those produced by the 48 wt.% mixture. For the 48 wt.% mixture pores range between 14 and 3 nm. The resolution of the HIM image for the 0 wt.% deposit was not as good, but it shows holes ranging between 29 and 9 nm. The deposit from the 2 wt.% micellar solution shows pores ranging between 26 and 10 nm. Here the HIM images could explain the high electroactivity obtained from the deposits produced from 10 wt.%.

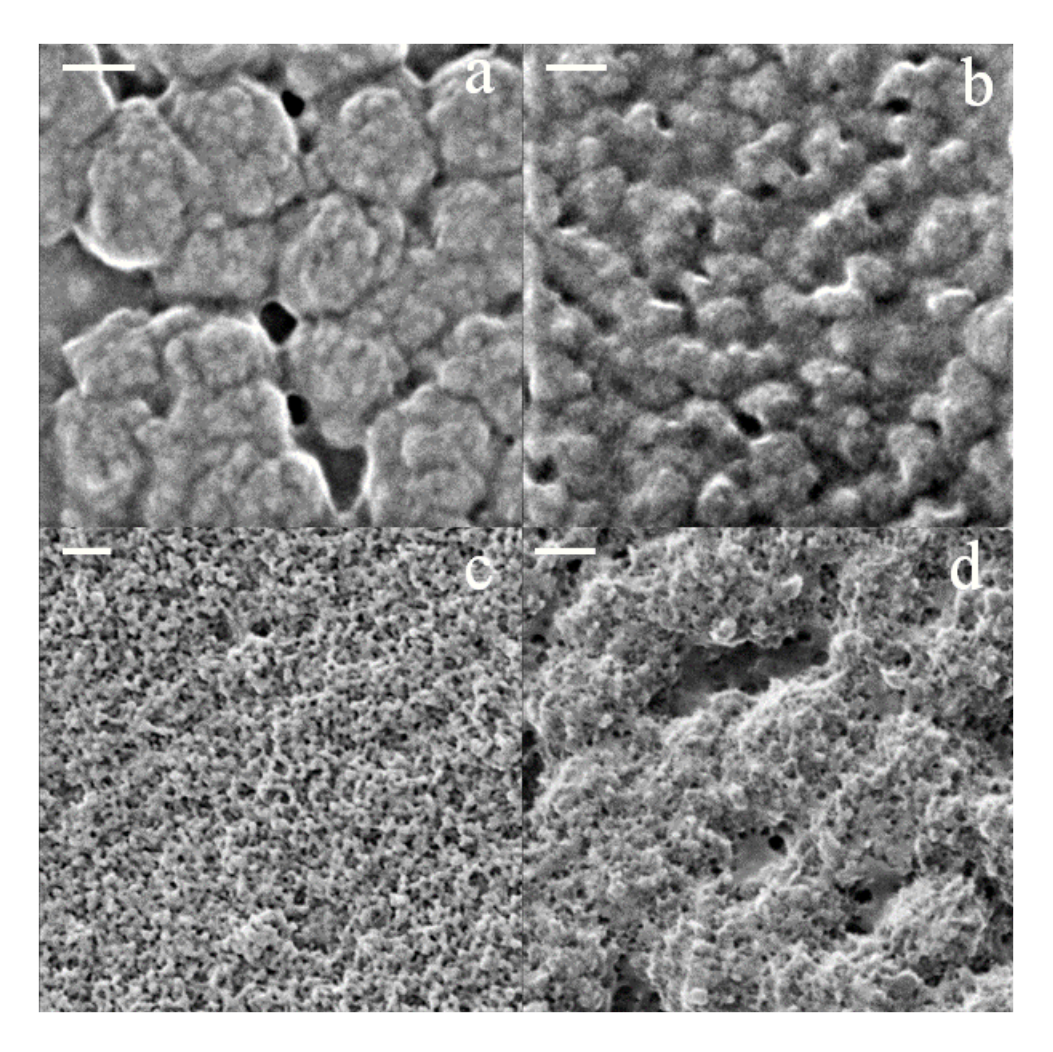


Figure 5-4 He ion microscopy images of Pd structures electrodeposited on GC after stepping from +0.7 V to -0.3 V vs. SCE for a 63.7 mC cm⁻² deposition charge. a) 0, b) 2, c) 10, and d) 48 wt. % surfactant. In all cases the scale bar is 50 nm long.

The deposits were further analysed by X-ray diffraction using a SmartLab X-ray diffractometer (Rikagu), with a Cu Kα radiation. The XRD patterns of palladium nanoparticles formed with the 10 and 48 wt.% mixtures are shown in Figure 5-5. The peaks observed at 40°, 46° and 68° are respectively assigned to diffraction from the (111), (200) and (220) planes of Pd. The XRD patterns were then compared with standards from the (ICSD) inorganic crystal structure database and this confirmed that the palladium is a cubic (fcc) crystal structure, in agreement with earlier reports.[52,188] The highest peak at 43° is assigned to C from the GC substrate. An attempt was made to estimate the crystallite size of the palladium using the broadening profile of the (111) peak at 40° but the presence of the C peak nearby made this analysis difficult and the calculated crystallite size, 1.3±0.9 nm for the film prepared with the 10 wt.% mixture, is surprisingly much smaller than the particles observed by FEG-SEM and HIM.

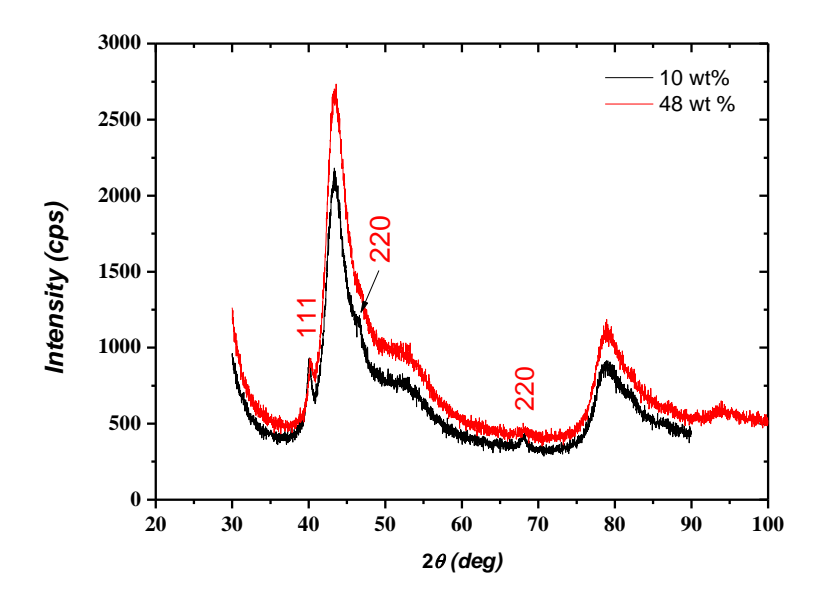


Figure 5-5 XRD patterns of palladium nanoparticles electrodeposited on GC after stepping from +0.7 V to -0.3 V vs. SCE for a 63.7 mC cm⁻² deposition charge.

5.2 Characterization by voltammetry in acid

The palladium deposits were characterised by voltammetry in 1 M sulphuric acid, Figure 5-6. Irrespective of the plating mixture used the GC electrodes produce voltammograms consistent with polycrystalline Pd electrodes in acids.[189] The following characteristic voltammetric signatures are observed: a) the double layer region, b) waves for the formation of Pd oxides, c) a peak for the stripping of Pd oxides, d) a peak for the adsorption of H on the Pd, e) a shoulder for the absorption of H to form the α -Pd hydride phase, f) a peak for the absorption of H to form the β -Pd hydride phase, g) a peak for the extraction of H from the β -Pd hydride, h) a shoulder for the extraction of H from the α -Pd hydride and i) a peak for the desorption of H from the Pd surface. These features are significantly influenced by the amount of surfactant present in the plating mixture.

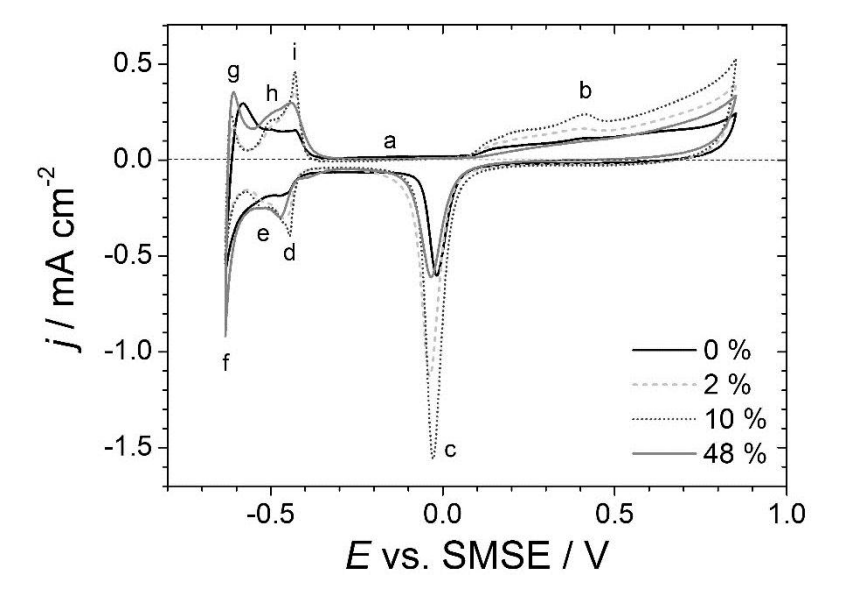


Figure 5-6 Voltammograms (5th cycle) recorded in 1 M $\rm H_2SO_4$ at 20 mV s⁻¹ with 3 mm Ø glassy carbon discs decorated with Pd structures electrodeposited by stepping the potential from +0.7 V to -0.3 V vs. SCE up to a 63.7 mC cm⁻² deposition charge. The legend indicates the corresponding plating mixtures. a) double layer region, b) oxide formation, c) oxide stripping, d) H adsorption, e) H absorption to form α-PdH, f) H absorption to form β-PdH, g) H extraction from β-PdH, h) H extraction from α-PdH, i) H desorption.

The 0 and 48% mixtures present similar voltammetric features with broadly identical peak positions, shapes and magnitudes. In contrast the 2 and 10% mixtures present more resolved peaks in the hydrogen region and significantly more current in the oxide region. The oxide stripping peak current increases systematically from 0 to 2 to 10 wt. % surfactant but decreases significantly for 48 wt. % to a level comparable to the 0 wt. % mixture. The trend is consistent with the morphology of the deposits observed by SEM, Figure 5-3, with the deposits becoming more divided when going from the 0% to 2 and 10% mixtures but recovering a granular texture similar to the 0% mixture when prepared with 48 wt. % surfactant.

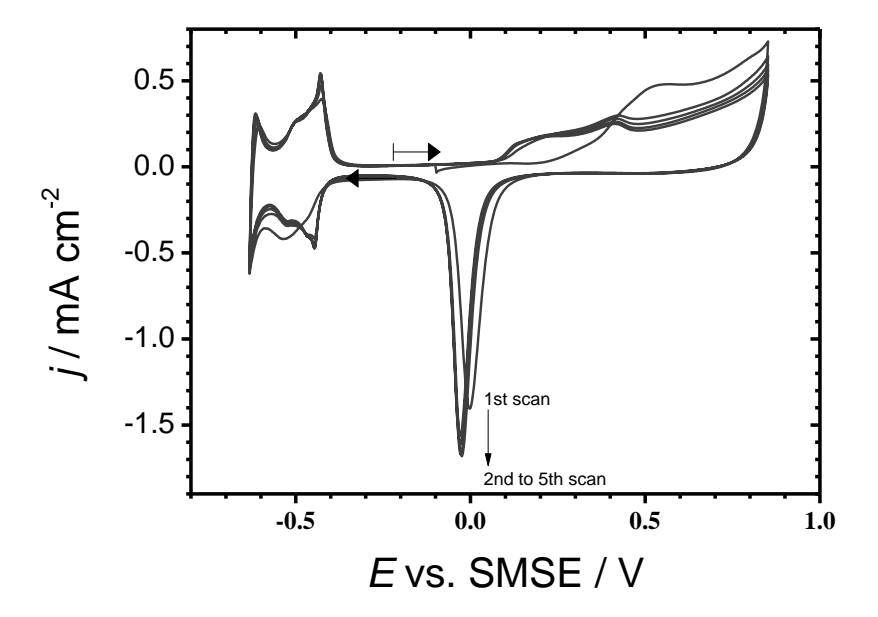


Figure 5-7 Voltammograms (first 5 cycles) recorded in 1 M H_2SO_4 at 20 mV s⁻¹ with 3 mm Ø glassy carbon disc decorated with Pd structures electrodeposited by stepping the potential from +0.7 V to -0.3 V vs. SCE up to a 63.7 mC cm⁻² deposition charge. The deposition conditions were as shown in figure 5-6

Figure 5-7 shows a set of voltammograms for the Pd modified GC disc electrodes in 1 M sulphuric acid solution at $20~\text{mV}~\text{s}^{-1}$ vs SMSE. The film was soaked in water for a day after deposition to remove the surfactant, with regular replacement of the water. On the reverse scan, the reduction of the formed surface oxide gives rise to a well-defined peak at -0.05 V vs SMSE which will be used to calculate the charge and therefore the surface area.

The peak height for the reduction of the Pd surface oxide increases with each successive cycle. This happens because the surfactant is not completely removed from the electrode surface even after soaking in water. As a consequence the electrochemically active surface area in contact with the acid solution increases and this leads to the increase of the charge associated to the removal of the surface oxide layer. Very little change was observed beyond the 5th cycle; it was therefore used for the calculation of the Pd oxide reduction charge.

The area under each voltammetric peak in figure 5-6 represents the charge involved in the corresponding redox process and can be used to determine the electroactive area. The latter was calculated from the oxide stripping peak after subtraction of the charge for the rearrangement of the double layer and using a conversion factor of $424 \,\mu\text{C} \,\text{cm}^{-2}$, the charge corresponding to the adsorption of a monolayer of Pd oxide.[190,191] This data is summarised in Table 5-1 for the four plating mixtures. To have a monolayer of PdO the upper reversal potential was chosen to be 0.85 V vs SMSE, according to the article by Rand and Woods.[190,191] Jerkiewicz et al.[192] also discuss the formation of oxide monolayers on palladium in acid however, their films were grown by potential

steps rather than potential sweeps. They assumed that PdO mainly forms when 0.95 V \leq E \leq 1.40 V vs RHE while for 1.40 V \leq E \leq 1.80 V vs RHE they concluded that PdO₂ was formed on top of the PdO layer.

Table 5-1 Dependence of the Pd oxide stripping charge, Q_{Pd} , roughness factor, R_f and specific area, S on the amount of surfactant present in the plating template. * evaluated from the voltammograms in Figure 5-6. The results presented in the table refer to a single experiment response for each mixture.

C ₁₆ EO ₈ wt.%	Q_{Pd}^{*} / mC cm $^{-2}$	R_f	$S / m^2 g^{-1}$
0	1.87	4	12.7
2	4.13	10	28.0
10	4.98	12	33.8
48	2.57	6	17.5

The specific area was calculated from the mass of Pd deposited assuming 100% Faradaic efficiency. Although oxygen reduction occurs during plating the concentration of oxygen, typically 230 μ M for a 0.5 M KCl solution at room temperature is sufficiently small compared to that of the Pd salt to neglect its influence on the plating efficiency. Even in the very viscous hexagonal phase the plating efficiency of Pd was reported to be between 95 and 98% from electrochemical quartz microbalance experiments. [163]

Even the deposit from 0% surfactant is rough and the presence of surfactant increases the roughness further. Overall the micellar phase yields electroactive areas slightly larger than the hexagonal phase (48%) or the plating solution without surfactant (0%). The 10% mixture offers the largest electroactive area with a corresponding specific area reaching circa 34 m² g⁻¹. In the following sections we examine the electrocatalytic activity of the Pd deposits using the oxidation of formic acid and ethanol, the evolution of hydrogen and oxygen and the reduction of oxygen as test reactions. These processes are central to the development of fuel cells and electrolyzers and their kinetics is known to be very sensitive to the availability and reactivity of the electrocatalysts.

5.3 Electrocatalytic activity:

5.3.1 Oxidation of formic acid and ethanol

Voltammograms for the oxidation of formic acid recorded with the Pd modified GC electrodes are shown in Figure 5-7. GC itself shows no activity in sulphuric acid. Interestingly the Pd deposit prepared without surfactant only shows a small peak around +0.05 V on the forward scan. In contrast deposits prepared with surfactant present the small peak circa +0.05 V followed by a much larger peak between +0.2 and +0.3 V and a shoulder around +0.6 V. For these deposits, the small peak was found to disappear on subsequent cycles (not shown). On the reverse scan the activity lost at high

potentials during the formation of Pd oxide is mostly recovered when the reduction of the Pd oxide regenerates a fresh Pd surface. Overall the voltammetric features are consistent with the voltammetry for formic acid oxidation observed with different Pd electrocatalysts.[193,194] While the potential of the main oxidation peak does not vary much between the electrodes for the 2, 10 and 48 wt. % mixtures, the corresponding peak current density (current divided by geometric area of the 3 mm diameter GC disc), respectively 13, 33 and 21 mA cm⁻² (all taken on the forward peak), varies significantly and clearly demonstrates important differences in electrocatalytic activity. The largest oxidation current density observed (10% mixture) corresponds to a specific activity of 13.3 A cm⁻² mg⁻¹.

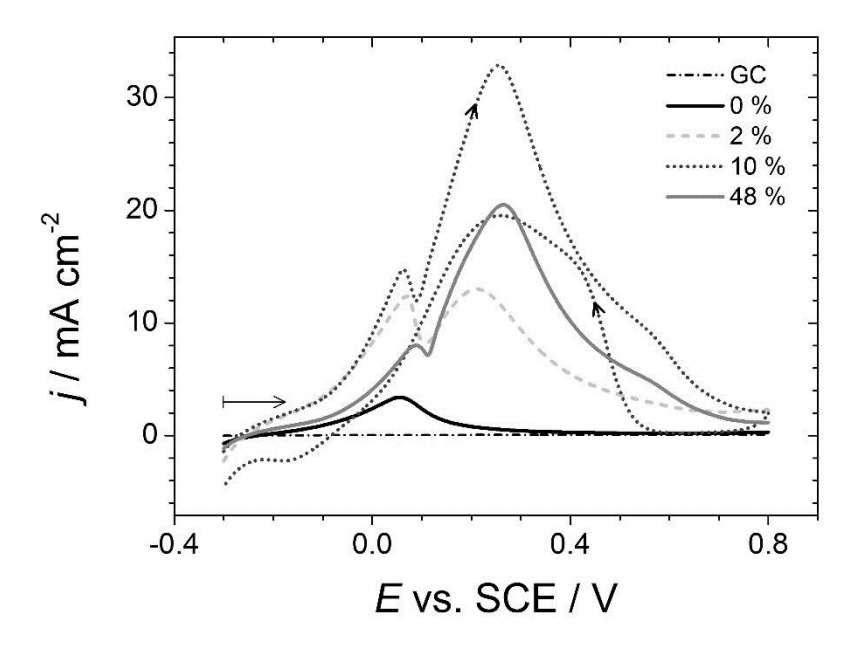


Figure 5-8 Voltammograms for the oxidation of formic acid recorded in Ar purged 0.5 M HCOOH + 0.5 M H_2SO_4 at 100 mV s^{-1} with GC electrodes decorated with the Pd deposits. The legend indicates the corresponding plating mixtures. For clarity the reverse sweep is only shown for the 10% mixture.

Figure 5-8 presents the voltammograms recorded for the oxidation of ethanol in 0.1 M KOH. While peak positions are similar for all electrodes, the oxidation peak currents present large variations depending on the amount of surfactant used to prepare the plating template. For the 0, 2, 10 and 48 wt. % mixtures the peak current densities measured on the forward scan are respectively 6, 16, 58 and 19 mA cm⁻².

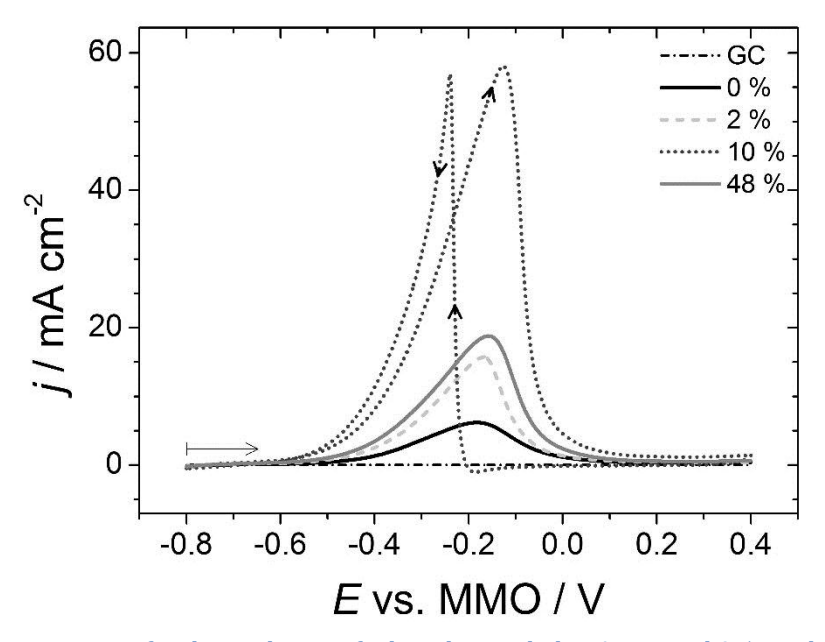


Figure 5-9 Voltammograms for the oxidation of ethanol recorded in Ar purged 0.5 M ethanol + 0.1 M KOH at 100 mV s⁻¹ with GC electrodes decorated with the Pd deposits. The legend indicates the corresponding plating mixtures. For clarity the reverse sweep is only shown for the 10% mixture.

The bare GC electrode is not active but all the Pd modified electrodes show good activity in the KOH solution, in agreement with previous reports.[195] Once again the electrode electroplated with 10 wt. % surfactant stands out as the most active (nine times more than the electrode prepared without surfactant and three times more than that prepared with the hexagonal phase) and reaches a specific activity over 23.4 A cm⁻² mg⁻¹. The sharp drop in current after the forward oxidation peak is consistent with the loss of activity due to the formation of Pd oxide[196] and the recovery of the activity observed on the reverse scan is consistent with a fresh electrode surface resulting from the removal of the Pd oxide.

5.3.2 Electrocatalytic activity: oxygen and hydrogen evolution

Figure 5-9 presents voltammograms for the hydrogen evolution reaction recorded with the Pd modified GC electrodes. The bare glassy carbon electrode shows no activity for hydrogen evolution while the Pd deposits prepared without surfactant show modest activity. Those prepared with the 2 and 48% mixtures are much more active but their activity is dwarfed by that of the deposits prepared with the 10% mixture. At -0.1 V the latter amounts to a specific activity circa 1.0 A cm⁻² mg⁻¹ and the current densities scale as follows with respect to the 10% solution: $j_{10\%}=4\times j_{2\%}=4\times j_{48\%}=26\times j_{0\%}$.

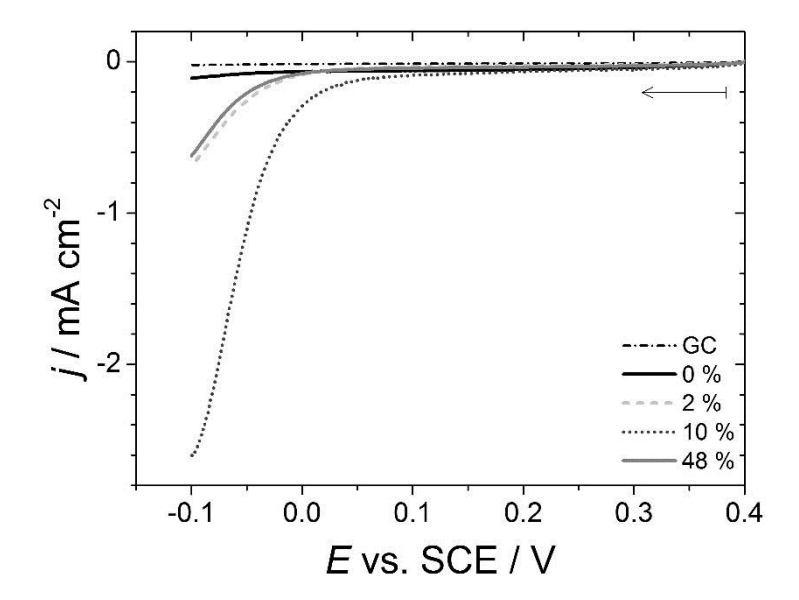


Figure 5-10 Linear sweep voltammograms for the evolution of H recorded in Ar purged 0.5 M HClO₄ at 100 mV s⁻¹ with GC electrodes decorated with the Pd deposits. The legend indicates the corresponding plating mixtures.

The voltammetry for the oxygen evolution reaction presents a similar pattern, Figure 5-10. The bare GC electrode and Pd deposits prepared without surfactant have poor activity, the 2% and 48% mixtures have roughly similar performance with much larger current densities and the 10% mixture produces even larger current densities amounting to a specific activity around 52.4 A cm⁻² mg⁻¹ at +1.2 V. At this potential the current densities scale as follows with respect to the 10% solution: $j_{10\%}=2\times j_{2\%}=3\times j_{48\%}=25\times j_{0\%}$.

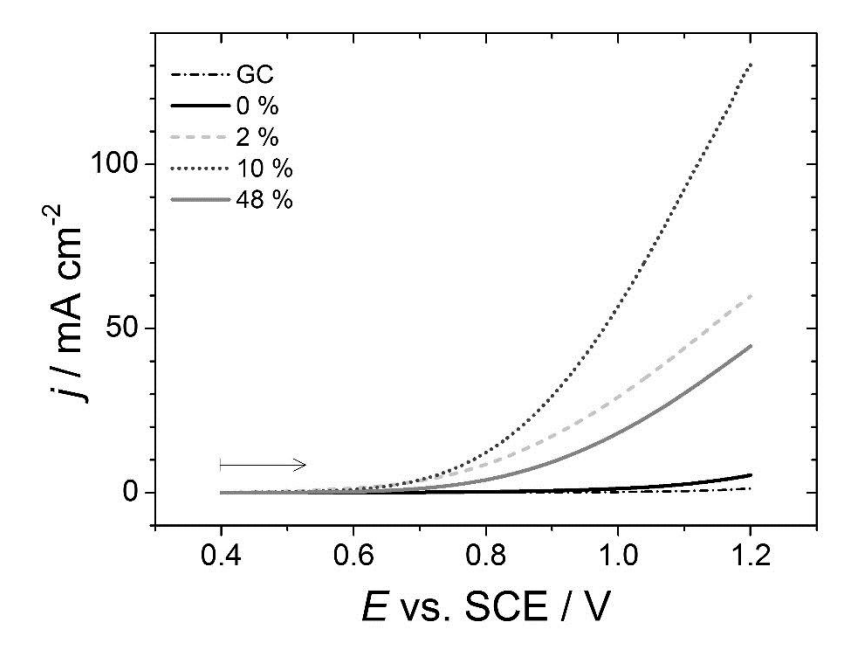


Figure 5-11 Linear sweep voltammograms for the evolution of O_2 recorded in Ar purged 0.5 M ethanol + 0.5 M KOH at 100 mV s⁻¹ with GC electrodes decorated with the Pd deposits. The legend indicates the corresponding plating mixtures.

5.3.3 Electrocatalytic activity: oxygen reduction

Figure 5-11 shows the voltammograms recorded for the reduction of dissolved oxygen in alkaline conditions. In presence of Pd the voltammograms have two reduction waves typical of the reduction of oxygen via the peroxide route but the first reduction peak is much more pronounced when the Pd deposit is prepared using the surfactant template. The electrodes perform in a similar way as for the oxygen and hydrogen evolution reactions with bare GC and the 0% mixture yielding very low activity, the 2 and 48% mixtures yielding similar activity and the 10% mixture providing the best performance. At circa -0.11 V the specific activity of the deposits prepared with the 10% mixture amounts to 0.7 A cm⁻² mg⁻¹ and the current densities scale as follows with respect to this mixture: $j_{10\%}=2\times j_{2\%}=3\times j_{48\%}=39\times j_{0\%}$.

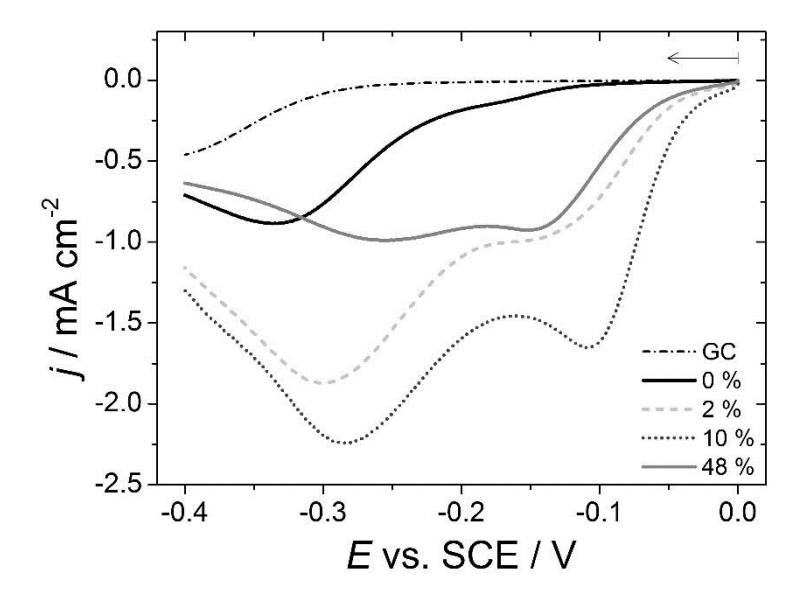


Figure 5-12 Linear sweep voltammograms for the reduction of oxygen recorded in O_2 saturated 0.5 M KOH at 100 mV s⁻¹ with GC electrodes decorated with the Pd deposits. The legend indicates the corresponding plating mixtures.

Similar voltammograms were recorded in oxygen saturated 0.5 M HClO₄ Figure 5-12. Except for the bare GC electrode which showed no activity all the Pd deposits behaved in a broadly similar way compared to their performance for ORR in KOH. The 10% mixture produced slightly more active deposits with a specific activity reaching 0.6 A cm⁻² mg⁻¹ circa +0.34 V; at this potential the current densities scaled as follows with respect to the 10% mixture: $j_{10\%}=1.2 \times j_{2\%}=1.7 \times j_{48\%}=2.2 \times j_{0\%}$.

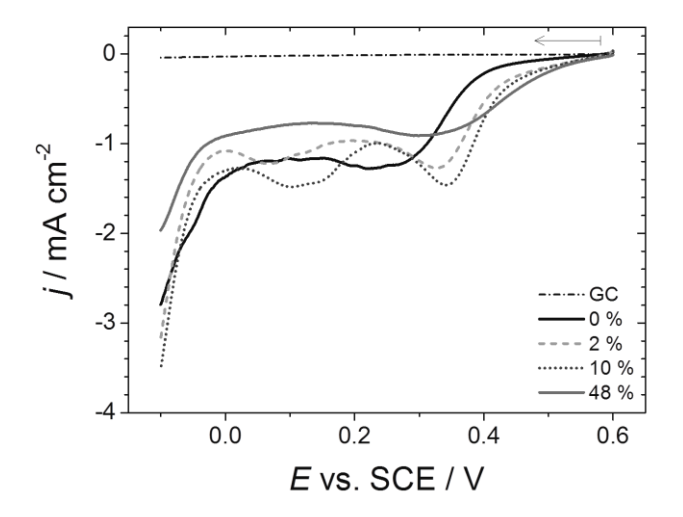


Figure 5-13 Linear sweep voltammograms for the reduction of oxygen recorded in O_2 saturated 0.5 M $HClO_4$ at 100 mV s⁻¹ with GC electrodes decorated with the Pd deposits. The legend indicates the corresponding plating mixtures.

5.4 Analysis

Table 5-2 summarises the specific activities recorded with the different Pd deposits for the test reactions considered.

Table 5-2 Specific activities recorded with the Pd modified GC electrodes for the formic acid oxidation reaction (FAOR), ethanol oxidation reaction (EOR), hydrogen evolution reaction (HER), oxygen evolution reaction (OER) and oxygen reduction reaction (ORR). The results presented in the table refer to a single experiment response for each mixture.

C ₁₆ EO ₈	Specific activities / A cm ⁻² mg ⁻¹				
wt.%	FAOR ^a	EOR ^b	HER ^c	OER ^d	ORR ^e
0	1.3	2.5	0.04	2.1	0.02
2	5.2	6.4	0.3	24.0	0.3
10	13.3	23.4	1.0	52.4	0.7
48	8.2	7.6	0.2	17.8	0.3

a) from Figure 5-7 at the forward peak, b) from Figure 5-8 at the forward peak, c) from Figure 5-9 at -0. 099 V, d) from Figure 5-10 at +1.198 V and e) from Figure 5-11 at -0.109 V.

In this table, each experiment was undertaken with the same amount of Pd deposited. Since the criterion chosen to assess activity was different for each reaction, respectively the peak current for the formic acid and ethanol oxidations and the current at a fixed potential for the H and O2 evolution and O2 reduction reactions, Table 5-2 is not designed to compare the performance of a given deposit across all reactions but rather to compare the performance of the different deposits for a given reaction. Overall the 10% mixture produces the most active deposits followed by the 2 and 48% mixtures which share similar activities; nonetheless the deposits formed without surfactant are reasonably active. These results are consistent with the morphology observed with the FEG-SEM images, Figure 5-2 and with the voltammetry recorded in acid, Figure 5-6. The Pd nanoparticles which form the building blocks of the clusters and agglomerates observed appear clearer in the SEM for the 10% mixture than with the other mixtures. They are not more dispersed as distances between the nanoparticles are similar for all deposits, even in absence of surfactant; rather the flaky 2D texture of the deposits formed within the 10% mixture is thought to give more exposure of the particles to the solution and this is reflected in their enhanced electrochemical activity. Although no attempt was made to conduct an exhaustive comparison of the activities obtained with those previously reported, they generally compare well.[77,197-200] In all cases the deposits prepared with the surfactant template perform overwhelmingly better than those prepared without the template however normalising the electroactive areas and specific activities to the

corresponding quantities obtained in absence of surfactant reveals a striking and unexpected outcome as presented in Table 5-3.

Table 5-3 Normalised electroactive areas (electroactive area of the particles formed in the given mixture divided by the electroactive area of the particles formed in the 0 wt.% mixture) and normalised specific activities (activity of the particles formed in the given mixture divided by the activity of the particles formed in the 0 wt.% mixture) for the 2%, 10% and 48% mixtures taking the 0% mixture as the reference.

	C ₁₆ EO ₈	Normalised	Normalised specific activities				
	C ₁₆ EO ₈ wt.%	electroactive area	FAOR ^a	EOR ^b	HER ^c	OER ^d	ORR ^e
	2	2.2	4	3	7	11	19
	10	2.7	10	9	26	25	39
Ī	48	1.4	6	3	6	8	15

a) from Figure 5-7 at the forward peak, b) from Figure 5-8 at the forward peak, c) from Figure 5-9 at -0. 099 V, d) from Figure 5-10 at +1.198 V and e) from Figure 5-11 at -0.109 V.

Table 5-3 shows that the use of the surfactant template produces large enhancements in electrochemical activity which are far in excess of those expected on the basis of the increased electroactive areas. For example the electroactive area of the deposits prepared with the 10% mixture is 2.7 times larger than that prepared with the 0% mixture but its activity for the formic acid oxidation is ten times larger. The template produces modest increases in electroactive areas, irrespective of the surfactant weight ratio, but the electrochemical activities obtained are significantly larger, especially for the 10% mixture. The voltammograms for the test reactions were repeated several times with different GC electrodes under the same experimental conditions; we found the same trend of particle activity in terms of wt.% of surfactant in the plating mixture. In all cases the Pd modified GC electrodes prepared from micellar solutions were more active and the highest activity for all test reactions was obtained with particles prepared with the 10 w.t% mixture.

5.5 Electrodeposition of Pd from lyotropic liquid crystal mixtures on highly ordered pyrolytic graphite (HOPG)

The effect of surfactant on the deposition of Pd nanoparticles was investigated on HOPG. The electrodeposition of Pd was carried out under the same conditions that were used with GC. A fresh cleaved layer of HOPG electrode placed in the centre of sandwich cell, then a sufficiently negative voltage (-0.3 V vs SCE) to the electrode was applied in order to reduce metal ions to metal atoms. 10 mM (NH₄)₂PdCl₄ + 0.5 mol dm⁻³ aerated KCl and different concentrations of surfactant were used as with GC discussed previously. The potential was stepped from +0.7 V where no reaction is taking place to -0.3 V vs. SCE. For all mixtures the deposition was stopped when the charge reached 63.7 mC cm⁻². Figure 5-13 shows SEM images for the morphology of the deposits prepared with the four

mixtures. Metal clusters form in preference to a metal monolayer because the graphite surface possesses an extremely low interfacial energy.[201,202] High nucleation density occurred at step edges at 0 wt.% and the range of particle sizes suggests a progressive nucleation. The Pd nanoparticles distributed randomly on the surface with 2 wt.% and 10 wt.% and the lower dense number of clusters can be observed. When the surfactant increased to 48 wt.%, the nuclei density dropped and the number of clusters decreased.

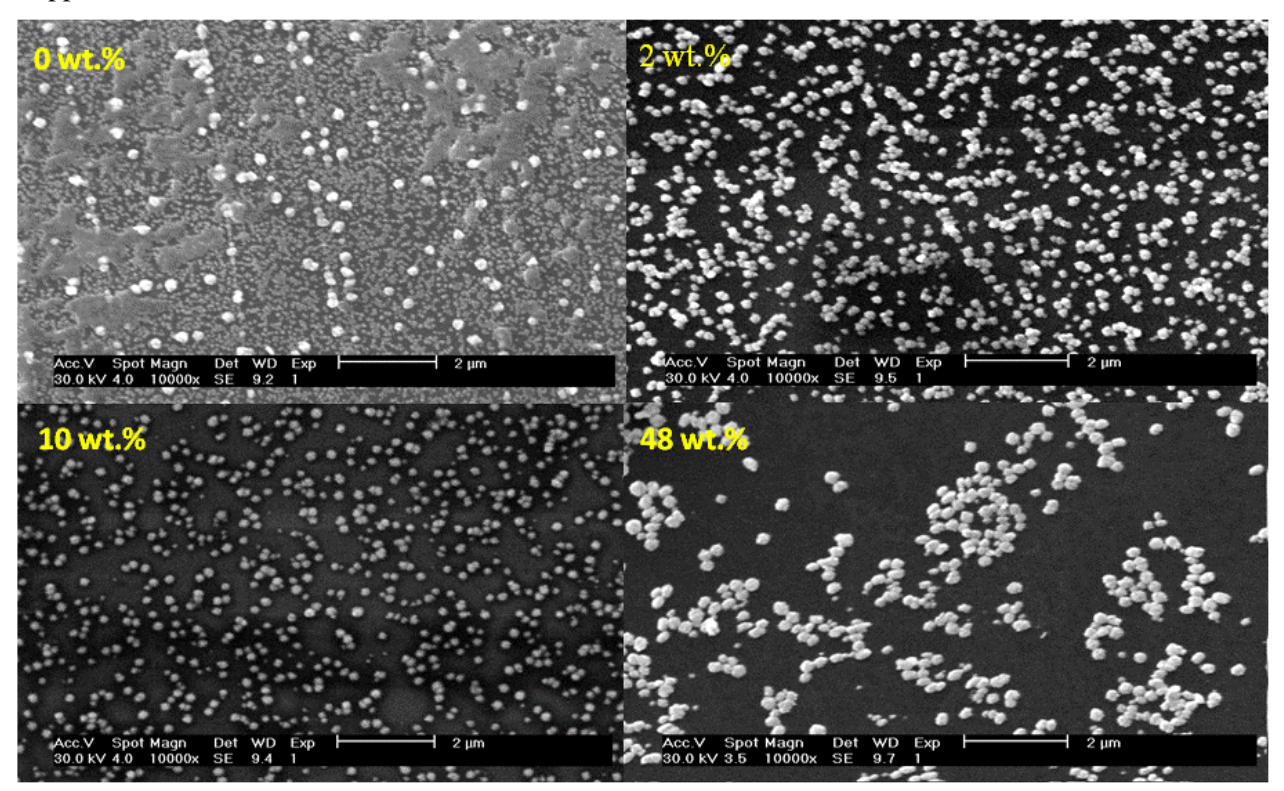


Figure 5-14 SEM (low magnification) images of Pd structures electrodeposited on HOPG after stepping from +0.7 V to -0.3 V vs. SCE for a 63.7 mC cm⁻² deposition charge, in aerated 10 mM (NH₄)₂PdCl₄ + 0.5 M KCl with 0, 2, 10 and 48 wt. % of $C_{16}EO_8$ as indicated by the legend.

Figure 5-14 shows the same samples imaged using FEG-SEM. The Pd particles prepared from 0 wt.% agglomerate together and form clusters with size of 52 nm, each cluster had small particles ranging between 17-10 nm. Furthermore, the Pd deposits from 2 wt.% and 10 wt.% had a hemispherical shape clusters with size of 49 nm and (166-1000) nm respectively. Nanoparticles formed from 2 wt.% was in range of 16-10 nm, while the 10 wt.% produced small particles in range of 3-7 nm. Deposits formed in the 48 wt.% mixture had a completely different structure; with Pd deposited as one or two layers of large flakes, it was difficult to estimate the size of their particles which appeared as compact, close-packed arrangements.

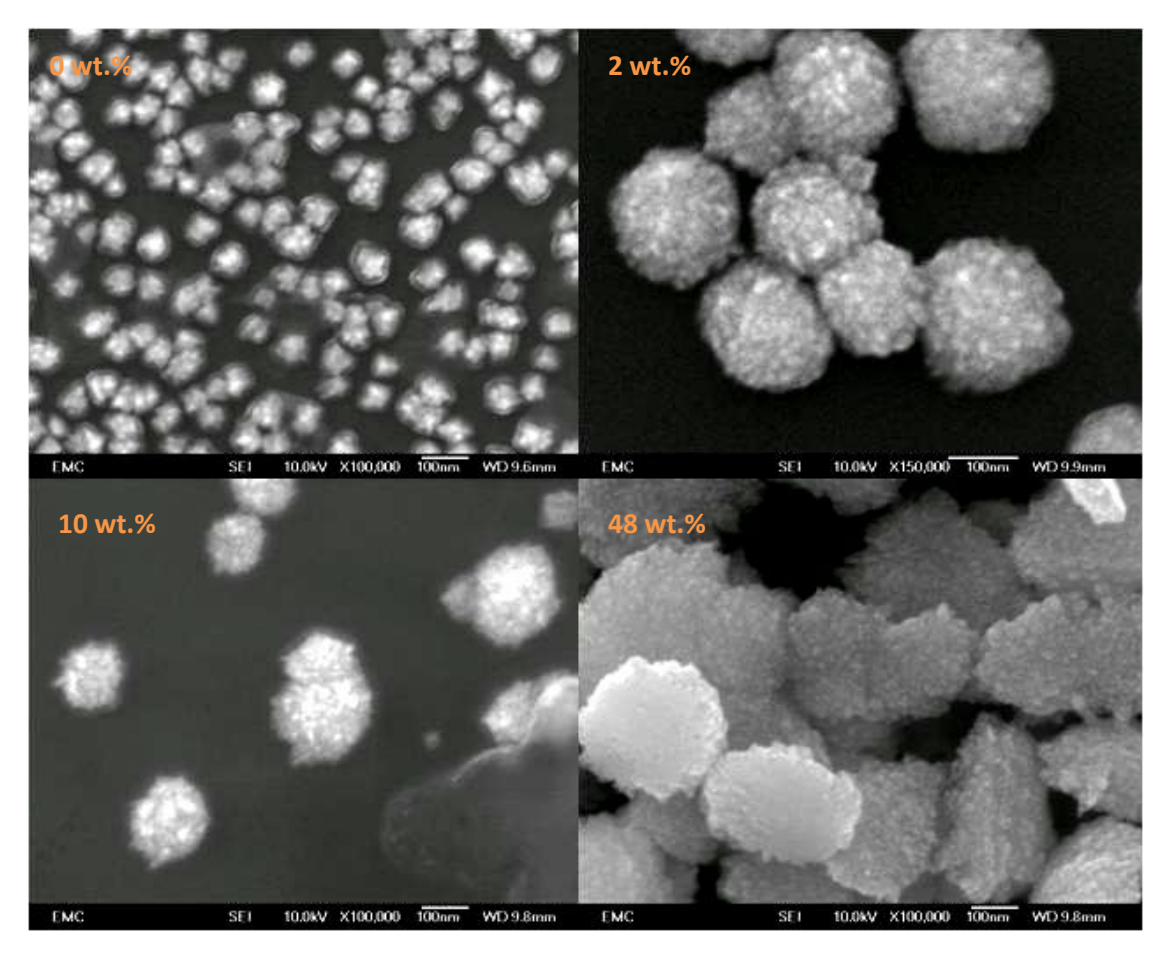


Figure 5-15 FEG-SEM (high magnification) images of Pd structures electrodeposited on HOPG after stepping from +0.7 V to -0.3 V vs. SCE for a 63.7 mC cm⁻² deposition charge.

The activity of Pd deposited on HOPG was tested toward the ethanol oxidation reaction; Fig. 5-15 presents the voltammograms recorded for the oxidation of ethanol in 0.1 M KOH. For the 0, 2, 10 and 48 wt% mixtures the peak current densities measured on the forward scan were, respectively, 2.7, 33.2, 62.3 and 28.4 mA cm⁻². As for the deposits formed on GC, all the Pd modified HOPG electrodes showed good activity in the KOH solution but the electrode electroplated in 10 wt.% surfactant stands out as the most active (twenty three times more than the electrode prepared without the surfactant and two times more than that prepared with the hexagonal phase).

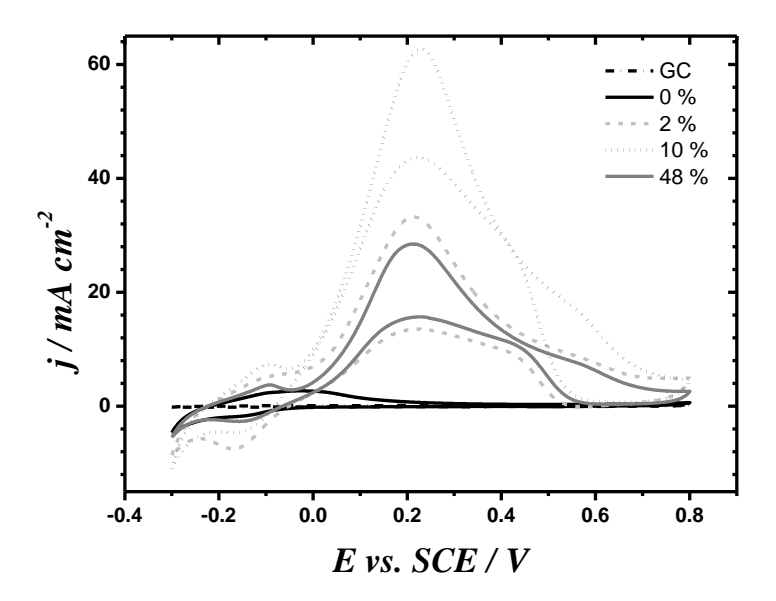


Figure 5-16 Voltammograms for the oxidation of ethanol recorded in Ar purged 0.5 M ethanol + 0.1 M KOH at 100 mV s⁻¹ with with 5 mm \emptyset HOPG electrodes decorated with the Pd deposits. The legend indicates the corresponding plating mixtures.

5.6 Conclusion

These results clearly demonstrate that the lyotropic liquid crystal template influences the morphology and electrochemical activity of the Pd deposits prepared on the GC and HOPG substrates. The differences in morphology are reflected in the voltammetry recorded in acid but the electroactivity of the deposits for all the test reactions considered far exceeds what might be reasonably expected on the basis of the electroactive areas. It was beyond the scope of the study to investigate the structure of the nanoparticles but a possible explanation is that the presence of the template and the use of large overpotentials produced facetted particles with far more atoms on edges than those produced without surfactant. We have no explanation to support the superior performance of the deposits prepared with the 10% mixture and future work should consider investigating the structure-activity relationship over a range of surfactant weight ratios within the micellar phase.

In the next chapter palladium nanostructured films (from ammonium tetrachloropalladate (II)) deposited on gold microdisc electrodes will be studied using cyclic voltammetry and chronoamperometry. A set of deposition mixtures were studied with varying concentrations of the non-ionic surfactant octaethylene glycol monohexadecyl ether ($C_{16}EO_8$) ranging from purely aqueous to the micellar and hexagonal phases of the surfactant water mixtures.

6. Nanostructured films of palladium from lyotropic liquid crystal mixtures on gold microelectrodes

In this chapter palladium nanostructured films will be prepared on gold microelectrodes by electrodeposition within plating mixtures containing the non-ionic surfactant octaethylene glycol monohexadecyl ether ($C_{16}EO_8$), which is known to form lyotropic liquid crystal phases in the correct concentrations when mixed with water.[82,203,204] The aqueous, micellar and hexagonal phases will be investigated. The influence of the lyotropic liquid crystal on the modified gold electrode will be studied by cyclic voltammetry, chronoamperometry and scanning electron microscopy. Gold is a metal of choice to be used in combination with palladium due to its inertness, low electrical resistance, high corrosion resistance and also the lower price and greater availability of gold compared to that of platinum.[205,206] The gold electrodes used in this research study are in the form of microdisc electrodes.

6.1 Electrodeposition of Pd from lyotropic liquid crystal mixtures on gold microelectrode

It is reported that Pd nanostructures have received great attention for their unique properties and catalytic performance. Pd nanostructures exhibit unique properties, as enhanced electrocatalytic activity, they show an enhancement of hydrogen related reactions by orders of magnitude. It was reported that the catalytic activity for the hydrogen oxidation reaction and hydrogen evolution reaction increases considerably with decreasing amount of catalyst material. In this section, the investigation on palladium electrodeposited onto a gold microlectrodes from aqueous ammonium tetrachloropalladate (II) in the presence of surfactant, will be discussed.

6.1.1 Electrodeposition via cyclic voltammetry

In this section we report the deposition of nanostructured palladium by cyclic voltammetry of palladium ions dissolved in aqueous domains of the different lyotropic liquid crystalline phases (hexagonal and micellar), also we focus on the characterization of the deposited nanostructured Pd film. We will investigate the surface morphology using scanning electron microscopy.

The electrodeposition of palladium was recorded at smaller surface area electrode, with the long term aim to produce low Pd loadings with limited deposition charge densities. A cyclic voltammogram in 1 M sulphuric acid was initially recorded on a polished gold electrode before proceeding with further measurements.

Cyclic voltammetry depositions were performed in each of the surfactant mixtures before each set of chronoamperometry experiments to determine the appropriate deposition potentials. Gold microdisc electrodes, 25 and 50 µm Ø, were used as working electrodes. Figure 6-1 displays the cyclic voltammograms collected during deposition from surfactant mixtures (0, 2, 10 and 48 wt.%). For

mixture 0 wt.% on the forward scan the onset of reduction is observed at +0.3 V vs. SCE. The reverse scan displays no positive stripping current which implies that only deposition has occurred within this potential window. It can be seen that the forward scan for the second cycle produces a much larger current density than seen on the first cycle and proceeds at a steeper current gradient. The scans for other mixtures in presence of surfactant follow a similar pattern but with the key difference of later onsets of reduction during the forward scan. For 2 wt.% this occurs at +0.29 V, for the 10 wt.% the onset begins at +0.27 V and the onset for 48 wt.% occurs at +0.19 V vs. SCE. The current density during each of the depositions is observed to decrease with increasing surfactant concentration; this decrease in current density can be attributed to the increased viscosity of the surfactant mixtures as the concentration of surfactant is increased. The mass transport of palladium ions to the electrode surface is slowed by the increased viscosity. The limit on mass transport slows the reduction reaction rate and leads to the lower current densities observed in the CV.

Table 6-1 illustrates the deposition charge for the reduction wave for each mixture; the charges for the first Q_{pd-1st} and second Q_{pd-2nd} reduction waves were calculated. The 0 wt.% has the largest charge passed and the increase in surfactant concentration leads to a significant drop in the deposition charge. It is obvious that Q_{pd-2nd} is greater than Q_{pd-1st} ; especially for 0 wt.% the charge passed Q_{pd-2nd} is almost the double of the Q_{pd-1st} value.

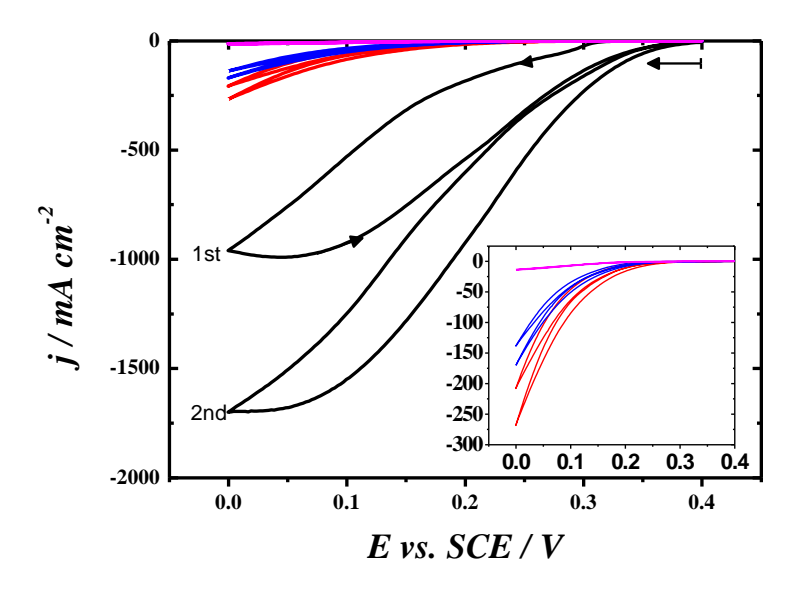


Figure 6-1 Cyclic voltammograms for the deposition of palladium in varying surfactant mixtures, 0 wt.% (black), 2 wt% (red), 10 wt.% (blue) and 48 wt.% (pink), recorded on gold microelectrodes (\emptyset = 50 μ m diameter) with a scan rate of 10 mV s⁻¹.

Table 6-1 Analysis of voltammograms used to deposit Pd on gold electrodes: mixture, charge density of 1^{st} scan Q_{Pd-1st} , charge density of 2^{nd} scan Q_{Pd-2nd} , total charge density Q_{Pd-T} , film thickness measured via SEM, after CV deposition in varying surfactant mixtures.

Surfactant wt.%	$Q_{Pd ext{-}1st}$ / mC	$Q_{Pd ext{-}2nd}$ / mC	$Q_{Pd ext{-}T}$ / mC
0	32.60	63.40	96.00
2	3.00	4.00	9.00
10	2.00	2.50	4.50
48	0.29	0.31	0.60

The characterisation by CV in acid for the different surfactant mixtures is shown in figure 6-2. The cyclic voltammograms display the expected palladium oxide reduction peak, and hydrogen adsorption/desorption peaks, but the 0 wt.% shows only the onset of hydrogen evolution and hydrogen adsorption/desorption are poorly resolved. None of the voltammograms display any gold features which indicates that the film have achieved full coverage of the electrode. The current density for the palladium oxide reduction peak is observed to decrease from films prepared in micellar solution to Pd modified gold electrode formed in absence of surfactant, while the deposits from 48 wt.% gave a very small reduction peak. This would suggest that reduced palladium loading has occurred as the concentration of surfactant is increased which is to be expected after the pattern of reduced current densities observed in the deposition cyclic voltammograms, figure 6-2. The palladium oxide reduction peaks were analysed to produce information about the deposited palladium films. This data is summarised in table 6-2.

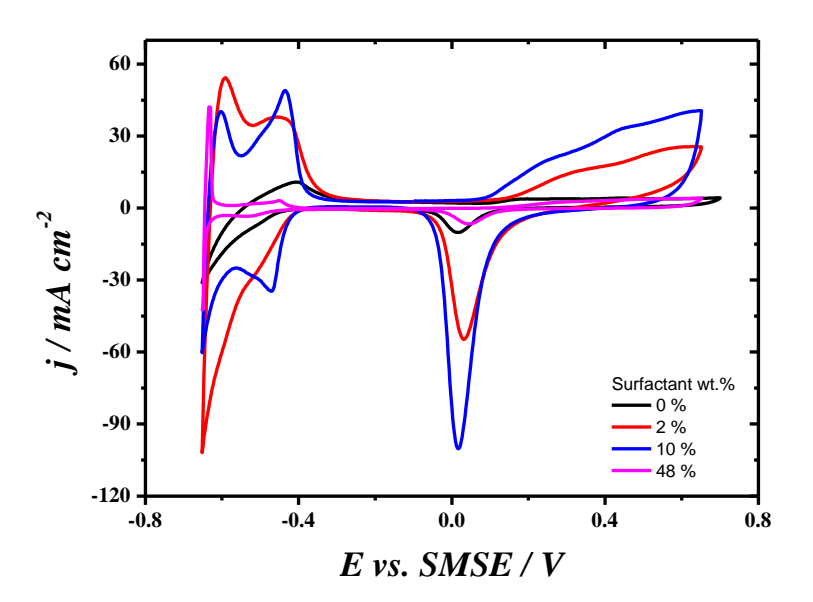


Figure 6-2 Cyclic voltammograms recorded with Pd modified gold microdisc electrodes (\emptyset = 50 μ m diameter) that shown in Figure 6-1 in 1 M H₂SO₄ at 20 mV s⁻¹. The plating mixtures used to prepare the Pd deposits are shown in the legend.

The palladium oxide reduction peaks were analysed to produce information about the deposited palladium films. Pd oxide reduction charge Q_{Pd} roughness factor R_f and specific catalyst area S were evaluated from the CVs. The Pd oxide reduction charge and therefore the electroactive area were calculated by assuming a specific charge of 424 μ C cm⁻² (conversion factor) for the palladium oxide reduction, so the charge under the peak was divided by the conversion factor to provide the electroactive area of the electrode surface in units of cm². As mentioned previously this approach relies on the choice of upper reversal potential to ensure that only one monolayer of oxide is formed.

$$A_{elec} = \frac{Q_{Pd}}{Q_{mono}} \tag{6-1}$$

This electroactive area is divided by the geometric area, A_{geo} , of the electrode giving a roughness factor, R_f .

$$R_f = \frac{A_{elec}}{A_{geo}} \tag{6-2}$$

In addition the specific catalytic area, S in m^2 g^{-1} was calculated by a modification of the equation for the R_f .

$$S = \frac{A_{elec}}{A_{geo} \times W} \times 100 \tag{6-3}$$

where W is the mass of palladium deposited per cm², the palladium loading, with units of μg cm⁻².

$$W = \frac{QM}{nF} \tag{6-4}$$

where Q is the charge passed in the reaction, M is the molecular weight of palladium and F is Faraday's constant. As expected from the deposition voltammograms the charge density for the deposition drops as the surfactant concentration is increased which has been attributed to the slower reaction rates with the increased viscosity of the mixtures. The highest roughness factor and specific catalytic area produced were with the 10 wt.% mixture. The fact that these figures are so much higher than for the plain palladium film, 0 wt. %, would suggest that a nanostructure has been templated into the film. This is also most likely the case for the 2 wt.% mixture since the roughness factor is again much higher than that calculated for the plain palladium mixture. The low specific catalytic area calculated for the 48 wt.% mixture implies that the hexagonal nanostructure has not been templated onto the film, if this had been the case it would be expected roughness factors and specific catalytic area values to exceed those observed for mixture 10 wt.%. The film thickness decreases as expected from the reducing charge density that is observed. The films produced via CV deposition were characterised by SEM. The images are shown in figure 6-3.

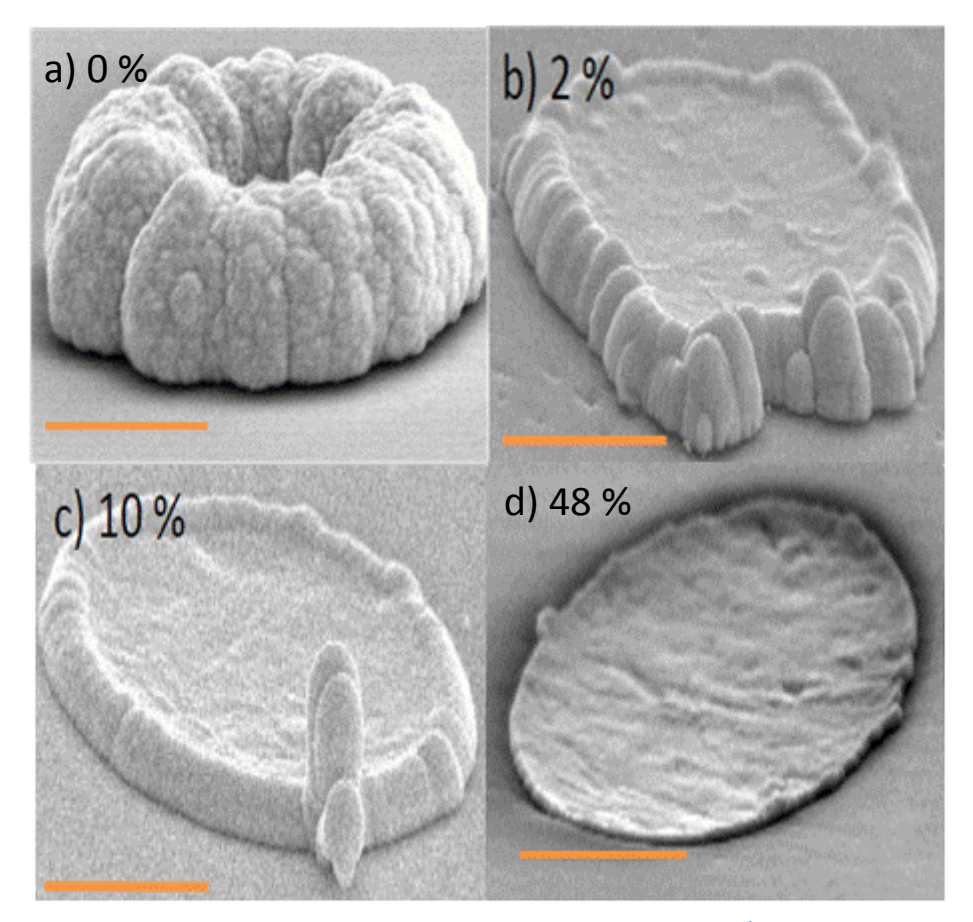


Figure 6-3 SEM images of the palladium coated gold microelectrodes (\emptyset = 50 μ m diameter) after undergoing two consecutive cyclic voltammograms in ammonium tetrachloropalladate (II) (a) aqueous solution (b) and (c) micellar phase of LLC mixture (d) hexagonal phase. The scale bare is 20 μ m.

Table 6-2 Analysis of the Pd deposits formed by voltammetry on gold microdisk electrodes ($\emptyset = 50 \, \mu m$ diameter), from left to right: mixture, charge density passed during deposition, charge for the palladium oxide reduction peak, roughness factor, specific catalytic area, film thickness via SEM. (assuming a specific charge of 424 μC cm⁻² (conversion factor) for the reduction of one monolayer of palladium oxide).

Surfactant wt.%	Q / C cm ⁻²	Q_{Pd} / $\mathrm{C~cm^{-2}}$	$R_{\rm f}({ m Pd})$	$S / m^2 g^{-1}$	Film thickness / μm (SEM)
0	96.00	0.030	71	0.13	14.0
2	7.00	0.260	613	15.88	7.0
10	4.50	0.440	1037	41.79	3.0
48	0.44	0.028	66	27.20	0.3

The SEM images show the reduction in thickness of the film as the wt.% of surfactant is increased. The SEM images also confirm that thick Pd films have been produced in all cases. There is a clear edge effect which decreases from the extreme case in the 0 wt.% to being barely perceptible in the 48 wt.%; the reason for this is that the charge densities are very high for mixtures 0, 2 and 10 wt.% which has led to fast deposition. Microelectrodes experience enhanced mass transport to the edges and the fast rate of reaction has caused this effect to be exaggerated in most of the films. The suspected template structure for the 2 and 10 wt.% mixtures could not be observed under SEM as the resolution

is too low. Also, the morphology of the film appears smoother in presence of surfactant; in contrast, the film in absence of surfactant appears rough with lots of defects. In this section the cyclic voltammograms were studied to indicate the potential region for the reduction of palladium for all mixtures, in the next section the electrodeposition will be carried out using chronoamperometry.

6.1.2 Electrodeposition via chronoamperometry

1) Electrodeposition in absence of surfactant

The nanostructured film was formed by stepping the potential from the zero current region (0.4 V vs SCE) to several overpotentials. A set of chronoamperometry experiments was carried out in aqueous solution by stepping the potential from (+0.4 V versus SCE) to different deposition potentials, 0.0-0.3 V vs. SCE, these potentials are very much in the foot of the deposition wave (see Figure 6-1 the black CV) to grow the film under kinetic control, the deposition charge density was kept fixed at 2.5 C cm⁻². The current transients in figure 6-4 appear as expected with a trend of increasing current densities with more negative deposition potentials. The increased overpotential should lead to a faster reaction rate and therefore a higher current density. The transients at 0, 0.1 and 0.2 V vs. SCE did not show the decay of the falling part for the typical characteristic shape for an electrochemically driven, diffusion controlled because they were stopped too soon. The shorter deposition time is referred to larger overpotential and the difference in deposition time between all transients is because the charge was fixed. The potential at +0.3V corresponds to the start of the palladium reduction wave and produces a different shape transient from the others as the current in this case is kinetically controlled. The transient at +0.4 V was also used but is not shown on this figure, because the current was too low and went on for a very long time.

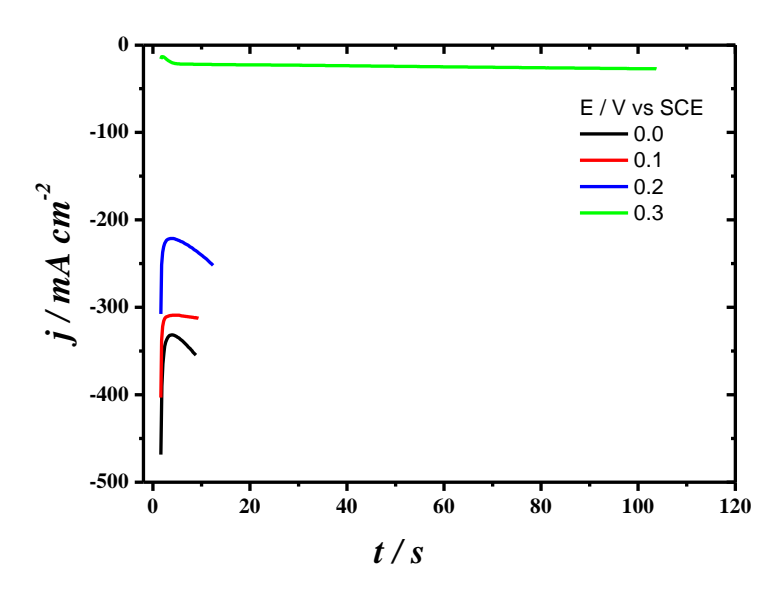


Figure 6-4 Current density vs. time transients recorded in 10 mM (NH₄)₂PdCl₄ + 0.5 M KCl after stepping from 0.4 V to different deposition potentials with a fixed deposition charge density (2.5 C cm⁻²), working electrode Au (\emptyset = 50 μ m).

Figure 6-5 shows the acid CVs of the palladium coated gold microelectrodes prepared by potential steps in the different plating mixtures. All cyclic voltammograms exhibit the characteristic features for polycrystalline palladium with unpronounced hydrogen region.

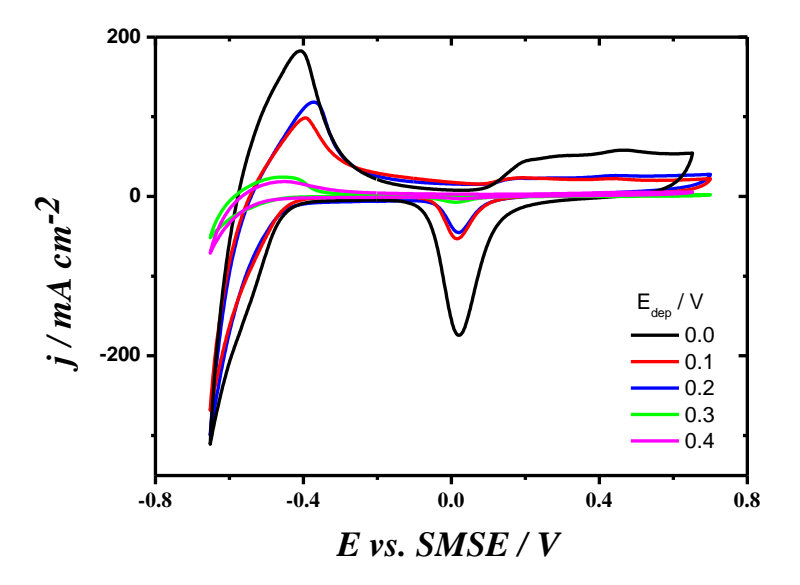


Figure 6-5 Cyclic voltammograms recorded at 20 mV / s in 1 M sulphuric acid with the palladium coated gold microelectrodes (50 μ m diameter) prepared in figure 6-4. The legend indicates the deposition potentials used to prepare the Pd deposits.

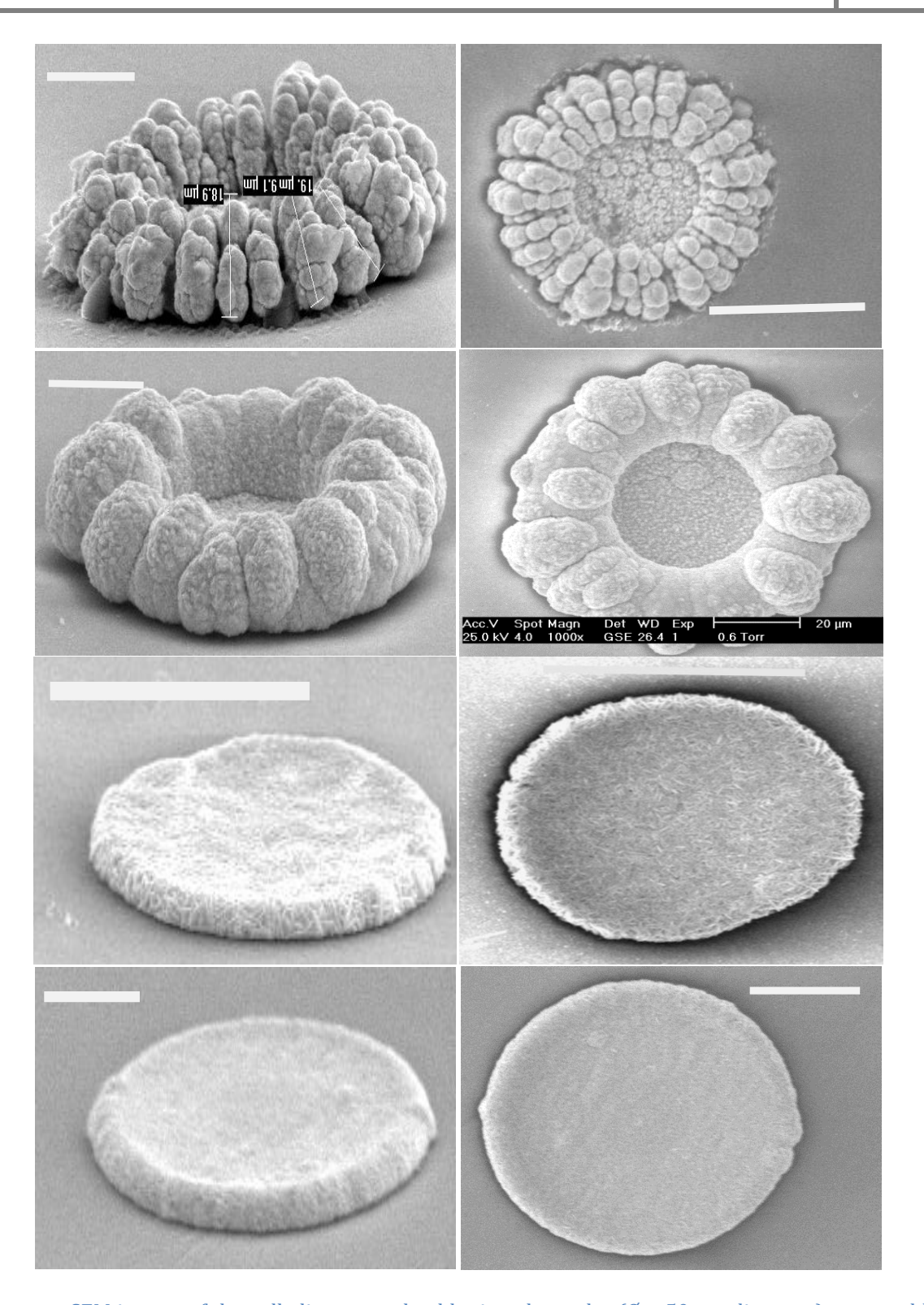


Figure 6-6 SEM images of the palladium coated gold microelectrodes (\emptyset = 50 μ m diameter) prepared by stepping the potential from +0.4 V to different deposition potentials (from top to bottom: +0.0, +0.1, +0.2 and +0.3 V vs. SCE) until a fixed deposition charge density passed (2.5 C cm⁻²), in aerated 10 mM (NH₄)₂PdCl₄ + 0.5 M KCl. The left images were taken at 0°. The images on the right were taken with a 70° tilt for the same films shown on the left. The scale bar is 20 μ m for rows 1,2 and 4 and 50 μ m for row 3.

The morphology of the films was studied with SEM. In figure 6-6, an extreme edge effect can be observed for the deposits; this is due to the large overpotential which has caused rapid deposition of palladium around the edge of the microdisc electrode. The films deposited at 0 and 0.1 V present huge edge effects and a very granular texture. The edge effect is much less pronounced on the electrodes prepared at 0.2 and 0.3 V, also the texture is much finer with fine needles at 0.2 V and fine granules at 0.3 V. The electrode prepared at 0.3 V displays a very smooth and uniform film with a slight edge effect visible. Full coverage is observed on all the electrodes. In the next section the surfactant will be added to the deposition bath in order to form the micellar phase.

2) Electrodeposition in micellar mixtures

Similar experiments were carried out in solutions containing low concentrations of surfactant, 2 and 10 wt. %, to yield the micellar phase. The transients in the 2 wt.% mixture, figure 6-7, display a trend of increasing current density with less positive potential, as expected when the overpotential increases. The steep gradients observed for 0, 0.05 and 0.1 V suggest a rapid growth of the deposits. The deposition at +0.3 V vs. SCE took over 15 times as long as the other depositions; this is due to the fact that, as seen from the CV, figure 6-1, this potential is far from the onset of Pd reduction when surfactant is present in solution.

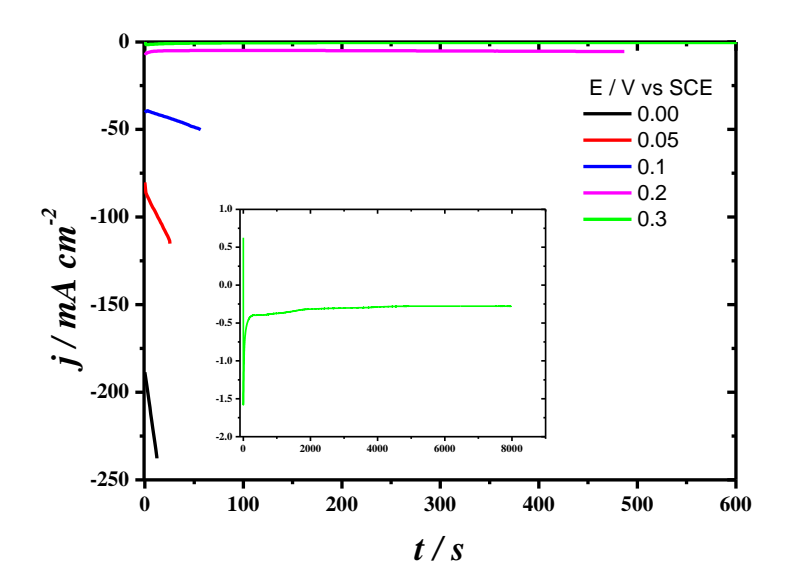


Figure 6-7 Current density vs. time transients recorded in aerated 10 mM (NH₄)₂PdCl₄ + 0.5 M KCl with 2 wt. % of $C_{16}EO_8$ after stepping from 0.4 V to different deposition potentials with fixed deposition charge density (2.5 C cm⁻²), working electrode Au (\emptyset = 50 μ m). The inset shows the transient at 0.3 V.

Examining the modified electrodes by voltammetry in acid, figure 6-8, confirms the presence of nanostructured palladium for all of the electrodes. The hydrogen region is well resolved for deposition potentials from 0.0 - 0.2 V. The size of the palladium oxide peak follows the expected trend of

decreasing with decreasing overpotentials. There are no gold features observed which indicates that there is full electrode coverage.

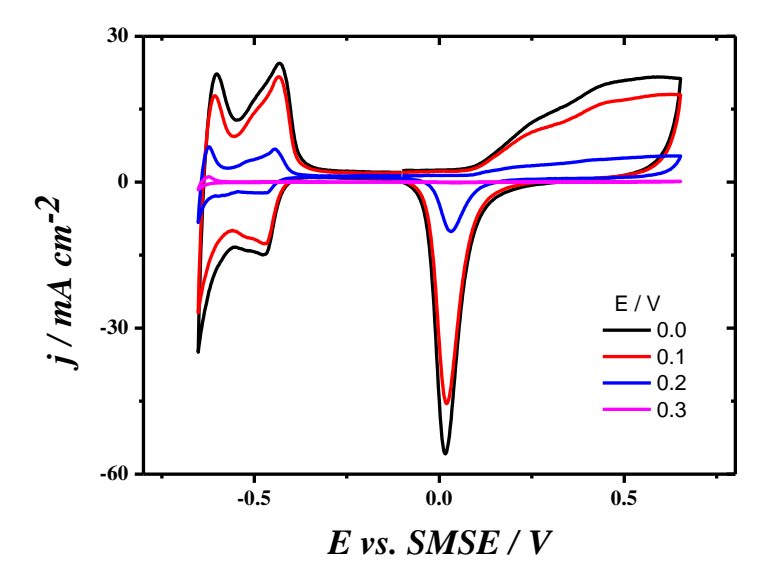


Figure 6-8 Cyclic voltammograms recorded at 20 mV / s in 1 M sulphuric acid of the electrodes prepared in figure 6-7, by stepping from 0.4 V to different deposition potentials with fixed deposition charge density (2.5 C cm⁻²), working electrode Au (\emptyset = 50 μ m) in aerated 10 mM (NH₄)₂PdCl₄ + 0.5 M KCl with 2 wt. % of C₁₆EO₈.

Similar experiments were performed in the 10 wt.% mixture, figure 6-9, then acid CVs were carried out to prove the presence of Pd, figure 6-10. The CVs produce the expected trend of decreasing palladium oxide reduction peaks for decreasing overpotentials. No gold features were observed in these scans; this implies that yet again full coverage of the electrode was achieved. Interestingly the hydrogen region is resolved for all deposition potentials thereby suggesting a high electroactive area consistent with the presence of a nanostructure.

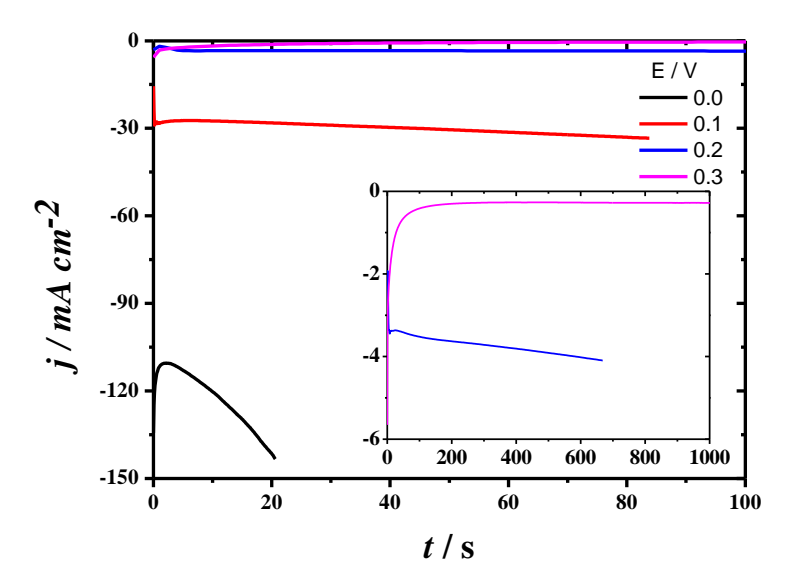


Figure 6-9 Current density vs. time transients recorded in aerated 10 mM (NH₄)₂PdCl₄ + 0.5 M KCl with 10 wt. % of $C_{16}EO_8$ after stepping from 0.4 V to different deposition potentials with a fixed deposition charge density (2.5 C cm⁻²), working electrode Au (\emptyset = 50 μ m). Inset shows transient at 0.2 and 0.3 V.

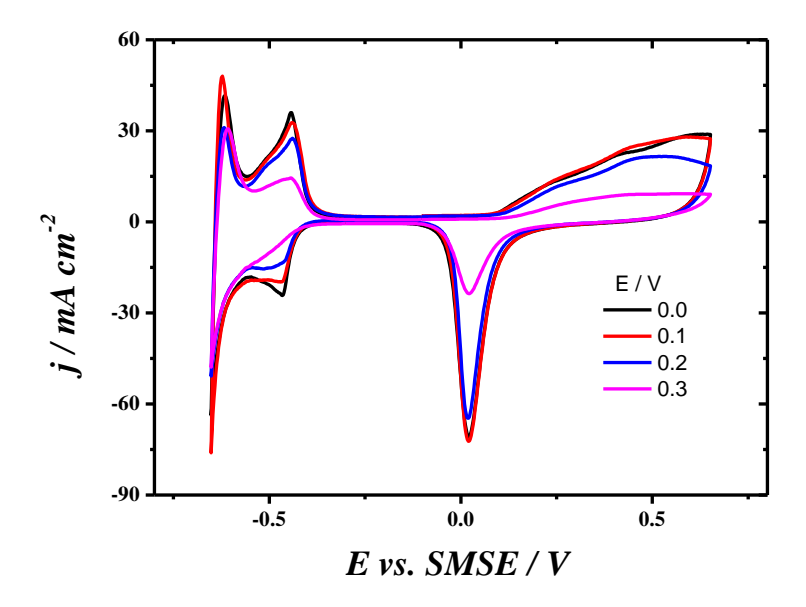


Figure 6-10 Cyclic voltammograms recorded at 20 mV s⁻¹ in 1 M sulphuric acid for the electrodes prepared in figure 6-9 by stepping from 0.4 V to different deposition potentials with a fixed deposition charge density of 2.5 C cm⁻², working electrode Au (\emptyset = 50 μ m) in aerated 10 mM (NH₄)₂PdCl₄ + 0.5 M KCl with 10 wt. % of C₁₆EO₈.

The SEM images in figure 6-11 confirm that full electrode coverage has occurred. It is observed that there is an edge effect present on all of the electrodes. Many secondary deposits due to edge effects are seen on the 0.0 V electrode. Reducing the deposition potential improves the smoothness and leads to more uniform films, but even at 0.3 V, electrode surface defects are seen.

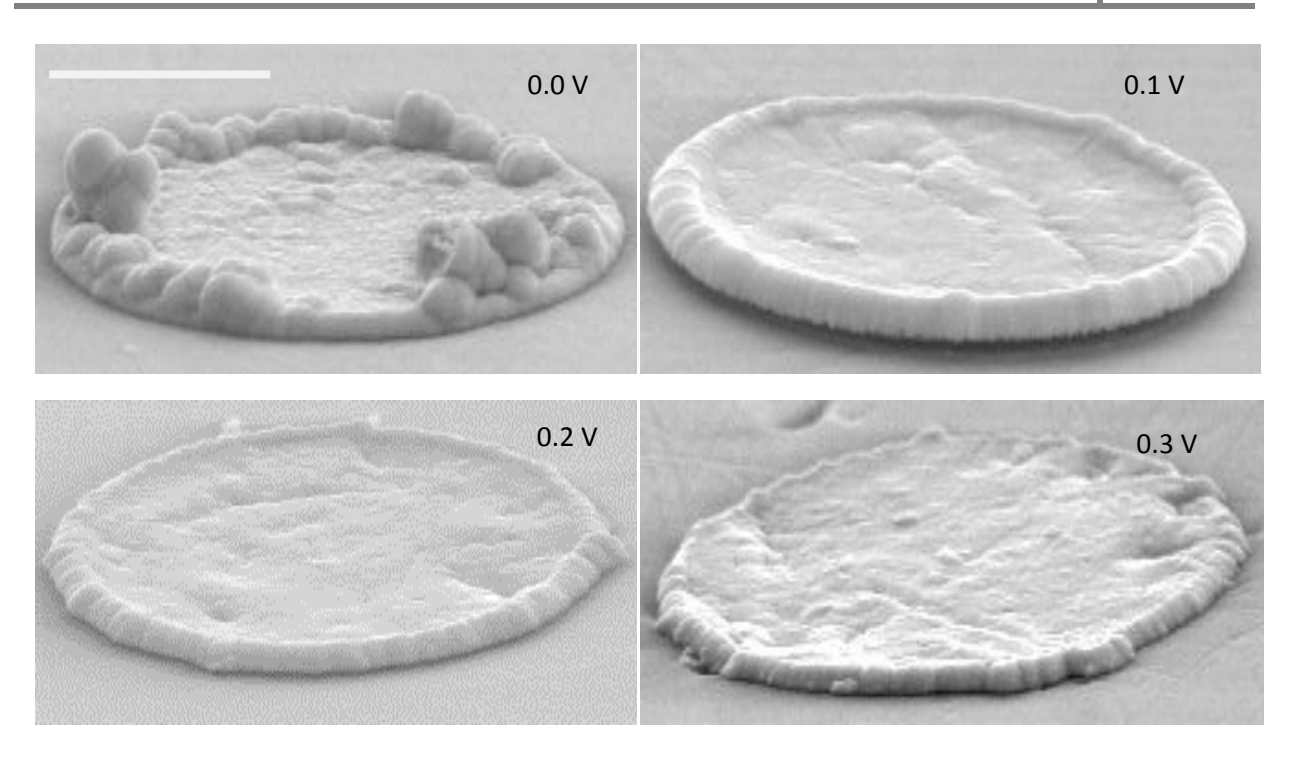


Figure 6-11 SEM images of the palladium coated microelectrodes prepared in figure 6-9 by stepping from 0.4 V to different deposition potentials versus SCE at fixed deposition charge density (2.5 C cm⁻²), in mixture 10 wt.%. (\emptyset = 50 μ m diameter). Scale bare is 20 μ m for all electrodes.

3) Electrodeposition in the hexagonal phase

The 48 wt.% mixture was used to investigate the role of the hexagonal LLC phase during electrodeposition of Pd on the Au microdiscs. Current density vs. time transients were recorded for different deposition overpotentials. The transients (not shown) follow the expected trend of decreasing the current density when applying positive potential. For the film deposited at 0.3 V it was difficult to achieve the same deposition charge passed due to the high viscosity of Pd paste with is affected by the long deposition time. Referring to the palladium deposition CV in Figure 6-1, we can notice that, the reduction wave moves to more negative potentials as the surfactant concentration increases. Hence the deposition potentials used correspond to lower overpotentials every time when increase the surfactant concentration. The CVs in acid are shown in figure 6-12.

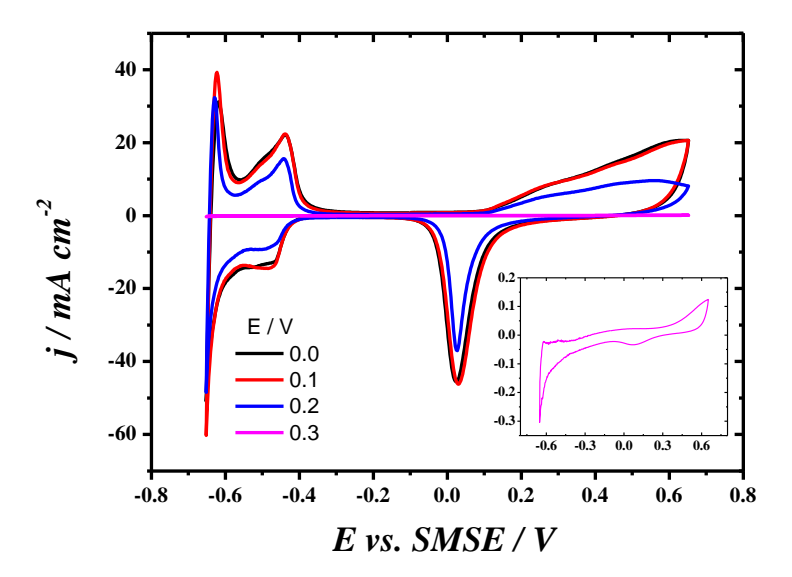


Figure 6-12 Cyclic voltammograms in 1 M sulphuric acid for the electrodes prepared by stepping from 0.4 V to different deposition potentials with a fixed deposition charge density (2.5 C cm⁻²), working electrode Au (\emptyset = 50 µm) in aerated 10 mM (NH₄)₂PdCl₄ + 0.5 M KCl with 48 wt. % of C₁₆EO₈.

The palladium reduction peaks for the film formed at 0.3 V are extremely small, because this potential is much positive and it is at the foot of reduction wave as shown in CV deposition in Figure 6-1. There is evidence that palladium has been deposited to full coverage on all the electrodes as no gold features are present but the hydrogen region is less resolved at the electrode deposited at 0.3 V vs SEM images show edge effects on the depositions at 0.0 and 0.1 V, becoming less pronounced at 0.2 V and disappearing at 0.3 V. Also the deposits at 0.3 V shows lots of surface defects that come from the polishing, indicating a very thin Pd film. The deposits were analysed by EDX and the pattern confirmed the presence of Pd, figure 6-14.

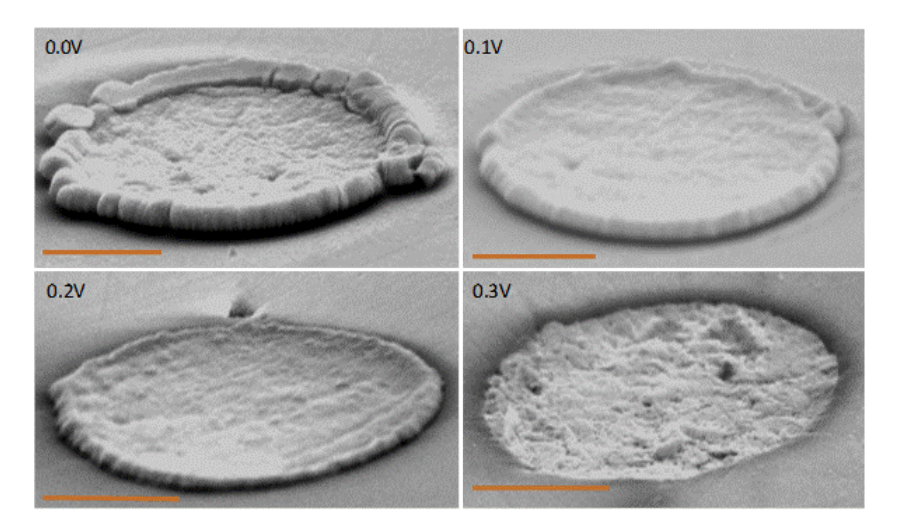


Figure 6-13 SEM images of the palladium coated microelectrodes prepared by stepping from 0.4 V to different deposition potentials for a fixed deposition charge density (2.5 C cm⁻²), in the mixture 48 wt.%. (\emptyset = 50 μ m diameter). Scale bare is 20 μ m.

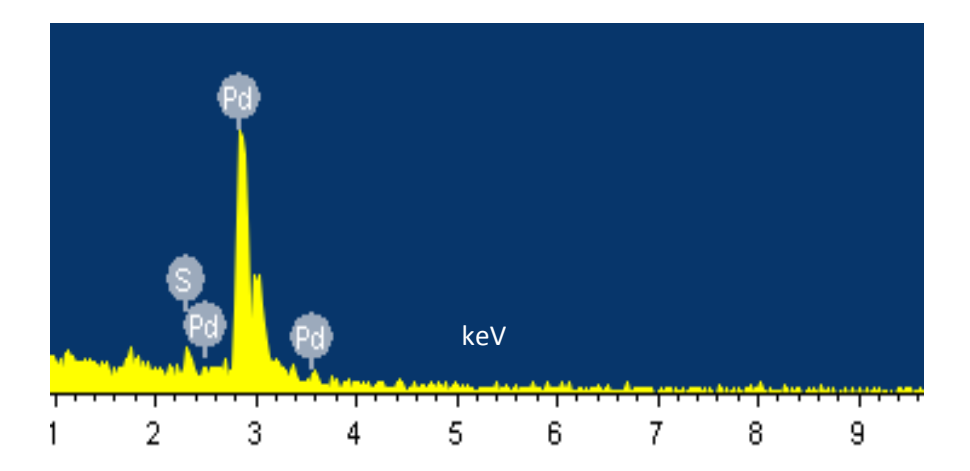


Figure 6-14 EDX analysis of the Pd coated gold microdisk electrode Au(\emptyset = 50 μ m) prepared by potential step from +0.4 V to 0.3 V vs. SCE with fixed deposition charge density (2.5 C cm⁻²), in 10 mM (NH₄)₂PdCl₄ + 0.5 M KCl with 48 wt. % of C₁₆EO₈.

6.1.3 Summary of films parameters evaluated from the CVs in 1 M H_2SO_4 and the current transient in different ratios of surfactant

The voltammetric responses in acid for the different surfactant mixtures is shown in figures 6-5, 6-8, 5-10 and 6-12 exhibit the characteristic features for polycrystalline palladium. All the parameters evaluated from the palladium oxide reduction peak are summarized in tables 6-3. The comparison of Q_{Pd} , R_f and S will be discussed in term of E_{dep} and wt.%,

The palladium stripping charge Q_{Pd} , R_f and S decrease when applying high over potential and this observation is valid in all mixtures, and this due to yield more thicker films at higher overpotential.

In terms of wt.%, it can be notice that the Q_{pd} increases systematically from 48 to 2 to 10 wt. % surfactant but decreases significantly for 0 wt. %. This would suggest the largest electroactive area obtained in micellar solution might be attributed to the very porous structure of the film. This needs to be confirmed by taking TEM images to observe the nanopore structure. Surprisingly, the specific catalyst area of palladium film prepared from micellar solution is greater than those produced in hexagonal lyotropic phase.

Overall, these results clearly demonstrate that the lyotropic liquid crystal template influences the electroactive area and specific catalyst area of Pd deposits prepared on the Au substrates, the deposits prepared with the 10% mixture has largest specific active area and that calculated from the Pd oxide reduction peak from the acid CV despite that the same charge passed during the deposition for all mixtures. These results in agreement with what we found in chapter five on carbon microelectrodes, which the specific active area for the Pd modified carbon electrode that prepared from 10 wt.% surfactant is higher than those Pd nanoparticles formed from 48 and 0 wt.% surfactant. Also, we

cannot make any comparison between the S values obtained on different substrates because the deposition charges are not the same.

Table 6-3 Dependence of the Pd oxide stripping charge, Q_{Pd} , roughness factor, R_f and specific area, S on the amount of surfactant present in the plating template. * evaluated from the voltammograms in acid.

0 wt.%			
E/ V	Q_{Pd}^* / mC cm^{-2}	R_{f}	$S/m^2 g^{-1}$
0.0	37.0	88	6.4
0.1	22.0	51	3.7
0.2	11.0	27	1.96
0.3	2.5	6	0.43

10 wt.%			
E/ V	Q ^{Pd} * / mC cm ⁻²	Rf	S / m2 g-1
0.0	300	707	51.2
0.1	300	707	51.2
0.2	240	566	41.0
0.3	110	259	18.8

2 wt.%			
E/V	Q_{Pd}^* / mC cm^{-2}	R_{f}	S/m^2g^{-1}
0.0	240	566	41.0
0.1	230	542	39.3
0.2	170	400	290
0.3	60	141	10.2

48 wt.%			
E/V	Q _{Pd} */mC cm ⁻²	R_{f}	S/m^2g^{-1}
0.0	200	471	36.2
0.1	190	448	32.5
0.2	120	283	20.5
0.3	-	-	-

6.2 Conclusion

In this chapter we aimed to fabricate palladium nanostructured film onto gold electrodes via the use of the lyotropic liquid crystal phases of the non-ionic surfactant octaethylene glycol monohexadecyl ether (C₁₆EO₈₎. The findings during the experiments performed on gold displayed that increasing concentration of surfactant leads to a shift to more negative potentials for the onset of reduction. The effect of the increasing surfactant concentration was observed to dramatically reduce the edge effect observed on microelectrodes with the same charge density. The increasing surfactant concentration progressively produced thinner palladium films. Surprisingly, that the modified palladium coated gold electrode formed from micellar solution produced highest electroactive area, thus specific catalyst area than those films prepared either from hexagonal or aqueous deposition baths. This result is in agreement with the results obtained in chapter five when deposited palladium nanoparticles on glassy carbon and HOPG.

7. Electrodeposition of ZnSe semiconductor

This chapter is still concerned with the electrodeposition of nanometre size centres but this time we are investigating the electrodeposition of a semiconductor. The long term aim of the project is to develop a nano-scale (<200 nm) light emitting diode (LED) by electrochemical deposition of semiconductors to establish a p-n junction between two electrically conductive carbon nanowires. Such light source could then be used as a sub-wavelength illumination device to provide highly localised excitation of fluorescent molecules such as green fluorescent protein (GFP) and enable super resolution fluorescence live imaging. In order to achieve the formation of light emitting p-n junction by electrochemical deposition the following sub-aims were set:

- a. Establish the reliable deposition of Zn and Se nanostructures from ZnSO₄ and SeO₂ respectively on glassy carbon and Pt substrates.
- b. Establish the reliable co-deposition of ZnSe on glassy carbon and Pt substrates.
- c. Characterise the size and composition ratio of ZnSe deposits by scanning electron microscopy (SEM) and X-ray diffraction (XRD). Adjust the conditions of co-deposition to achieve the correct proportion of Zn and Se.
- d. Characterise the photocurrent generated by ZnSe deposits under blue (450 nm) light illumination and adjust the conditions of co-deposition to achieve efficient photocurrent generation.
- e. Establish the reliable deposition of p- and n-type doped ZnSe by co-deposition with ammonium sulphate $(NH_4)_2SO_4$ and gallium sulphate $Ga_2(SO_4)_3$ respectively.
- f. Confirm ZnSe deposits by XPS and optimise the conditions of co-deposition to achieve reliable doping.
- g. Form a ZnSe p-n junction between two electrically conductive carbon nanowires prepared by pyrolytic decomposition of butane inside a double-barrel fused silica nanopipette and test it for light emission.

The formation of p- and n- type deposits of ZnSe by co-deposition with (NH₄)₂SO₄ and Ga₂(SO₄)₃ on two separate nanowires in nanometre vicinity is challenging. Therefore, as a backup and to prove the concept of light emission from an electrodeposited semiconductor p-n junction, we planned to electroplate the p- and n-type deposits on two separate nanoelectrodes and subsequently establish electrical contact by micropositionning the two nanoelectrodes under optical control. In case of successful light emission we planned to re-iterate steps d to g to improve the efficiency of the light emission. The next section describes a selection of the experimental results obtained for the preparation of ZnSe deposits on large electrodes made of glassy carbon (GC) or carbon paper as well as on micrometre and sub-micrometre size disc electrodes made of Pt. Results are presented for their characterisation by SEM, XRD, energy dispersive X-ray (EDX) analysis and electroanalytical

methods. Particular effort was devoted to controlling and determining the p- or n-type nature of the deposits and several experimental results are presented to illustrate this part of the investigation. In this project electrodeposition is used to prepare the films as it is simple, fast and allows a fine degree of control over the growth, especially the film thickness and to some extent the film morphology. The electrodeposition of the semiconductor was carried out on different substrates, namely glassy carbon (3 mm \varnothing), platinum microdisc electrodes (25 μ m \varnothing), carbon paper and sub-micrometre diameter Pt wires (0.8 < \varnothing < 4 μ m) sealed in glass capillaries. Before each experiment the substrate electrode was characterised by recording cyclic voltammograms in 1 M H₂SO₄ until a stable voltammogram showing characteristic features was obtained. Where possible the electrodes were also characterised by recording diffusion-controlled voltammograms for the reduction of ruthenium hexamine, a model redox system with very fast electron transfer kinetics. For each microdisc the radius was determined from the limiting current observed on the diffusion controlled voltammograms and confirmed by observation in the SEM.

7.1 Voltammetry of Zn, Se and ZnSe films on GC electrode

In order to investigate the deposition potential for each constituent a series of experiments was carried out to determine the potential window for plating Zn and Se separately before proceeding to the codeposition of the two metals. Firstly, the applied potential was scanned towards negative values in acid solutions containing only Zn²⁺, Figure 7-1 (top).

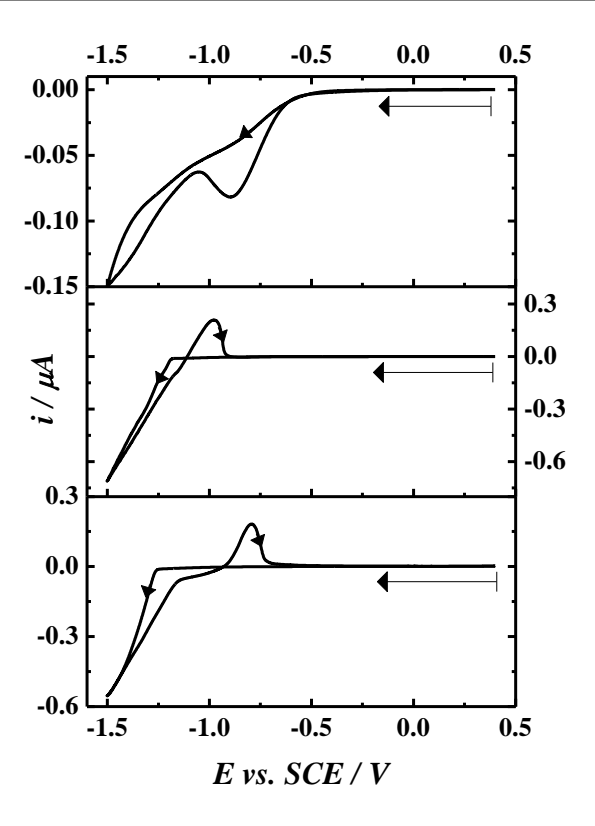


Figure 7-1 Cyclic voltammograms recorded at 10 mV s⁻¹ with a glassy carbon electrode (3 mm \varnothing) in (top) 0.01 M ZnSO₄, (middle) 0.01 M SeO₂, and (bottom) 0.03 M ZnSO₄ + 0.01 M SeO₂ pH=2.5 (pH was adjusted by adding a small drop of H₂SO₄), Ar purged for 20 min, at 25° C.

The current increase observed below -1 V corresponds to the beginning of Zn deposition.[207] The continued growth of the Zn deposit produces a greater current on the reverse scan until the potential is too positive and a sharp oxidation peak indicates the stripping of the Zn deposit; also it is reported that the reduction wave of Zn overlapped with hydrogen evolution.[208,209] Figure 7-1 (middle) illustrates the electrodeposition of Se in 0.01 M SeO₂. The reduction wave for the deposition of Se starts at a potential more positive than that for Zn but no stripping peak is observed on the reverse scan. This is evidenced by the red coloration of deposited amorphous selenium.[210]

$$H_2SeO_3 + 4H^+ + 4e^- \rightarrow Se + 3H_2O$$
 (7-1)

Figure 7-1 (bottom) shows the co-deposition of Zn and Se in a 0.03 M $ZnSO_4 + 0.01$ M SeO_2 pH 2.5 solution respectively. In figure 7-1 (bottom), the parameters were chosen to follow the conditions reported by Kröger [211,212], namely that the concentration of $ZnSO_4$ should be higher than that of SeO_2 ,

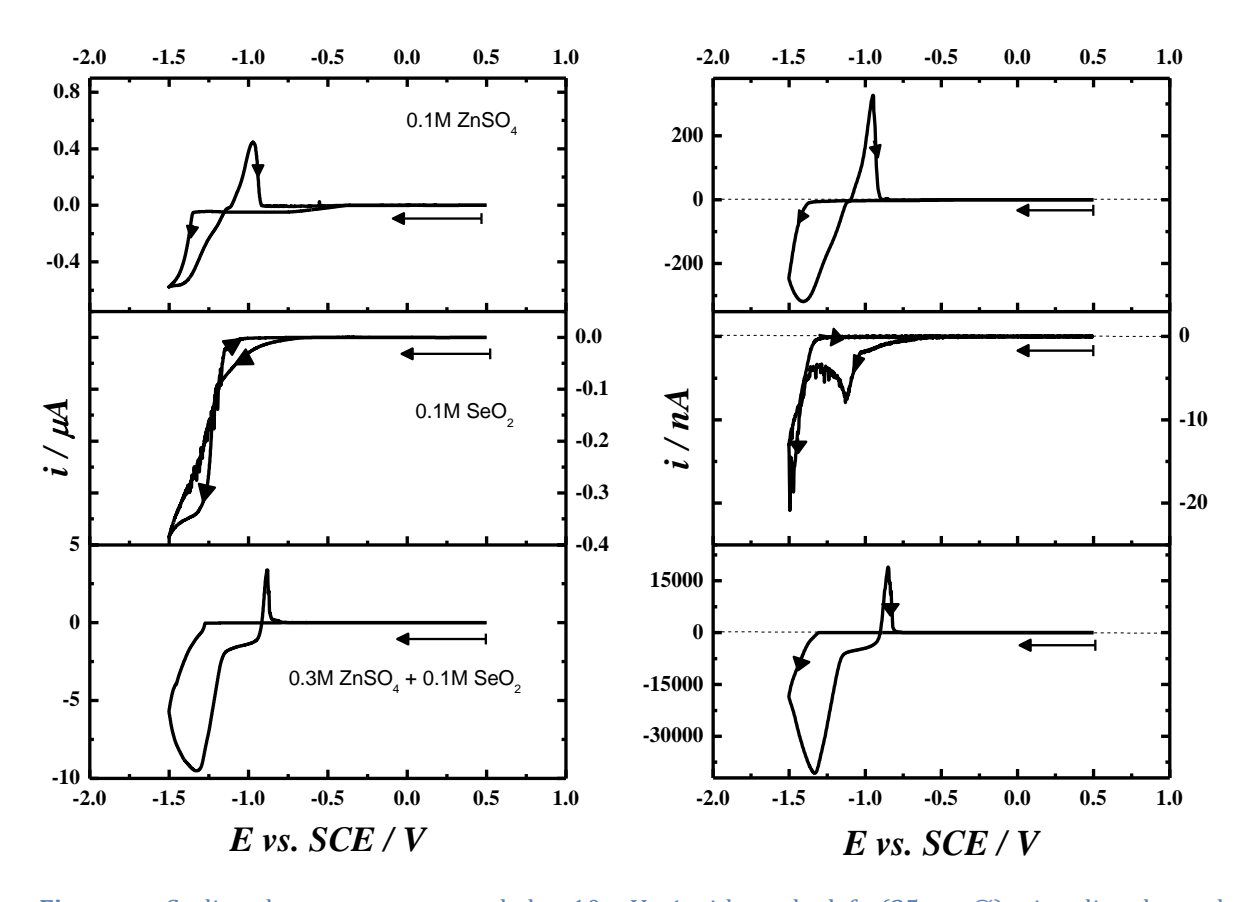


Figure 7-2 Cyclic voltammograms recorded at 10 mV s⁻¹ with on the left (25 μ m \varnothing) microdisc electrode, on the right Pt (3 μ m \varnothing) electrode in (a) 0.01 M ZnSO₄, (b) 0.01 M SeO₂ and (c) 0.03 M ZnSO₄ + 0.01 M SeO₂, pH=2.5 (pH was adjusted by adding a small drop of H₂SO₄), Ar purged for 20 min, at 25° C.

and that the pH should be limited to the window of H_2SeO_3 stability to avoid the presence of other selenium ions such as $HSeO_3^-$ or $SeO_3^{2^-}$ which could be simultaneously reduced on the electrode. Figure 7-2 (bottom) presents two reduction waves, one for the deposition of Se around -0.8 V and one for the co-deposition of Se and Zn around -1.2 V.[209,213-216]

$$Zn^{+2} + Se + 2e^{-} \rightarrow ZnSe \tag{7-2}$$

In figure 7-2, the electrochemistry of Zn, Se and co-deposition were investigated on Pt wires with different sizes. Both CVs in Figure 7-2 show the same features for the Zn, Se and co-deposition reduction waves as those shown in figure 7-1. The main observation is that the current for the co-deposition of ZnSe is significantly larger (about three times at -1.5 V after multiplying the Zn deposition current by three to account for the 0.3 M concentration used for the co-deposition) than the sum of currents for both reduction waves when deposition is carried in separate solutions. The other observation is that the co-deposition wave has lost the sigmoidal shape observed when Zn and Se are deposited separately. This shape is characteristic of steady state diffusion control at a microdisc. The change of shape and additional current suggest that the formation of ZnSe promoted the evolution of

hydrogen to more positive potentials. This is in agreement with the presence of bubbles during the codeposition of Zn and Se on larger electrodes.

Since ZnSe is a semiconductor known to produce a photocurrent under illumination,[209] the deposition process was also recorded under artificial illumination with a 450 nm (~2.76 eV) light emitting diode, Figure 7-3 red trace. Deposition under illumination shifts the reduction wave towards more positive potentials but the most striking feature is a doubling of the deposition current for the codeposition of Zn and Se [217]. A photocurrent in the cathodic region is consistent with the photoelectrochemical response of a p-type semiconductor; the current-voltage curve observed during plating under illumination therefore suggests that the deposited ZnSe film behaves as a p-type material.

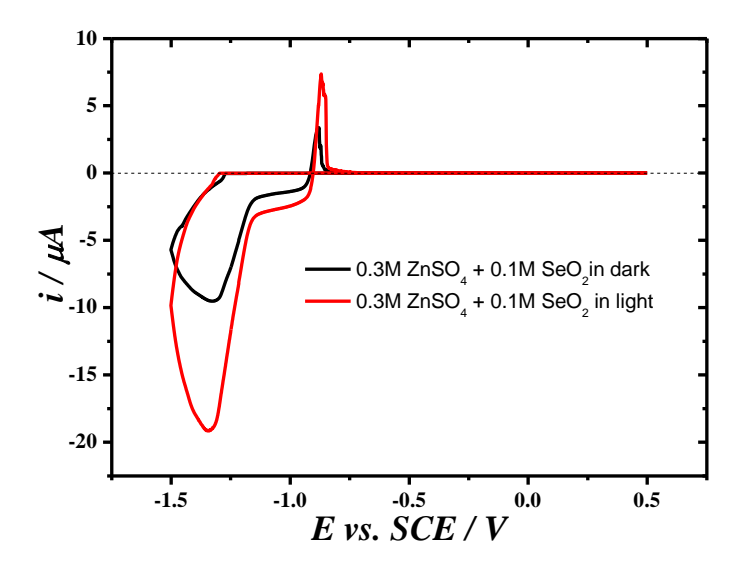


Figure 7-3 Cyclic voltammograms recorded at 10 mV s⁻¹ with a Pt microdisc (25 μ m \varnothing) in 0.03 M ZnSO₄ + 0.01 M SeO₂, pH=2.5 (pH was adjusted by adding a small drop of H₂SO₄), Ar purged for 20 min, at 25° C. Voltammogram recorded in the dark (Black) and under artificial illumination with a 450 nm light emitting diode (Red).

7.1.1 Voltammetry when doping with N and Ga

Doping is the introduction of impurities into a semiconductor to modify its conductivity. The dopant is integrated into the lattice structure of the semiconductor crystal and the number of valence electrons defines the type of doping. Elements with 3 valence electrons are used for p-type doping and valence 5 elements for n-doping. In this section the p- and n-type doping will be attempted using an electrochemical approach.

Attempts were therefore made to control the type of semiconductor produced by doping with an electron acceptor (to create p-type ZnSe) or donor (to create n-type ZnSe). While doping is normally performed in a subsequent step we decided to include the dopant in the plating solution to simplify the procedure especially because the objective was to electrodeposit two contiguous ZnSe centres

respectively doped p- and n-type. Figure 7-4 shows current voltage curves recorded during the codeposition of Zn and Se in presence of gallium, a group III element chosen to act as an electron acceptor.[218] The red CV shows similar voltammograms recorded in presence of nitrogen, a group V element chosen to donate electrons, while the black curve shows the voltammograms for deposition in absence of dopant. The insertion of dopant material affects the current and the position of the wave along the potential axis. The Se reduction wave starts to be seen at a potential of -0.4 V for undoped and n-doped but shifts more positive, to -0.14 V, when adding Ga. Moreover, the second reduction wave starts at -1.1 and -1.2 V for both undoped and n-type respectively but shifted around -1.0 V in presence of Ga. The highest current at -1.3 V is corresponding to undoped electrode. This electrodeposition can be performed while sweeping the potential as in Figures 7-4 but control of the film thickness and morphology is better achieved by electroplating at constant potential. Therefore in each case three lower potential limits were considered to select the appropriate plating potential for long depositions.

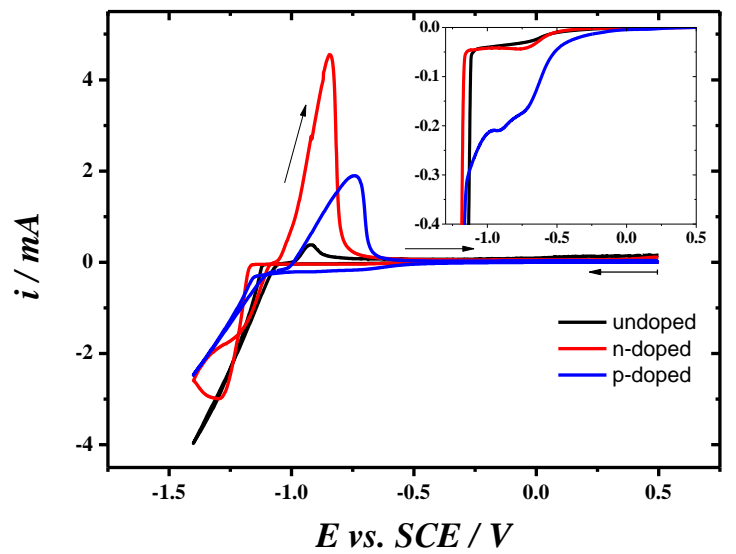


Figure 7-4 Cyclic voltammograms recorded at 50 mV s⁻¹ with a 3 mm \emptyset GC electrode: undoped (black) ZnSe using 1 mM SeO₂ and 0.1 M ZnSO₄; N doped (red) ZnSe using 1 mM SeO₂, 0.1 M ZnSO₄ and 0.5 M (NH₄)₂SO₄; Ga doped (blue) ZnSe using 1 mM SeO₂, 0.1 M ZnSO₄ and 0.5 M Ga₂(SO₄)₃. All were measured at **60** °C, a pH of 2.4 (pH was adjusted by adding a small drop of H₂SO₄) and purged with argon for 20 minutes. The inset shows the forward scan. The inset shows the forward scan (The y-axis is "i / mA" and the x-axis is "E / V" vs. SCE).

The following experiments aim to prepare three electrodes with the same deposition condition then test the electrodes electrochemically, to determine the type of semiconductor by studying the influence of the light on the semiconductor. Figure 7-5 shows current transients for the three types of semiconductors, electrodeposited on glassy carbon electrode, when stepping the potential from 0.4 V to -1.3 V vs SCE. This potential was chosen to ensure that both materials can be formed on the electrode. The transient for Ga doped material does not show double layer charging, then the current

increases as if a film was growing but then it decreases. The N doped transient has double layer charging initially then continuous growth of a phase, it is probably affected by H_2 bubbles. The N doped transient has similar shape that is consistent with the growth of a film. The undoped transient has a strange peak at the start then seems to show the growth of a film as the current increases.

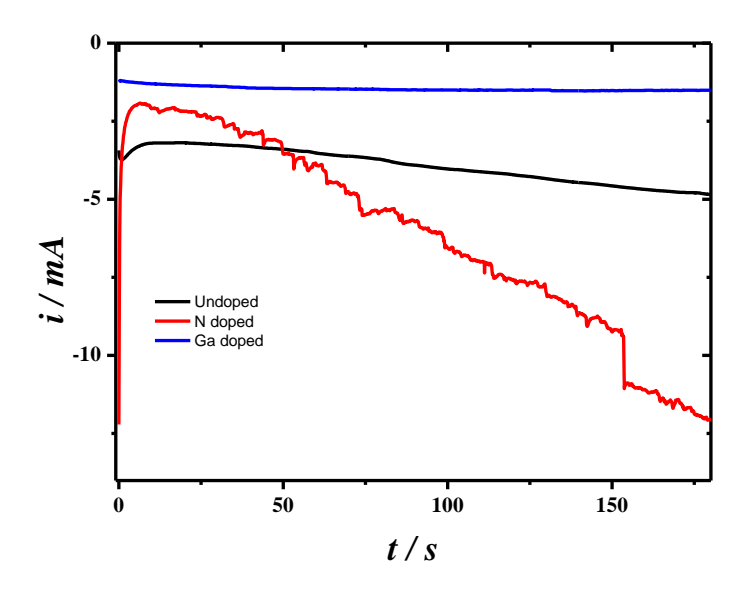


Figure 7-5 Current transients for ZnSe films on a 3 mm \emptyset GC electrode at -1.3 V vs. SCE for 180 s. Undoped (black) ZnSe using 1 mM SeO₂ and 0.1 M ZnSO₄; N doped (red) ZnSe using 1 mM SeO₂, 0.1 M ZnSO₄ and 0.5 M (NH₄)₂SO₄; Ga doped (blue) ZnSe using 1 mM SeO₂, 0.1 M ZnSO₄ and 0.5 M Ga₂(SO₄)₃.

The films prepared in Figure 7-5 were characterised by voltammetry in a separate solution in the dark and under illuminated conditions (450 nm LED) and the photocurrent (current under illumination minus current in the dark) was calculated, figure 7-6. The electron transfer at semiconductors can involve minority carriers generated by the light, and while in the dark only small currents flow when a depletion layer is formed at the semiconductor solution interface, illumination of the electrode gives rise to much larger photocurrents. The current – voltage curves for semiconductor electrodes are therefore not only dependent on whether the semiconductor is n- or p-type but also on whether the electrode is in the dark or illuminated with light of sufficient energy to promote electrons from the valence band to the conduction band. Instead of symmetrical Butler-Volmer plots obtained for metal electrodes, essentially diode-like behaviour is expected for extrinsic semiconductor (doped – semiconductor) electrodes.

Figure 7-6 shows the current voltage curves in the dark and under illumination for the undoped, Ga doped and N doped films. In contrast to the observation made in Figure 7-3, the undoped film shows a photocurrent in the anodic region, therefore suggesting it behaves as an n-type semiconductor. The Ga doped film shows a strong photocurrent in the cathodic region indicating a p-type behaviour while the

N doped film shows a significant photocurrent in the anodic regions with a large shift of the current voltage curve to negative potentials therefore indicating an n-type behaviour.

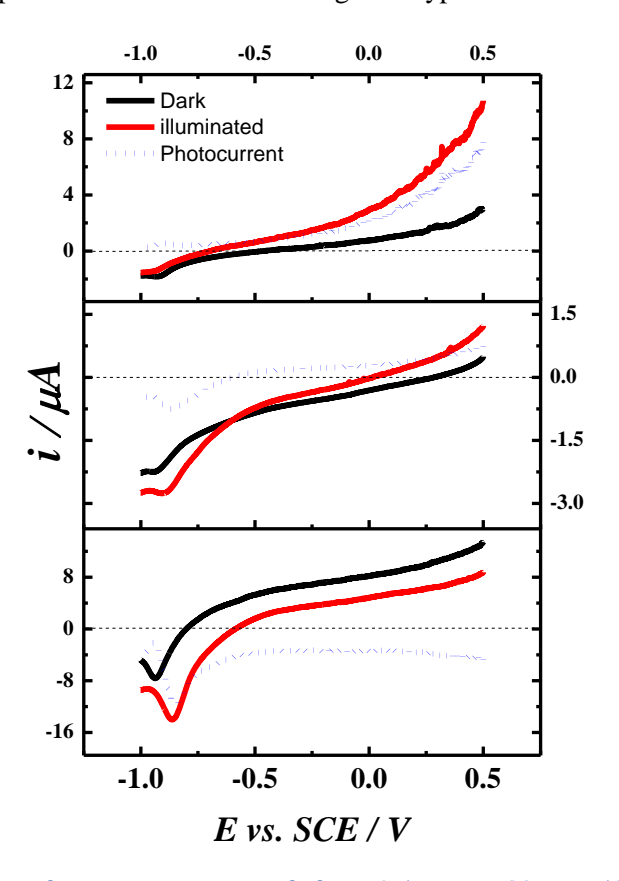


Figure 7-6 Linear sweep voltammograms recorded in 0.5 M Na $_2$ SO $_4$ at 50 mV s $^{-1}$ for ZnSe film electrodeposited on 3 mm Ø GC electrode by stepping the potential from 0.5 V to -1.2 V for 180 s to grow the film. Undoped (top) ZnSe using 1 mM SeO $_2$ and 0.1 M ZnSO $_4$; N doped (middle) ZnSe using 1 mM SeO $_2$, 0.1 M ZnSO $_4$ and 0.5 M (NH $_4$) $_2$ SO $_4$; Ga doped (bottom) ZnSe using 1 mM SeO $_2$, 0.1 M ZnSO $_4$ and 0.5 M Ga $_2$ (SO $_4$) $_3$. All purged with argon for 20 minutes. Illumination with a 450 nm LED. The photocurrent is the illuminated current minus the dark current.

A series of measurements was carried out with electrochemical impedance spectroscopy (EIS) to record the capacitance of the semiconductors as a function of applied potential under depletion conditions and produce a Mott-Schottky plot in order to determine the semiconductor type (n- or p-), estimate the flat band potential, $E_{\rm fb}$, and the number of acceptor and/or donor per cm³ in the semiconductor. The measurements were done with a Metrohm Autolab PGSTAT 302N with ECD and FRA modules. The bath contained 0.5 mol L⁻¹ Na₂SO4 and measurements were made by superimposing an a.c. potential, at frequencies of 1 kHz, on the applied potential (-0.6-0.2 V vs SCE). This oscillating voltage range was chosen to avoid inducing any Faradaic currents. Two assumptions were considered for the calculations to obtain the Nyquist plot (not shown):

a) There are two capacitances involved; the first one is referred to the space charge region and the second one to the double layer. Since these capacitances are in series, the total capacitance is the sum

of their reciprocals. The space charge capacitance is much smaller than the double layer capacitance (2-3 orders of magnitude), so the contribution of the double layer capacitance to the total capacitance is negligible. Therefore, the capacitance value calculated from the Nyquist plot is assumed to be the value of the space charge capacitance.

b) The equivalent circuit used in this model is a series combination of a resistor and a capacitance (the space charge capacitance). The capacitance is calculated from the imaginary component of the impedance (Z") using the relationship $Z'' = 1/2\pi fC$. The model is adequate provided the frequency is high enough (on the order of kHz). After that The Mott-Schottky plot was produced as follows:

The Mott Schottky relationship:

$$\frac{1}{C_{SC}^2} = \frac{2}{e\varepsilon\varepsilon_0 N_{a,d}} \left(E - E_{fb} - \frac{kT}{e} \right) \tag{7-3}$$

where $C_{\rm sc}$ = capacitance of the space charge region, ε = dielectric constant of the semiconductor, $\varepsilon_{\rm o}$ = permittivity of free space, $N_{a,d}$ = donor density (electron donor concentration for an n-type semiconductor or hole acceptor concentration for a p-type semiconductor), E = applied potential and $E_{\rm fb}$ = flat band potential.[219,220]

Plotting (C_{SC}^{-2} vs. E) produced linear responses with opposite gradients. For the undoped ZnSe film the negative gradient is consistent with a p-type material, while for the N doped ZnSe film the positive gradient indicates an n-type material and the Ga doped ZnSe film also shows p-type characteristics, figure 7-7. The flat band potential can be obtained by extrapolating the linear part of the C_{SC}^{-2} vs. E plot to the $C_{SC}^{-2} = 0$ axis (infinite capacitance), at which: E_{fb} - kT/e_0 where kT/e_0 is a temperature-dependent term equal to 0.0257 V at 298 K. This term represents the contribution of the conduction band electrons and is generally neglected in the calculations. The density of acceptors and/or donors in the semiconductor can be calculated from the slope of the plot of C_{SC}^{-2} against E, the flat band potential of p-type electrode is more anodic (positive) than that of n-type electrode.[220] Analysing the data obtained by the electrochemical impedance according to Mott-Schottky plots was not always accurate, since the linearity in some plots was not clear such as for the plot related to the Ga-doped film. The flat band potential E_{fb} and the number of donor and acceptor were calculated from equation 7-3, E_{fb} were -0.452 V and -0.5 V for the film doped with Ga and N respectively. The number of acceptor from the film doped with Ga is 3.15×10^{17} cm⁻² and the number of donor from the film doped with N is 2×10^{13} cm⁻². This analysis by electrochemical impedance only carried out once.

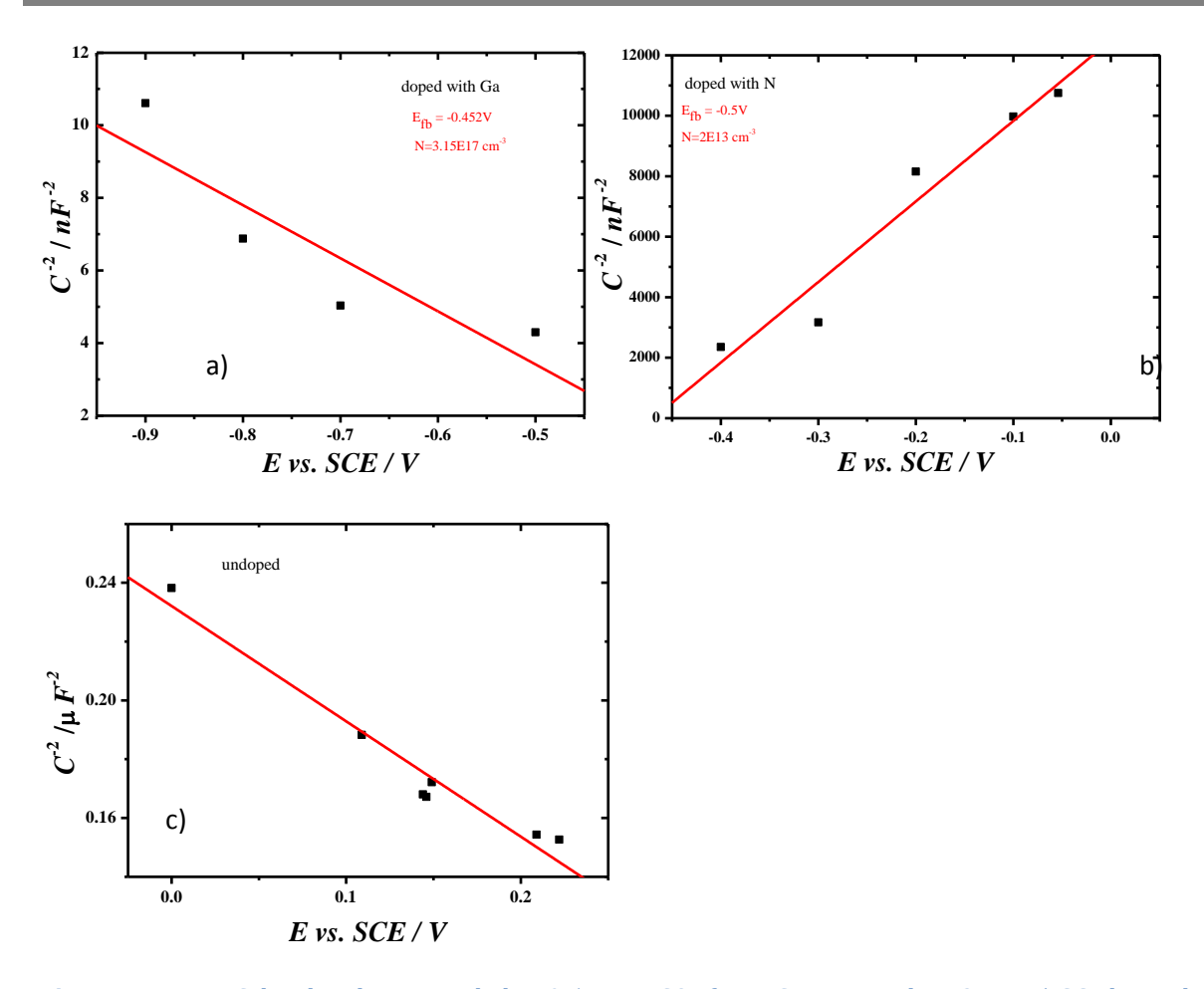


Figure 7-7 Mott-Schottky plots recorded in 0.5 M Na₂SO₄ for ZnSe prepared on 3 mm \emptyset GC electrode by stepping the potential from 0.5 V to -1.3 V vs. SCE for 180 s in: a) Ga doped ZnSe using 1 mM SeO₂, 0.1 M ZnSO₄ and 0.5 M Ga₂(SO₄)₃, b) N doped ZnSe using 1 mM SeO₂, 0.1 M ZnSO₄ and 0.5 M (NH₄)₂SO₄ and c) undoped ZnSe using 1 mM SeO₂ and 0.1 M ZnSO₄; All purged with argon for 20 minutes. **pH=2.5** (pH was adjusted by adding a small drop of H₂SO₄).

Further characterisation was carried in the SEM, Figure 7-8, to assess the thickness and texture of the films, and with EDX analysis to determine their elemental composition and the Zn/Se ratio. The ZnSe deposit forms small clumps on the GC surface and the morphology of the film varies when introducing impurities in the solution. It is clear that the films prepared in presence of dopant material have different structures. The more dense deposits are found on undoped electrode and it is in agreement with the CV where the highest current is found for undoped films. From SEM images the undoped film is a very dense agglomerate of undefined shape particles. When adding N the film has a needle-like structure; in contrast addition of Ga creates large spherical particles distributed randomly on the surface with sizes circa 17 μ m. The EDX analysis (not shown) of these three films revealed they consisted mostly of zinc and little selenium, probably because of the low concentration of Se used initially; so a new set of solutions, with a higher concentrations of SeO₂ was made to investigate the influence of concentration and potential on both components.

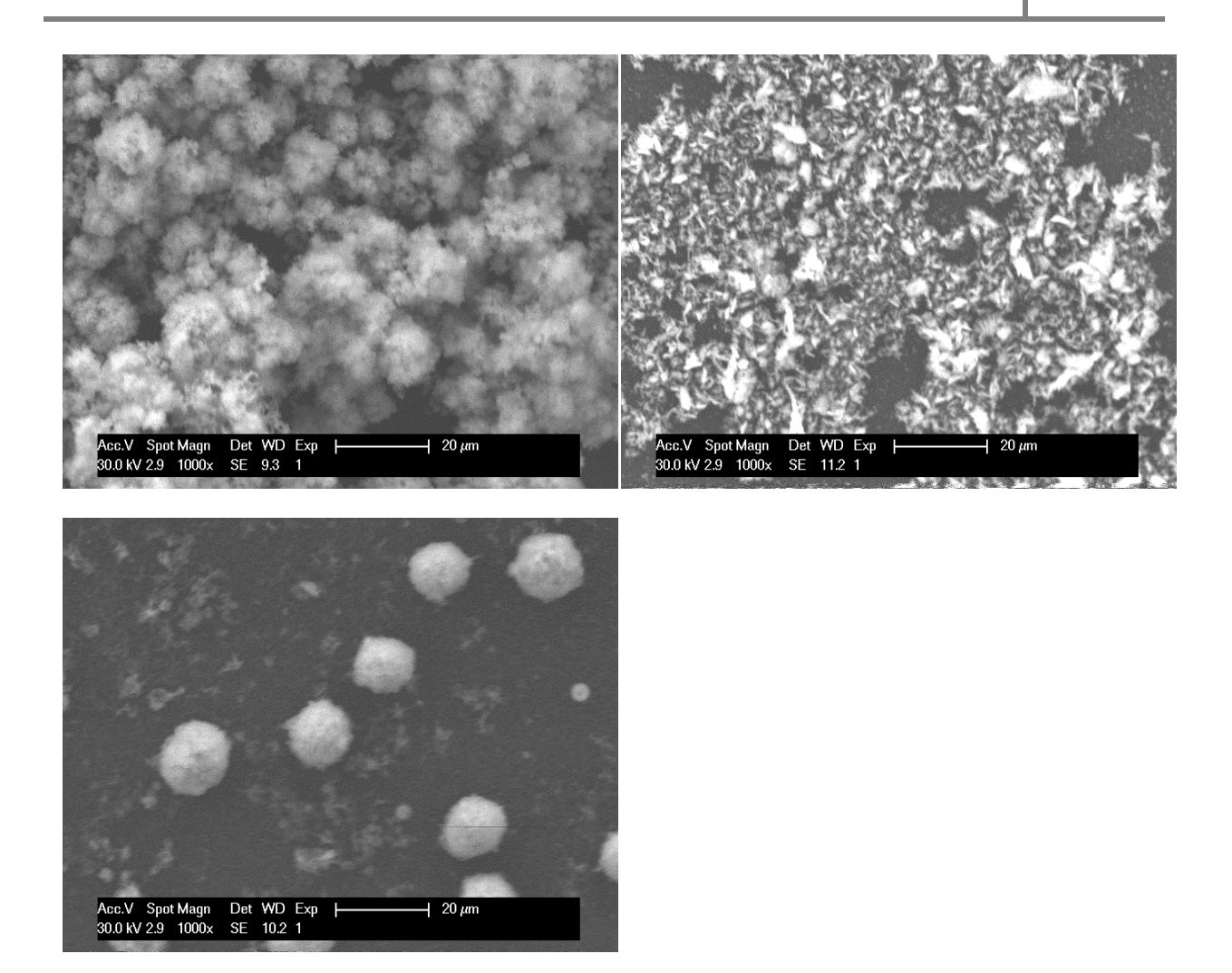


Figure 7-8 SEM images for ZnSe prepared on 3 mm \emptyset GC electrode by stepping the potential from 0.5 V to -1.3 V vs. SCE and in (top left) 0.1 M ZnSO₄ + 1 m M SeO₂ + 0.5 M (NH₄)₂SO₄, (top right) 0.1 M ZnSO₄ + 1 m M SeO₂, and (bottom) 0.1 M ZnSO₄ + 1 m M SeO₂ + 0.5 M Ga₂(SO₄)₃. All purged with argon for 20 minutes.

7.1.2 Influence of the SeO₂ concentration

Figure 7-9 shows CVs for the deposition of ZnSe from baths containing different SeO₂ concentrations. They were recorded at 50 mV s⁻¹ with 3 mm ϕ glassy carbon electrodes between 0.4 and -1.3 V vs. SCE. The plot in the top is related to N-doped electrodes with two different concentrations of selenium dioxide. On the forward scan, the Se reduction wave at higher concentration of SeO₂ has higher current than the one deposited with diluted SeO₂, while the second reduction wave of Zn starts more positive than the one with lower concentration of SeO₂. The current for Zn reduction is not significantly affected by the different concentrations of SeO₂ but the shape of the Zn reduction wave is much less clear. Moreover on the back scan, the anodic peak related to Zn stripping is smaller in the concentrated Se bath; we suspect this is due to the flaking of the film during hydrogen evolution.

The effect of SeO₂ was also studied in a solution containing Ga. The influence of SeO₂ on Ga-doped ZnSe CV shown in Figure 7-4 (bottom); the presence of Ga led to significant increase in current at

potential -1.3 V and also it affected the magnitude of maximum current of Zn stripping peak. The maximum current of Zn stripping peak increases three times when high concentration of SeO₂ was added to deposition bath.

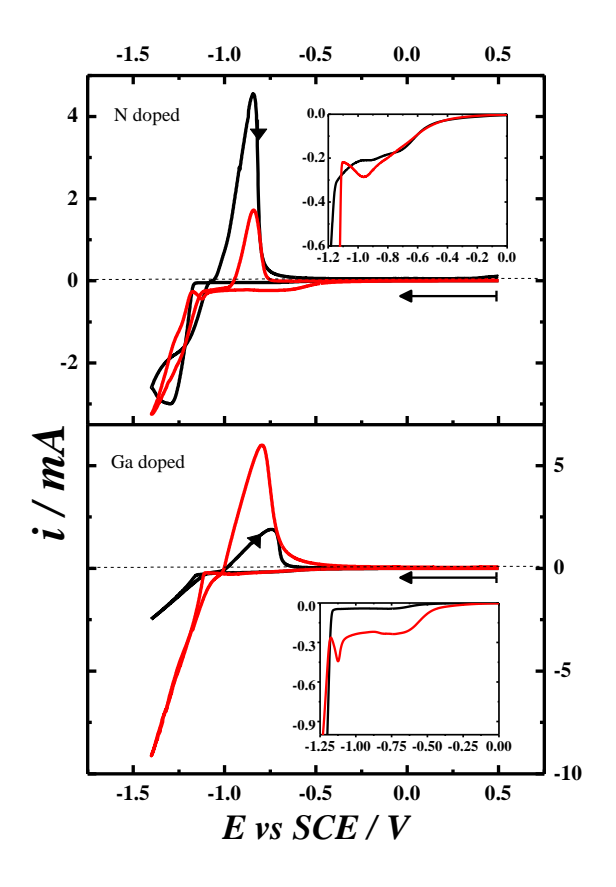


Figure 7-9 Cyclic voltammograms recorded at 50 mVs⁻¹ with a 3 mm Ø glassy carbon electrode in (top-black) a solution of 1 M ZnSO₄ + 0.001 M SeO₂ + 0.5 M (NH₄)₂SO₄; (top- red) a solution of 0.1 M ZnSO₄ + 0.01 M SeO₂ + 0.5 M (NH₄)₂SO₄; (bottom black) in a solution of 0.1 M ZnSO₄ + 0.001 M SeO₂ + 0.5 M Ga₂(SO₄)₃; (bottom- red) a solution of 0.1 M ZnSO₄ + 0.01 M SeO₂ + 0.5 M Ga₂(SO₄)₃. Magnifications of the reduction peak of the 1st forward scan are shown in the bottom right corner of each graph. All solutions were kept at a constant temperature of 60 °C and within a pH range of 2- 2.4 during the measurements. Between measurements, the solutions were purged with argon for 20 minutes. The inset shows the forward scan (The y-axis is "i / mA" and the x-axis is "E / V" vs. SCE).

Chronoamperometry experiments were then carried out (not shown) in order to bring the ratio of Zn / Se in the films close to 1:1. The potential was swept from 0.5 V to the deposition potential of -1.3 V vs. SCE and held for 180 s to grow the films. All solutions were purged with argon for 20 minutes. After the deposition the films were characterised using EDX. All the results obtained from EDX are summarised in table 7-1. It is obvious from the table that the best ratio Zn / Se for both doped materials was obtained with 0.01 M of SeO₂.

Table 7-1 EDX results for ZnSe films after stepping from 0.5 V to -1.3 V vs. SCE on 3 mm Ø glassy carbon
electrode for different concentrations of SeO ₂ (as shown in the table) for 180 s.

Dopant element	SeO ₂ / M	Potential / V	% Weight Zn	% Weight Se
Ga	0.01	-1.3	44	56
Ga	0.001	-1.3	93	7
N	0.01	-1.3	44	57
N	0.001	-1.3	68	32

7.1.3 **Influence of the deposition potential**

Due to the desire to achieve a reasonable Zn / Se ratio, experiments were carried out to investigate the role of the deposition potential using the best concentration of SeO_2 , 0.01 M. For each type of semiconductor, several films were prepared from the same solution, using different deposition potentials. The potential was stepped from 0.4 V to different values ranging from -1.25 to -1.3 V vs. SCE. The films were then analysed using EDX, figure 7-10, and SEM.

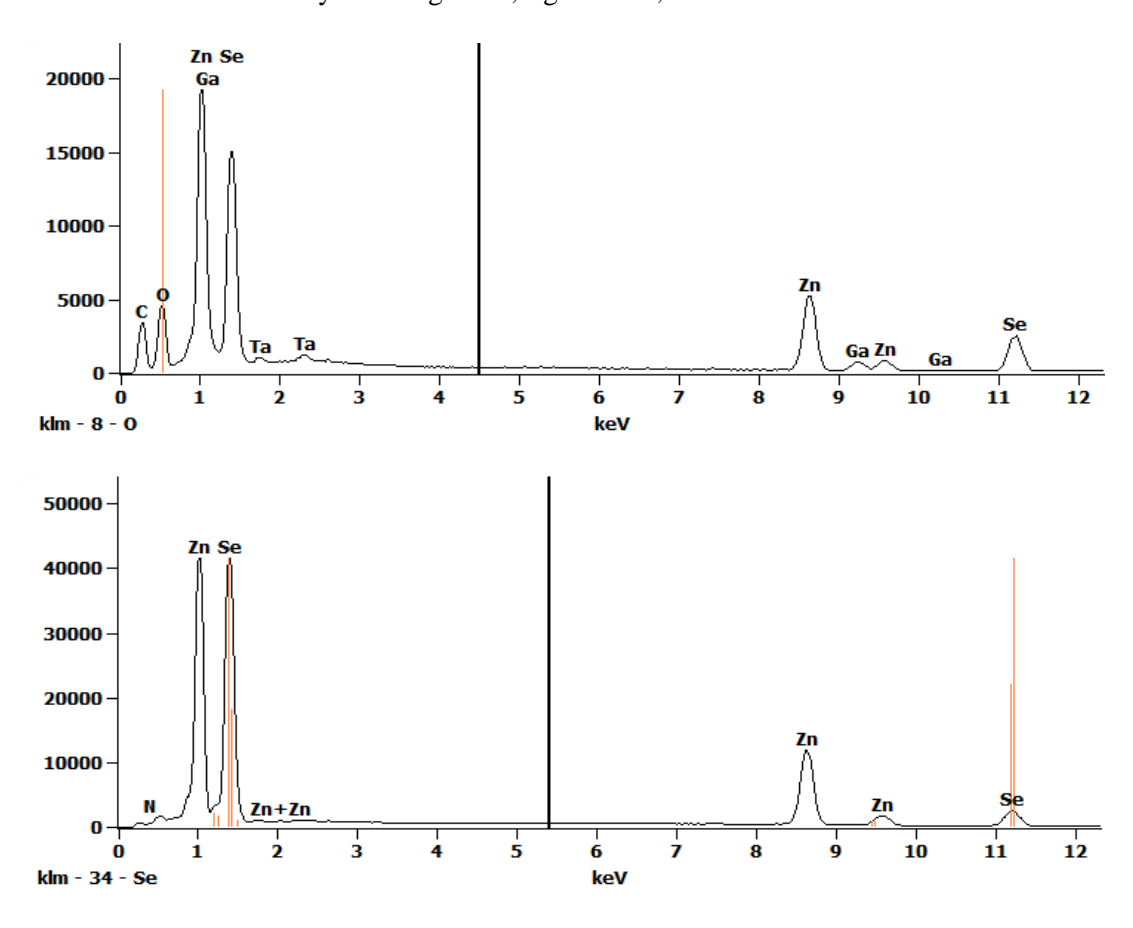


Figure 7-10 EDX spectra for ZnSe films deposited on a 3 mm Ø glassy carbon electrode in 0.1 M ZnSO₄+ 0.01 M SeO₂ and: (top) 0.5 M Ga₂(SO₄)₃ deposited by stepping from 0.5 V to -1.15 V vs. SCE. (bottom) 0.5 M (NH₄)₂SO₄ deposited by stepping from 0.5 V to -1.2 V. The deposition time was kept constant at 180 s. The accelerating voltage was 10 KeV.

All the EDX patterns clearly indicate the presence of zinc and selenium and confirm that the samples are composed of Zn and Se elements. Figure 7-10 shows the best sample for both doped electrodes.

From the results of EDX analysis, table 7-2, it can be seen that for Ga doped films a good ratio of Zn / Se was found at potential of -1.3 and -1.15 V vs. SCE while for N doped film the best Zn / Se was found at -1.3 and -1.2 V vs. SCE. However, large overpotentials such as -1.3 V should be avoided because some deposits were observed to fall of the electrode under the effect of hydrogen evolution. As a result, all subsequent depositions were performed at the foot of the reduction wave, negative enough to deposit the film, but hopefully positive enough not to activate hydrogen evolution. Table 7-2 summarises all the results obtained from EDX.

Table 7-2 Summary of EDX results for ZnSe films deposited on a 3 mm \emptyset glassy carbon electrode in 0.1 M ZnSO₄+ 0.01 M SeO₂, and: a) 0.5 M Ga₂(SO₄)₃ and b) 0.5 M (NH₄)₂SO₄, by stepping from 0.5 V to different deposition potentials (shown in the table). The deposition time was kept constant at 180 s.

Dopant material	E / V vs. SCE	% Weight Zn	% Weight Se
	-1.300	44	57
a) Ga- doped	-1.200	17	84
	-1.175	17	83
	-1.150	55	45
	-1.300	68	32
b) N-doped	-1.275	85	15
_	-1.250	83	17
	-1.200	63	37

The SEM images show different textures when varying the deposition potentials. Moreover, in all cases the deposits appear granular, rough and porous. None of the conditions used produced smooth films. In all cases the deposits do not appear to adhere well to the GC substrate thus indicating they will be easily lost from the electrode. Moreover, it was noticed that the lower overpotential applied led to more dense deposits as seen in figure 7-11. In contrast, the films deposited at high overpotential appeared to produce less dense deposits, due to the influence of hydrogen bubbles evolved at this overpotential; this makes the film less adhesive to the substrate and easily lost. For films deposited in the presence of $GaSO_4$ it seems that the more negative the deposition potential the finer the deposit is. Images a and b in figure 7-11 almost show films. They are obviously very porous but at least they seem to look like films. Images c and d show a random distribution of micrometric centres. In presence of $(NH_4)_2SO_4$ the deposits appear to form feathery structures, figure 7-11 (f and g). In Figure 7-11g the film appeared as a soft aggregation of particles with narrow size distribution. Figure 7-11h clearly shows a granular deposit.

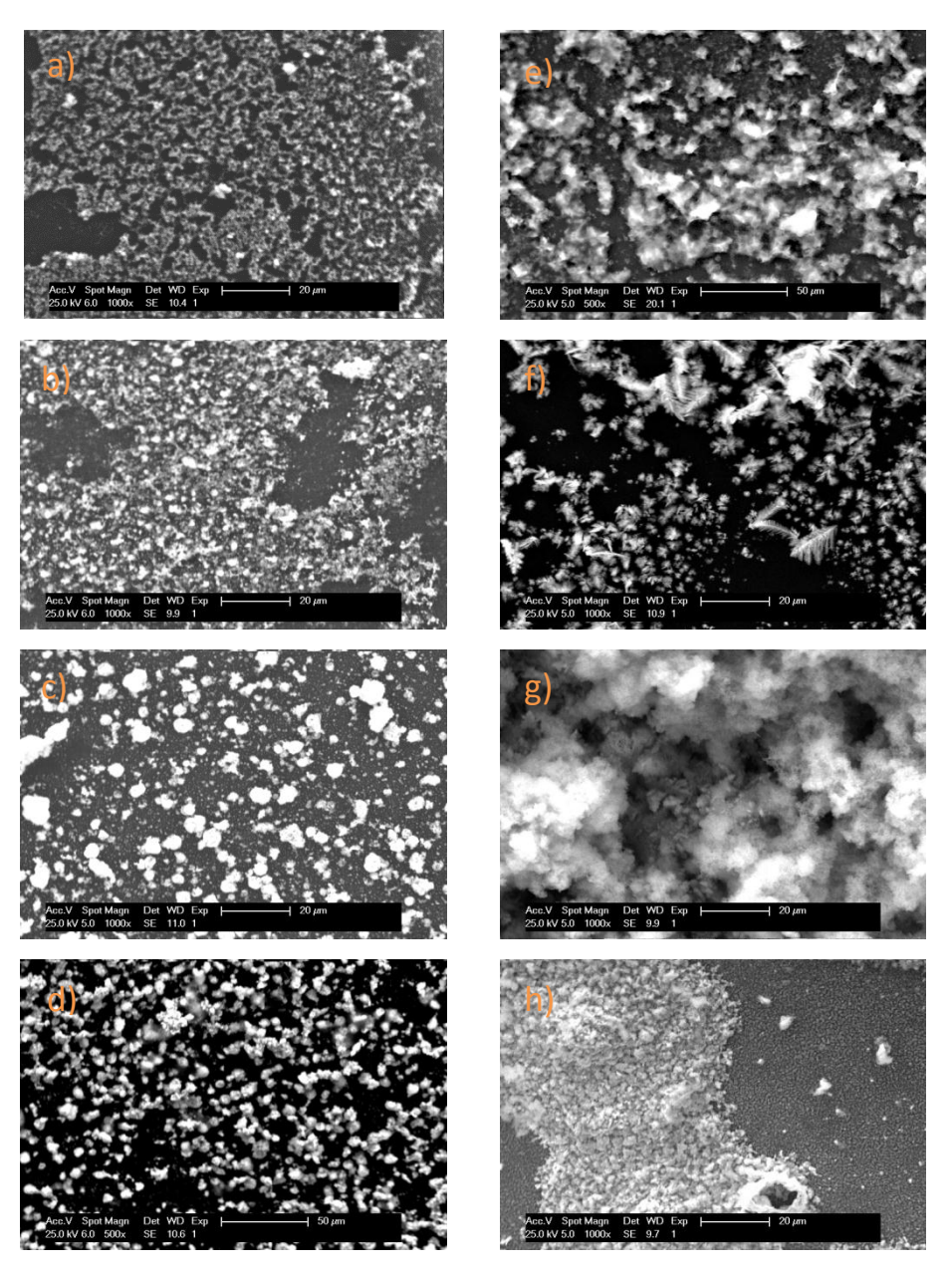


Figure 7-11 SEM images for ZnSe films deposited on 3 mm Ø glassy carbon electrodes in 0.1 M ZnSO₄ + 0.01 M SeO₂ and: (left column) 0.5 M Ga₂(SO₄)₃ (right column) 0.5 M (NH₄)₂SO₄. The films were deposited by stepping the potential from 0.5 V vs. SCE to (a)-1.3 V, (b)-1.2 V, (c)-1.175 V, (d)-1.15 V, (e)-1.3 V, (f)-1.275 V, (g) -1.25 V and (h)-1.2 V. The deposition time was kept 180 s.

7.2 Electrodeposition of ZnSe on carbon paper

Due to the difficulty in characterising the films deposited on glassy carbon by XRD, the carbon paper (TGP-H-060) was chosen as a substrate for several tests. The carbon paper was cut in small square shapes with dimensions of 5 mm \times 5 mm; before use the electrode was cleaned by soaking in acetone then in distilled water. It was then connected to the potentiostat in a three electrode configuration. Micrometre thick films of ZnSe were electrodeposited on the carbon paper at constant potential and subsequently annealed at 300 $^{\circ}$ C to induce crystallisation.

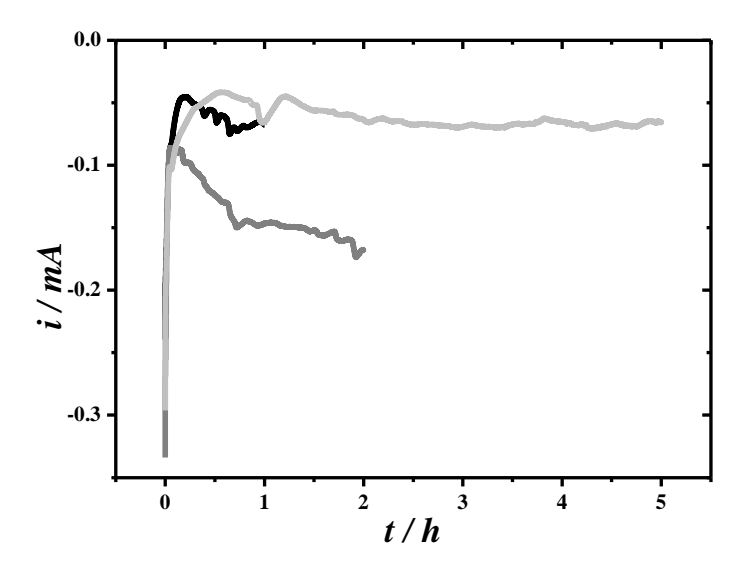


Figure 7-12 Current transients for the deposition of ZnSe on a carbon paper electrode. The potential was stepped from +0.4 V to -1.3 V vs. SCE for (black) 1 hr, (dark grey) 2 hr, and (light grey) 5 hr in 0.03 M ZnSO₄ + 0.01 M SeO₂, pH=2.5, Ar purged for 20 min, at 25° C.

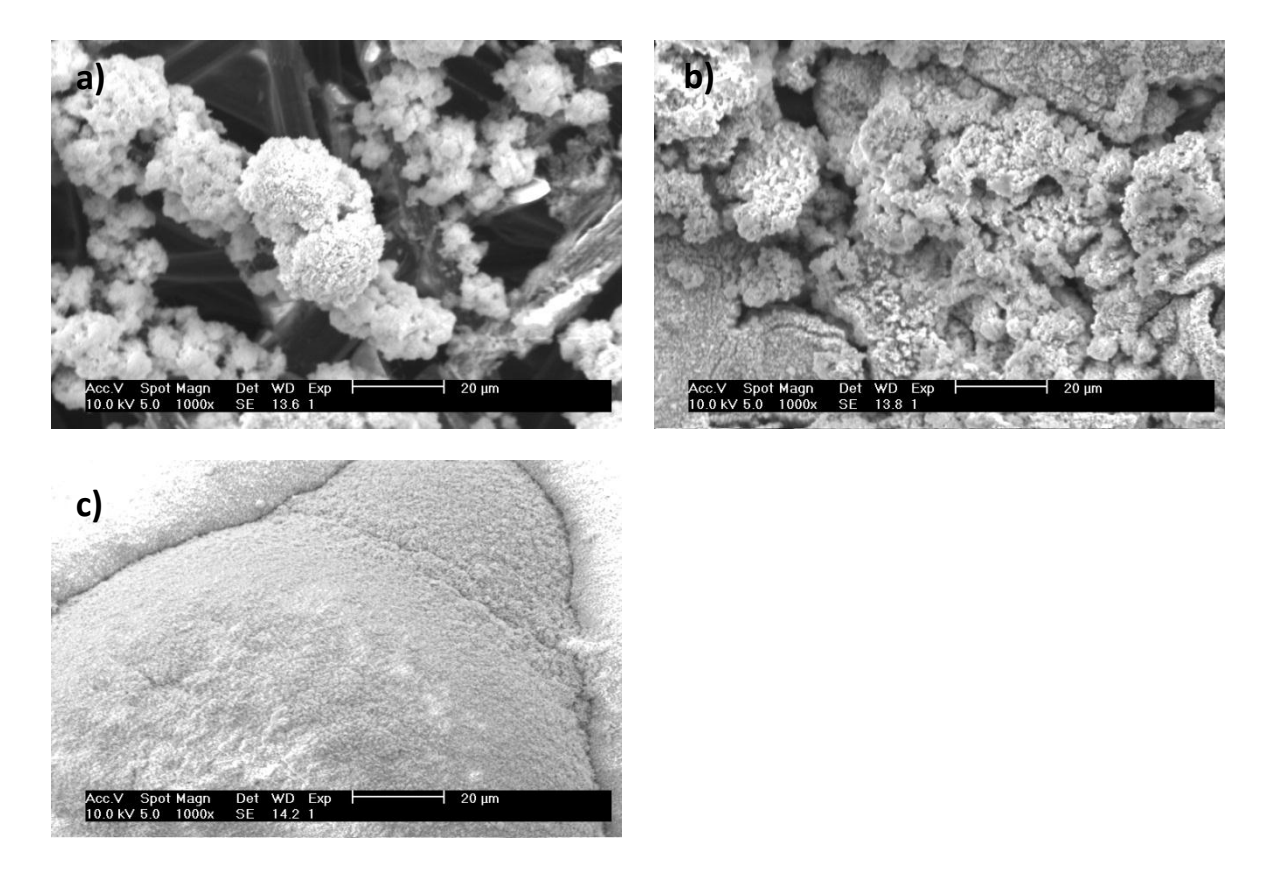


Figure 7-13 SEM images of the ZnSe coated carbon paper electrode after undergoing a potential step from +0.4 V to -1.3 V vs. SCE for (a) 1 hr, (b) 2 hr, and (c) 5 hr in 0.03 M ZnSO₄ + 0.01 M SeO₂, pH=2.5, Ar purged for 20 min at 25° C.

Figure 7-12 shows the current transients for three samples recorded for three deposition times. The difference in the magnitude of the current transients is due the use of different pieces of carbon paper for each experiment. The surface morphology of carbon paper shows fibres held together (it is clear in figure 7-12a) each piece of carbon fibre might have different arrangement of those fibres. Further characterisation was carried in the SEM, Figure 7-13, to assess the thickness and texture of the films, and with EDX analysis to determine their elemental composition. Within 1 hr the deposit forms small clumps along the C fibres of the paper; after 2 hr the film completely covers the fibres and after 3 hr it is no longer possible to distinguish the C fibre mesh. Throughout, the texture seems to consist of submicrometre size platelets. The C paper was initially chosen to facilitate analysis by XRD but its woven network of C fibres turned out to be useful in demonstrating that micrometre and submicrometre deposits could be formed on individual C fibres akin to individual microelectrodes. EDX analysis, figure 7-14, clearly shows the films consist of Zn and Se but that the Zn/Se ratio decreases as the deposition time increases. The film is slightly richer in Zn after 1 h, the two elements appear in equal quantity after 2 h but hardly any Zn is found after 5 h.

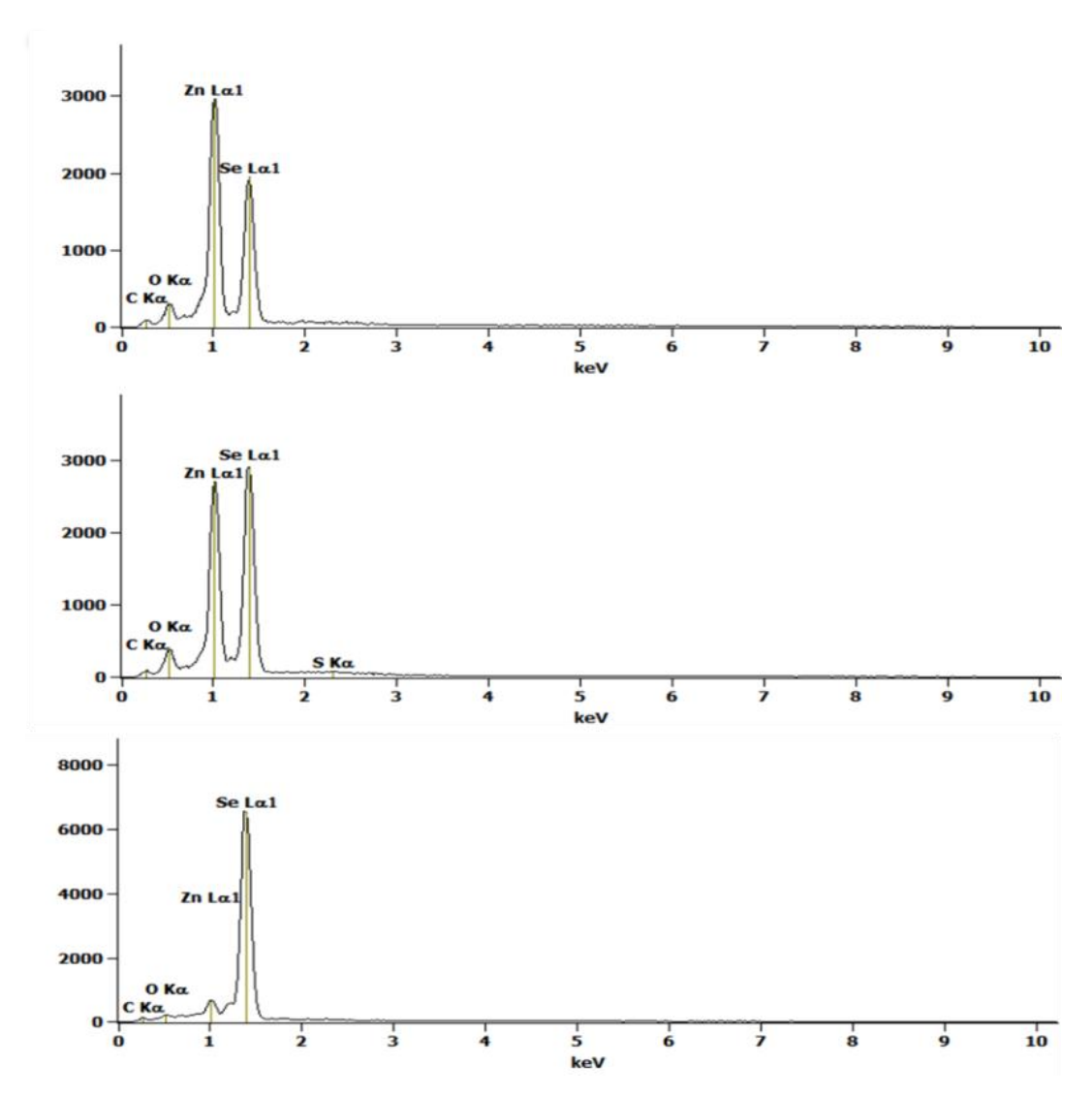


Figure 7-14 EDX analysis of the ZnSe coated carbon paper electrodes prepared by potential step from +0.4 V to -1.3 V vs. SCE for (top) 1 hr, (middle) 2 hr and (bottom) 5 hr in 0.03 M ZnSO₄ + 0.01 M SeO₂, pH=2.5, Ar purged for 20 min at 25° C. The accelerating voltage wad 10 KeV

7.2.1 Effect of ZnSO₄ and SeO₂ concentrations

To study the effects of ZnSO₄ and SeO₂ concentrations on the N-doped ZnSe thin film composition, several solutions, with varying concentrations of these two compounds, were prepared. Table 7-3 below summarises the concentration of each compound in these solutions. Most of the solutions were within a pH range of 2-2.5. However, due to the high concentrations of SeO₂, solutions H and I were more acidic, with pHs of 1.84 and 1.83 respectively.

Table 7-3 Summary of the $ZnSO_4$, SeO_2 and $(NH_4)_2SO_4$ concentrations used to study the effect Zn salt and SeO_2 concentrations on the N-doped ZnSe thin film composition.

Solution	ZnSO ₄ concentration / M	SeO ₂ concentration / M	(NH ₄) ₂ SO ₄ concentration / M
A	0.1	0.001	0.5
В	0.2	0.001	0.5
С	0.3	0.001	0.5
D	0.1	0.010	0.5
Е	0.2	0.01	0.5
F	0.3	0.01	0.5
Н	0.2	0.1	0.5
I	0.3	0.1	0.5

For each solution, the following experiments were performed using a $5 \text{ mm} \times 5 \text{ mm}$ carbon paper electrode:

- > Cyclic voltammetry at 50 mV s⁻¹ for all solutions listed in table 7-3.
- ➤ Chronoamperometry for two hours at a deposition potential that had been determined from the CV.
- ➤ Images of the films deposited onto the C paper were recorded using an electron microscope. EDX analysis was also taken.
- ➤ The films were annealed in a 300 °C oven for approximately 50 minutes. Any colour change was noted.
- ➤ Images of the annealed films were recorded using the electron microscope and EDX analysis was performed.

Figure 7-16 shows the effect of varying the SeO₂ concentration using 0.1, 0.01 and 0.001 M. The CVs for the three compositions are similar to those obtained with glassy carbon; the clearest observation appears to be that the Zn reduction wave is significantly affected by the SeO₂ concentration. The reduction wave of Zn started to be observed at -1.15, -1.2 and -1.3 V, with corresponding currents of 0.06, 0.08 and 0.4 mA, for baths containing selenium dioxide of 0.001, 0.01 and 0.1 M respectively. The maximum current for the Zn reduction on the forward scan was found at -23.6, -14.28 and -5.3 mA for 0.001, 0.01 and 0.1 M respectively. It is found that the concentration of SeO₂ influenced the amount of Zn deposited on the substrate with less Zn obtained with higher concentration of SeO₂. Using high concentrations of Se compound lead to lower the ratio of Zn / Se.[221]

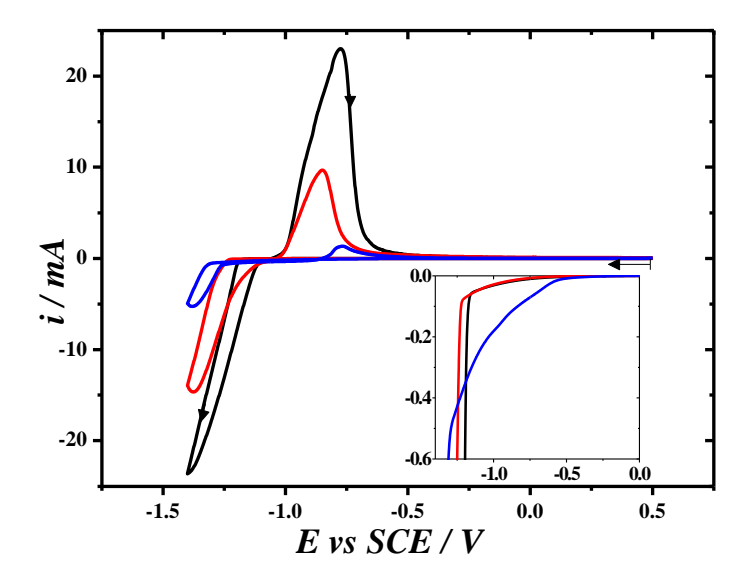


Figure 7-15 CVs of N-doped ZnSe solutions (pH= 2-2.5) containing 0.5 M (NH₄)₂SO₄, 0.3 M ZnSO₄ and SeO₂ concentrations of: (**black**) 0.001 M, solution C; (**red**) 0.01 M, solution F; (blue) 0.1 M, solution I. All CVs were recorded at room temperature, without temperature control, on a 5 mm X 5 mm carbon paper electrode. All solutions were purged with argon for 20 minutes before experiments. The inset plot shows a zoom on the reduction waves of ZnSe, the y-axis is "i / mA" and the x-axis is "E / V" vs SCE

Chronoamperometry experiments were carried out for two hours in these baths. The potential was stepped from 0.4 V vs. SCE to potentials chosen in the foot of the Zn reduction waves to avoid the influence of hydrogen bubbles which evolved at slightly more negative potentials. Then the films were characterized by SEM and EDX to observe the structure of the films and assess their Zn/Se ratio.

SEM images, figure 7-16, show that all the deposits have a high porosity, roughness and non-uniform structure. With 0.001 M SeO₂ the ZnSe nanoparticles aggregate into randomly distributed flower-shaped structures which cover the entire surface; each flower unit is about 100 μm in diameter. When the concentration was 0.01 M a different structure was obtained. Image 7-16, 2nd row, still shows some flower shaped structures but also micro porous spheres with diameters circa 88 μm. The formation of micro spheres might be attributed to hydrogen evolution as the hydrogen bubbles may adsorb on the electrode surface,[221] then force the deposits to form around the bubbles. Various hydrogen bubble sizes may lead to different pores size.[222] The pore diameters were found to range between 3 and 5 μm.

Figure 7-16, 3^{rd} row, shows that a high concentration of selenium produced dense aggregated granules of ZnSe. At higher magnification (not shown) the particle size was found to range between 0.1 and 1 μ m.

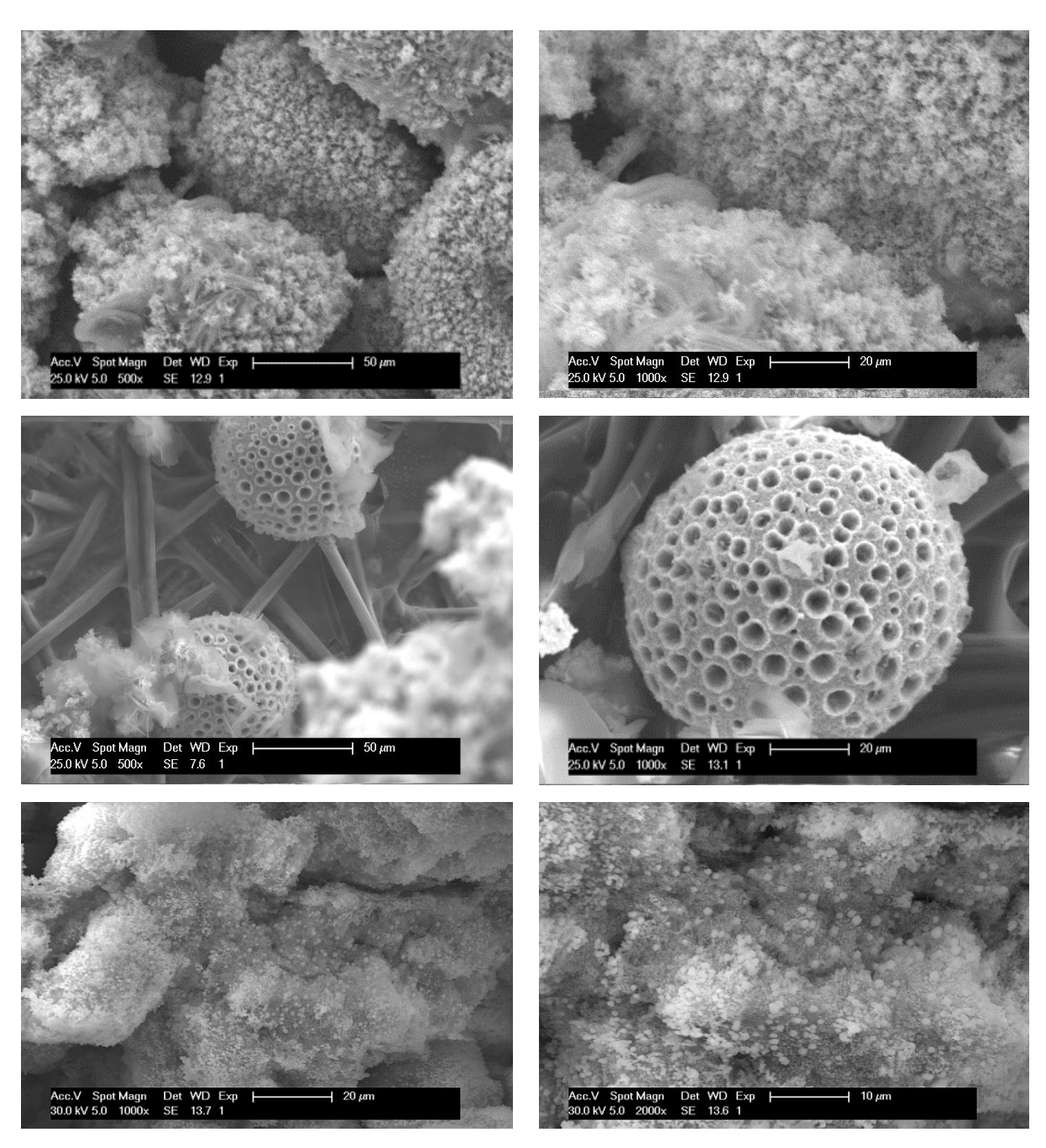


Figure 7-16 SEM of ZnSe films deposited in solutions (pH= 2-2.5) containing 0.5 M (NH₄)₂SO₄, 0.3 M ZnSO₄ and SeO₂ concentrations of: (top) 0.001 M, solution C; (middle) 0.01 M, solution F; (bottom) 0.1 M, solution I. The deposits were prepared by stepping the potential from 0.5 V to -1.195 V, -1.24 V and -1.315 V respectively for 2 h at room temperature, without temperature control, on a 5 mm X 5 mm carbon paper electrode. Images in the right column were taken with higher magnification than the images in left column.

The second set of experiments was carried out in three baths containing fixed concentrations of $0.2 \,\mathrm{M}$ ZnSO₄, $0.5 \,\mathrm{M}$ (NH₄)₂SO₄ with pH kept constant between 2 and $2.5 \,\mathrm{and}$ SeO₂ concentrations respectively of 0.001, 0.01 and $0.1 \,\mathrm{M}$. So the only difference with the previous experiment was the lower Zn salt concentration. Figure 7-17 shows the voltammograms recorded on carbon paper in the

three solutions. The Se reduction waves started at -0.7, -0.67 and -0.61 V respectively with corresponding current of -0.004, -0.009 and -0.01 mA. Also the Zn reduction waves shifted negatively when increasing the SeO_2 concentration, to potentials -1.18, -1.2 and -1.3 V and the currents were -0.05, -0.13 and -0.36 mA for 0.001, 0.01 and 0.1 M respectively.

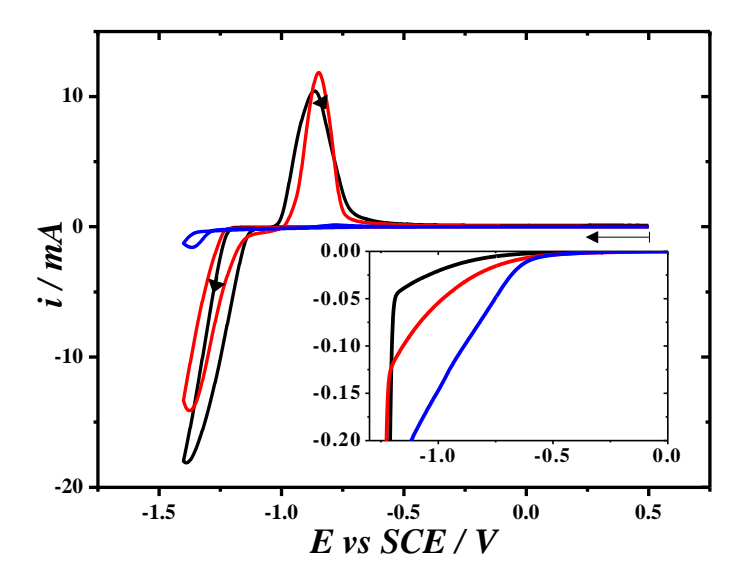


Figure 7-17 CVs for the deposition of ZnSe in solutions (pH= 2-2.5) containing 0.5 M (NH₄)₂SO₄, 0.2 M ZnSO₄ and SeO₂ concentrations of: (black) 0.001 M, solution B; (red) 0.01 M, solution E; (blue) 0.1 M, solution H. All CVs were recorded at room temperature, without temperature control, on 5 mm X 5 mm carbon paper electrodes. All solutions were purged with argon for 20 minutes before experiments. The foot of the reduction peak is magnified in the inset, the y-axis is "i / mA" and the x-axis is "E / V" vs SCE.

To investigate the effect of Se concentration, experiments were carried out by potential step. The condition of deposition such deposition time, the deposition potential and temperature were kept constant for all the experiments, but different structures of ZnSe were obtained. The films morphology and the effect of annealing the samples at temperature of 300 $^{\circ}$ C are shown in figure 7-18. It was reported that annealing can increase the crystallinity and change the film colour.[209] Before annealing a flower-like structure of ZnSe can be seen with a size circa 80-140 μ m; particles smaller than 0.2 μ m can be found surrounded with petal-like shapes in the centre of each flower-like structure. These petals were lost after annealing and this is clear in the second row images. Comparing images 7-18a with 7-16(top) the flower-like structure are the same, therefore, decreasing Zn salt concentration did not affect the structure of the ZnSe films.

When increasing the Se concentration to 0.01 M, the low magnification SEM image, Figure 7-18b, shows that ZnSe has numerous random oriented small needle deposits which partially cover the surface. In some region we can observe approximately $80~\mu m$ diameter spherical agglomerates randomly distributed on the carbon fibres. These spheres have micro-scale porous bone-like structure with size ranging between 12 and $0.8~\mu m$. The spheres surface is granular. Moreover, the spheres have

the same shape as that shown in figure 7-16b, which again suggests that the Zn salt concentration has not affected the morphology of the deposits. After annealing the sample, the deposits that covered the spheres is completely disappeared.

Figure 7-18c shows the ZnSe films are decorated by branched structures which are totally different from those seen in figure 7-16 (bottom).

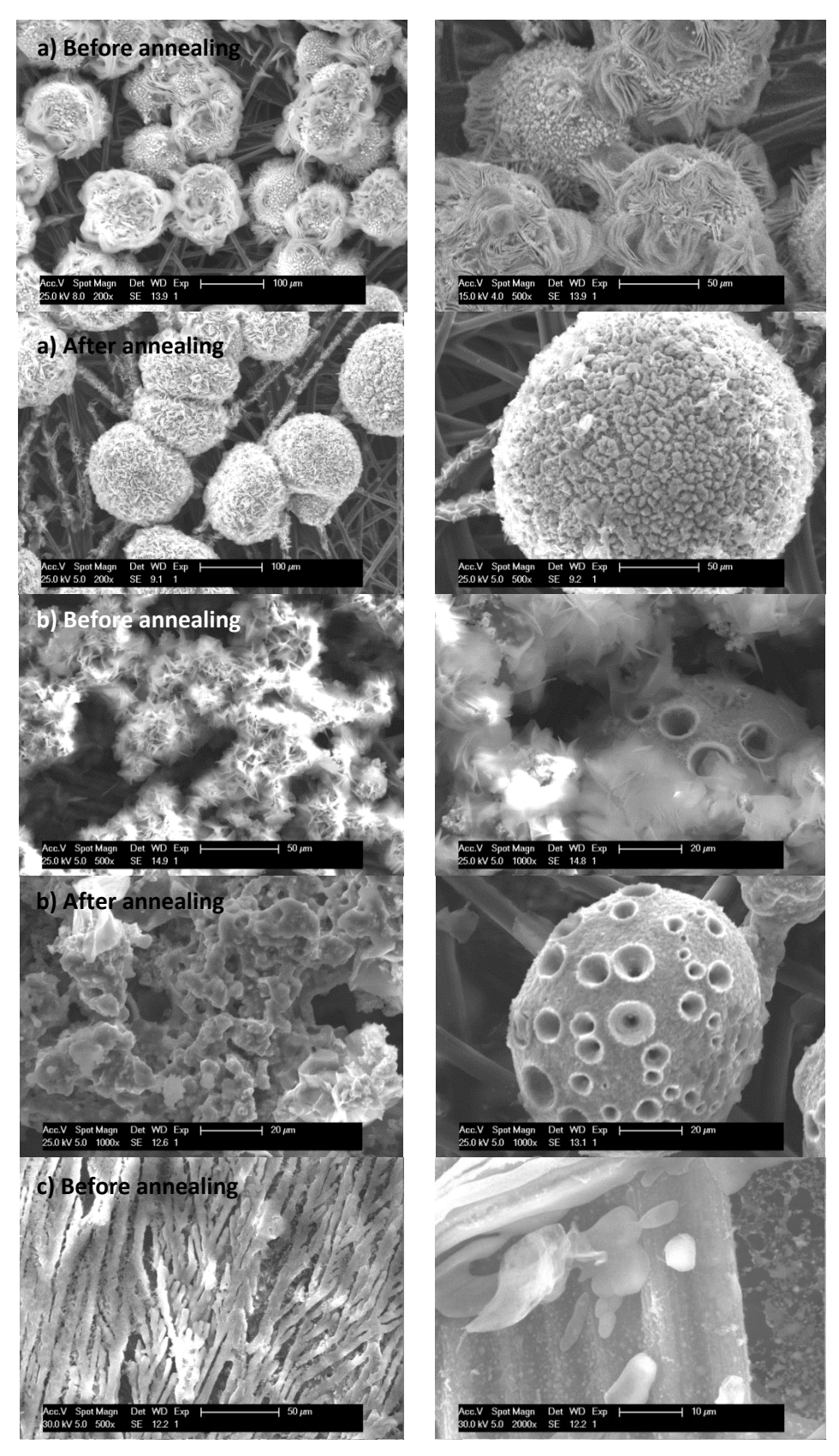


Figure 7-18 SEM images of ZnSe deposits prepared in solutions (pH= 2-2.5) containing 0.5 M (NH₄)₂SO₄, 0.2 M ZnSO₄ and SeO₂ concentrations of: (a) 0.001 M, solution B; (b) 0.01 M, solution E; (c) 0.1 M, solution H. All the films were prepared by stepping the potential from 0.5 to -1.215 V, -1.24 V and -1.33 V vs. SCE respectively, at room temperature, on a 5 mm X 5 mm carbon paper electrode. The thermal treatment of ZnSe crystal was done in a nitrogen atmosphere at a temperature of $300 \,^{\circ}\text{C}$.

Figure 7-19 shows the effect of the SeO₂ concentration on the Zn and Se reduction waves; in this experiments the concentration of Zn salt was kept low at 0.1 M and the dopant element was 0.5 M (NH₄)₂SO₄. Once again we observe that the low concentration of SeO₂ (0.001 M) requires a larger overpotential to drive the reduction of Se. The Zn reduction wave shifted positively with concentrated solution of SeO₂ was used.

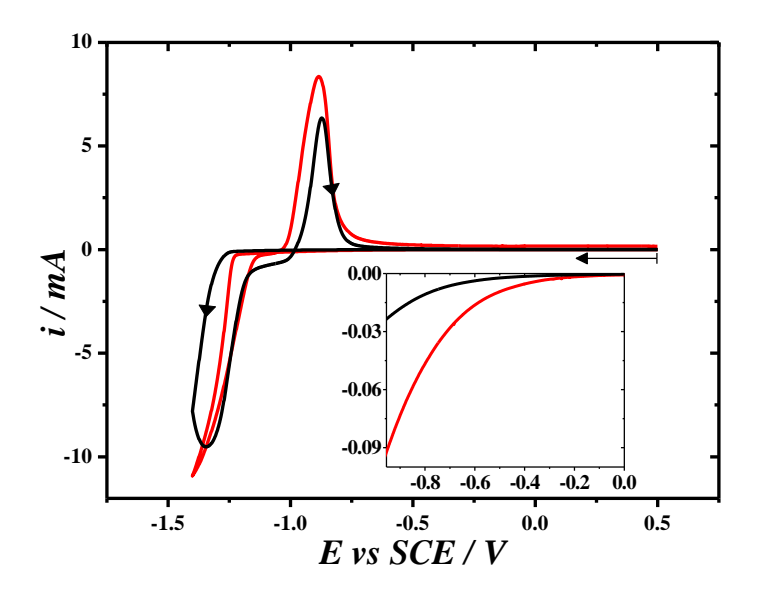


Figure 7-19 CVs for the deposition of ZnSe in solutions (pH= 2-2.5) containing 0.5 M (NH₄)₂SO₄, 0.1 M ZnSO₄ and SeO₂ concentrations of: (black) 0.001 M, solution A; (red) 0.01 M, solution D. All CVs were recorded at room temperature, without temperature control, on a 5 mm X 5 mm carbon paper electrode. All solutions were purged with argon for 20 minutes before experiments. The inset shows the Se reduction wave on the forward scan, the y-axis is "i / mA" and the x-axis is "E / V" vs SCE.

Potential steps were chosen to deposit films on C paper, in both solutions the composition was 0.5 M (NH₄)₂SO₄, 0.1 M ZnSO₄ and SeO₂ concentrations of 0.001 M, solution A and 0.01 M for solution D. The potential was stepped from 0.5 V to -1.23 V and -1.27 V vs. SCE for solution A and D respectively for two hours. The films were analysed by SEM and EDX. Figure 7-20 shows the films structure and the annealing influence. The film deposited from solution A has a flower structure; annealing did not seem to have any effect on the film. The ZnSe film prepared from solution D shows nanoparticles aggregated to form a flower-shaped structure distributed randomly and covering the entire surface. After annealing the film at 300 °C in nitrogen atmosphere, micro porous spheres were observed.

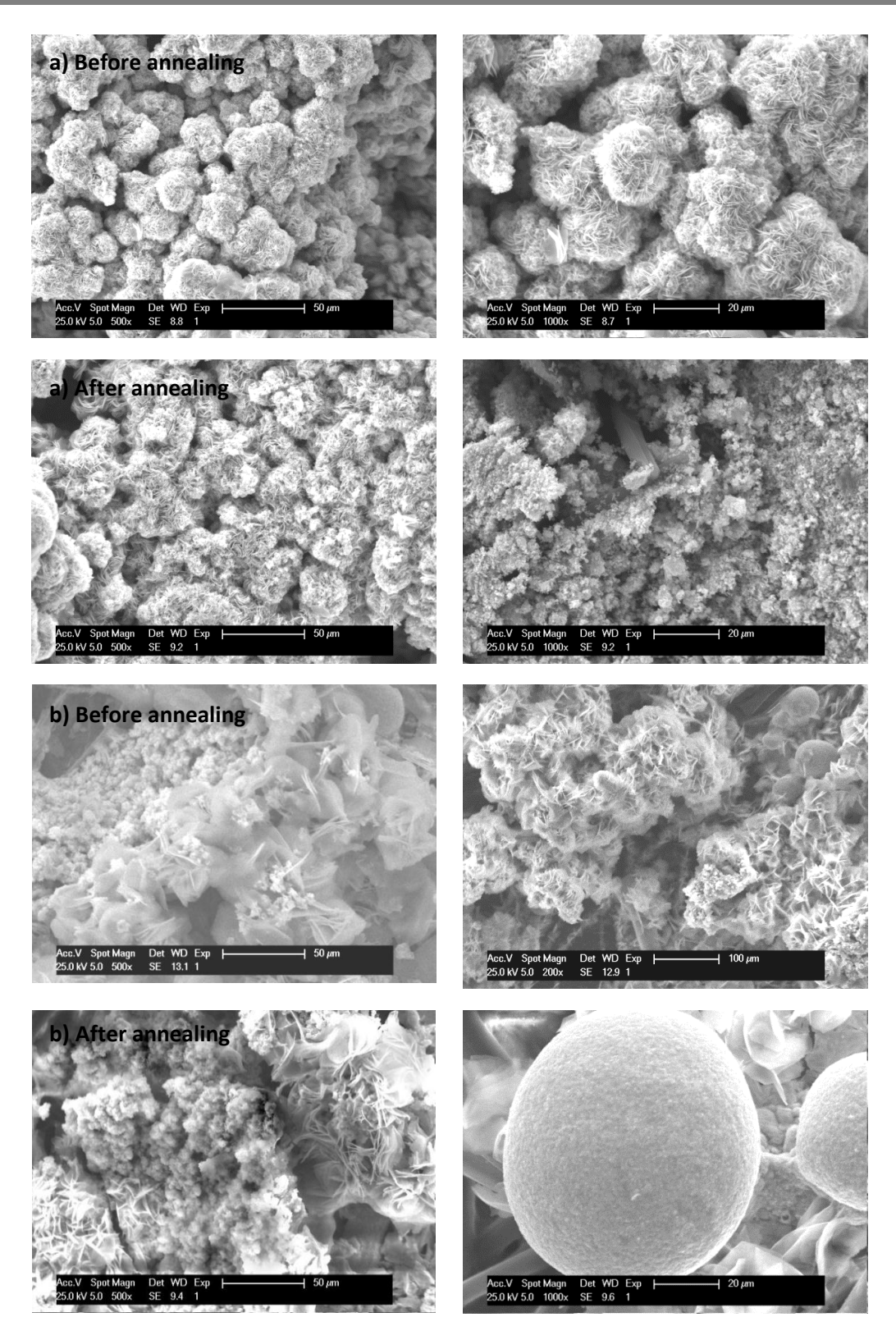


Figure 7-20 SEM images of ZnSe deposits prepared in solutions (pH= 2-2.5) containing 0.5 M (NH₄)₂SO₄, 0.1 M ZnSO₄ and SeO₂ concentrations of: (a) 0.001 M, solution A and (b) 0.01 M, solution D. The potential was stepped from 0.5 V to -1.23 V and -1.27 V vs. SCE for solution A and D respectively for two hours at room temperature, on a 5 mm X 5 mm carbon paper electrode. The thermal treatment of ZnSe crystal was done in the nitrogen atmosphere at $300 \,^{\circ}\text{C}$.

The EDX pattern shows elements Zn and Se for all the samples and the atomic ratio is found to vary when changing the concentration of these elements in the deposition bath. Table 7-4 shows the composition of the solutions tested, the % weight of each element found in the film and the colour of the ZnSe films before and after annealing. Samples F, H and I gave the best Zn/Se ratios (i.e. were the nearest to 50/50). The EDX patterns for these three samples are shown in figure 7-21.

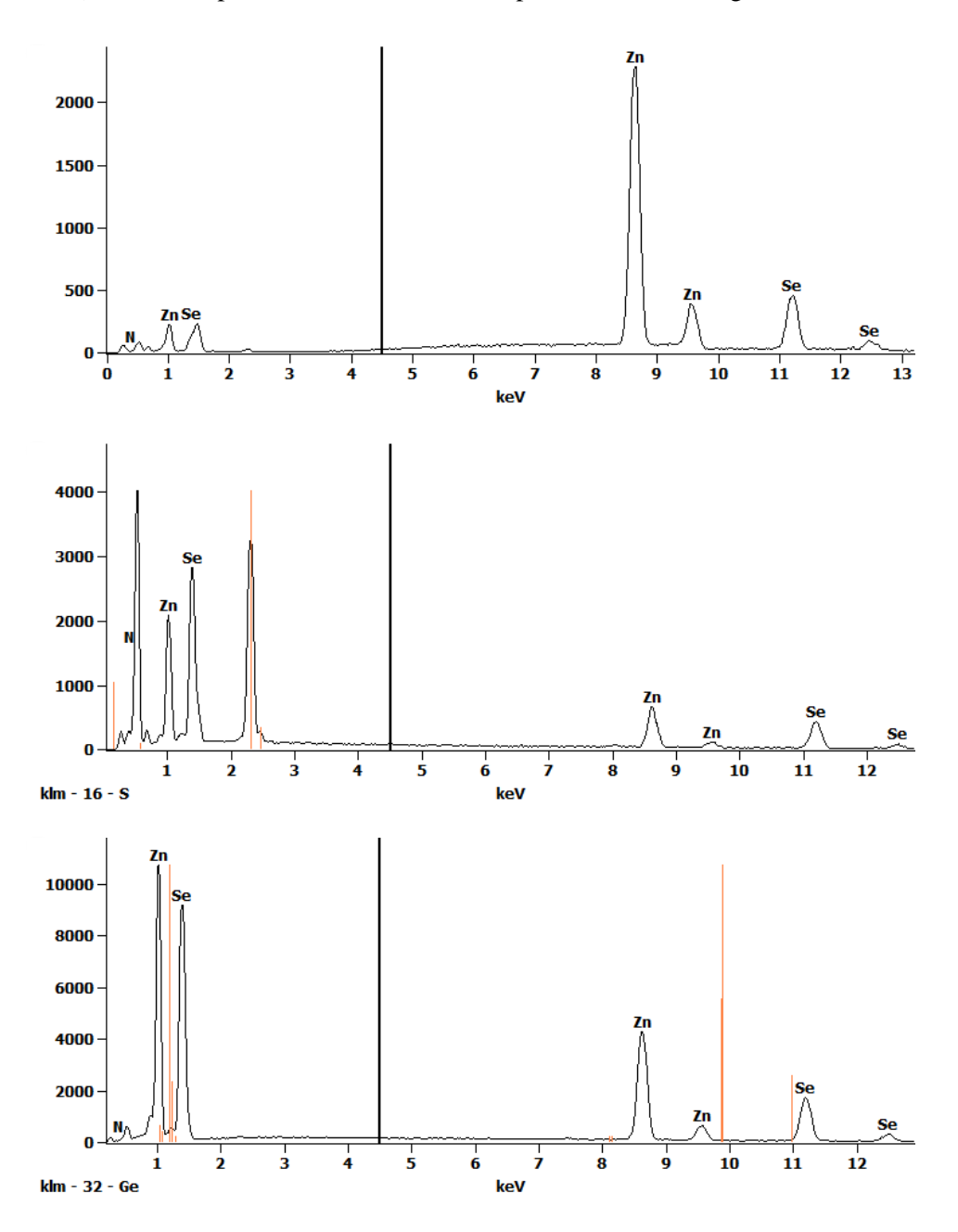


Figure 7-21 EDX patterns of the ZnSe deposits prepared in solutions (pH= 2-2.5) containing 0.5 M $(NH_4)_2SO_4$ and :(top) solution **F** 0.3 M ZnSO₄, 0.01 M SeO₂, (middle) solution **H** 0.2 M ZnSO₄, 0.1 M SeO₂ and (bottom) **I** 0.3 M ZnSO₄, 0.1 M SeO₂. The potential was stepped from 0.5 V to -1.24 V, -1.33 V and -1.315 vs. SCE for solution F, H and I respectively for two hours at room temperature, on a 5 mm X 5 mm carbon paper electrode. The accelerating voltage was 10 KeV.

Solution	ZnSO ₄ /	SeO ₂ /	$(NH_4)_2SO_4$ /	% Weight	% Weight	Colour	Colour after
	M	M	M	Zn	Se	before	Colour arter
A	0.1	0.001	0.5	100	0	grey	yellow/grey*
В	0.2	0.001	0.5	83	17	grey	grey
C	0.3	0.001	0.5	94	6	grey	grey
D	0.1	0.010	0.5	88	12	grey/red*	yellow/grey
E	0.2	0.010	0.5	85	15	grey	grey
F	0.3	0.010	0.5	54	46	grey	grey
Н	0.2	0.100	0.5	46	54	grey/red	grey/yellow
I	0.3	0.100	0.5	44	55	grey/red*	yellow/grey*

Table 7-4 Summary of the composition of the ZnSe solutions discussed in this section, % weight of the EDX analysis before annealing and the colour of ZnSe films before and after annealing.

The three ZnSe films that gave reasonable ratio of Zn/Se were also analysed using XRD to confirm the presence of ZnSe. The XRD analysis for ZnSe modified carbon paper electrodes for sample H and I did not confirm the presence of ZnSe, instead, ZnO and SeO₂ were found in those samples. Sample F was analysed and it was found that the characteristic peaks in figure 7-22 could be attributed to the cubic ZnSe phase. The diffraction peaks at $2\theta^{\circ}$ =27.26°, 45.24° and 53.52° were attributed to (111), (220) and (311) planes, respectively of the cubic ZnSe phase. This is in agreement with previous reports on deposited ZnSe films which showed that the films can form a cubic zinc blende.[223-227] ZnO was also found in this sample and the ratio of ZnSe/ZnO was 3.

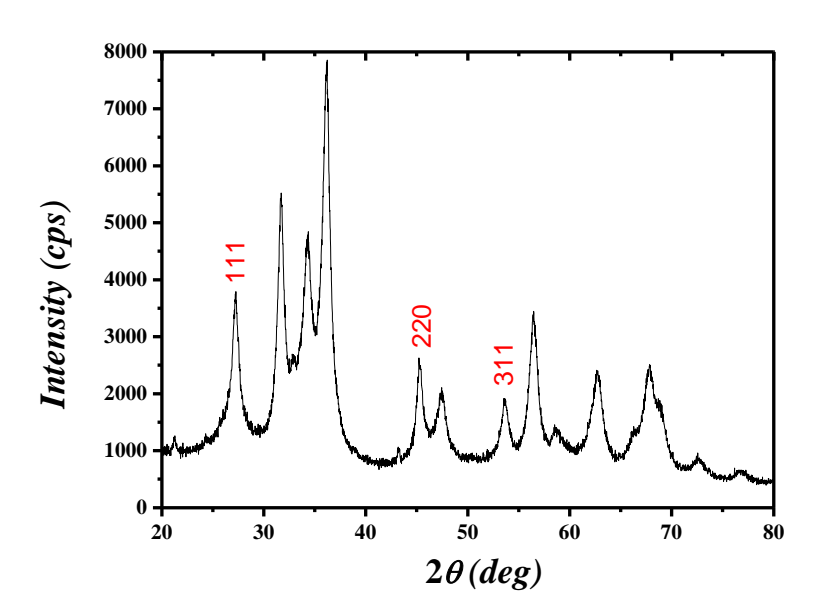


Figure 7-22 XRD pattern of a ZnSe thin film deposited on carbon paper electrode prepared from a solution containing 0.3 M ZnSO₄, 0.1 M SeO₂ and 0.5 M (NH₄)₂SO₄. The film was prepared by potential step from +0.5 V to -1.315 V vs. SCE for two hours.

^{*} The colour of these films was not uniform, which might indicate different compounds formed on the substrate.

7.2.2 Simple p-n junction diodes

In order to test the electrical properties of the ZnSe layers grown by the electrodeposition method, simple p-n junction diodes were fabricated using the best samples, i.e. those that gave the Zn/Se ratios close to 50/50; so from table 7-3 sample F was chosen as n-type and the same condition was followed to prepare a p-type sample using 0.5 M of Ga salt instead. The two samples were brought physically in contact in air. I-V curve was recorded with a waveform generator (PPR1 from Hi-Tek) connected to software (AxoScope 10.3) and the software used for processing the data was Clampfit 10.3. The current was measured by a two electrode system consisting of a PPR1 waveform generator and a current follower. Figure 7-23 exhibits a good rectification and it is obvious that there is no current flowing when reverse bias is applied. The I-V response is in agreement with published work.[134, 227, 228] The difficulties in producing a p-n junction come from the structure of the deposit, it is very fragile and when the two samples were brought in contact, the deposit was easily lost or broken. The initial results observed are encouraging and are the best voltammogram observed to date.

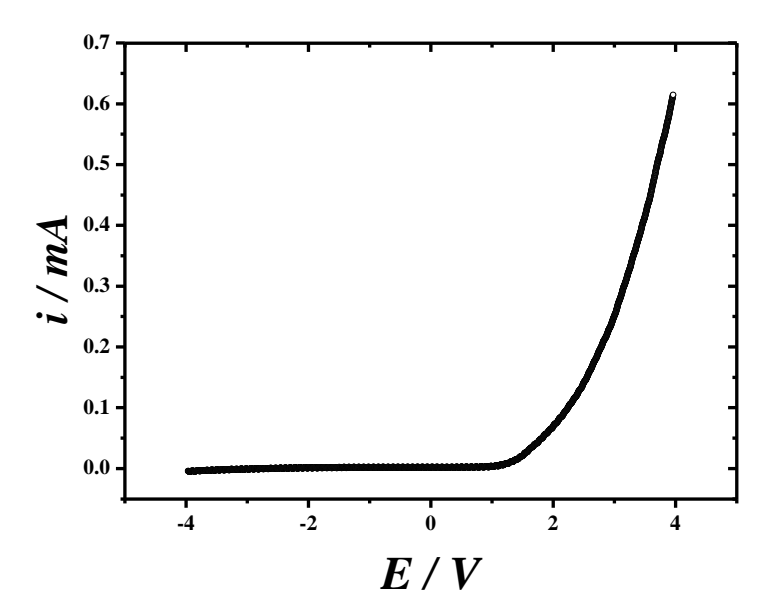


Figure 7-23 A waveform generator response for *I-V* recorded in air with two ZnSe films, respectively p-and n-doped, brought into physical contact. The films were electrodeposited on carbon paper by potential step from +0.5 V to -1.315 V vs. SCE for two hours at room temperature in 0.3 M ZnSO₄, 0.1 M SeO₂ and 0.5 M (NH₄)₂SO₄ for n-type or 0.5 M $Ga_2(SO_4)_3$ for p-type.. Both films were annealed at 300 °C in an Ar atmosphere.

7.3 Conclusion

Overall several of the initial objectives have been met but key aspects of the project remain to be investigated. Although we successfully achieved the co-deposition of ZnSe nanostructures and the simultaneous p- and n- type, doping with Ga_2SO_4 and $(NH_4)_2(SO_4)_3$ respectively, we did not manage

to proceed to the XPS characterisation stage and light generation trials. The results obtained so far are nevertheless very encouraging.

EDX confirmed the presence of both Zn and Se in the films and showed that their ratio was affected by the deposition time and the respective concentrations. The photoelectrochemical characterization suggested the material is n-type when deposited in the presence of N, and p-type when depositing in presence of Ga. The measurements carried out with electrochemical impedance spectroscopy identified p- and n-type when using Ga and N respectively. However these experiments should be repeated to confirm the EIS results. Physical contact in air between p- and n-type films presented a current-voltage curve with diode-like characteristics but reproducibility was poor, possibly because of moisture within the films. XRD confirmed the presence of cubic ZnSe but the deposits were not entirely pure as XRD also showed the presence of ZnO. The photoelectrochemical and EIS characterisation should however be repeated to assess the variability in electrochemical performance between deposits. Future work should also aim to refine some of the parameters for co-deposition and doping of the ZnSe semiconductor deposits, perform XPS characterisation, and crucially, perform light emitting tests by creating an electrical contact between separate electrodes, respectively bearing a p- and n-type ZnSe centre; this could be done by micromanipulation under an optical microscope.

8. Conclusions and future work

The main aim of this project was to deposit metal nanocentres and study the initial stages of their nucleation and growth by either observing the shape of the current transient or obtaining quantitative information about the nanoparticles, and then to examine their properties toward different reactions. Nanoparticles of palladium, platinum (see appendix) and ZnSe were successfully electrodeposited. Initially, the substrate was the first issue investigated to determine which one was ideal to study the early stages of nucleation and growth. The ideal substrate was to have few defects and require no treatment to improve the reproducibility. Different types of carbon electrodes were used to study the nucleation and growth. The nucleation and growth of palladium particles was studied on C fibres; a set of experiments was carried out by varying the deposition potential and the deposition time. The potentials were chosen in different regions from the palladium cyclic voltammogram and it was decided to choose a low overpotential (-0.15 V vs. SCE) located in the start of the reduction wave where the electrodeposition is thought to be kinetically controlled; this potential was chosen to drop the density of particles and to prevent their aggregation. Using high resolution electron microscopy enabled us to clearly observe particles ranging between 50 and 20 nm. The density of Pd nanoparticles decreased with decreasing deposition times. Moreover we noticed that the structure of the CF affected the deposits; it was clear in some images that the preferred area of deposition was the lines related to the structure of the CF. Nanoparticles were successfully electrodeposited on HOPG, where we found the best conditions were a deposition potential of 0.2 V vs. SCE and deposition time ≤ 10 s. With these conditions the particle size ranged between 18 and 1.5 nm. The particles were observed by AFM since it is considered as one of the best techniques to determine the particle height. The way of peeling off the layers of graphite might affect the likelihood of having a similar substrate each time. Even with a substrate as flat as HOPG, it is clear that the substrate texture, structure and defects offer an array of active sites which influence the nucleation and growth process and thus determine the distribution of particles. Therefore we decided to use surfactant templates to help reduce the chances of overlap between centres.

Further work focused on the influence of the surfactant on the nucleation and growth of Pd nanoparticles on glassy carbon over a range of deposition potentials. Voltammetry and chronoamperometry were used to form the palladium centres and study their growth. Theoretical models were used to investigate the effect of the surfactant on the early stages of nucleation and growth of the Pd nanoparticles by analysing the current transients. We first used the Cottrell equation to calculate the diffusion coefficient D for the Pd salt from the deposition current at long times. We found that the D values hardly changed with E_{dep} . In contrast, the diffusion coefficient decreased as the percentage weight of surfactant increased. This behaviour reflected the dependence of the diffusion coefficient on viscosity. Secondly the transients were normalized and analysed with the

Scharifker-Hills model (SH) to assess whether the dimensionless curves (i/i_{max} vs. t/t_{max}) had the characteristic shape for instantaneous or progressive nucleation. The SH model suffers from the requirement to determine t_{max} and i_{max} which are not easily obtained when low overpotential is applied. The SH model can just describe the limiting cases of instantaneous and progressive nucleation and cannot predict accurately the changes that occur at the transition from one nucleation type into the other; our experimental current transients did not really match either nucleation mechanisms. Thirdly, the transients were analysed with the Heerman and Tarallo model (HT) to estimate the number of active sites N_o and nucleation rate A as a function of experimental conditions. The non-linear fitting of the experimental transients to the HT model was done with and without weighting to assess the validity of the parameters produced by non-linear regression. After comparing all the parameters resulting from the fitted data, we found that the different weighting methods gave very different values which could not be trusted. So the analysis of the nucleation and growth parameters in terms of the surfactant weight percent was made with the values obtained with unweighted non-linear regression. Irrespective of the plating mixture used, A and N_0 values were found to decrease when the deposition potential was made more positive for each set of potentials. The surfactant wt.% was found to affect the nucleation and growth with both A and N_o decreasing from 0 to 2 to 10 wt.%; interestingly, A and N_o were found to be significantly larger in the 48 wt.% mixture. The reason behind this is unknown. One of the most important observations made was that the lyotropic liquid crystal template influences the morphology and electrochemical activity of the Pd deposits prepared on the GC substrates. The differences in morphology are reflected in the voltammetry recorded in acid but the electroactivity of the deposits for all the test reactions considered far exceeds what might be reasonably expected on the basis of the electroactive areas. It was beyond the scope of the study to investigate the structure of the nanoparticles but a possible explanation is that the presence of the template and the use of large overpotentials produced facetted particles with far more atoms on edges than those produced without surfactant. We have no explanation to support the superior performance of the deposits prepared with the 10% mixture. Preliminary work was undertaken to explore the micellar region but results are not included in this thesis as it still needs further investigation. However the new results confirmed what we had observed with the micellar mixtures, but they still do not offer an explanation as to why there is a peak of electrochemical activity for particles produced in the micellar phase. For future work, we are planning to investigate the structure-activity relationship over a range of surfactant weight ratios within the micellar phase, and then study their activity for some reactions. XRD is suggested to be a good technique to estimate the nanocrystal size while helium ion microscopy can reveal more detailed information about the morphology of the particles and the substrate. The same work could also be done by dropping the deposition charge density below 63.7 mC cm⁻² and applying lower overpotentials to make the reduction even more kinetically controlled and reduce the charge passed until particles appear unconnected.

Producing nanoparticles of p- and n-type ZnSe was the second aim in this research. The ZnSe was electrochemically deposited on different carbon substrates and conditions were investigated to control the Zn/Se composition ratio and dope the deposits during the deposition. There is a shortage of studies in this field specially using an electrochemical technique to deposit nanoparticles of semiconductor and crucially dope them appropriately, so the long term aim in this research was to exploit the skills developed in the nucleation and growth of metal particles to try and produce individual semiconducting particles smaller than 200 nm in size. At the start the work was done with large electrodes for a few reasons: the ease of handling large electrodes and to facilitate the characterization as most techniques require thick deposits to study the morphology or the composition. Overall several of the initial objectives were met but key aspects of the project remain to be investigated. Although we successfully achieved the co-deposition of ZnSe nanostructures and the simultaneous p-, respectively n-type, by doping in situ with Ga_2SO_4 and $(NH_4)_2(SO_4)_3$ respectively, we did not manage to proceed to the XPS characterisation stage and light generation trials. The results obtained so far are encouraging but the photoelectrochemical and impedance characterization need to be repeated to confirm that depositing in presence of N produced an n-type material while depositing in presence of Ga produced a p-type material. EDX confirmed the presence for both deposited material of Zn and Se and by varying both of their concentrations we managed to get the targeted equal amount of Zn and Se in the deposits. The characterization by XRD confirmed the presence of a cubic ZnSe phase attributed to the sample prepared from solution containing 0.3 M ZnSO₄, 0.1 M SeO₂ and 0.5 M $(NH_4)_2SO_4$ for n-type or 0.5 M $Ga_2(SO4)_3$ for p-type; the diffraction peaks found at $2\theta = 27.26^{\circ}$, 45.24° and 53.52° were attributed to (111), (220) and (311) planes respectively. This sample was not pure ZnSe as ZnO was also found on the XRD pattern. The same sample exhibited good rectifying currentvoltage characteristics. Lots of difficulties arose in this project; the structure of the deposits made it challenging to characterize the films, for example when losing the film while trying to record I-V curves, so it will be important for developing this project to find some additives that can improve the quality of the deposits. Also, the evolution of hydrogen bubbles during the co-deposition was one issue that made the deposits less adhesive on the electrode even when applying low overpotentials. For future work, we have several suggestions to improve this project; changing the electroplating bath to a non-aqueous solvent could help prevent hydrogen bubbles formation and produce good films with fewer defects. Future work should also consider refining some of the parameters for co-deposition and doping of the ZnSe semiconductor deposits, perform XPS characterisation, and crucially, perform light emitting tests by creating an electrical contact between separate electrodes, respectively bearing a p- and n-type ZnSe centre, for example by micromanipulation under an optical microscope.

9. Electrodeposition of platinum from lyotropic liquid crystals mixture

The lyotropic liquid crystal mixture, specifically hexagonal phase has been widely used in providing templates for electrodeposition, as it self-assembles in the mixture forming nanostructure moulds. In the earlier studies, the electrodeposition of platinum on gold substrate had always been a continuous layer of platinum deposited onto the electrode surface. Therefore, in this study, the lyotropic liquid crystalline mixture is used with the aim to produce small isolated platinum centres on gold microdisc substrate at low charge density. The reduction of platinum (IV) in the presence of the lyotropic liquid crystal mixture, specifically in micellar and hexagonal phases, has been investigated.

9.1 Electrodeposition via cyclic voltammetry

The cyclic voltammogram in each of the plating mixture is recorded at gold microelectrode as shown in Figure 9-1. The inset shows the magnified voltammetric response recorded in the hexagonal phase. The two different phases of liquid crystals, the micellar phase (2 wt.% C₁₆EO₈: 84 wt.% H₂O: 14 wt.% H₂PtCl₆) and (10 wt.% C₁₆EO₈: 77 wt.% H₂O: 13 wt.% H₂PtCl₆), the hexagonal phase (42 C₁₆EO₈: 49.7 wt.% H₂O: 8.3 wt.% H₂PtCl₆) and also the aqueous solution of wt.% hexachloroplatinate (IV) acid (0 wt.% C₁₆EO₈: 86 wt.% H₂O: 14 wt.% H₂PtCl₆) were investigated at room temperature.

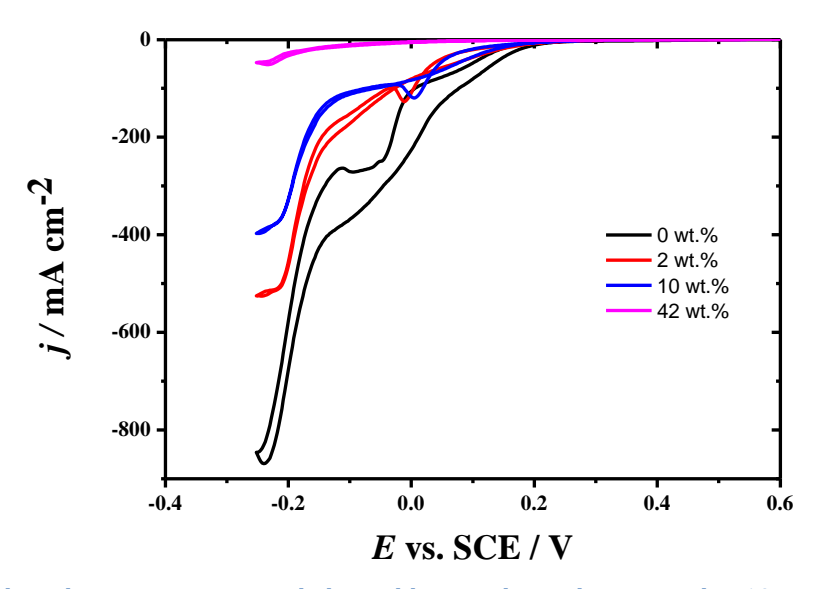


Figure 9-1 Cyclic voltammograms recorded at gold microelectrodes scanned at 10 mV s⁻¹ in different ratio of lyotropic liquid crystals mixture; (a) 0 wt.% C₁₆EO₈: 86 wt.% H₂O: 14 wt.% H₂PtCl₆ (b) 2 wt.% C₁₆EO₈: 84 wt.% H₂O: 14 wt.% H₂PtCl₆ (c) 10 wt.% C₁₆EO₈: 77 wt.% H₂O: 13 wt.% H₂PtCl₆ (d) 60 wt.% C₁₆EO₈: 34 wt.% H_2O : 6 wt.% H_2PtCl_6 . Voltammograms (a) , (b) and (c) recorded at 25 μm and (d) at 50 μm diameter.

The voltammograms were recorded within the same potential window ranging from +0.6 V to -0.25 V with respect to SCE with a potential scan rate of 10 mV s⁻¹. A platinum mesh and saturated calomel electrode are used as the counter and reference electrodes respectively. All the electrodes were immersed in the plating bath mixtures. However due to the high viscosity, the hexagonal phase plating mixture was placed onto a platinum mesh that acts as the counter electrode. The working and reference electrodes were arranged closely together and immersed into the mixture. On the forward scan, the cathodic wave started to be observed at +0.2 V with respect to SCE, followed by a sharp reduction peak produced in all voltammograms except d, Moreover, with same radius the current density measured at the reduction peak decreases as the plating mixture becomes more viscous. The current density observed at the first reduction peak is highest in aqueous hexachloroplatinate (IV) acid solution. Although similar concentration of hexachloroplatinate (IV) acid used in each of the plating mixture, the increase in amount of surfactant influenced the mass transport of the species reaching the electrode surface; high viscosity of plating mixture leads to lower rate of diffusion, thereby smaller current density obtained. The reduction peak is followed by an increase in current density that is assigned for the onset of hydrogen evolution. The current density for the hydrogen evolution also increases with the amount of platinum deposited.

On the reverse scan, there are two drawn out reduction waves with the presence of characteristic nucleation loop observed at potentials negative to +0.4 V vs SCE. Again there is no anodic current observed on the reverse scan. Thus, there is no platinum being removed from the electrode surface. In addition, a background current (not shown) also recorded at gold microelectrode in a mixture containing a ratio of 42 wt. % octaethyleneglycol monohexadecylether and 58 wt. % hydrochloric acid (~ 0.4 M). There is no increase in current density within the same potential window. Hence, the cathodic waves produced negative to +0.4 V are attributed only to the reduction of platinum (IV).

1) Characterisation of mesoporous metal films by voltammetry in acid

The deposition of platinum onto the gold microelectrode surface has been characterised in 1 M sulphuric acid. Figure 9-2 illustrates cyclic voltammograms in 1M sulphuric acid recorded at the platinum coated gold microelectrode after undergoing two consecutive cyclic voltammograms in different composition of plating mixtures scanned at 200 mV s⁻¹. It is clear that all cyclic voltammograms exhibit the characteristic features for polycrystalline platinum. It is observed that the features characteristic of platinum oxide reduction / oxidation peaks and hydrogen adsorption / desorption peaks. This seems that the gold microelectrodes covered with continuous layer of platinum.

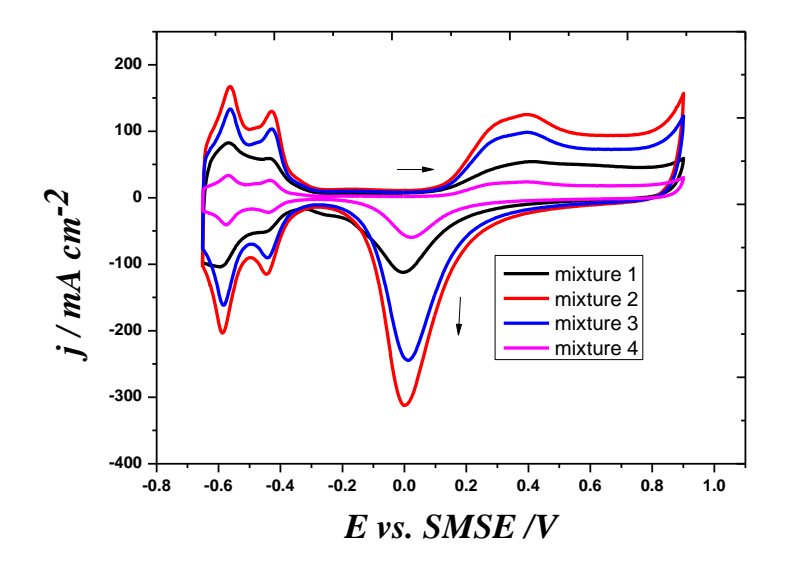


Figure 9-2 Cyclic voltammograms recorded at gold microelectrodes scanned at 10 mV s⁻¹ in different ratio of lyotropic liquid crystals mixture; (mixture 1) 0 wt.% C₁₆EO₈: 86 wt.% H₂O: 14 wt.% H₂PtCl₆ (mixture 2) 2 wt.% C₁₆EO₈: 84 wt.% H₂O: 14 wt.% H₂PtCl₆ (mixture 3) 10 wt.% C₁₆EO₈: 77 wt.% H₂O: 13 wt.% H_2PtCl_6 (mixture 4) 60 wt.% $C_{16}EO_8$: 34 wt.% H_2O : 6 wt.% H_2PtCl_6 . Voltammograms (mixture 1), (mixture 2) and (mixture 3) recorded at 25 µm and (mixture 4) at 50 µm diameter.

Table 9-1 the charge passed, deposition time, charge of (Average of the hydrogen adsorption / desorption peaks), roughness factor, platinum loading and the specific catalyst area of the platinum coated gold microelectrode.

Mixture	Q _{passed} / C	Q _{pt} / C	Q _{(ads+des)/2}	$R_{\rm f}({\rm Pt})$	W/ μg cm ⁻²	S/m^2g^{-1}	Film
wt.%	cm ⁻²	Qpt / ℃	/ C cm ⁻² (Pt)	Ι (Ι ()	νν με οπ	57 m g	thickness
			/ C ciii (Pt)				(µm)
0	40.29	0.086	0.070	333	2.0×10^4	1.67	9.49
2	25.91	0.289	0.139	662	1.3×10^4	5.09	6.11
10	19.64	0.237	0.114	543	1.0×10^4	5.43	4.63
42	2.17	0.055	0.026	124	0.2×10^4	6.19	0.51

The surface area of each electrodeposited film was determined by cyclic voltammetry in 1 M sulphuric acid, then integrated the areas under the hydrogen adsorption and desorption peaks, in order to get the charge $Q_{(ads+des)/2}$. The hydrogen area is easily integrated, while with Pd the hydrogen area is quiet complicated because of desorption and absorption process. Thus the electroactive area can be calculated by dividing $Q_{(ads+des)/2}$ with a conversion factor of 210 μ C cm⁻² Q_{mono} .

$$A_{elec} = \frac{Q_{ads+des}}{Q_{mono}}$$
 (5)

The total deposition charge density passed after recording two consecutive cyclic voltammograms in aqueous hexachloroplatinate (IV) acid at 25 µm diameter gold electrode is 40 C cm⁻². A smooth platinum layer with thickness of 9.49 µm has been observed with a roughness factor of 333. The specific catalyst area is found to be 1.67 m² g⁻¹. The electrodeposition of platinum in hexagonal phase (42 wt.% $C_{16}EO_8$: 77 wt.% H_2O : 13 wt.% H_2PtCl_6) has the highest value of the specific catalyst area of (6.19 m² g⁻¹), Although the only total deposition charge density passed 2.17 C cm⁻² with 123.81 and 0.511 µm of the roughness factor and layer thickness respectively.

The specific catalyst area of the platinum coated gold microelectrode is higher when the deposition is done in the presence of surfactant. The roughness factor obtained from the cyclic voltammogram in acid solution for both micellar phases were great value comparable with aqueous solution, although the charge density passed during electrodeposition in aqueous solution is much bigger the amount in the micellar phase. So, the increase in the electroactive area can be assigned to the presence of nanostructured platinum, however the nanostructured platinum on the gold was not observable in the scanning electron microscope. This experiments indicate the effect of surfactant, we found that although, passing large total deposition charge in the 42 wt.% there is slight different in the specific catalyst between micellar phase and hexagonal phase.

2) Characterisation of mesoporous metal films by Scanning Electron Microscopy (SEM)

The morphology of the electrode surface is also observed under the scanning electron microscope. Figure 9-3 shows the SEM images of the electrode surfaces after the electrodeposition in the different plating mixtures. The thickness of the films were measured from SEM images and estimated from Faraday's law and Table 9-2 displays the actual measurements and the estimated thickness layer of the platinum film after the electrodeposition. The actual thickness of the deposit at the edge is recorded using the scanning electron microscope. In all cases we found that the Pt formed films that completely covered the electrodes.

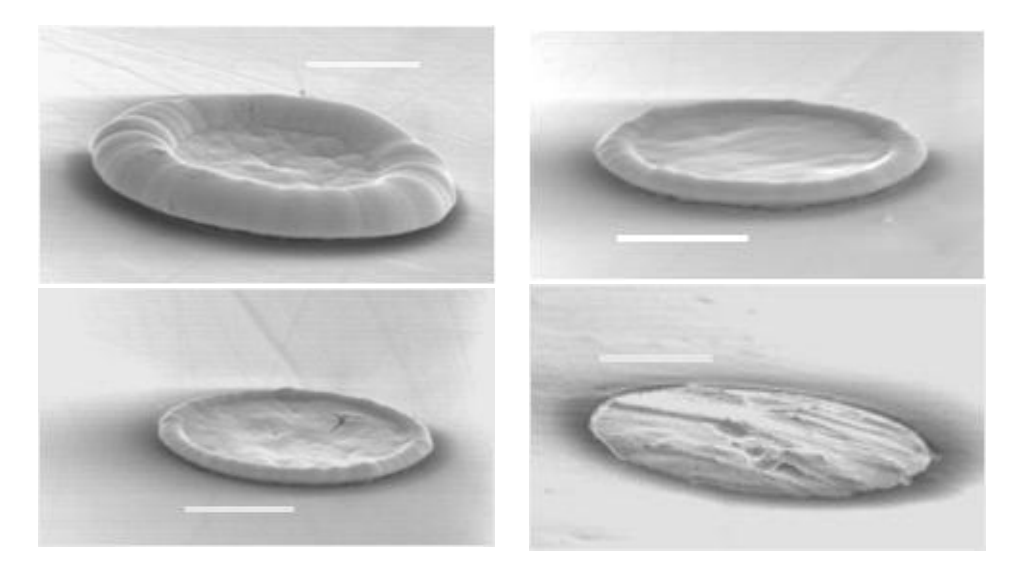


Figure 9-3 SEM images of the platinum coated microelectrodes after undergoing two consecutive cyclic voltammograms in (a) 0 wt.% C₁₆EO₈: 86 wt.% H₂O: 14 wt.% H₂PtCl₆ (b) 2 wt.% C₁₆EO₈: 84 wt.% H₂O: $14 \text{ wt.}\% \text{ H}_2\text{PtCl}_6$ (c) $10 \text{ wt.}\% \text{ C}_{16}\text{EO}_8$: $77 \text{ wt.}\% \text{ H}_2\text{O}$: $13 \text{ wt.}\% \text{ H}_2\text{PtCl}_6$ (d) $60 \text{ wt.}\% \text{ C}_{16}\text{EO}_8$: $34 \text{ wt.}\% \text{ H}_2\text{O}$: $6 \text{ wt.$ wt.% H_2PtCl_6 . (a), (b) and (c) recorded at 25 μ m and (d) at 50 μ m diameter electrodes. Scale bar is 10 μ m.

Table 9-2 The thickness layer of platinum deposit measured using the SEM and estimated value using the Faraday's law.

Wt.%	Measured by SEM	Estimated thickness using Faraday's law / µm
0	4.80	9.49
2	1.98	6.11
10	1.61	4.63
42	0.45	0.51

9.2 Electrodeposition of platinum at various charge densities

A set of single potential step experiments display in figure 9-4 was carried out in a mixture containing 42 wt.% C₁₆EO₈: 49.7 wt.% H₂O: 8.3 wt.% H₂PtCl₆ for different deposition charges ranging from 2 to 0.1 C cm⁻². The potential was stepped from +0.6 V to a very positive potential (0.0 V vs SCE) for different deposition total charge passed. For every single experiment, a different gold microelectrode was used as a substrate.

In all of the experiments, rising transients are observed initially resulting from the nucleation and growth of the platinum nuclei onto the gold. The response shows that all current transients are not identical which corresponds to low level of reproducibility between electrodes. It might be attributed to using different physical substrates, and the way to initiate and distribute the deposited small amount of platinum might be affected.

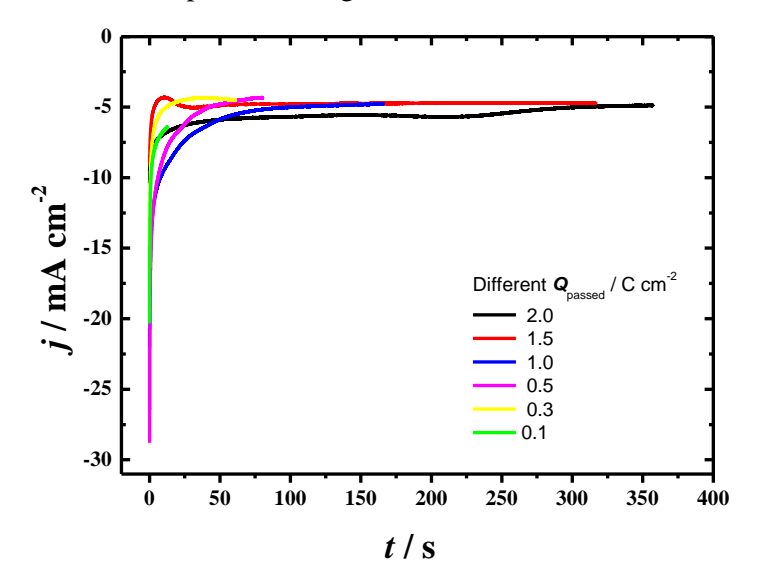


Figure 9-4 Current transients recorded in 42 wt.% $C_{16}EO_8$: 49.7 wt.% H_2O : 8.3 wt.% H_2PtCl_6 at fixed electrodeposition potential 0.0 V vs SCE, at 50 μ m Au diameter microdisc.

The cyclic voltammograms recorded after passing different charge densities presents in figure 9-5. All CVs demonstrated features characteristic of bulk platinum with the presence of platinum oxide reduction / oxidation peaks and hydrogen adsorption / desorption peaks. In addition, at small charge densities the gold oxide reduction peak is observed indicating that the

platinum deposits have not fully covered the entire gold surface and that clear from the CV which can be seen both of oxide reduction peaks for Pt and Au.

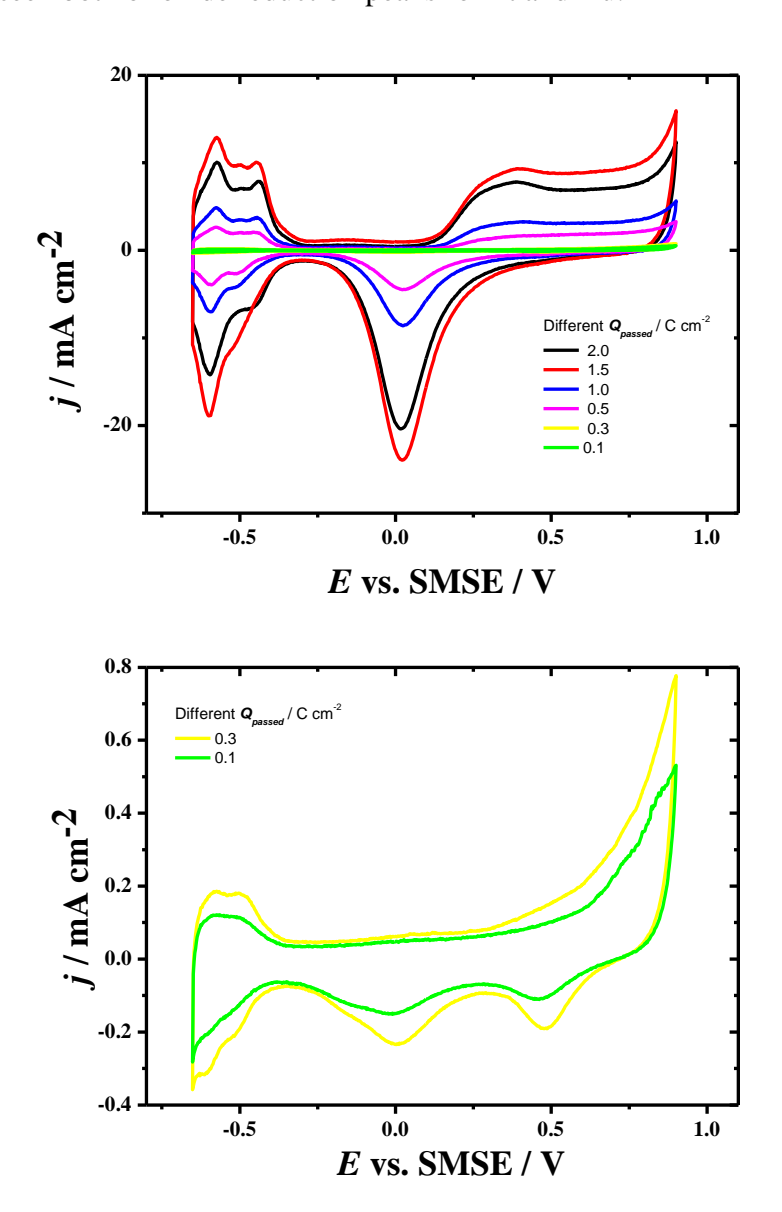


Figure 9-5 CVs in 1 M H₂SO₄ at 200 mV s⁻¹ after undergoing potential step at different charge densities and at fixed electrodeposition potential 0.0~V, at $50~\mu m$ Au diameter microdisc. The inset shows CVs in acid at small charge densities of 0.3 and 0.1 C cm⁻² respectively. In the top all CVs for all deposition charges, the figure in the bottom show rescaled CVs for Q = 0.3 and 0.1 C/ cm⁻².

Table 9-3 summarizes film parameters evaluated from the CVs in 1 M H₂SO₄; as the charge density increases, the Pt oxide charge and roughness factor increase as well. On the other hand, the Pt film becomes smooth as the deposition charge was chosen to be less than 0.5 C cm⁻².

Table 9-3 Deposition charge, charge of Pt oxide reduction, average charge for hydrogen adsorption /desorption peaks, roughness factor and the specific catalyst area of the platinum coated gold microelectrode. Q_{passed} = 2.5 C cm⁻², E_{dep} = 0.0 V after undergoing the potential step in 42 wt.% $C_{16}EO_8$: 49.7 wt.% H_2O : 8.3 wt.% H_2PtCl_6 .

Q/C cm ⁻²	Q _{pt oxide reduction} / C cm ⁻²	Q _{(ads+des)/2} / C cm ²	R_{f}	S/m^2g^{-1}
2.0	0.020	9.07×10 ⁻³	43	4.3
1.5	0.023	0.012	57	7.5
1.0	8.44×10 ⁻³	4.31×10 ⁻³	21	4.1
0.5	4.33×10 ⁻³	2.49×10 ⁻³	12	4.7
0.3	1.91×10 ⁻⁴	1.60×10 ⁻⁴	1	0.5
0.1	1.13×10 ⁻⁴	9.25×10 ⁻⁵	0	0.9

The same observations were found with the platinum electrodeposition by cyclic voltammetry in the presence of surfactant as well as aqueous solution. It was found that a high viscosity of plating mixture leads to lower rate of diffusion; thereby smaller current density is obtained. This may be attributed to the possibility of the surfactant adsorbing on the electrode surface, thus inhibiting the nucleation of platinum. Furthermore, Pt electrodeposition in presence of surfactant has slightly higher specific catalytic area. The deposition bath with no surfactant solution has produced a film with the lowest specific catalytic area, although applying the same deposition conditions. Partial coverage of platinum deposited can be obtained by controlling electrodeposition potential and the charge density. Thus, lower deposition potential and small deposition charge smaller than 0.4 C cm⁻² could offer the best conditions to obtained partial coverage.

10. References

- [1] L. Zhang, Z. Fang, G.C. Zhao, X.W. Wei, Int. J. Electrochem. Sci. 3 (2008) 746.
- [2] J.M. Elliott, P.R. Birkin, P.N. Bartlett, G.S. Attard, Langmuir 15 (1999) 7411.
- [3] G.S. Attard, P.N. Bartlett, N.R.B. Coleman, J.M. Elliott, J.R. Owen, J.H. Wang, Science 278 (1997) 838.
- [4] S. Hrapovic, Y. Liu, K.B. Male, J.H. Luong, Anal. Chem. 76 (2004) 1083.
- [5] M. Yang, Y. Yang, Y. Liu, G. Shen, R. Yu, Biosens. Bioelectron. 21 (2006) 1125.
- [6] Y. Sun, Y. Xia, Science 298 (2002) 2176.
- [7] W.P. Halperin, Rev. Mod. Phys. 58 (1986) 533.
- [8] A.S. Edelstein, R. Cammaratra, Nanomaterials: synthesis, properties and applications, CRC Press, New York, 1998.
- [9] C. Petit, A. Taleb, M.-P. Pileni, Adv. Mater. 10 (1998) 259.
- [10] W. Lu, B. Wang, K.D. Wang, X.P. Wang, J.G. Hou, Langmuir 19 (2003) 5887.
- [11] C. Murray, D.J. Norris, M.G. Bawendi, J. Am. Chem. Soc. 115 (1993) 8706.
- [12] H.Y. Zhang, Z.Q. Hu, K. Lu, Nanostruct. Mater. 5 (1995) 41.
- [13] F.L. Li, B.L. Zhang, S.J. Dong, E.K. Wang, Electrochim. Acta 42 (1997) 2563.
- [14] R. Rioux, H. Song, M. Grass, S. Habas, K. Niesz, J. Hoefelmeyer, P. Yang, G. Somorjai, Top. Catal. 39 (2006) 167.
- [15] R. Narayanan, M.A. El-Sayed, J. Am. Chem. Soc. 126 (2004) 7194.
- [16] I.G. Casella, M. Contursi, Electrochim. Acta 52 (2007) 7028.
- [17] A. Robertson, U. Erb, G. Palumbo, Nanostruct. Mater. 12 (1999) 1035.
- [18] P.M. Anderson, C. Li, Nanostruct. Mater. 5 (1995) 349.
- [19] H. Gleiter, Acta Mater. 48 (2000) 1.
- [20] H. Natter, M. Schmelzer, R. Hempelmann, J. Mater. Res. 13 (1998) 1186.
- [21] L.P. Bicelli, B. Bozzini, C. Mele, L. D'Urzo, Int. J. Electrochem. Sci. 3 (2008) 356.
- [22] J. Eskhult, Doctor of philosophy, Kristianstad University, 2007.
- [23] D. Pletcher, A First Course in Electrode Processes, the Royal Society of Chemistry, Cambrige, 2009
- [24] R. Kjellander, Trans. Faraday Soc. 78 (1982) 2025.
- [25] K.S. Choi, E.W. McFarland, G.D. Stucky, Adv. Mater. 15 (2003) 2018.
- [26] H. Randriamahazaka, V. Noel, C. Chevrot, J. Electroanal. Chem. 472 (1999) 103.
- [27] M. Fleischmann, H. Thirsk, Electrochim. Acta 2 (1960) 22.
- [28] A. Krause, M. Uhlemann, A. Gebert, L. Schultz, Thin Solid Films 515 (2006) 1694.
- [29] A. Milchev, L. Heerman, Electrochim. Acta 48 (2003) 2903.
- [30] J.W. Cahn, Acta Metall. 4 (1956) 449.
- [31] B. Scharifker, G. Hills, Electrochim. Acta 28 (1983) 879.
- [32] M. Peykova, E. Michailova, D. Stoychev, A. Milchev, Electrochim. Acta 40 (1995) 2595.
- [33] M.E. Hyde, R.G. Compton, J. Electroanal. Chem. 549 (2003) 1.
- [34] M. Fleischmann, H. Thirsk, Electrochim. Acta 1 (1959) 146.
- [35] M. Fleischmann, H. Thirsk, J. Electrochem. Soc. 110 (1963) 688.
- [36] M. Fleischmann, J. Mansfield, H. Thirsk, H. Wilson, L. Wynne-Jones, Electrochim. Acta 12 (1967) 967.
- [37] M. Fleischmann, H. Thirsk, Adv. Electrochem. Sci. Eng. 3 (1963) 123.
- [38] D. Astley, J. Harrison, H. Thirsk, J. Electroanal. Chem. 19 (1968) 325.
- [39] G. Hills, D. Schiffrin, J. Thompson, Electrochim. Acta 19 (1974) 657.
- [40] D. Astley, J. Harrison, H. Thirsk, Trans. Faraday Soc. 64 (1968) 192.
- [41] K.J. Vetter, Zeitschrift für Elektrochemie, Berichte der Bunsengesellschaft für physikalische Chemie 59 (1955) 435.
- [42] W. Plieth, J. Phys. Chem. 86 (1982) 3166.
- [43] G. Gunawardena, G. Hills, I. Montenegro, B. Scharifker, J. Electroanal. Chem. 138 (1982) 225.

- [44] D. Grujicic, B. Pesic, Electrochim. Acta 47 (2002) 2901.
- [45] M. Sluyters-Rehbach, J. Wijenberg, E. Bosco, J. Sluyters, J. Electroanal. Chem. 236 (1987) 1.
- [46] J. Mostany, M. Palomar Pardavé, I. González, J. Electrochem. Soc. 146 (1999) 1005.
- [47] L. Heerman, A. Tarallo, J. Electroanal. Chem. 451 (1998) 101.
- [48] L. Heerman, A. Tarallo, Electrochem. Commun. 2 (2000) 85.
- [49] M. Pourbaix, Atlas of electrochemical equilibria in aqueous solutions, National Association of Corrosion Engineers, Houston, 1974.
- [50] X.D. Mu, D.G. Evans, Y.A. Kou, Catal. Lett. 97 (2004) 151.
- [51] R.W.J. Scott, H.C. Ye, R.R. Henriquez, R.M. Crooks, Chem. Mater. 15 (2003) 3873.
- [52] S.W. Kim, J. Park, Y. Jang, Y. Chung, S. Hwang, T. Hyeon, Y.W. Kim, Nano Lett. 3 (2003) 1289.
- [53] H. Ye, R.M. Crooks, J. Am. Chem. Soc. 127 (2005) 4930.
- [54] C. Batchelor-McAuley, C.E. Banks, A.O. Simm, T.G.J. Jones, R.G. Compton, Analyst 131 (2006) 106.
- [55] M.N. Nadagouda, R.S. Varma, Green Chem. 10 (2008) 859.
- [56] C.H. Liang, W. Xia, M. van den Berg, Y.M. Wang, H. Soltani-Ahmadi, O. Schluter, R.A. Fischer, M. Muhler, Chem. Mater. 21 (2009) 2360.
- [57] S. Mubeen, T. Zhang, B. Yoo, M.A. Deshusses, N.V. Myung, J. Phys. Chem. C 111 (2007) 6321.
- [58] T. Teranishi, M. Hosoe, T. Tanaka, M. Miyake, J. Phys. Chem. B 103 (1999) 3818.
- [59] M.T. Reetz, M. Winter, B. Tesche, Chem. Commun. (1997) 147.
- [60] S. Sugano, H. Koizumi, Microcluster Physics: édition en anglais, Springer, New York, 1998.
- [61] W.D. Knight, K. Clemenger, W.A. Deheer, W.A. Saunders, M.Y. Chou, M.L. Cohen, Phys. Rev. Lett. 52 (1984) 2141.
- [62] Y. Wang, N. Toshima, J. Phys. Chem. B 101 (1997) 5301.
- [63] Z. Wang, Z. Zha, C. Zhou, Org. Lett. 4 (2002) 1683.
- [64] W.Y. Yu, W.X. Tu, H.F. Liu, Langmuir 15 (1999) 6.
- [65] T. Yonezawa, T. Tominaga, N. Toshima, Langmuir 11 (1995) 4601.
- [66] H. Bönnemann, W. Brijoux, R. Brinkmann, T. Joußen, B. Korall, E. Dinjus, Angew. Chem., Int. Ed. Engl. 30 (1991) 1312.
- [67] J. Bitter, K. Seshan, J. Lercher, J. Catal. 171 (1997) 279.
- [68] Y. Zhou, C.Y. Wang, Y.R. Zhu, Z.Y. Chen, Chem. Mater. 11 (1999) 2310.
- [69] G. Schmid, Chem. Rev. 92 (1992) 1709.
- [70] G. Schmid, U. Giebel, W. Huster, A. Schwenk, Inorg. Chim. Acta 85 (1984) 97.
- [71] M.N. Vargaftik, I.I. Moiseev, D.I. Kochubey, K.I. Zamaraev, Faraday Discuss. 92 (1991) 13.
- [72] T. Teranishi, M. Miyake, Chem. Mater. 10 (1998) 594.
- [73] Y. Xiong, J. Chen, B. Wiley, Y. Xia, S. Aloni, Y. Yin, J. Am. Chem. Soc. 127 (2005) 7332.
- [74] Y. Sun, H.H. Wang, Adv. Mater. 19 (2007) 2818.
- [75] B.A. Zhang, D.D. Ye, J. Li, X. Zhu, Q. Liao, J. Power Sources 214 (2012) 277.
- [76] J. Lović, A. Tripković, S.L. Gojković, K.D. Popović, D. Tripković, P. Olszewski, A. Kowal, J. Electroanal. Chem. 581 (2005) 294.
- [77] C. Du, M. Chen, W. Wang, G. Yin, P. Shi, Electrochem. Commun. 12 (2010) 843.
- [78] W.P. Zhou, A. Lewera, R. Larsen, R.I. Masel, P.S. Bagus, A. Wieckowski, J. Phys. Chem. B 110 (2006) 13393.
- [79] K. Lee, S.W. Kang, S.U. Lee, K.H. Park, Y.W. Lee, S.W. Han, ACS appl. mater. inter 4 (2012) 4208.
- [80] S. Singh, Liquid crystals: fundamentals, World Scientific, Singapore, 2002.
- [81] P.J. Collings, M. Hird, Introduction to Liquid Crystals: Chemistry and Physics, Taylor & Francis, 1997.
- [82] P.N. Bartlett, Electrochem. Soc. Interface 13 (2004) 28.
- [83] D.J. Mitchell, G.J.T. Tiddy, L. Waring, T. Bostock, M.P. Mcdonald, Trans. Faraday Soc. 79 (1983) 975.

- [84] S. Kumar, Liquid crystals: experimental study of physical properties and phase transitions, Cambridge University Press, Cambridge, 2001.
- [85] P.J. Wojtowicz, P. Sheng, E. Priestley, Introduction to Liquid Crystals, Springer, New York, 1975.
- [86] P.V. Braun, S.I. Stupp, Mater. Res. Bull. 34 (1999) 463.
- [87] M. Andersson, V. Alfredsson, P. Kjellin, A.E.C. Palmqvist, Nano Lett. 2 (2002) 1403.
- [88] S. Paasch, F. Schambil, M.J. Schwuger, Langmuir 5 (1989) 1344.
- [89] J.K. Zhao, X. Chen, L.Y. Jiao, Y.C. Chai, L.Y. Wang, Scripta Mater. 51 (2004) 593.
- [90] A.M.F. Neto, S.R. Salinas, The Physics of Lyotropic Liquid Crystals: Phase Transitions and Structural Properties: Phase Transitions and Structural Properties, Oxford University Press, Oxford, 2005.
- [91] D.J. Guo, S.K. Cui, J. Solid State Electrochem. 12 (2008) 1393.
- [92] A.N. Golikand, M.G. Maragheh, S.S. Sherehjini, K.M. Taghi Ganji, M. Yari, Electroanalysis 18 (2006) 911.
- [93] R.N. Goldberg, L.G. Hepler, Chem. Rev. 68 (1968) 229.
- [94] F.A. Cotton, G. Wilkinson, C.A. Murillo, M. Bochmann, Advanced inorganic chemistry, John Wiley & Sons, Canada, 1988.
- [95] J. Jiang, A. Kucernak, J. Electroanal. Chem. 543 (2003) 187.
- [96] A.H. Whitehead, J.M. Elliott, J.R. Owen, J. Power Sources 81 (1999) 33.
- [97] G. Attard, N. Coleman, J. Elliott, Stud. Surf. Sci. Catal. 117 (1998) 89.
- [98] L.M. Plyasova, I.Y. Molina, A.N. Gavrilov, S.V. Cherepanova, O.V. Cherstiouk, N.A. Rudina, E.R. Savinova, G.A. Tsirlina, Electrochim. Acta 51 (2006) 4477.
- [99] G.S. Attard, P.N. Bartlett, N.R.B. Coleman, J.M. Elliott, J.R. Owen, Langmuir 14 (1998) 7340.
- [100] H. Härelind Ingelsten, J.-C. Béziat, K. Bergkvist, A. Palmqvist, M. Skoglundh, H. Qiuhong, L.K. Falk, K. Holmberg, Langmuir 18 (2002) 1811.
- [101] F. Mafuné, J.-y. Kohno, Y. Takeda, T. Kondow, J. Phys. Chem. B 107 (2003) 4218.
- [102] G. Surendran, L. Ramos, B. Pansu, E. Prouzet, P. Beaunier, F. Audonnet, H. Remita, Chem. Mater. 19 (2007) 5045.
- [103] J. Elliot, G. Attard, P. Bartlett, J. Owen, N. Ryan, G. Singh, J. New Mater. Electrochem. Syst. 2 (1999) 239.
- [104] M. Balkanski, Semiconductor physics and applications, Oxford University Press, Oxford, 2000.
- [105] A.K. Vijh, Electrochemistry of metals and semiconductors: the application of solid state science to electrochemical phenomena, M. Dekker, California, 1973.
- [106] V.A. Myamlin, Y.V. Pleskov, Electrochemistry of semiconductors. Springer Verlag Gmbh, New York, 1967, p. 430.
- [107] H.R. Kricheldorf, O. Nuyken, G. Swift, Handbook of polymer synthesis, CRC Press, New York, 2010.
- [108] G. Parker (Ed.)^(Eds.), Introductory Semiconductor Device Physics. Institute of physics publishing, London, 2004.
- [109] H.F. Wolf, Semiconductors, Wiley-Interscience New York, Michigan, 1971.
- [110] P.F. Kane, G.B. Larrabee, S. Knight, J. Electrochem. Soc. 117 (1970) 411C.
- [111] D.A. Neamen, B. Pevzner, Semiconductor physics and devices: basic principles, McGraw-Hill New York, New York, 2003.
- [112] K. Singh, Basic Physics, Prentice-Hall Of India Pvt. Ltd., New Delhi, 2009.
- [113] J.C. Whitaker, The electronics handbook, CRC Press, Boca Raton, 1996.
- [114] R.K. Rajput, Basic Electrical and Electronics Engineering, Laxmi Publications Ltd., New Delhi, 2007.
- [115] M. Neeraj, Textbook Of Engineering Physics, Prentice-Hall Of India Pvt. Lim., New Delhi, 2008.
- [116] U.A.B.A.P. Godse, Electronic Devices And Circuits I, Technical Publications, India, 2010.

- [117] W. Brattain, C. Garrett, Bell Syst. tech. j. 34 (1955) 129.
- [118] A.K. Vijh, Electrochemistry of metals and semiconductors; the application of solid state science to electrochemical phenomena, M. Dekker, New York, 1973.
- [119] C.Y. Cummings, PhD, University of Bath, UK, 2012.
- [120] N. Sato, Electrochemistry at Metal and Semiconductor Electrodes, Elsevier Science, Amsterdam, 1998.
- [121] A.W. Bott, Current Separations 17 (1998) 87.
- [122] M.X. Tan, P.E. Laibinis, S.T. Nguyen, J.M. Kesselman, C.E. Stanton, N.S. Lewis, Prog. Inorg. Chem. 41 (1994) 21.
- [123] G. Hodes, Electrochemistry of Nanomaterials, Wiley-VCH Verlag GmbH, Weinheim, 2001.
- [124] D. Lincot, Thin Solid Films 487 (2005) 40.
- [125] D.J. Doughery, PhD, Massachusetts Institute of Technology, California, USA, 1997.
- [126] H. Cheng, J. DePuydt, J. Potts, T. Smith, Appl. Phys. Lett. 52 (1988) 147.
- [127] F. Sakurai, M. Motozawa, K. Suto, J. Nishizawa, J. Cryst. Growth 172 (1997) 75.
- [128] J.i. Nishizawa, R. Suzuki, Y. Okuno, J. Appl. Phys. 59 (1986) 2256.
- [129] K. Matsuura, F. Takeda, K. Kurisu, Method of producing a ZnSe blue light emitting device. Sumitomo Electric Industries, Ltd, 1995.
- [130] K. Akimoto, T. Miyajima, Y. Mori, Jpn. J. Appl. Phys., Part 1 28 (1989).
- [131] M. Migita, A. Taike, M. Shiiki, H. Yamamoto, J. Cryst. Growth 101 (1990) 835.
- [132] K. Singh, J. Rai, Phys. Status Solidi. A 99 (1987) 257.
- [133] K. Kurisu, K. Matsuura, F. Takeda, Method for producing a zinc selenide blue light emitting device. Sumitomo Electric Industries, Ltd., 1993.
- [134] R.S. Nicholson, Anal. Chem. 37 (1965) 1351.
- [135] A.J. Bard, L.R. Faulkner, Electrochemical methods: fundamentals and applications, John Wiley & Sons, INC., New York, 1980.
- [136] S.P. Kounaves, Voltammetric techniques in F.A. Settle (Ed.), Handbook of instrumental techniques for analytical chemistry. Prentic Hall PTR, New Jersy, USA, 1997, p. 709.
- [137] R.G. Compton, A.C. Fisher, M.H. Latham, C.M.A. Brett, A.M.C.F.O. Brett, J. Phys. Chem. 96 (1992) 8363.
- [138] J. Vazquez-Arenas, M. Pritzker, Educ. Chem. Eng. 5 (2010) e78.
- [139] J. Goldstein, D.E. Newbury, D.C. Joy, C.E. Lyman, P. Echlin, E. Lifshin, L. Sawyer, J.R. Michael, Scanning electron microscopy and X-ray microanalysis, Springer, USA, 2003.
- [140] S.J.B. Reed, Electron microprobe analysis and scanning electron microscopy in geology, Cambridge University Press Cambridge, Cambridge, 2005.
- [141] E. Meyer, Prog. Surf. Sci. 41 (1992) 3.
- [142] F.J. Giessibl, Rev. Mod. Phys. 75 (2003) 949.
- [143] Y. Wang, S.A. Boden, D.M. Bagnall, H.N. Rutt, C.H. de Groot, Nanotechnology 23 (2012) 395302.
- [144] P. Soundarrajan, F. Schweighardt, Hydrogen Fuel: Production, Transport, and Storage, CRC Press, Boca Raton (2009) 495.
- [145] B. Pierozynski, Int. J. Electrochem. Sci. 8 (2013) 634.
- [146] S. Song, K. Taniguchi, L. Sun, Z. Cai, Electrochem. Commun. 12 (2010) 1555.
- [147] J.W. Hearle, W.E. Morton, Physical properties of textile fibres, Elsevier, UK, 2008.
- [148] M.I. Montenegro, I. Montenegro, M.A. Queirós, J.L. Daschbach, Microelectrodes: Theory and Applications: Theory and Applications, Springer, Portugal, 1991.
- [149] F. von Sturm, Angew. Chem. 100 (1988) 1260.
- [150] R. Le Penven, W. Levason, D. Pletcher, J. Appl. Electrochem. 20 (1990) 399.
- [151] J.Y. Lee, T.C. Tan, J. Electrochem. Soc. 137 (1990) 1402.
- [152] M. Rezaei, S.H. Tabaian, D.F. Haghshenas, Electrochim. Acta 59 (2012) 360.
- [153] C.A. Schneider, W.S. Rasband, K.W. Eliceiri, Nat Meth 9 (2012) 671.
- [154] Y. Kopelevich, P. Esquinazi, Adv. Mater. 19 (2007) 4559.

- [155] X.K. Lu, H. Huang, N. Nemchuk, R.S. Ruoff, Appl. Phys. Lett. 75 (1999) 193.
- [156] X.K. Lu, M.F. Yu, H. Huang, R.S. Ruoff, Nanotechnology 10 (1999) 269.
- [157] P.A. Thrower, Chemistry & Physics of Carbon, CRC Press, New York, 1996.
- [158] http://gwyddion.net/download/user-guide/gwyddion-user-guide-en.pdf.
- [159] K. Kinoshita, Carbon: electrochemical and physicochemical properties, Wiley, New York, 1988.
- [160] W. Van der Linden, J.W. Dieker, Anal. Chim. Acta 119 (1980) 1.
- [161] N.L. Pocard, D.C. Alsmeyer, R.L. Mccreery, T.X. Neenan, M.R. Callstrom, J. Am. Chem. Soc. 114 (1992) 769.
- [162] P.J.F. Harris, Philos. Mag. 84 (2004) 3159.
- [163] P. Bartlett, B. Gollas, S. Guerin, J. Marwan, PCCP 4 (2002) 3835.
- [164] L. Heerman, A. Tarallo, J. Electroanal. Chem. 470 (1999) 70.
- [165] Z. Grubač, M. Metikoš-Huković, Electrochim. Acta 43 (1998) 3175.
- [166] A.G. Munoz, S.B. Saidman, J.B. Bessone, J. Electrochem. Soc. 146 (1999) 2123.
- [167] N. Vinokur, B. Miller, Y. Avyigal, R. Kalish, J. Electrochem. Soc. 146 (1999) 125.
- [168] G. Oskam, P.M. Vereecken, P.C. Searson, J. Electrochem. Soc. 146 (1999) 1436.
- [169] J.C. Ziegler, R.I. Wielgosz, D.M. Kolb, Electrochim. Acta 45 (1999) 827.
- [170] A. Milchev, E. Michailova, I. Lesigiarska, Electrochem. Commun. 2 (2000) 407.
- [171] J. Mostany, J. Mozota, B. Scharifker, J. Electroanal. Chem. 177 (1984) 25.
- [172] M.L. Yang, Z.B. Hu, J. Electroanal. Chem. 583 (2005) 46.
- [173] D. Grujicic, B. Pesic, Electrochim. Acta 49 (2004) 4719.
- [174] M.R. Majidi, K. Asadpour-Zeynali, B. Hafezi, Electrochim. Acta 54 (2009) 1119.
- [175] D. Grujicic, B. Pesic, Electrochim. Acta 51 (2006) 2678.
- [176] M. Morbidelli, A. Varma, Chem. Eng. Sci. 38 (1983) 289.
- [177] L.H. Mendoza-Huizar, J. Robles, M. Palomar-Pardave, J. Electroanal. Chem. 545 (2003) 39.
- [178] K. Marquez, G. Staikov, J.W. Schultze, Electrochim. Acta 48 (2003) 875.
- [179] M. Arbib, B. Zhang, V. Lazarov, D. Stoychev, A. Milchev, C. Buess-Herman, J. Electroanal. Chem. 510 (2001) 67.
- [180] G.R. Iversen, M. Gergen, M.M. Gergen, Statistics: the conceptual approach, Springer, USA, 1997.
- [181] J.C. Ballesteros, P. Diaz-Arista, Y. Meas, R. Ortega, G. Trejo, Electrochim. Acta 52 (2007) 3686.
- [182] V. Tsakova, A. Milchev, J. Electroanal. Chem. 235 (1987) 237.
- [183] G.S. Attard, J.M. Corker, C.G. Göltner, S. Henke, R.H. Templer, Angew. Chem., Int. Ed. Engl. 36 (1997) 1315.
- [184] G.S. Attard, S.A.A. Leclerc, S. Maniguet, A.E. Russell, I. Nandhakumar, P.N. Bartlett, Chem. Mater. 13 (2001) 1444.
- [185] P.N. Bartlett, S. Guerin, Anal. Chem. 75 (2003) 126.
- [186] G. Denuault, C. Milhano, D. Pletcher, PCCP 7 (2005) 3545.
- [187] T. Imokawa, K.-J. Williams, G. Denuault, Anal. Chem. 78 (2006) 265.
- [188] K. Naka, H. Itoh, Y. Chujo, Nano Lett. 2 (2002) 1183.
- [189] L.D. Burke, J.K. Casey, J. Electrochem. Soc. 140 (1993) 1284.
- [190] D.A.J. Rand, R. Woods, J. Electroanal. Chem. 31 (1971) 29.
- [191] D.A.J. Rand, R. Woods, J. Electroanal. Chem. 35 (1972) 209.
- [192] L.H. Dall'Antonia, G. Tremiliosi-Filho, G. Jerkiewicz, J. Electroanal. Chem. 502 (2001) 72.
- [193] O. Winjobi, Z. Zhang, C. Liang, W. Li, Electrochim. Acta 55 (2010) 4217.
- [194] X. Wang, Y. Tang, Y. Gao, T. Lu, J. Power Sources 175 (2008) 784.
- [195] Y.W. Lee, M. Kim, Y. Kim, S.W. Kang, J.-H. Lee, S.W. Han, J. Phys. Chem. C 114 (2010) 7689.
- [196] Z.X. Liang, T.S. Zhao, J.B. Xu, L.D. Zhu, Electrochim. Acta 54 (2009) 2203.
- [197] Y.H. Qin, Yue-Jiang, H.H. Yang, X.S. Zhang, X.G. Zhou, L. Niu, W.K. Yuan, J. Power Sources 196 (2011) 4609.
- [198] L.D. Zhu, T.S. Zhao, J.B. Xu, Z.X. Liang, J. Power Sources 187 (2009) 80.

- [199] H. Meng, S. Sun, J.P. Masse, J.P. Dodelet, Chem. Mater. 20 (2008) 6998.
- [200] V. Selvaraj, M. Alagar, I. Hamerton, Appl Catal B-Environ 73 (2007) 172.
- [201] R.M. Penner, J. Phys. Chem. B 106 (2002) 3339.
- [202] D.P. Woodruff, T.A. Delchar, Modern Techniques of Surface Science, Cambridge University Press, Cambridge, 1994.
- [203] P. Bartlett, B. Gollas, S. Guerin, J. Marwan, Physical Chemistry Chemical Physics 4 (2002) 3835.
- [204] A.H. Whitehead, J.M. Elliott, J.R. Owen, G.S. Attard, Chem. Commun. (1999) 331.
- [205] R. Adžić, A. Tripković, N. Marković, J. Electroanal. Chem. 114 (1980) 37.
- [206] V. Stamenkovic, T.J. Schmidt, P.N. Ross, N.M. Markovic, J. Phys. Chem. B 106 (2002) 11970.
- [207] L.H. Mendoza-Huízar, C.H. Rios-Reyes, M.G. Gómez-Villegas, J. Mex. Chem. Soc. 53 (2009) 243.
- [208] Y.F. Lin, I.W. Sun, Electrochim. Acta 44 (1999) 2771.
- [209] G. Riveros, H. Gomez, R. Henriquez, R. Schrebler, R.E. Marotti, E.A. Dalchiele, Sol. Energy Mater. Sol. Cells 70 (2001) 255.
- [210] Y.Q. Lai, F.Y. Liu, J. Li, Z.A. Zhang, Y.X. Liu, J. Electroanal. Chem. 639 (2010) 187.
- [211] R. Kowalik, P. Zabinski, K. Fitzner, Electrochim. Acta 53 (2008) 6184.
- [212] R. Kowalik, P. Żabiński, K. Fitzner, Electrochim. Acta 53 (2008) 6184.
- [213] R. Kumaresan, M. Ichimura, E. Arai, Thin Solid Films 414 (2002) 25.
- [214] A.P. Samantilleke, I.M. Dharmadasa, K.A. Prior, K.L. Choy, J. Mei, R. Bacewicz, A. Wolska, J. Mater Sci-Mater El 12 (2001) 661.
- [215] R. Chandramohan, C. Sanjeeviraja, T. Mahalingam, Phys. Status Solidi A 163 (1997) R11.
- [216] A.P. Samantilleke, M.H. Boyle, J. Young, I.M. Dharmadasa, J Mater Sci-Mater El 9 (1998) 289.
- [217] G. Riveros, H. Gomez, R. Henriquez, R. Schrebler, R. Marotti, E. Dalchiele, Sol. Energy Mater. Sol. Cells 70 (2001) 255.
- [218] F. Sakurai, K. Suto, J. Nishizawa, Y. Oyama, M. Motozawa, Y. Hara, J. Electrochem. Soc. 147 (2000) 747.
- [219] R. Van de Krol, A. Goossens, J. Schoonman, J. Electrochem. Soc. 144 (1997) 1723.
- [220] A. Manzoli, K.I.B. Eguiluz, G.R. Salazar-Banda, S.A.S. Machado, Mater. Chem. Phys. 121 (2010) 58.
- [221] T. Mahalingam, A. Kathalingam, S. Velumani, S. Lee, M.H. Sun, K.Y. Deak, J Mater Sci 41 (2006) 3553.
- [222] C. Natarajan, M. Sharon, C. Levyclement, M. Neumannspallart, Thin Solid Films 257 (1995)
- [223] Y.G. Gudage, N.G. Deshpande, A.A. Sagade, R. Sharma, J. Alloys Compd. 488 (2009) 157.
- [224] P.K.R. Kalita, B.K. Sarma, H.L. Das, Bull. Mater. Sci. 23 (2000) 313.
- [225] Q. Li, X. Gong, C. Wang, J. Wang, K. Ip, S. Hark, Adv. Mater. 16 (2004) 1436.
- [226] A. Rizzo, M. Tagliente, L. Caneve, S. Scaglione, Thin Solid Films 368 (2000) 8.
- [227] R.B. Kale, C.D. Lokhande, Appl. Surf. Sci. 252 (2005) 929.